

Dynamic Image and Fieldmap Joint Estimation Methods for MRI Using Single-Shot Trajectories

by

Antonis Matakos

A dissertation submitted in partial fulfillment
of the requirements for the degree of
Doctor of Philosophy
(Electrical Engineering: Systems)
in The University of Michigan
2013

Doctoral Committee:

Professor Jeffrey A. Fessler, Chair
Assistant Professor Rajesh R. Nadakuditi
Research Scientist Jon-Fredrik Nielsen
Professor Douglas C. Noll

© Antonios Matakos 2013

All Rights Reserved

TABLE OF CONTENTS

LIST OF FIGURES	v
LIST OF TABLES	ix
LIST OF APPENDICES	x
ABSTRACT	xi
CHAPTER	
I. Introduction	1
II. MRI Background	5
2.1 Magnetic Fields	5
2.2 Excitation	7
2.3 Spatial Encoding and Signal Equation	7
2.4 Field Inhomogeneity in MRI	9
2.4.1 Sources and effects of inhomogeneity	9
2.4.2 Correction methods	10
2.4.3 Through-plane dephasing	11
2.5 Sensitivity Encoding in Parrallel MRI	12
2.6 Nyquist Ghosting Artifacts in EPI Trajectories	13
III. Model Based Nyquist Ghost Correction for EPI	15
3.1 Introduction	15
3.2 Theory	17
3.3 Methods	20
3.3.1 Phase Map Model	20
3.3.2 Object Mask	20
3.3.3 Quadratic Surrogate Optimization for Single-Shot EPI	26

3.3.4	Alternating Minimization Method for Multi-Shot EPI	30
3.3.5	Initialization and Approximate Estimates	32
3.3.6	Tight FOV Considerations	35
3.4	Experiments	38
3.4.1	Phantom Study	38
3.4.2	Tight FOV	40
3.4.3	Approximate Parameter Estimation	40
3.5	Results	41
3.5.1	Phantom Study	41
3.5.2	Tight FOV	44
3.5.3	Approximate Parameter Estimation	46
3.6	Discussion	47
3.7	Appendix	49
3.7.1	Quadratic Surrogate Algorithm for 1D Correction of Multi-Shot EPI	49
IV. Joint Estimation of Dynamic Image and Fieldmap		52
4.1	Introduction	52
4.2	Theory	53
4.3	Materials and Methods	57
4.3.1	Reconstruction Quality Simulation Study	59
4.3.2	Functional MRI Simulation Study	60
4.3.3	Phantom Study	61
4.4	Results	63
4.4.1	Reconstruction Quality Simulation Study	63
4.4.2	Functional MRI Simulation Study	66
4.4.3	Phantom Study	68
4.5	Discussion	72
V. Dynamic MR Image and Fieldmap Joint Reconstruction Accounting for Through-Plane Fieldmap Gradients		73
5.1	Introduction	73
5.2	Theory	74
5.3	Materials and Methods	78
5.4	Simulation results	82
5.5	Discussion	82
5.6	Appendix	86
5.6.1	Error Analysis of Approximations in (5.7) and (5.8)	86
VI. Augmented Lagrangian (AL) Approach for Joint Estimation		88

6.1	Introduction	88
6.2	Definitions	88
6.3	System Models	90
6.4	Image Estimation with Known Fieldmap	92
	6.4.1 Quadratic Regularization	97
	6.4.2 Cartesian MRI	98
	6.4.3 Single Coil Imaging	99
6.5	Fieldmap Estimation with Known Image	101
	6.5.1 Quadratic Regularization	106
	6.5.2 Cartesian MRI	107
	6.5.3 Single Coil Imaging	109
6.6	Joint Image and Fieldmap Estimation	109
VII. Discussion and Future Work		114
APPENDICES		116
BIBLIOGRAPHY		163

LIST OF FIGURES

Figure

3.1	Selection of reconstruction mask. (a) Baseline image with residual ghosting. (b) Initial mask from image thresholding. (c) Reconstruction mask from expanding (dilating) initial mask to ensure that all non-zero pixels are included. (d) Phase estimation ROI “mask” based on including only pixels whose $M/2$ counterpart has zero spin-density. (e) ROI “mask” for 2-shot acquisition. (f) ROI “mask” for 4-shot acquisition	25
3.2	Example of tight FOV imaging. (a) Image at original FOV (192×216). (b) Image at tight FOV 192×192 with visible wraparound at the top and bottom. . .	35
3.3	(a) Magnitude and phase image $\mathbf{x}_+ = \mathbf{F}'_+ \mathbf{y}_+$ from positive direction echoes and (b) magnitude and phase image $\mathbf{x}_- = \mathbf{F}'_- \mathbf{y}_-$ from negative direction echoes. (e) Difference of the two phase images. Rectangle denotes area used for conventional 1D linear correction and 2D phase map fitting.	39
3.4	Sensitivity maps from the 8 head coils used in the multi-coil experiments.	39
3.5	(a) Support constraint (mask) for 2D phase map estimation. (b) Support constraint for image reconstruction using (3.53). (c) Support constraint corresponding to regularization matrix \mathbf{R} for image reconstruction using (3.54). (d) Support constraint for NRMS error calculation.	41
3.6	(a) Digital phantom used as true image, (b) support constraint for 2D phase map estimation, and (c) sensitivity maps used in approximate phase estimation experiments.	41
3.7	Ghost corrected images from single-coil acquisition using (a,b) single-shot, (c,d) 2-shot, and (e,f) 4-shot EPI. Images from left to right: Standard 1D linear phase correction, standard 2D phase map correction, proposed model based correction. (a,c,e) Illustration with gamma correction using $\gamma = 4$ to better visualize ghosting artifacts inside the object. (b,d,f) Illustration with gamma correction using $\gamma = 0.5$ to better visualize artifacts outside the object.	42
3.8	Ghost corrected images from multi-coil acquisition using (a,b) single-shot, (c,d) 2-shot, and (e,f) 4-shot EPI. Figure placement and gamma corrections same as in Figure 3.7.	43

3.9	Image reconstructions for tight FOV experiment using 2D phase map with large slope in y . (a) Reconstruction with model mismatch from model of (3.2). (b) Reconstruction from accurate model (3.49) using support constraint (3.53). (c) Reconstruction from accurate model (3.49) using regularization (3.54).	45
3.10	Image reconstructions for tight FOV experiment using 2D phase map with small slope in y . (a) Reconstruction with model mismatch from model of (3.2). (b) Reconstruction from accurate model (3.49) using support constraint (3.53). (c) Reconstruction from accurate model (3.49) using regularization (3.54).	45
3.11	Reconstructed images from (a) single-coil, and (b) multi-coil acquisitions, corrected with phase maps estimated with the approximate FFT-based method. From top-left to bottom-right we have uncorrected reconstruction followed by reconstruction with parameter estimation using 2, 4, 8, 12, 18, and 24 times oversampling of FFT and the bottom-right using the QS approach (3.35) for comparison. .	47
4.1	“Interleaved” single-shot trajectories used in simulations and phantom studies. . .	58
4.2	True image and fieldmap used in simulations.	60
4.3	(a) Initial R_2^* map without activation regions. (b) R_2^* map during simulated fMRI study with four activation regions. (c) Normalized difference of R_2^* maps of (a) and (b) to illustrate activation.	60
4.4	Reference (a) image, (b) R_2^* map, and (c) fieldmap along with (d) initial fieldmap estimate and (e) difference of reference and initial fieldmap, for phantom Study. .	62
4.5	Sensitivity maps for phantom study.	62
4.6	Reconstructed images and fieldmaps from “interleaved” EPI trajectory, with four coils at 55dB SNR. Top row shows the reconstructed images. From left to right: Uncorrected image; reconstructed image using standard, distorted, initial fieldmap; oracle image reconstructed using true fieldmap; jointly reconstructed image. Bottom row shows the reconstructed fieldmaps. From left to right: Standard, distorted initial fieldmap; oracle fieldmap reconstructed using true image; jointly reconstructed fieldmap.	64
4.7	Reconstructed images and fieldmaps from “interleaved” spiral trajectory, with four coils at 55dB SNR. Subfigures same as in Figure 4.6.	64
4.8	Reconstructed images and fieldmaps from standard EPI trajectory, with four coils at 55dB SNR. Subfigures same as in Figure 4.6.	65
4.9	Reconstructed images and fieldmaps from standard spiral trajectory, with four coils at 55dB SNR. Subfigures same as in Figure 4.6.	65
4.10	Reconstructed images and fieldmaps from “interleaved” EPI trajectory, with single coil at 55dB SNR. Subfigures same as in Figure 4.6.	67
4.11	Reconstructed images and fieldmaps from “interleaved” spiral trajectory, with single coil at 55dB SNR. Subfigures same as in Figure 4.6.	67

4.12	Top row (a,b,c) shows results from simulated fMRI study when R_2^* decay is ignored during reconstruction. Bottom row (d,e,f) shows results when R_2^* decay is accounted for during reconstruction using the R_2^* map of Figure 4.3a. (a,d) Reconstructed images at the beginning of study (denoted as f_1) corresponding to R_2^* map of Figure 4.3a without activation. (b,e) Reconstructed images during fMRI study (denoted as f_2) corresponding to R_2^* map of Figure 4.3b with activation regions. (c,f) Normalized difference of images (defined as $(f_1 - f_2)/f_1$) to illustrate identification of activation regions.	69
4.13	Reconstructed images and fieldmaps from phantom study using “interleaved” EPI trajectory, with eight coils. (a) Uncorrected image reconstruction. (b) Image reconstruction corrected with initial fieldmap estimate of Figure 4.4d. (c) “Oracle” image reconstruction corrected with reference fieldmap of Figure 4.4c. (d) Joint image reconstruction. (e) Joint fieldmap reconstruction.	70
4.14	Reconstructed images and fieldmaps from phantom study using standard EPI trajectory, with eight coils. Subfigure placement same as in Figure 4.13.	71
5.1	True image, fieldmap, and gradient map for 4 out of 20 slices. Slices 3, 8, 13 and 18 are shown from left to right.	80
5.2	“Oracle” image, fieldmap, and gradient map for 4 out of 20 slices. Slices 3, 8, 13 and 18 are shown from left to right.	81
5.3	Image and fieldmap reconstructions for one slice (slice 3 of sequence).	83
5.4	Jointly reconstructed image, fieldmap, and gradient map for 4 out of 20 slices. Slices 3, 8, 13 and 18 are shown from left to right.	84
5.5	(a) Fieldmaps and (b) gradient maps used in the error analysis of the approximations in (5.7) and (5.8).	86
5.6	NRMS error plots in log scale in terms of number of basis functions L . (a) Approximation of (5.7). (b) Approximation of (5.8).	87
A.1	Plot showing how echo-time is affected by the through-plane gradients. Horizontal axis represents the parameter y depending on the echo-time t , as $y = rt$. Each curve represents a different value of the parameter p (increasing value from bottom to top curve) that depends on the through-plane gradient g , as $p = wg/r$. The curves show that the optimal echo-time (value of y where curve attains minimum value) shifts to the left (smaller echo-time) as the through-plane gradient strength increases (increased values of p). The bottom line corresponds to the case where there are no through plane gradients.	124
A.2	Plot showing how echo-time is affected by the through-plane gradients similarly to Figure A.1. The bottom line corresponds to the case where there are no through plane gradients. Comparing to Figure A.1 we see that the optimal echo-times have slightly smaller values for the same value of the parameter p	130

B.1	Experiment 4 using 15×15 uniform blur: Restoration results using isotropic TV regularization. (a) Cameraman true image (242×242), scaled to the range $[0, 1]$. (b) Blurred and noisy image from Matlab's 'valid' <code>conv2</code> operation. (c) Restored image from purely circulant model (B.2). (d) Restored image from purely circulant model with data pre-processing (B.4). (e) Restored image using reflexive boundary conditions and DCT (B.5). (f) Restored image from proposed non-circulant model (B.8).	155
B.2	Experiment 3 using 15 pixel motion blur: Restoration results using isotropic TV regularization. (a) Cameraman true image (248×248), scaled to the range $[0, 1]$. (b) Blurred and noisy image from Matlab's 'valid' <code>conv2</code> operation. (c) Restored image from purely circulant model (B.2). (d) Restored image from purely circulant model with data pre-processing (B.4). (e) Restored image using reflexive boundary conditions and DCT (B.5). For this case, the results are inaccurate since this method is not applicable for non-symmetric PSF [1,2]. Also the image had to be scaled to fit the dynamic range of the rest of the reconstructed images. (f) Restored image from proposed non-circulant model (B.8).	156
B.3	Experiment 1 using 15×15 uniform blur: Restoration results using isotropic TV regularization. (a) Cameraman true image (248×248), scaled to the range $[0, 1]$. (b) Blurred and noisy image from Matlab's 'valid' <code>conv2</code> operation. (c) Restored image from purely circulant model (B.2). (d) Restored image from purely circulant model with data pre-processing (B.4). (e) Restored image using reflexive boundary conditions and DCT (B.5). (f) Restored image from proposed non-circulant model (B.8).	157
B.4	Experiment 3: Algorithm convergence speed results with convergence measured in terms of drop in NRMSE in dB, $\xi^{(k)}$, between the estimated image \hat{x} and the converged image $x^{(\infty)}$. Left column (a,c) is convergence per iteration, and right column (b,d) is convergence in run-time. First row (a,b) is from TV regularizer, and second row (c,d) is from wavelet l_1 norm regularizer.	161

LIST OF TABLES

Table

3.1	Table of NRMS error (in %) of estimated phase map parameters and reconstructed images. The $N \times$ denotes the amount of oversampling of FFT and NC denotes the uncorrected for ghosting artifacts reconstruction. The results from the QS method are included as reference.	46
4.1	Comparative table of NRMS error of reconstruction with all trajectory and coil settings. *Note: The same standard estimate was used for all cases as initial fieldmap for joint estimation.	68
5.1	Comparative table of RMS error of reconstruction methods, for all 20 slices. . . .	85
B.1	ISNR in dB for all experiments. The * denotes reconstruction using the purely circulant model with data pre-processing (B.4). For the case of motion blur the results for reflexive end conditions are not presented since the method is not appropriate for non symmetric PSF.	158
B.2	Outer iteration time of competing algorithms measured in milliseconds. L is the number of line-search iterations, M is the number of Chambolle-type iterations and N is the number of CG iterations.	160
B.3	Time and iteration number required for every algorithm to reach -50dB error compared to the converged image $\mathbf{x}^{(\infty)}$	160

LIST OF APPENDICES

Appendix

- A. CRB Analysis for Trajectory Optimization 117
- B. Accelerated Edge-Preserving Image Restoration Without Boundary Artifacts 139

ABSTRACT

Dynamic Image and Fieldmap Joint Estimation Methods for MRI Using Single-Shot Trajectories

by

Antonis Matakos

Chair: Jeffrey A. Fessler

In susceptibility-weighted MRI, ignoring the magnetic field inhomogeneity can lead to severe reconstruction artifacts. Correcting for the effects of magnetic field inhomogeneity requires accurate fieldmaps. Especially in functional MRI, dynamic updates are desirable, since the fieldmap may change in time. Also, susceptibility effects that induce field inhomogeneity often have non-zero through-plane gradients, which, if uncorrected, can cause signal loss in the reconstructed images. Most image reconstruction methods that compensate for field inhomogeneity, even using dynamic fieldmap updates, ignore through-plane fieldmap gradients. Another major consideration in MR image reconstruction is the trajectory selection, since the quality of the obtained results can greatly depend on the chosen trajectory. Therefore, optimizing the trajectory used for the problem at hand may greatly improve the reconstruction quality. Furthermore, the echo-planar (EPI) trajectories used for fast acquisitions are susceptible to misalignments due to scanner imperfections that lead to ghosting artifacts in the reconstructed images. Finally, standard optimization methods, like CG-based algorithms, may be slow to converge and recently proposed algorithms based on the Augmented Lagrangian (AL) framework have shown the potential to lead to more efficient optimization algorithms, especially in MRI reconstruction problems with non-quadratic regularization.

In this work, we propose a computationally efficient, model-based iterative method for joint reconstruction of dynamic images and fieldmaps in single coil and parallel MRI, using single-shot trajectories. We first exploit the fieldmap smoothness to perform joint estimation using less than two full data sets and then we exploit the sensitivity encoding from parallel imaging to reduce the acquisition length and perform joint reconstruction using just one full k-space dataset. Subsequently, we extend the proposed method to account for the through-plane gradients of the field

inhomogeneity. To improve the efficiency of the reconstruction algorithm we use a linearization technique for fieldmap estimation, which allows the use of the conjugate gradient algorithm. The resulting method allows for efficient reconstruction by applying fast approximations that allow the use of the conjugate gradient algorithm along with FFTs. Our proposed method can be computationally efficient for quadratic regularizers, but the CG-based algorithm is not directly applicable to non-quadratic regularization. To improve the efficiency of our method for non-quadratic regularization we propose an algorithm based on the AL framework with variable splitting. This new algorithm can also be used for the non-linear optimization problem of fieldmap estimation without the need for the linearization approximation.

In this work, we also explore the use of modified trajectories (both EPI and spiral) that provide full coverage of k-space and also contain enough inherent time differences to permit accurate fieldmap estimation. The need for modified trajectories is justified by performing variance predictions, based on the Cramér-Rao bound analysis, on the joint estimation using standard and modified EPI trajectories. Furthermore, to suppress the ghosting artifacts of the EPI-based reconstructions we developed a model-based iterative ghost correction method. The proposed method jointly estimates the correction factors and the reconstructed image and can be incorporated in our joint image and fieldmap reconstruction, instead of applying ghost correction as a post-processing step.

Finally, we investigate the effect of through plane dephasing in parameter estimation. We derive the Cramér-Rao bound for estimator variance and by its minimization we try to find optimal echo-times for parameter estimation including image and fieldmap. The goal is to theoretically explain what trajectories would be optimal for parameter estimation and then verify the theoretical expectations with simulation results. We develop a simple theoretical method that optimizes the choice of echo-time given the model parameters that we wish to estimate. Even though echo-time is just one trajectory parameter, it is possibly the most important one since image contrast and reconstruction quality can be greatly affected by the choice of echo time. In our method we derive the Cramér-Rao bound for the estimated parameters and minimize this lower bound on variance with respect to the echo-time.

CHAPTER I

Introduction

In functional MRI a series of dynamic images is reconstructed and to satisfy the need for high temporal resolution, fast single-shot acquisitions, such as echo-planar (EPI) or spirals, are commonly used. Also these acquisition usually have late echo-times (and consequently long readout time) to ensure good BOLD contrast. These characteristics of susceptibility-weighted MR imaging lead to increased sensitivity to magnetic field inhomogeneities and can lead to significant artifacts in the reconstructed image if uncorrected. Correcting for these effects requires accurate inhomogeneity fieldmaps and since the fieldmap may change in time, dynamic updates are desirable. The standard approach to correct for field inhomogeneities is to acquire a static fieldmap before the dynamic series and use this to correct all the subsequent images. This method can be inaccurate, since motion and fieldmap drifts are not taken into account when reconstructing. This motivated the development of methods that can jointly reconstruct undistorted images and undistorted dynamic fieldmaps, like [3], where one can reconstruct an undistorted image and undistorted dynamic fieldmap using spiral-in/spiral-out acquisition. However, acquiring two full datasets in a single acquisition may result in very long readout times and more severe inhomogeneity artifacts. This work presents a method for jointly estimating the image and dynamic fieldmap in parallel MRI [4], using a single-shot acquisition that uses just one full dataset by exploiting the sensitivity encoding [5]. This method retains the advantage of high temporal resolution of single-shot trajectories along with the advantage of shorter readout time by exploiting the coil sensitivity encoding. The shorter readout time has the potential to improve the reconstruction quality since it leads to less distortion due to field inhomogeneity and through-plane gradient effects. We also propose the use of modified single-shot trajectories (both EPI and spiral) that provide full coverage of k-space and also allow for enough time differences between regions of k-space so that the fieldmap estimation is facilitated (see §4.3).

Apart from the longer readout times, another disadvantage of the method in [3] is that the

method used for fieldmap estimation is nonlinear and computationally demanding. The linearization method described in [6] can significantly reduce the computation time of fieldmap estimation, by enabling efficient use of conjugate gradient (CG). CG converges much faster than the gradient descent (GD) method used in [3]. In this work we use the linearization technique for fieldmap estimation [6] to improve the efficiency of our reconstruction algorithm.

Furthermore, most methods correcting for field inhomogeneity, even the model-based iterative ones, treat the inhomogeneity within each voxel as being a constant. However, susceptibility effects usually cause nonzero through-plane gradients that lead to spin dephasing across the slice within each voxel. Ignoring through-plane gradients can cause signal loss in the reconstructed images, especially in functional MR imaging where acquisitions with long readouts and late echo-times are used. To correct for the through-plane gradient effects, a fast, iterative reconstruction method is proposed in [7]. The drawback of this method is the assumption that the through-plane gradients are static and known beforehand, thus being unable to handle dynamic fieldmap changes. Motivated by our earlier work [4], this work presents a computationally efficient, model based, iterative method that jointly reconstructs images and dynamic fieldmaps, accounting for through-plane gradient effects [8]. The proposed algorithm uses the signal model presented in [7] and applies the fast approximations introduced in [9]. To improve the efficiency of the reconstruction algorithm, we employ the same linearization technique for fieldmap estimation [6], that was used in our previous work [4].

The iterative methods developed in this work for joint estimation [4, 8] use the conjugate gradient method (CG) which is computationally efficient for quadratic regularization. However, non-quadratic regularization can be beneficial to improve the reconstruction results at an increased computational cost. Recently there are several MRI reconstruction methods developed using the Augmented Lagrangian framework with variable splitting, that show accelerated convergence using non-quadratic regularizers. Motivated by [10] and our work in AL methods for image restoration [11] (presented in Appendix B) we propose a joint image and fieldmap estimation method based on the AL framework. Our proposed method would benefit from the faster convergence rate of the AL methods and the improved image reconstruction quality of non-quadratic regularization. Another advantage of the AL approach is that our proposed algorithm can also be used for the non-linear optimization problem of fieldmap estimation without the need for the linearization approximation [6].

Another important consideration when performing image reconstruction for MRI is the choice of trajectory, because the quality of the obtained results can greatly depend on that choice. Unfortunately there is no optimal trajectory that fits in all scenarios and choosing or designing the “best”

trajectory for the problem at hand is a difficult task. Having a theoretical framework that could be used to evaluate the performance of a given trajectory or provide optimal parameters that could help in trajectory design, would greatly help in addressing the problem of trajectory selection. In developing such a framework it would be important to use a generic model that accounts for various parameters that affect the reconstruction quality. Such parameters are the field inhomogeneity and the transverse relaxation (or R_2^* decay). Another effect that is usually ignored and is related to field inhomogeneity is the effect of through plane gradients [7, 8]. In this work we propose a way of theoretical analysis that provides optimal trajectory parameters (optimal echo-time), given the problem parameters that we wish to estimate. Our analysis is based on the derivation of the Cramér-Rao bound for estimator variance. In particular, we derive the CRB for the parameter(s) that we wish to estimate and then we find the optimal echo-time that minimizes this bound, which effectively is the echo-time that minimizes the estimator variance. We especially focus on the effect of through-plane gradients, since this is an effect that it is not well studied and we would like to better asses how it affects the echo-time optimization.

Throughout our joint estimation work we validated our algorithms using modified “interleaved” trajectories (EPI and spirals) that exhibited improved performance compared the the standard ones. The fact that “interleaved” trajectories resulted in superior reconstruction quality was the motivation to develop a method to assess the trajectory performance. For this purpose we performed complex CRB analysis [12] on the resulting reconstructions for both standard and “interleaved” trajectories. Focusing on the EPI trajectories, enabled us to apply fast approximations leading to a computationally efficient method for variance prediction. Our findings show significantly reduced variance for joint reconstruction when the “interleaved” trajectories are used, which supports our choice of these trajectories. Unfortunately an analytical method that would results in an optimal trajectory for joint estimation is still elusive, but we could use our developed method to evaluate other trajectory choices.

Finally, our joint estimation methods depend heavily on the use of EPI-based trajectories where multiple lines of k-space are acquired after each RF excitation pulse, using readout gradient pulses of alternating polarity along with phase-encode “blips”. Due to eddy currents or other gradient imperfections, the k-space data from positive and negative readouts are not perfectly aligned leading to Nyquist ghosting artifacts in the reconstructed images [13]. These misalignments are more prominent in the frequency-encoding direction, but can also appear along the phase-encoding direction in oblique-plane imaging or due to cross-eddy currents. To effectively correct for these effects one requires an accurate 2D phase map, usually acquired from reference scans [14]. Other methods for ghosting artifact correction are proposed [15–19], but they may not be readily applica-

ble to our model-based reconstruction framework or may not be suitable for the “interleaved” EPI trajectories used in this work. Thus, we developed a new model-based iterative ghost correction method that uses a joint estimation method to acquire the ghost-correction factors and an artifact-free image. Our proposed method incorporates the corrections into the system model and can be easily incorporated into the joint estimation techniques used throughout this work. Furthermore, the proposed ghost correction method does not depend on the “structure” of the EPI acquisition making it suitable for correcting the artifacts of our “interleaved” EPI trajectories.

CHAPTER II

MRI Background

In this section we will give the necessary background information for MRI leading to the formulation of the signal equation on which the subsequent analysis is based. Then we will address some additional considerations like field inhomogeneity and parallel imaging that will be necessary in understanding the work presented in subsequent sections.

Magnetic Resonance Imaging (MRI) is a medical imaging modality that uses magnetic fields to exploit the magnetic properties of certain atoms with odd number of protons or neutrons. These atoms, frequently referred to simply as *spins*, possess a nuclear spin angular momentum that gives rise to a small magnetic moment μ . In biological specimens, hydrogen with a single proton (1H), is the most abundant (source is H₂O), the most sensitive (highest SNR) and the most studied. Therefore, we will assume 1H (proton) imaging. The nature of MR is based on the interaction of spins with three types of magnetic fields which will be discussed in the following section.

2.1 Magnetic Fields

Without the presence of a magnetic field the spins are randomly oriented and the net magnetic moment is zero. By applying a magnetic field B_0 (conventionally along the z direction) the magnetic moments of the spins tend to align in the direction of B_0 , thus creating a net magnetic moment. In addition spins exhibit resonance, by precessing around the z direction, at a well-defined frequency called the Larmor frequency ω , which relates to the strength of the applied magnetic field by the simple expression

$$\omega = \gamma B_0 \tag{2.1}$$

where γ is a unique constant for each type of atom, called the gyromagnetic ratio.

In the presence of a main magnetic field B_0 the equilibrium state of the magnetic moment is to be aligned in the direction of B_0 . To obtain an MR signal, a radiofrequency (RF) magnetic pulse B_1 tuned to the resonant frequency of the spins is applied in the xy (transverse) plane. This pulse excites the spins out of equilibrium by effectively applying a torque which rotates the magnetization vectors. The rotation angle depends on the strength of B_1 and its duration. If the excitation is set for a 90° tip angle, then when the excitation is turned off, the tipped vectors precess in the xy plane at the Larmor frequency.

After excitation, relaxation back to equilibrium for the magnetic moments occurs. The recovery of the magnetic moments along the z-axis (longitudinal axis), is characterized by the time constant T_1 and the decay of the xy-plane component (transverse component) of the magnetization vector is characterized by the time constant T_2 . The values of both time constants depend on the type of tissue, with typical values of T_1 being in the range 100-1500ms and T_2 being in the range 20-300ms. Both relaxation processes behave in an exponential fashion, with T_1 describing the recovery of the longitudinal magnetization

$$M_z(t) = M_{z0} (1 - e^{-t/T_1})$$

and T_2 describing the recovery of the transverse magnetization

$$M_{xy}(t) = M_{z0} e^{-t/T_2}.$$

Macroscopically, the magnetization vector precesses at the Larmor frequency back to equilibrium. By Faradays Law, the rotating magnetization vectors induce an electromagnetic force in an RF receiver coil. This signal, called Free Induction Decay (FID), is essentially the MRI signal. As we see it depends not only on spin density, but also on the T_1 and T_2 time constants.

In the presence only of the main magnetic field B_0 it is impossible to excite a selected portion of the volume, since all the spins precess at the same resonant frequency. For the same reason we cannot distinguish the signals generated from different spatial locations. To account for this problem and achieve spatial localization we can apply linear gradient magnetic fields. These magnetic fields are applied in the direction of B_0 but their strength varies linearly with spatial location (in x,y or z axis). By having a spatially varying magnetic field the frequency of the spins becomes a function of their location

$$\omega(x, y, z) = \gamma(B_0 + G_x x + G_y y + G_z z).$$

This location dependent frequency can be exploited in two major ways. First in selective excitation where we can excite only a slice of the entire volume and second in image reconstruction by performing spatial encoding.

2.2 Excitation

If the RF pulse B_1 is applied in the presence of B_0 alone, then all the spins are tipped since they are at the same resonant frequency and the excitation is called *non-selective*. In this case the entire volume contributes signal, thus some form of 3D imaging must be performed. 3D imaging is usually very time consuming and is not preferred for functional MRI applications. Hence, it is desirable to reduce the 3D imaging problem into a more manageable 2D problem and this can be achieved by exciting a plane instead of the entire volume. This *selective excitation* is performed by applying a linear gradient field along with B_1 in the presence of B_0 . To excite a plane perpendicular to the z-axis we apply a z gradient during the RF excitation. Because B_1 must be tuned to the Larmor frequency and the spin frequencies vary linearly with z, B_1 must possess a temporal frequency bandwidth that matches the bandwidth of resonance frequencies of the spins at the slice of interest. Hence, a rectangular excitation profile requires the frequency content of B_1 to be a rectangle function, which in turn means that B_1 must be an infinite sinc pulse. Because of the Fourier Transform relationship, finding the ideal RF pulse is difficult because both the RF pulse itself and the resultant slice profile are necessarily band limited. An infinite sinc pulse is impossible to create in practice, as is the ideal rectangular slice profile. In practice, truncated sines or Gaussian pulses are used. However, many algorithms in MRI are based upon the ideal of an infinitely thin and/or rectangular slice profile achieved in the excitation phase.

2.3 Spatial Encoding and Signal Equation

After excitation of a slice, all the magnetization vectors precess at the same frequency, regardless of spatial location. This indicates that for the reconstruction of an image to be achievable, the signal that the RF receivers detect, needs to include a spatial encoding. Going back to the precessing magnetization vectors, we can envision them as being a map of tiny magnetic oscillators at each position (x, y) in the slice. Each oscillator possesses a certain magnitude $m(x, y; t)$, and a phase term $\phi(x, y; t)$. Thus the signal from each oscillator at position (x, y) can be expressed as $m(x, y; t) e^{i\phi(x, y; t)}$. Suppose the receiver coil is uniformly sensitive over the whole slice, then the received signal $s(t)$ is the summation of all the oscillators in the plane, i.e.

$$s(t) = \iint m(x, y; t) e^{-i\phi(x, y; t)} dx dy \quad (2.2)$$

Since frequency is equal to the time rate of change in phase and by using equation (2.2) above, we observe that the rate of change in $\phi(x, y; t)$ can be described by

$$\frac{d}{dt}\phi(x, y; t) = \omega(x, y; t) = \gamma B(x, y; t)$$

and thus,

$$\phi(x, y; t) = \int_0^t \omega(x, y; \tau) d\tau = \gamma \int_0^t B(x, y; \tau) d\tau \quad (2.3)$$

where we assume the initial phase to be zero. To detect the spatial locations of all the oscillators in the slice we can use a combination of gradient fields and the main magnetic field B_0 , such that spatial information is encoded into the frequency distribution. Using this approach, $B(x, y; \tau)$ in equation (2.3) has the following form,

$$B(x, y; \tau) = B_0 + G_x(\tau)x + G_y(\tau)y$$

where B_0 is the strength of the main magnetic field and $G_x(t)$ and $G_y(t)$ are gradient fields used to encode spatial information into the signal. Using this in equation (2.3), we then get

$$\begin{aligned} \phi(x, y; t) &= \gamma \int_0^t B_0 d\tau + \left(\gamma \int_0^t G_x(\tau) d\tau \right) x + \left(\int_0^t G_y(\tau) d\tau \right) y \\ &= \omega_0 t + 2\pi k_x(t)x + 2\pi k_y(t)y \end{aligned} \quad (2.4)$$

where

$$k_x(t) \triangleq \gamma \int_0^t G_x(\tau) d\tau, \quad k_y(t) \triangleq \gamma \int_0^t G_y(\tau) d\tau$$

further showing how the gradient fields enable control of the phase of the oscillators. Using this expression in equation (2.2) and demodulating to remove the $\omega_0 t$ factor we now get the signal

equation:

$$s(t) = \iint m(x, y; t) e^{-i2\pi(k_x(t)x+k_y(t)y)} dx dy. \quad (2.5)$$

Equation (2.5) is a 2D Fourier-like transform if $m(x, y; t)$ is independent of t or approximately so, while the data is being acquired. Using this model, one can reconstruct $m(x, y; t)$ from $s(t)$, using Fourier reconstruction. By convention in MR literature the space of $k_x(t)$ and $k_y(t)$ is called k-space which is in units of cycles/cm, equivalent to spatial frequency. The acquired signal $s(t)$ thus maps directly from the trajectory in k-space as determined by the time integrals of the gradient waveforms $G_x(t)$ and $G_y(t)$ as was shown in equation (2.4). There are numerous trajectories that can be used to acquire the signal, such as the cartesian, the echo planar imaging (EPI) and the spiral trajectory. The time point when DC is sampled for any trajectory is called the echo-time or TE. The contrast of the reconstructed MR image is strongly connected to the echo-time, thus making it an important concept in MRI and functional MRI.

2.4 Field Inhomogeneity in MRI

When formulating the signal equation (2.5) we assumed a homogeneous main magnetic field B_0 . However, due to the nature of objects being imaged as well as the difficulty in engineering perfect magnetic coils, fields are usually inhomogeneous. This field inhomogeneity, if uncorrected, can severely affect the quality of the reconstructed images in many important MRI applications, including functional MRI (fMRI).

Field inhomogeneity is location dependent and can be described (in 2D) by a frequency term $\omega(x, y)$. For a signal model that accounts for inhomogeneity, the signal equation becomes:

$$s(t) = \iint m(x, y; t) e^{-i\omega(x,y)t} e^{-i2\pi(k_x(t)x+k_y(t)y)} dx dy. \quad (2.6)$$

2.4.1 Sources and effects of inhomogeneity

As we have seen in the Larmor equation, resonance frequency is directly related to the magnetic field strength. Thus, main field inhomogeneity causes different resonant frequencies at each spatial location. An inhomogeneous main magnet can usually be corrected for via shimming. However, inhomogeneity can also arise from the specific morphology of the imaged object. Differences in magnetic susceptibility of structures in the body cause macroscopic field inhomogeneity. Magnetic susceptibility is highest in areas where air and tissue meet; for example, in the sinuses and ear canal,

lungs, and the abdomen. Another source of inhomogeneity is chemical shift, which occurs because of outer electrons shielding the nucleus and slightly reducing the magnetic field experienced by the nucleus. This causes a small change in the resonant frequency as well. This chemical shift is experienced usually by fat and causes the fatty parts of an image to be shifted or blurred depending on the trajectory.

Field inhomogeneity can cause various effects in the reconstructed image and these effects are strongly trajectory dependent. The longer the readout time of the trajectory the more significant are the effects of inhomogeneity. Imaging using simple multi-shot cartesian trajectories does not exhibit significant inhomogeneity effects due to the short readout time (only a single line of k-space is traversed in each readout). In these cases we can safely ignore inhomogeneity and still get high reconstruction quality. The disadvantage of these trajectories is the long scan time, since we have to wait for the magnetization to return to equilibrium before scanning the next line of k-space. From the other hand, in functional MRI we want to acquire a series of images by performing a series of short scans each resulting in a single image. To keep the total scan time short, it is required to use trajectories with long readout times that traverse most, if not all, of k-space in a single-shot acquisition, so that we can reconstruct an image from a single readout. Imaging using these trajectories exhibits significant effects of field inhomogeneity because of the long readout times. To achieve good quality reconstructions it is necessary that we correct for this effect.

Inhomogeneity can affect the amplitude of the signal and result in signal loss. Under field inhomogeneity, the object has a distribution of different resonant frequencies which leads to phase incoherence of the spins. When the signal adds up all the contributions from each spin, this dephasing causes a signal loss. This effect is referred to as T_2^* decay and causes a much faster decay in the transverse magnetization. (Sometimes, the reciprocal of T_2^* or R_2^* is used). With longer readout times, this problem becomes even more severe and results in significant signal loss. If the T_2^* decay is severe, the k-space trajectory can become weighted, creating a blur in the final image.

Another important effect of inhomogeneity is geometric distortion. In simpler trajectories, such as cartesian or echo-planar, the resulting geometric distortion due to field inhomogeneity is a shift. However, in more complex spiral trajectories the effect of inhomogeneity causes a blur in the resulting image which is harder to correct for.

2.4.2 Correction methods

Correcting for field inhomogeneity requires the use of an inhomogeneity field map. These field maps can be acquired from separate baseline scans or simultaneously along with the image reconstruction [3]. The simplest and most used (so far) correction methods are the conjugate phase

methods, which attempt to compensate for the phase at each voxel (e.g., [20]). These methods require a spatially smooth field map and do not perform well where this assumption breaks down. Other methods of correction have also been developed including iterative methods in frequency domain [21], and image domain [3].

2.4.3 Through-plane dephasing

Most methods correcting for field inhomogeneity, even the model-based iterative ones, treat the inhomogeneity within each voxel as being a constant. This is not always the case, since susceptibility effects often have nonzero through-plane gradients that lead to spin dephasing across the slice within each voxel. Ignoring the through-plane gradient effect and not correcting for it can cause signal loss in the reconstructed images.

To correct for through-plane gradient effects we need a signal model that accounts for the slice profile and the through plane gradients of the field inhomogeneity (assumed to be determined by a pre-scan). By incorporating these parameters in the signal model, as introduced in [7], the signal equation (in 3D form) becomes:

$$s(t) = \iiint h(z - z_0) m(x, y, z) e^{-i\omega(x, y, z)t} e^{-i2\pi(k_x(t)x + k_y(t)y)} dx dy dz, \quad (2.7)$$

where $h(z)$ denotes the (known) slice-selection profile, z_0 denotes the axial center of the slice, $m(x, y, z)$ denotes the (unknown) transverse magnetization (not depending on time) and $\omega(x, y, z)$ denotes the field map. Since the slice location z_0 is fixed we can consider the magnetization as only a function of the (x, y) location as $m(x, y) = m(x, y, z_0)$.

We can simplify the above expression by considering a Taylor series expansion of the fieldmap around z_0 and considering a fixed $z = z_0$ for the entire slice, so that the fieldmap depends spatially only on the (x, y) coordinates. This can be expressed as:

$$\begin{aligned} \omega(x, y, z) &= \omega(x, y, z_0) + 2\pi g(x, y, z_0)(z - z_0) \\ &= \omega(x, y) + 2\pi g(x, y)(z - z_0), \end{aligned}$$

where $g(\cdot)$ is the through plane gradient at location (x, y) measured in units of Hz/cm. Using this

expression in the signal model we get

$$\begin{aligned}
s(t) &= \iint \left[\int_z h(z - z_0) e^{-i2\pi g(x,y)t(z-z_0)} dz \right] m(x, y) e^{-i\omega(x,y)t} e^{-i2\pi(k_x(t)x+k_y(t)y)} dx dy \\
&= \iint H(g(x, y) t) m(x, y) e^{-i\omega(x,y)t} e^{-i2\pi(k_x(t)x+k_y(t)y)} dx dy,
\end{aligned} \tag{2.8}$$

where $H(v)$ is the Fourier transform of the slice profile. This last equation is the signal equation accounting for through plane dephasing and is the model that we will use in subsequent analysis.

2.5 Sensitivity Encoding in Parallel MRI

The signal equation (2.5) represents the signal at the receiver coil. Up till now we assumed a single receiver RF coil in our derivations. Also, it is known that each receiver coil has its own sensitivity which is location dependent and earlier we ignored that effect by assuming a uniform sensitivity. In a more realistic setting, where we account for receiver sensitivity, the contribution of a signal source to the induced voltage varies with its relative position. This means that knowledge of spatial receiver sensitivity implies information about the origin of detected MR signals, which may be utilized for image generation. Sensitivity is a receiver property and therefore, we can obtain distinct information content from one object by using multiple receivers in parallel (parallel MRI), which implies the possibility of reducing scan time by reducing the k-space sampling [5].

In a parallel MRI setting we use K receiver coils and each of them has its own spatial sensitivity $c_k(x, y)$. Based on the signal equation, the received signal from each coil is:

$$s_k(t) = \iint c_k(x, y) m(x, y; t) e^{-i2\pi(k_x(t)x+k_y(t)y)} dx dy \text{ for } k = 1, \dots, K. \tag{2.9}$$

Even though these signals refer to the same object, separation between them is possible because each superimposed signal occurs with different weights that depend on the coil sensitivity. The main idea of parallel imaging is to use these distinct signals to produce a single image.

The extra information provided by the multiple coils allows the reduction of k-space sampling without losing the ability to correctly reconstruct an image. Normally, in single coil imaging, reduction of k-space sampling means reduced field of view (FOV) and aliasing. In parallel imaging we can account for the reduced k-space samples by using the distinct information content from each coil and thus acquire a dataset adequate for full FOV reconstruction without aliasing. This idea is described in [5] and is applied mainly in Fourier imaging with cartesian sampling. In our work

we will make implicit use of the sensitivity encoding information in the formulation of our system model.

2.6 Nyquist Ghosting Artifacts in EPI Trajectories

In echo-planar imaging (EPI) the k-space is sampled in a Cartesian grid and the k-space lines are traversed with alternating positive and negative gradient polarities. For an ideal EPI, when inhomogeneity effects are ignored the system matrix reduces to a simple $(MN \times MN)$ 2D Fourier encoding matrix $\mathbf{F} \triangleq \mathbf{F}_y \otimes \mathbf{F}_x$, where \mathbf{F}_x and \mathbf{F}_y are 1D $(N \times N)$ and $(M \times M)$ Fourier encoding matrices respectively, with elements:

$$\begin{aligned} f_{x(k,n)} &= e^{-i2\pi kn/N} \\ f_{y(l,m)} &= e^{-i2\pi lm/M}. \end{aligned}$$

In reality, though, due to eddy currents and other imperfections the sampled k-space lines from positive and negative gradients are not perfectly aligned. This misalignment can be modeled as a small shift of k-space along the x and y directions such that the elements of the sub-sampled DFT matrix, corresponding to the negative readout direction, become

$$\begin{aligned} f_{(k,l),(m,n)} &= e^{-i2\pi((k+\delta_x)n/N+(l+\delta_y)m/M)} \\ &= e^{-i2\pi(kn/N+lm/M)} e^{-i2\pi(\delta_x n/N+\delta_y m/M)} \end{aligned} \quad (2.10)$$

and thus the encoding matrix can be expressed as

$$\tilde{\mathbf{F}}_- \triangleq \mathbf{F}_- \text{diag } e^{-i\boldsymbol{\theta}}, \quad (2.11)$$

where \mathbf{F}_- is a standard sub-sampled DFT matrix and $\boldsymbol{\theta}$ is a phase map such that

$$\theta[n, m] = 2\pi(\delta_c + \delta_x n/N + \delta_y m/M). \quad (2.12)$$

The Eddy currents and other gradient imperfections also lead to the appearance of the constant term δ_c in (2.12) along with the linear terms δ_x and δ_y .

For an ideal EPI, reconstructing the positive and negative lines of k-space independently would

result in

$$\hat{f}_+[n, m] = (f[n, m] + f[n, m + M/2]) / 2 \quad (2.13)$$

$$\hat{f}_-[n, m] = (f[n, m] - f[n, m + M/2]) / 2 \quad (2.14)$$

From the above we see that combining the two images perfectly eliminates the $M/2$ aliasing ghost. In contrast, in an actual EPI, due to the k-space misalignment the reconstruction from the negative readout becomes

$$\check{f}_-[n, m] = (f[n, m] e^{-i\theta[n, m]} - f[n, m + M/2] e^{-i\theta[n, m + M/2]}) / 2 \quad (2.15)$$

and in this case a combination of the two images will not lead to cancellation of the $N/2$ ghosting artifact.

If the phase map θ is known then the actual image $f[n, m]$ can be obtained from $\hat{f}_+[n, m]$ and $\check{f}_-[n, m]$ in the following way [14]

$$f[n, m] = 2 \frac{\hat{f}_+[n, m] e^{i\theta[n, m + M/2]} + \check{f}_-[n, m]}{e^{i\theta[n, m]} + e^{i\theta[n, m + M/2]}} \quad (2.16)$$

For multi-shot EPI or when parallel imaging is used then one can acquire the ghost-free image by solving a system of linear equations as presented in [19].

CHAPTER III

Model Based Nyquist Ghost Correction for EPI

This paper describes a novel method for EPI ghost artifact correction. The method does not require any reference pre-scans, and is applicable to any coil configuration (single- or multi-coil) and number of shots, at an arbitrary oblique or double-oblique orientation. A parametric model for the ghost correction 2D phase-map is used and, unlike existing methods, the correction is incorporated in the system model rather than being applied as a post-processing step. The parametric phase map and the artifact free image are jointly estimated using maximum likelihood (ML) estimation. A first-order linear model was used for the correction phase-map and the method was applied for single-shot and multi-shot EPI using single or multiple coils at an axial scan plane. In simulation and phantom experiments with several types of acquisitions, the proposed method greatly suppressed ghosting artifacts, outperforming conventional correction methods (both 1D and 2D) for multi-shot EPI trajectories especially for single-coil acquisitions. The proposed method requires no calibration or modification of the acquisition pattern and can be easily incorporated into model-based reconstruction schemes.

3.1 Introduction

In echo-planar imaging (EPI), multiple lines of k-space are acquired after each RF excitation pulse, using readout gradients of alternating polarity along with phase-encode “blips”. Due to eddy currents or other gradient imperfections, the k-space data from positive and negative readouts are not perfectly aligned, leading to Nyquist ghosting artifacts in the reconstructed images if uncorrected [13].

The work in this chapter appears in [22].

The authors would like to acknowledge Scott Hoge for helpful discussions and insights on ghost correction.

The most significant misalignment occurs along the frequency-encoding direction and there are several methods designed to correct this effect. Since this misalignment corresponds to a linear phase in one dimension these methods are called 1D correction methods. Conventionally, the 1D phase can be estimated from a non-phase encoded reference scan [13, 23] or from two phase-encoded reference scans [24]. In some cases the 1D correction can also be estimated directly from the scanned data as proposed in [25, 26] without any pre-scans, but these methods do not work well in multi-shot EPI acquisitions. Using an odd number of shots with alternating polarities [27, 28] allows correction of $N/2$ ghosts in multi-shot acquisitions, but requires modification of the acquisition scheme and introduces constraints in the readout. Alternatively, an iterative phase cycling method, with the disadvantage of increased computation time, can be used to estimate the 1D correction [29] and it is also applicable to multi-shot EPI [30].

Conventional 1D correction methods can usually reduce most of the ghosting artifacts, but in many cases there may be significant ghosting even after 1D correction. This can happen in oblique-plane imaging [31] or in the presence of cross-term eddy currents [32]. In these cases a 2D correction is usually applied by computing 2D phase maps from reference scans [14]. Methods that rely on reference scans have the disadvantage of being susceptible to variations of the 2D phase map during a long study which can lead to uncorrected ghosting artifacts [18]. The 2D phase errors can be corrected with the PLACE method [16] that modifies the acquisition pattern and combines data from different temporal frames, thus reducing the temporal resolution, or the method in [18] that does not incur any loss of temporal resolution but is inapplicable to multi-shot EPI. These methods, along with PAGE [15] and real-time PAGE [17], also rely on parallel imaging and are not applicable to single-coil acquisitions. In addition, to avoid the latency of PAGE, real-time PAGE uses incoherent combination of the reconstructed images that loses image phase information. For single-coil imaging and multi-shot EPI one could use a phase cycling method like [19] to estimate the 2D correction with the main disadvantage of significantly increased computation time.

Apart from using a correction method, one can reconstruct ghost-free images using a “fly-back” EPI acquisition (*i.e.*, each k-space line is sampled twice, once in the positive and once in the negative gradient direction) [33]. Fly-back EPI methods increase echo-train length, doubling the readout interval and exaggerating the geometric distortion caused by field inhomogeneity effects. This drawback can be partially alleviated by using an undersampled EPI with parallel imaging as in [34], although undersampling reduces the SNR or reduces the potential acceleration factor.

In this work we present 2D model-based correction methods. In contrast with existing methods that apply correction as a post-processing step, our method integrates the 2D correction with the image estimation using a joint ML estimation approach. Our method requires no reference scans

or additional data during the acquisition and it is also robust to time varying effects (*e.g.*, scanner drifts) since the corrections can be updated in each time frame of a dynamic study if needed. Furthermore, our approach does not require parallel imaging for the 2D correction and also works effectively in multi-shot EPI trajectories. Also, as we observed in our study, in multi-shot EPI the amount of misalignment of positive and negative direction gradients may vary from one shot to the next and there may also be misalignment between the shots. The proposed ML method can efficiently compensate for these effects by estimating individual 2D correction factors for each shot with minimal additional computation cost.

3.2 Theory

For an ideal EPI scan with a N samples in the frequency encoding direction and M samples in the phase encoding direction, the $NM \times NM$ Fourier encoding matrix can be expressed as:

$$\check{\mathbf{F}} = \begin{bmatrix} \mathbf{F}_+ \\ \mathbf{F}_- \end{bmatrix}, \quad (3.1)$$

where \mathbf{F}_+ and \mathbf{F}_- are the $NM/2 \times NM$ sub-matrices of the orthonormal DFT corresponding to positive and negative echoes respectively.

By the (k -space) shift property of the Fourier transform, the misalignment of positive and negative direction echoes in standard single-shot EPI usually can be accurately modeled with a 2D phase map $\boldsymbol{\theta} \in \mathbb{R}^{NM}$, where NM is the number of pixels in a 2D slice. In this work we incorporate the phase map in the encoding matrix (system model) \mathbf{F} . Accounting for the misalignment of echoes the system matrix for a single coil becomes:

$$\mathbf{F}(\boldsymbol{\theta}) \triangleq \begin{bmatrix} \mathbf{F}_+ \\ \mathbf{F}_- \mathbf{P}(\boldsymbol{\theta}) \end{bmatrix}, \quad (3.2)$$

where $\mathbf{P}(\boldsymbol{\theta}) \triangleq \text{diag}\{e^{-i\boldsymbol{\theta}}\}$ is a $NM \times NM$ diagonal matrix with elements $e^{-i\theta[n,m]}$ along its diagonal, where $\theta[n, m]$ denotes the 2D phase map with $n = 0, \dots, N - 1$ and $m = 0, \dots, M - 1$.

We also consider the case of L receiver coils where the system matrix is

$$\mathbf{F}(\boldsymbol{\theta}) \triangleq \begin{bmatrix} \mathbf{F}_+ \mathbf{S}_1 \\ \vdots \\ \mathbf{F}_+ \mathbf{S}_L \\ \mathbf{F}_- \mathbf{S}_1 \mathbf{P}(\boldsymbol{\theta}) \\ \vdots \\ \mathbf{F}_- \mathbf{S}_L \mathbf{P}(\boldsymbol{\theta}) \end{bmatrix}, \quad (3.3)$$

with \mathbf{S}_l being an $NM \times NM$ diagonal matrix of sensitivity values for the l th coil, *i.e.*,

$$\mathbf{S}_l \triangleq \text{diag}\{s_l[n, m]\} \text{ for } l = 1, \dots, L, \quad (3.4)$$

where $s_l[n, m]$ is the sensitivity map for the l th coil. The system model in (3.2) is just a special case of (3.3) for $L = 1$ and $\mathbf{S}_1 = \mathbf{I}_{NM}$, where \mathbf{I}_d denotes the $d \times d$ identity matrix. We will present methods applicable to multi-coil acquisitions; however, our proposed methods do not require the use of parallel imaging.

Using the system matrix (3.3), we model the acquired k-space data as

$$\begin{bmatrix} \mathbf{y}_+ \\ \mathbf{y}_- \end{bmatrix} = \mathbf{F}(\boldsymbol{\theta}) \mathbf{x} + \boldsymbol{\varepsilon}, \quad (3.5)$$

where \mathbf{x} is the unknown image, $\boldsymbol{\varepsilon}$ is complex zero-mean Gaussian noise and \mathbf{y}_+ and \mathbf{y}_- are the data vectors (each of length $LN M/2$) from the positive and negative echoes respectively.

We propose to jointly estimate the image \mathbf{x} and phase map $\boldsymbol{\theta}$ from the k-space data in (3.5) by minimizing the following least squares cost function:

$$\left(\hat{\mathbf{x}}, \hat{\boldsymbol{\theta}} \right) = \underset{\mathbf{x}, \boldsymbol{\theta}}{\text{argmin}} \left\{ \Psi(\boldsymbol{\theta}) \triangleq \|\mathbf{y} - \mathbf{F}(\boldsymbol{\theta}) \mathbf{x}\|_2^2 \right\}. \quad (3.6)$$

Under the usual complex Gaussian noise model [35, 36], (3.6) is equivalent to the joint maximum likelihood (ML) estimate of \mathbf{x} and $\boldsymbol{\theta}$. If needed one could include a regularizer for \mathbf{x} in this cost function, but we did not find that necessary in our experiments. For a *known* phase map $\boldsymbol{\theta}$, finding the ML estimate of \mathbf{x} by minimizing (3.2) is equivalent to the 2D phase map correction method in [19], when inhomogeneity effects are ignored.

Jointly estimating the image and an arbitrary phase map would be under-determined for single-shot EPI and the estimated phase map values would be inaccurate in regions with low signal without regularizing the phase map. Instead of using regularization, since the phase map can be modeled accurately with a linear or second order polynomial [14, 18, 19], we adopt a parametric model

$$\boldsymbol{\theta} \triangleq \mathbf{T}\boldsymbol{\phi}, \quad (3.7)$$

where $\boldsymbol{\theta}$ is the $(NM \times 1)$ parameterized phase map, $\boldsymbol{\phi}$ is the $(p \times 1)$ unknown parameter vector and \mathbf{T} is the $(NM \times p)$ known coefficient matrix. Using the parametric model in (3.7) the number of unknowns is significantly reduced ($p \ll NM$), reducing the computational cost of the joint estimation and avoiding inaccuracies in the phase map estimation without the need for an additional regularization term.

Incorporating the parametric model of (3.7) in the cost function in (3.6), the joint estimation problem becomes

$$\left(\hat{\mathbf{x}}, \hat{\boldsymbol{\phi}}\right) = \underset{\mathbf{x}, \boldsymbol{\phi}}{\operatorname{argmin}} \left\{ \Psi(\boldsymbol{\phi}) \triangleq \|\mathbf{y} - \mathbf{F}(\mathbf{T}\boldsymbol{\phi}) \mathbf{x}\|_2^2 \right\}. \quad (3.8)$$

This minimization problem can be tackled with a variety of methods like gradient descent, conjugate gradient with a linearization approximation [6], or variable projection [37].

We adopt the variable projection approach [37] because it exploits the fact that (3.8) is quadratic in \mathbf{x} and reduces the minimization problem to finding the parameter vector $\boldsymbol{\phi}$. The minimizer $\hat{\mathbf{x}}$ for a given parameter $\boldsymbol{\phi}$ is:

$$\hat{\mathbf{x}}(\boldsymbol{\phi}) = [\mathbf{F}'(\mathbf{T}\boldsymbol{\phi}) \mathbf{F}(\mathbf{T}\boldsymbol{\phi})]^{-1} \mathbf{F}'(\mathbf{T}\boldsymbol{\phi}) \mathbf{y}, \quad (3.9)$$

where \mathbf{F}' denotes the Hermitian transpose of \mathbf{F} . Substituting (3.9) into the cost function (3.8) and simplifying, the ML estimate $\hat{\boldsymbol{\phi}}$ is found by solving the following p -dimensional maximization problem (where typically $p = 3$):

$$\hat{\boldsymbol{\phi}} = \underset{\boldsymbol{\phi}}{\operatorname{argmax}} \left\{ \mathcal{L}(\boldsymbol{\phi}) \triangleq \mathbf{y}' \mathbf{F}(\mathbf{T}\boldsymbol{\phi}) [\mathbf{F}'(\mathbf{T}\boldsymbol{\phi}) \mathbf{F}(\mathbf{T}\boldsymbol{\phi})]^{-1} \mathbf{F}'(\mathbf{T}\boldsymbol{\phi}) \mathbf{y} \right\}, \quad (3.10)$$

where $\mathcal{L}(\boldsymbol{\phi})$ is the likelihood function. For certain cases where the columns of $\mathbf{F}(\mathbf{T}\boldsymbol{\phi})$ are orthonormal, the Hessian matrix of (3.8), which appears as $\mathbf{F}'(\mathbf{T}\boldsymbol{\phi}) \mathbf{F}(\mathbf{T}\boldsymbol{\phi})$ in the middle of (3.10), reduces to an identity matrix. In these cases, the problem of estimating the phase map parameters

via (3.10) simplifies to

$$\hat{\phi} = \operatorname{argmax}_{\phi} \left\{ \mathcal{L}(\phi) \triangleq \|\mathbf{F}'(\mathbf{T}\phi) \mathbf{y}\|_2^2 \right\}. \quad (3.11)$$

After finding the phase estimate $\hat{\phi}$ using (3.10) or (3.11), we reconstruct the ghost-corrected image $\hat{\mathbf{x}}$ by substituting $\hat{\phi}$ into (3.9) and solving for \mathbf{x} using conjugate gradient (CG) iterations.

The next section presents methods for solving (3.10) and (3.11) based on optimization transfer methods (also known as majorize-minimize methods [38]) using quadratic surrogates, as well as a simple FFT-based approach. For cases where these simpler methods are unfeasible, we will also present an alternating minimization method for joint estimation.

3.3 Methods

3.3.1 Phase Map Model

Following [14] we used the following standard 2D linear model for the phase map:

$$\begin{aligned} \phi &\triangleq \begin{bmatrix} \phi_c & \phi_x & \phi_y \end{bmatrix}' \\ \mathbf{T} &\triangleq \begin{bmatrix} \mathbf{1} & \mathbf{n}_x & \mathbf{n}_y \end{bmatrix}, \end{aligned}$$

where $\mathbf{1}$ denotes the vector of $(NM \times 1)$ ones, \mathbf{n}_x and \mathbf{n}_y are the $(NM \times 1)$ vectors of the (x, y) coordinates of the reconstructed pixels. Higher order polynomial models can also be used with minimal increase in the computation cost, but we did not observe any improved results from such models compared to the simple linear model. Furthermore, the linear model is consistent with a shift of the k-space samples, unlike nonlinear phase models.

3.3.2 Object Mask

Using a parametric model (3.7) for the phase map significantly reduces the number of unknown parameters; however, the problem can still be under-determined for single-coil acquisitions because we have NM measurements and $NM + p$ unknowns, where typically $p = 3$ for single-shot 2D correction. We overcome this problem by using a support constraint — a “mask” around the object of interest, thus reconstructing only the pixels with non-zero spin density. For a mask with $K < NM$ pixels, the number of unknowns becomes $K + p$ so the problem potentially is over-determined when $K + p < NM$.

To illustrate the importance of the mask we consider the simpler 1D parametric model where $\boldsymbol{\phi} \triangleq [\phi_c \ \phi_x]'$ and $\mathbf{T} \triangleq [\mathbf{1} \ \mathbf{n}_x]$. Under this model, because the 2D DFT acts separately on the rows and columns of an image, we can write $\mathbf{F}_+ \triangleq \mathbf{F}_x \otimes \mathbf{F}_{y,+}$ and $\mathbf{F}_- \triangleq \mathbf{F}_x \otimes \mathbf{F}_{y,-}$, where \mathbf{F}_x is a fully sampled $N \times N$ 1D DFT matrix along the readout direction x , $\mathbf{F}_{y,+}$ and $\mathbf{F}_{y,-}$ are undersampled $M \times M/2$ 1D DFT matrices along the phase encode direction y , and \otimes denotes the Kronecker product. Using DFT properties, including orthogonality, it is easy to show that

$$\mathbf{F}_x' \mathbf{F}_x = \mathbf{F}_x \mathbf{F}_x' = \mathbf{I}_N \quad (3.12)$$

$$\mathbf{F}_{y,+}' \mathbf{F}_{y,+} = \frac{1}{2} \begin{bmatrix} \mathbf{I}_{M/2} & \mathbf{I}_{M/2} \\ \mathbf{I}_{M/2} & \mathbf{I}_{M/2} \end{bmatrix} \quad (3.13)$$

$$\mathbf{F}_{y,-}' \mathbf{F}_{y,-} = \frac{1}{2} \begin{bmatrix} \mathbf{I}_{M/2} & -\mathbf{I}_{M/2} \\ -\mathbf{I}_{M/2} & \mathbf{I}_{M/2} \end{bmatrix} \quad (3.14)$$

$$\mathbf{F}_{y,+} \mathbf{F}_{y,+}' = \mathbf{F}_{y,-} \mathbf{F}_{y,-}' = \mathbf{I}_{M/2} \quad (3.15)$$

$$\mathbf{F}_{y,+} \mathbf{F}_{y,-}' = \mathbf{F}_{y,-} \mathbf{F}_{y,+}' = \mathbf{0}_{M/2} \quad (3.16)$$

where the off-diagonal elements of the matrices in (3.13) and (3.14) correspond to the well known “ $N/2$ ghosts” ($M/2$ in our notation). Furthermore, we can write the phase matrix as

$$\mathbf{P}(\mathbf{T}\boldsymbol{\phi}) \triangleq \mathbf{P}_x(\mathbf{T}\boldsymbol{\phi}) \otimes \mathbf{P}_y(\mathbf{T}\boldsymbol{\phi}), \quad (3.17)$$

where

$$\mathbf{P}_x(\mathbf{T}\boldsymbol{\phi}) \triangleq \text{diag}\{e^{-i(\phi_c + n\phi_x)}\} \text{ for } n = 0, \dots, N - 1, \quad (3.18)$$

$$\mathbf{P}_y(\mathbf{T}\boldsymbol{\phi}) \triangleq \text{diag}\{e^{-m\phi_y}\} \text{ for } m = 0, \dots, M - 1. \quad (3.19)$$

For the case of 1D ghost correction we have $\phi_y = 0$ and thus, $\mathbf{P}_y(\mathbf{T}\boldsymbol{\phi}) = \mathbf{I}_M$.

Using the variable projection formulation of (3.10), and (3.13), (3.14) and (3.17), the Hessian

of (3.8) for the single-coil case is

$$\begin{aligned}
\mathbf{F}'(\mathbf{T}\phi) \mathbf{F}(\mathbf{T}\phi) &= \mathbf{F}'_+ \mathbf{F}_+ + \mathbf{P}'(\mathbf{T}\phi) \mathbf{F}'_- \mathbf{F}_- \mathbf{P}(\mathbf{T}\phi) \\
&= (\mathbf{F}'_x \mathbf{F}_x) \otimes (\mathbf{F}'_{y,+} \mathbf{F}_{y,+}) + (\mathbf{P}'_x(\mathbf{T}\phi) \mathbf{F}'_x \mathbf{F}_x \mathbf{P}_x(\mathbf{T}\phi)) \otimes (\mathbf{F}'_{y,-} \mathbf{F}_{y,-}) \\
&= \mathbf{I}_N \otimes (\mathbf{F}'_{y,+} \mathbf{F}_{y,+}) + \mathbf{I}_N \otimes (\mathbf{F}'_{y,-} \mathbf{F}_{y,-}) \\
&= \mathbf{I}_N \otimes (\mathbf{F}'_{y,+} \mathbf{F}_{y,+} + \mathbf{F}'_{y,-} \mathbf{F}_{y,-}) \\
&= \mathbf{I}_{NM}.
\end{aligned} \tag{3.20}$$

Thus, the optimization problem reduces to the form of (3.11) and, using (3.12), (3.15), and (3.16), the likelihood function for 1D correction in the single-coil case simplifies to

$$\begin{aligned}
\mathcal{L}(\phi) &= \|\mathbf{F}'(\mathbf{T}\phi) \mathbf{y}\|_2^2 \\
&= \mathbf{y}' \begin{bmatrix} \mathbf{F}_+ \\ \mathbf{F}_- \mathbf{P}(\mathbf{T}\phi) \end{bmatrix} \begin{bmatrix} \mathbf{F}'_+ & \mathbf{P}'(\mathbf{T}\phi) \mathbf{F}'_- \end{bmatrix} \mathbf{y} \\
&= \mathbf{y}' \begin{bmatrix} \mathbf{F}_+ \mathbf{F}'_+ & \mathbf{F}_+ \mathbf{P}'(\mathbf{T}\phi) \mathbf{F}'_- \\ \mathbf{F}_- \mathbf{P}(\mathbf{T}\phi) \mathbf{F}'_+ & \mathbf{F}_- \mathbf{F}'_- \end{bmatrix} \mathbf{y} \\
&= \mathbf{y}' \begin{bmatrix} (\mathbf{F}_x \mathbf{F}'_x) \otimes (\mathbf{F}_{y,+} \mathbf{F}'_{y,+}) & (\mathbf{F}_x \mathbf{P}'_x(\mathbf{T}\phi) \mathbf{F}'_x) \otimes (\mathbf{F}_{y,+} \mathbf{F}'_{y,-}) \\ (\mathbf{F}_x \mathbf{P}_x(\mathbf{T}\phi) \mathbf{F}'_x) \otimes (\mathbf{F}_{y,-} \mathbf{F}'_{y,+}) & (\mathbf{F}_x \mathbf{F}'_x) \otimes (\mathbf{F}_{y,-} \mathbf{F}'_{y,-}) \end{bmatrix} \mathbf{y} \\
&= \mathbf{y}' \begin{bmatrix} \mathbf{I}_{NM/2} & (\mathbf{F}_x \mathbf{P}'_x(\mathbf{T}\phi) \mathbf{F}'_x) \otimes \mathbf{0} \\ (\mathbf{F}_x \mathbf{P}_x(\mathbf{T}\phi) \mathbf{F}'_x) \otimes \mathbf{0} & \mathbf{I}_{NM/2} \end{bmatrix} \mathbf{y} \\
&= \mathbf{y}' \mathbf{y}.
\end{aligned} \tag{3.21}$$

The likelihood (3.21) is independent of ϕ ; thus, estimation of the phase map clearly requires further assumptions or constraints.

We use a mask that excludes pixels outside of the object support to reduce the degrees of freedom. This constraint enables estimation of the phase map parameters ϕ . To illustrate, we consider (for simplicity) a single-coil, single-shot acquisition, 1D phase map, and noiseless data, *i.e.*, $\mathbf{y} = \mathbf{A}(\tilde{\phi}) \mathbf{z}$, where $\tilde{\phi}$ is the true parameter vector,

$$\mathbf{A}(\phi) \triangleq \mathbf{F}(\mathbf{T}\phi) \mathbf{M} \tag{3.22}$$

is the $(NM \times K)$ system matrix, \mathbf{M} is the $(NM \times K)$ matrix for the mask with $K < NM - p$, and $\mathbf{z} \in \mathbb{C}^K$ is a vector that denotes the K possibly non-zero elements of the image $\mathbf{x} \triangleq \mathbf{Mz}$. The

support constraint matrix \mathbf{M} (mask) can be obtained from an identity matrix \mathbf{I}_{NM} by removing the $NM - K$ columns that correspond to known zero elements of the image \mathbf{x} . Thus, we have $\mathbf{M}'\mathbf{M} = \mathbf{I}_K$ and $\mathbf{M}\mathbf{M}'$ is an $NM \times NM$ diagonal matrix with 0s and 1s along the diagonal.

Under these assumptions, $\mathbf{A}'(\phi)\mathbf{A}(\phi) = \mathbf{M}'\mathbf{F}'(\mathbf{T}\phi)\mathbf{F}(\mathbf{T}\phi)\mathbf{M} = \mathbf{M}'\mathbf{M} = \mathbf{I}_K$ using (3.20) above, and ML estimation for ϕ is similar to (3.11) with the following likelihood:

$$\begin{aligned}
\mathcal{L}(\phi) &= \|\mathbf{A}'(\phi)\mathbf{y}\|_2^2 \\
&= \|\mathbf{M}'\mathbf{F}'(\mathbf{T}\phi)\mathbf{y}\|_2^2 \\
&= \left\| \mathbf{M}\mathbf{F}'(\mathbf{T}\phi)\mathbf{F}(\mathbf{T}\tilde{\phi})\mathbf{M}\mathbf{z} \right\|_2^2 \\
&= \left\| \mathbf{M}' \left[(\mathbf{F}'_x\mathbf{F}_x) \otimes (\mathbf{F}'_{y,+}\mathbf{F}_{y,+}) + (\mathbf{P}'_x(\mathbf{T}\phi)\mathbf{F}'_x\mathbf{F}_x\mathbf{P}_x(\mathbf{T}\tilde{\phi})) \otimes (\mathbf{F}'_{y,-}\mathbf{F}_{y,-}) \right] \mathbf{M}\mathbf{z} \right\|_2^2 \\
&= \left\| \mathbf{M}' \left[\mathbf{I}_N \otimes (\mathbf{F}'_{y,+}\mathbf{F}_{y,+}) + (\mathbf{P}'_x(\mathbf{T}\phi)\mathbf{P}_x(\mathbf{T}\tilde{\phi})) \otimes (\mathbf{F}'_{y,-}\mathbf{F}_{y,-}) \right] \mathbf{M}\mathbf{z} \right\|_2^2. \tag{3.23}
\end{aligned}$$

For a single-shot acquisition the matrix $\mathbf{F}'(\mathbf{T}\phi)\mathbf{F}(\mathbf{T}\tilde{\phi})$ is banded diagonal that corresponds to $M/2$ aliasing and it can be rearranged to a block diagonal with $NM/2$ blocks, each of size 2×2 . Using (3.13) and (3.14), each 2×2 block can be written as

$$\begin{aligned}
\mathbf{B}_{nm} &\triangleq \frac{1}{2} \begin{bmatrix} 1 & 1 \\ 1 & 1 \end{bmatrix} + \frac{1}{2} e^{i(\phi_c+n\phi_x)} e^{-i(\tilde{\phi}_c+n\tilde{\phi}_x)} \begin{bmatrix} 1 & -1 \\ -1 & 1 \end{bmatrix} \\
&= \frac{1}{2} \begin{bmatrix} 1 + e^{i\delta_n} & 1 - e^{i\delta_n} \\ 1 - e^{i\delta_n} & 1 + e^{i\delta_n} \end{bmatrix}, \tag{3.24}
\end{aligned}$$

where $\delta_n \triangleq \phi_c - \tilde{\phi}_c + n(\phi_x - \tilde{\phi}_x)$ denotes the difference map between the true phase $\tilde{\phi}$ and a candidate phase parameter ϕ .

After appropriate permutations, the likelihood (3.23) becomes

$$\mathcal{L}(\phi) = \sum_{n=0}^{N-1} \sum_{m=0}^{M/2-1} [\mathbf{M}\mathbf{z}]'_{nm} \mathbf{B}'_{nm} \mathbf{M}_{nm} \mathbf{B}_{nm} [\mathbf{M}\mathbf{z}]_{nm},$$

where $[\mathbf{M}\mathbf{z}]_{nm} \triangleq \left[x[n, m] \quad x[n, m + M/2] \right]'$ for $n = 0, \dots, N - 1$ and $m = 0, \dots, M/2 - 1$, and \mathbf{M}_{nm} is a 2×2 block along the diagonal of $\mathbf{M}\mathbf{M}'$ permuted.

It is easy to verify that $\mathbf{B}'_{nm} \mathbf{B}_{nm} = \mathbf{I}_2$ and thus, the terms of the summation where $\mathbf{M}_{nm} = \mathbf{I}_2$ reduce to components of the form $[\mathbf{M}\mathbf{z}]'_{nm} [\mathbf{M}\mathbf{z}]_{nm}$ that are independent of ϕ and do not contribute to the likelihood. However, for pairs of aliased pixels where one is within the mask and the other

is outside of the mask, we have

$$\mathbf{M}_{nm} = \begin{bmatrix} 1 & 0 \\ 0 & 0 \end{bmatrix},$$

and also $[\mathbf{Mz}]_{nm} = \begin{bmatrix} x[n, m] & 0 \end{bmatrix}'$ (since the excluded pixels contain no signal) and

$$\begin{aligned} \mathbf{B}_{nm}[\mathbf{Mz}]_{nm} &= \frac{1}{2} \begin{bmatrix} 1 + e^{i\delta_n} & 1 - e^{i\delta_n} \\ 1 - e^{i\delta_n} & 1 + e^{i\delta_n} \end{bmatrix} \begin{bmatrix} x[n, m] \\ 0 \end{bmatrix} \\ &= \frac{1}{2} \begin{bmatrix} 1 + e^{i\delta_n} \\ 1 - e^{i\delta_n} \end{bmatrix} x[n, m]. \end{aligned}$$

Hence, the corresponding summation term is written as:

$$\begin{aligned} \mathbf{C}_{nm} &\triangleq [\mathbf{Mz}]_{nm}' \mathbf{B}_{nm}' \mathbf{M}_{nm} \mathbf{B}_{nm} [\mathbf{Mz}]_{nm} \\ &= \frac{1}{4} x^*[n, m] \begin{bmatrix} 1 + e^{i\delta_n} \\ 1 - e^{i\delta_n} \end{bmatrix}' \begin{bmatrix} 1 & 0 \\ 0 & 0 \end{bmatrix} \begin{bmatrix} 1 + e^{i\delta_n} \\ 1 - e^{i\delta_n} \end{bmatrix} x[n, m] \\ &= \frac{1}{2} |x[n, m]|^2 (1 + \cos(\delta_n)). \end{aligned} \tag{3.25}$$

Therefore the overall likelihood function is

$$\mathcal{L}(\phi) = \sum_{\mathbf{M}_{mn} \neq \mathbf{I}_2} \frac{1}{2} |x[n, m]|^2 (1 + \cos(\delta_n)). \tag{3.26}$$

The likelihood function (3.26) is maximized when $\delta_n = 0$, *i.e.*, the parameter vector that maximizes the likelihood function is $\hat{\phi} = \tilde{\phi}$ for noiseless data.

The above analysis indicates that an appropriate mask selection enables estimation of the parameter vector in the single coil case. Another important finding is that not all pixels that contribute signal are useful for the estimation process and thus, we can reduce computation by selecting an appropriate ROI type of “mask” that includes only pixels such that only one of $x[n, m]$ and $x[n, m + M/2]$ is non-zero (see Figure 3.1d).

The mask can be selected manually or semi-automatically by thresholding a baseline full FOV image and then expanding the resulting binary image by a few pixels around the boundaries. To create an ROI “mask” the original mask is shifted by $M/2$ along y and only the non-overlapping

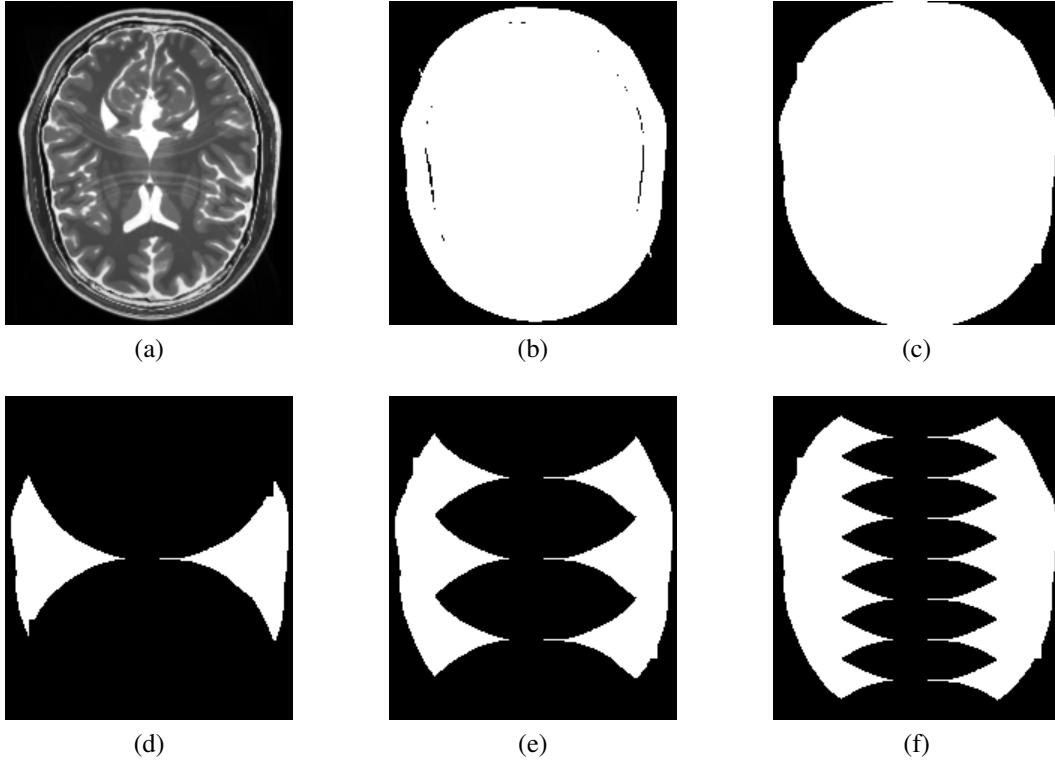


Figure 3.1: Selection of reconstruction mask. (a) Baseline image with residual ghosting. (b) Initial mask from image thresholding. (c) Reconstruction mask from expanding (dilating) initial mask to ensure that all non-zero pixels are included. (d) Phase estimation ROI “mask” based on including only pixels whose $M/2$ counterpart has zero spin-density. (e) ROI “mask” for 2-shot acquisition. (f) ROI “mask” for 4-shot acquisition

pixels are retained using binary operations between the original and shifted masks¹.

For a multi-shot acquisition with N_s shots one can show that phase map estimation is possible when choosing an ROI “mask” that includes locations such that not all of the $x[n, m + kM/(2N_s)]$ for $k = 0, \dots, N_s - 1$ pixels contribute signal, *i.e.*, $x[n, m + kM/(2N_s)] = 0$ for some $k \in \{1, \dots, N_s - 1\}$. In this case the ROI “mask” is created as follows. The reconstruction mask (Figure 3.1c) is shifted by $m + kM/(2N_s)$ along y to create $2N_s - 1$ replicates and the common regions of all $2N_s$ masks are identified (binary AND). Then these regions are removed from the original reconstruction mask (binary XOR) to create the ROI “mask”. Figures 3.1e and 3.1f show examples of these masks for 2-shot and 4-shot acquisitions. The results in §3.5.1 show that phase map estimation is feasible even in cases where fully unaliased regions cannot be obtained (as is common for multi-shot acquisitions). Hence, unlike conventional methods, our approach is useful

¹In Matlab notation these operations are expressed as: `mask_roi = xor(mask, circshift(mask, [0 M/2])) & mask`

even in multi-shot acquisitions without the requirement for odd number of shots with alternating polarities [27, 28].

The analyses presented in this section also apply to 2D parametric phase map estimation, though the derivations are more complicated and were omitted for clarity of presentation. Also in the case where parallel imaging is used (with suitable sensitivity maps) the mask is not required for estimation, but (as illustrated in §3.3.3) using an ROI “mask” facilitates the formulation of a quadratic surrogate algorithm for solving the optimization problem in (3.10).

3.3.3 Quadratic Surrogate Optimization for Single-Shot EPI

This section presents an algorithm for solving the optimization problem in (3.10) based on the majorize-minimize approach using quadratic surrogates [38]. The method is applicable to both 2D and 1D parametric phase map estimation for single-shot acquisitions and for 1D phase maps for multi-shot acquisitions. Here we consider the case of parallel imaging with L receiver coils with known sensitivity maps, and a 2D parametric phase map model (the derivations are similar for the simpler 1D case). Single coil scans are a simple special case of the method.

Under these assumptions for single-shot scans the Hessian of the ML cost function $\|\mathbf{y} - \mathbf{A}(\boldsymbol{\phi})\mathbf{z}\|_2^2$ is

$$\begin{aligned} \mathbf{H}(\boldsymbol{\phi}) &\triangleq \mathbf{A}'(\boldsymbol{\phi}) \mathbf{A}(\boldsymbol{\phi}) = \mathbf{M}' \mathbf{F}'(\mathbf{T}\boldsymbol{\phi}) \mathbf{F}(\mathbf{T}\boldsymbol{\phi}) \mathbf{M} \\ &= \mathbf{M}' \mathbf{G}(\boldsymbol{\phi}_y) \mathbf{M}, \end{aligned} \tag{3.27}$$

where

$$\begin{aligned}
\mathbf{G}(\phi_y) &\triangleq \sum_{l=1}^L \mathbf{S}'_l (\mathbf{F}'_+ \mathbf{F}_+ + \mathbf{P}'(\mathbf{T}\phi) \mathbf{F}'_- \mathbf{F}_- \mathbf{P}(\mathbf{T}\phi)) \mathbf{S}_l \\
&= \sum_{l=1}^L \mathbf{S}'_l [(\mathbf{F}'_x \mathbf{F}_x) \otimes (\mathbf{F}'_{y,+} \mathbf{F}_{y,+}) + (\mathbf{P}'_x(\mathbf{T}\phi) \mathbf{F}'_x \mathbf{F}_x \mathbf{P}_x(\mathbf{T}\phi)) \otimes (\mathbf{P}'_y(\mathbf{T}\phi) \mathbf{F}'_{y,-} \mathbf{F}_{y,-} \mathbf{P}_y(\mathbf{T}\phi))] \mathbf{S}_l \\
&= \sum_{l=1}^L \mathbf{S}'_l [\mathbf{I}_N \otimes (\mathbf{F}'_{y,+} \mathbf{F}_{y,+}) + \mathbf{I}_N \otimes (\mathbf{P}'_y(\mathbf{T}\phi) \mathbf{F}'_{y,-} \mathbf{F}_{y,-} \mathbf{P}_y(\mathbf{T}\phi))] \mathbf{S}_l \\
&= \sum_{l=1}^L \mathbf{S}'_l [\mathbf{I}_N \otimes (\mathbf{F}'_{y,+} \mathbf{F}_{y,+} + \mathbf{P}'_y(\mathbf{T}\phi) \mathbf{F}'_{y,-} \mathbf{F}_{y,-} \mathbf{P}_y(\mathbf{T}\phi))] \mathbf{S}_l \\
&= \sum_{l=1}^L \mathbf{S}'_l \left[\mathbf{I}_N \otimes \left(\frac{1}{2} \begin{bmatrix} \mathbf{I}_{M/2} & \mathbf{I}_{M/2} \\ \mathbf{I}_{M/2} & \mathbf{I}_{M/2} \end{bmatrix} + \frac{1}{2} \begin{bmatrix} \mathbf{I}_{M/2} & -e^{-i\phi_y M/2} \mathbf{I}_{M/2} \\ -e^{i\phi_y M/2} \mathbf{I}_{M/2} & \mathbf{I}_{M/2} \end{bmatrix} \right) \right] \mathbf{S}_l \\
&= \sum_{l=1}^L \mathbf{S}'_l \left(\mathbf{I}_N \otimes \begin{bmatrix} \mathbf{I}_{M/2} & \rho_y \mathbf{I}_{M/2} \\ \rho_y^* \mathbf{I}_{M/2} & \mathbf{I}_{M/2} \end{bmatrix} \right) \mathbf{S}_l \tag{3.28}
\end{aligned}$$

with \mathbf{S}_l and $\mathbf{P}(\mathbf{T}\phi)$ as defined in (3.4) and (3.17) respectively, and $\rho_y \triangleq (1 - e^{-i\phi_y M/2})/2$.

The matrix \mathbf{G} in (3.28) has a banded diagonal structure and can be rearranged into a block diagonal matrix consisting of $NM/2$ blocks of size 2×2 . Each block is given by

$$\begin{aligned}
[\mathbf{G}(\phi_y)]_{nm} &\triangleq \begin{bmatrix} s_{11}[n, m] & s_{12}[n, m] \\ s_{12}^*[n, m] & s_{22}[n, m] \end{bmatrix}, \tag{3.29} \\
s_{11}[n, m] &\triangleq \sum_{l=1}^L |s_l[n, m]|^2, \\
s_{22}[n, m] &\triangleq \sum_{l=1}^L |s_l[n, m + M/2]|^2, \\
s_{12}[n, m] &\triangleq \rho_y \sum_{l=1}^L s_l^*[n, m] s_l[n, m + M/2].
\end{aligned}$$

From (3.29) we see that, in addition to the coupling of locations separated by $M/2$, the Hessian also depends on the parameter vector ϕ through the component ϕ_y . When $\phi_y = 0$, corresponding to 1D phase correction, then $s_{12}[n, m] = 0$ and $[\mathbf{G}]_{nm}$ is diagonal.

By defining the following coil combination images (*cf.* [39, eqn. 20]):

$$\mathbf{v}_+ \triangleq \sum_{l=1}^L \mathbf{S}'_l \mathbf{F}'_+ \mathbf{y}_{l,+}, \quad \mathbf{v}_- \triangleq \sum_{l=1}^L \mathbf{S}'_l \mathbf{F}'_- \mathbf{y}_{l,-}, \quad (3.30)$$

and also

$$\begin{aligned} \mathbf{u}_+ &\triangleq \mathbf{M}' \mathbf{v}_+, & \mathbf{u}_- &\triangleq \mathbf{M}' \mathbf{v}_-, \\ \tilde{\mathbf{T}} &\triangleq \mathbf{M}' \mathbf{T}, & \mathbf{P}(\tilde{\mathbf{T}}\phi) &\triangleq \mathbf{M}' \mathbf{P}(\mathbf{T}\phi), \end{aligned}$$

the likelihood function in (3.10) becomes

$$\begin{aligned} \mathcal{L}(\phi) &= (\mathbf{v}_+ + \mathbf{P}'(\mathbf{T}\phi) \mathbf{v}_-)' \mathbf{M}(\mathbf{H}(\phi))^{-1} \mathbf{M}' (\mathbf{v}_+ + \mathbf{P}'(\mathbf{T}\phi) \mathbf{v}_-) \\ &= \Re \left\{ \mathbf{u}'_+ (\mathbf{H}(\phi))^{-1} \mathbf{P}'(\tilde{\mathbf{T}}\phi) \mathbf{u}_- \right\} + \mathbf{u}'_- \mathbf{P}(\tilde{\mathbf{T}}\phi) (\mathbf{H}(\phi))^{-1} \mathbf{P}'(\tilde{\mathbf{T}}\phi) \mathbf{u}_-, \end{aligned} \quad (3.31)$$

ignoring constant terms independent of ϕ .

Due to the $M/2$ coupling introduced by \mathbf{H} , the likelihood in (3.31) does not easily lead to an efficient optimization algorithm. This problem can be alleviated by choosing an ROI support constraint (like the mask in Figure 3.1d) where only pixels whose $M/2$ counterpart is zero are included. This choice of mask effectively eliminates the $M/2$ coupling and the dependence on ϕ_y , since each 2×2 block $[\mathbf{G}]_{nm}$ is either completely eliminated or only one element along the main diagonal is retained when forming the Hessian using (3.27). Therefore, using this type of mask, the Hessian simplifies to a $(K \times K)$ diagonal matrix

$$\mathbf{H} = \mathbf{S}_K \triangleq \mathbf{M}' \left(\sum_{l=1}^L \mathbf{S}'_l \mathbf{S}_l \right) \mathbf{M}, \quad (3.32)$$

with elements

$$s_k \triangleq \sum_{l=1}^L |s_l[n_k, m_k]|^2,$$

where k corresponds to a pixel location $[n_k, m_k]$ that is included in the mask.

Using the simplified form of the Hessian in (3.32), the likelihood function in (3.31) becomes

$$\begin{aligned}\mathcal{L}(\boldsymbol{\phi}) &= \Re\left\{\mathbf{u}'_+ \mathbf{S}_K^{-1} \mathbf{P}'(\tilde{\mathbf{T}}\boldsymbol{\phi}) \mathbf{u}_-\right\} \\ &= \sum_{k=1}^K w_k \cos\left(\left[\tilde{\mathbf{T}}\boldsymbol{\phi}\right]_k - \eta_k\right),\end{aligned}\quad (3.33)$$

and the estimate of $\boldsymbol{\phi}$ is found by minimizing the following cost function resulting from (3.33):

$$\hat{\boldsymbol{\phi}} = \underset{\boldsymbol{\phi}}{\operatorname{argmin}} \left\{ \Psi(\boldsymbol{\phi}) \triangleq \sum_{k=1}^K w_k \left(1 - \cos\left(\left[\tilde{\mathbf{T}}\boldsymbol{\phi}\right]_k - \eta_k\right)\right) \right\}, \quad (3.34)$$

where \mathbf{w} is a $(K \times 1)$ vector with elements $w_k \triangleq |u_{+,k}| |u_{-,k}| / s_k$, and $\boldsymbol{\eta}$ is a $(K \times 1)$ vector with elements $\eta_k \triangleq \angle u_{+,k} - \angle u_{-,k}$.

The form of the cost function in (3.34) is similar to the one used in [21] for fieldmap estimation, so we can develop an optimization transfer algorithm of a similar form. By defining \odot as the element-wise multiplication of vectors and $\operatorname{sinc}(t) \triangleq \sin(t)/t$ for $t \neq 0$ and $\operatorname{sinc}(t) \triangleq 1$ for $t = 0$, the quadratic surrogate algorithm can be expressed as

$$\begin{aligned}\mathbf{t}^{(n)} &= \tilde{\mathbf{T}}\boldsymbol{\phi}^{(n)} - \boldsymbol{\eta} \\ \mathbf{c}^{(n)} &= \mathbf{w} \odot \operatorname{sinc}(\mathbf{t}^{(n)}) \\ \nabla\Psi(\boldsymbol{\phi}^{(n)}) &= \tilde{\mathbf{T}}' [\mathbf{c}^{(n)} \odot \mathbf{t}^{(n)}] \\ \mathbf{H}^{(n)} &= \tilde{\mathbf{T}}' \operatorname{diag}\{\mathbf{c}^{(n)}\} \tilde{\mathbf{T}} \\ \boldsymbol{\phi}^{(n+1)} &= \boldsymbol{\phi}^{(n)} - \left[\mathbf{H}^{(n)}\right]^{-1} \nabla\Psi(\boldsymbol{\phi}^{(n)}).\end{aligned}\quad (3.35)$$

The steps of the algorithm are computationally inexpensive since the matrix inversions are only 3×3 (or 2×2 for 1D parametric phase map). Because the cost function is non-convex we need a good initialization $\boldsymbol{\phi}^{(0)}$ to converge to the ‘‘correct’’ local minimum, as discussed in §3.3.5.

The algorithm (3.35) is applicable to single-shot acquisitions with one or more receiver coils and for both 1D and 2D phase correction. For multi-shot acquisitions formulating a simple quadratic surrogate algorithm for 2D parametric phase map estimation is difficult because the aliasing pattern of the Hessian $\mathbf{F}'(\mathbf{T}\boldsymbol{\phi}) \mathbf{F}(\mathbf{T}\boldsymbol{\phi})$ is more complicated. For realistic images that cover most of the vertical FOV one can rarely obtain an ROI mask where only one of the aliased locations contributes to the signal. Thus, the matrix inversion of (3.10) cannot be reduced to a diagonal form, which in turn prohibits the formulation of a simple algorithm like (3.35) for the single-shot case. For 2D

parametric phase map estimation one can use the alternating minimization method presented in the following section (§3.3.4). A quadratic surrogate optimization method for 1D parametric phase map estimation in multi-shot acquisitions is presented in this chapter's appendix.

3.3.4 Alternating Minimization Method for Multi-Shot EPI

In multi-shot EPI trajectories the misalignment of positive and negative direction echoes may be different in each shot and also there may be misalignment of the echoes between the shots. In this case using a single phase map may be inadequate for ghost artifact suppression, so we extended the proposed model by using multiple phase maps.

For multi-shot EPI with N_s shots we use the positive direction of the first shot as reference and model all the possible misalignments with $2N_s - 1$ phase maps (or parameter vectors for our model). However, for simplicity of presentation we define $2N_s$ phase maps, where $\phi_{+,1} = 0$ by definition. Thus, our system model for multi-shot EPI is

$$\mathbf{F}(\boldsymbol{\phi}) \triangleq \begin{bmatrix} \mathbf{F}_{+,1}\mathbf{P}(\mathbf{T}\boldsymbol{\phi}_{+,1}) \\ \vdots \\ \mathbf{F}_{+,N_s}\mathbf{P}(\mathbf{T}\boldsymbol{\phi}_{+,N_s}) \\ \mathbf{F}_{-,1}\mathbf{P}(\mathbf{T}\boldsymbol{\phi}_{-,1}) \\ \vdots \\ \mathbf{F}_{-,N_s}\mathbf{P}(\mathbf{T}\boldsymbol{\phi}_{-,N_s}) \end{bmatrix}, \quad (3.36)$$

where $\boldsymbol{\phi}_{+,j}$ is the parameter vector for the misalignment of the positive direction of the j th shot w.r.t the positive direction of the first shot and $\boldsymbol{\phi}_{-,j}$ is the corresponding parameter vector for the negative direction.

The system model in (3.36) can be written in a more convenient form as:

$$\mathbf{F}(\boldsymbol{\phi}) \triangleq \begin{bmatrix} \mathbf{F}_1\mathbf{P}(\mathbf{T}\boldsymbol{\phi}_1) \\ \vdots \\ \mathbf{F}_q\mathbf{P}(\mathbf{T}\boldsymbol{\phi}_q) \end{bmatrix}, \quad (3.37)$$

where $q = 2N_s$, $\boldsymbol{\phi}_j \triangleq \boldsymbol{\phi}_{+,j}$ for $j = 1, \dots, N_s$, $\boldsymbol{\phi}_{N_s+j} \triangleq \boldsymbol{\phi}_{-,j}$ for $j = 1, \dots, N_s$, $\mathbf{F}_j \triangleq \mathbf{F}_{+,j}$ for $j = 1, \dots, N_s$, and $\mathbf{F}_{N_s+j} \triangleq \mathbf{F}_{-,j}$ for $j = 1, \dots, N_s$. For parallel imaging with L receiver coils the model of (3.37) can be easily extended similarly to (3.3).

Using the modified system model in (3.37) the cost function in (3.8) becomes

$$\Psi(\mathbf{x}, \boldsymbol{\phi}) = \|\mathbf{y} - \mathbf{F}(\boldsymbol{\phi}) \mathbf{x}\|_2^2 = \sum_{j=1}^q \|\mathbf{y}_j - \mathbf{F}_j \mathbf{P}(\mathbf{T} \boldsymbol{\phi}_j) \mathbf{x}\|_2^2 \quad (3.38)$$

where $\boldsymbol{\phi} \triangleq (\phi_1, \dots, \phi_q)$, and $\mathbf{y} \triangleq \begin{bmatrix} \mathbf{y}'_1 & \dots & \mathbf{y}'_q \end{bmatrix}'$.

For joint minimization of the cost function in (3.38), in cases where solving (3.10) is not practical (*i.e.*, 2D parametric phase map with multi-shot acquisition), we employed an alternating minimization scheme, using CG, based on a linearization approximation similar to [4,6]. The linearization approximation enables the use of CG for estimating $\boldsymbol{\phi}$ since the cost function is non-quadratic in $\boldsymbol{\phi}$. For \mathbf{x} no approximation is necessary since the cost function is quadratic in \mathbf{x} . Under the proposed scheme at the k th step of alternating minimization we have:

$$\begin{aligned} \mathbf{x}^{(k+1)} &= \underset{\mathbf{x}}{\operatorname{argmin}} \left\| \mathbf{y} - \mathbf{F}(\boldsymbol{\phi}^{(k)}) \mathbf{x} \right\|_2^2 \\ &= \left[\mathbf{F}'(\boldsymbol{\phi}^{(k)}) \mathbf{F}(\boldsymbol{\phi}^{(k)}) \right]^{-1} \mathbf{F}'(\boldsymbol{\phi}^{(k)}) \mathbf{y} \end{aligned} \quad (3.39)$$

$$\begin{aligned} \boldsymbol{\phi}_j^{(k+1)} &= \underset{\boldsymbol{\phi}_j}{\operatorname{argmin}} \left\| \tilde{\mathbf{y}}_j^{(k)} - \tilde{\mathbf{F}}_j^{(k)} \boldsymbol{\phi}_j \right\|_2^2 \text{ for } j = 2, \dots, q \\ &= \Re \left\{ \left[(\tilde{\mathbf{F}}_j^{(k)})' \tilde{\mathbf{F}}_j^{(k)} \right]^{-1} (\tilde{\mathbf{F}}_j^{(k)})' \tilde{\mathbf{y}}_j^{(k)} \right\} \text{ for } j = 2, \dots, q, \end{aligned} \quad (3.40)$$

where

$$\begin{aligned} \tilde{\mathbf{F}}_j^{(k)} &\triangleq -i \mathbf{F}_j \mathbf{P}(\mathbf{T} \boldsymbol{\phi}_j^{(k)}) \operatorname{diag}\{\mathbf{x}^{(k+1)}\} \mathbf{T} \\ \tilde{\mathbf{y}}_j^{(k)} &\triangleq \mathbf{y}_j - \mathbf{F}_j \mathbf{P}(\mathbf{T} \boldsymbol{\phi}^{(k)}) \mathbf{x}^{(k+1)} + \tilde{\mathbf{F}}_j^{(k)} \boldsymbol{\phi}_j^{(k)}. \end{aligned}$$

We do not update $\boldsymbol{\phi}_{+,1}$, *i.e.*, $j = 1$, because it is set as zero by definition. We used CG to solve (3.39) for convenience, whereas we use a matrix inverse for the updates for $\boldsymbol{\phi}_j$ since they involve inverting only 3×3 matrices. The Hessian of (3.39) permutes to a block diagonal matrix and thus permits a more efficient implementation that inverts the small $2N_s \times 2N_s$ (where N_s is the number of shots) blocks directly. This approach, that is similar to SENSE “unfolding” [5], is used in [19, eqn. (2), (4)] and could improve the computational efficiency of our method.

Since the cost function is non-convex with respect to $\boldsymbol{\phi}$ we need a fairly accurate initialization $\boldsymbol{\phi}^{(0)}$ to ensure convergence in the “correct” local minimum. For the linear model used, the dominant effects are the constant term ϕ_c and the linear term ϕ_x along the readout direction, thus a good

initialization of these values is required as discussed in §3.3.5, whereas we have found it sufficient to initialize ϕ_y , the linear term along the phase encode direction y , to zero.

3.3.5 Initialization and Approximate Estimates

To find initial values $\phi^{(0)}$ for the iterative algorithms presented (quadratic surrogate and alternating minimization) the conventional approach would be to use a standard 2D plane fitting or 1D line fitting in the phase difference of an unaliased region of the images reconstructed with only the positive or negative readouts [14, 25, 26]. If an unaliased region is unavailable (tight FOV, or multi-shot acquisition) an initial estimate could be obtained from a reference scan or from previous scans of the same type if available. This section presents an alternative approach that uses only the acquired data and (as explained in §3.3.2) does not rely on the existence of unaliased regions, and thus is applicable to multi-shot acquisitions.

For single-shot acquisitions we can rewrite the likelihood (3.33) as follows:

$$\begin{aligned}
\mathcal{L}(\phi) &= \sum_{k=1}^K w_k \cos([\mathbf{T}\phi]_k + \eta_k) \\
&= \sum_{[n,m] \in Q} w[n, m] \cos(\phi_c + n\phi_x + m\phi_y + \eta[n, m]) \\
&= \Re \left\{ \sum_{[n,m] \in Q} \tilde{u}[n, m] e^{-i\phi_c} e^{-i(\phi_x n + \phi_y m)} \right\} \\
&= \Re \left\{ e^{-i\phi_c} \sum_{n=-\infty}^{\infty} \sum_{m=-\infty}^{\infty} u[n, m] e^{-i(\phi_x n + \phi_y m)} \right\} \\
&= \Re \{ e^{-i\phi_c} U(\phi_x, \phi_y) \}, \tag{3.41}
\end{aligned}$$

where Q is the set of locations $[n, m]$ included in the ROI “mask” (e.g., Figure 3.1d), $\tilde{u}[n, m] \triangleq w[n, m] e^{-i\eta[n, m]}$, $u[n, m]$ is a zero-padded signal such that $u[n, m] = \tilde{u}[n, m]$ if $[n, m] \in Q$ and $u[n, m] = 0$ otherwise, and $U(\cdot, \cdot)$ is the 2D discrete space Fourier transform (DSFT) of $u[\cdot, \cdot]$.

From (3.41) the ML estimate of the constant phase factor is

$$\hat{\phi}_c = \angle U(\phi_x, \phi_y). \tag{3.42}$$

Substituting into (3.41) the ML estimates for the linear phase terms are given by

$$\left(\hat{\phi}_x, \hat{\phi}_y\right) = \underset{\phi_x, \phi_y}{\operatorname{argmax}} |U(\phi_x, \phi_y)|. \quad (3.43)$$

Calculating the DSFT for all frequencies is not feasible, but we can calculate samples of it by taking an $N' \times M'$ point 2D DFT of $u[n, m]$, denoted as $U[k, l]$. Since $u[n, m]$ is space limited within an $N \times M$ region and by choosing $N' \geq N$ and $M' \geq M$, from the DFT/DSFT properties it follows that $U[k, l] = U(2\pi k/N', 2\pi l/M')$. Using this property we can find an approximate solution for (3.43) by finding the location $[\hat{k}, \hat{l}]$ where $|U[k, l]|$ attains its maximum value. The approximate values for the parameters are computed using the following relations:

$$\begin{aligned} \hat{\phi}_x &= 2\pi\hat{k}/N \\ \hat{\phi}_y &= 2\pi\hat{l}/M \\ \hat{\phi}_c &= \angle U[\hat{k}, \hat{l}]. \end{aligned} \quad (3.44)$$

Since the sample spacing of the DSFT depends on the number of samples N', M' , the quality of the approximation also depends on the number of samples of the DFT. Thus, we improve the initial estimates by zero-padding the signal $u[n, m]$ to a larger size. Choosing the amount of zero-padding is a compromise between accuracy of the initial estimate and computational complexity. From our experiments zero padding up to 4 times the initial size seemed to be sufficient for good initialization without significant computational cost. Apart from zero-padding, the accuracy of this method could be improved by using interpolation to achieve sub-sample accuracy when finding the locations that maximize $|U[k, l]|$. However implementing such interpolation method is beyond the scope of our work.

For multi-shot trajectories we cannot use the above approximation method to find estimates for a 2D parametric model. However, if we consider just 1D phase correction and a single parameter vector ϕ according to the model in (3.2) for the purposes of initialization, despite the model mismatch we can find fairly accurate initial values for the constant term ϕ_c and the linear term ϕ_x . These two terms are more important in initialization because usually the value of ϕ_y is small and initializing with 0 appears to be adequate for our iterative methods. For a 1D model, the likelihood

(3.33) becomes

$$\begin{aligned}
\mathcal{L}(\phi) &= \sum_{k=1}^K w_k \cos([\mathbf{T}\phi]_k + \eta_k) \\
&= \sum_{[m,n] \in Q} w[n, m] \cos(\phi_c + n\phi_x + \eta[n, m]) \\
&= \Re \left\{ \sum_{[m,n] \in Q} \tilde{u}[n, m] e^{-i\phi_c} e^{-i\phi_x n} \right\} \\
&= \Re \left\{ e^{-i\phi_c} \sum_{n=-\infty}^{\infty} \sum_{m=-\infty}^{\infty} u[n, m] e^{-i\phi_x n} \right\} \\
&= \Re \left\{ e^{-i\phi_c} \sum_{n=-\infty}^{\infty} v[n] e^{-i\phi_x n} \right\} \\
&= \Re \left\{ e^{-i\phi_c} V(\phi_x) \right\}, \tag{3.45}
\end{aligned}$$

where $v[n] \triangleq \sum_m u[n, m]$, and $V(\cdot)$ is the 1D DSFT of $v[\cdot]$. In this case the set of locations Q corresponds to a multi-shot ROI “mask” as in Figures 3.1e and 3.1f.

From (3.45) the ML estimate of the constant term is

$$\hat{\phi}_c = \angle V(\phi_x) \tag{3.46}$$

and substituting into (3.45) the ML estimate of the linear term is

$$\hat{\phi}_x = \operatorname{argmax}_{\phi_x} |V(\phi_x)|. \tag{3.47}$$

Similarly to the 2D formulation, by taking the N' point DFT of $v[n]$, with $N' \geq N$, we have $V[k] = V(2\pi k/N')$. We can find an approximate solution for (3.47) by finding the location \hat{k} where $|V[k]|$ attains its maximum value. The approximate values for the parameters are computed as follows:

$$\begin{aligned}
\hat{\phi}_x &= 2\pi \hat{k}/N \\
\hat{\phi}_c &= \angle V[\hat{k}]. \tag{3.48}
\end{aligned}$$

Again, as in the 2D case, the amount of zero-padding is a compromise between estimation accuracy and computational performance. However, since we only take an 1D FFT we can zero-pad to a

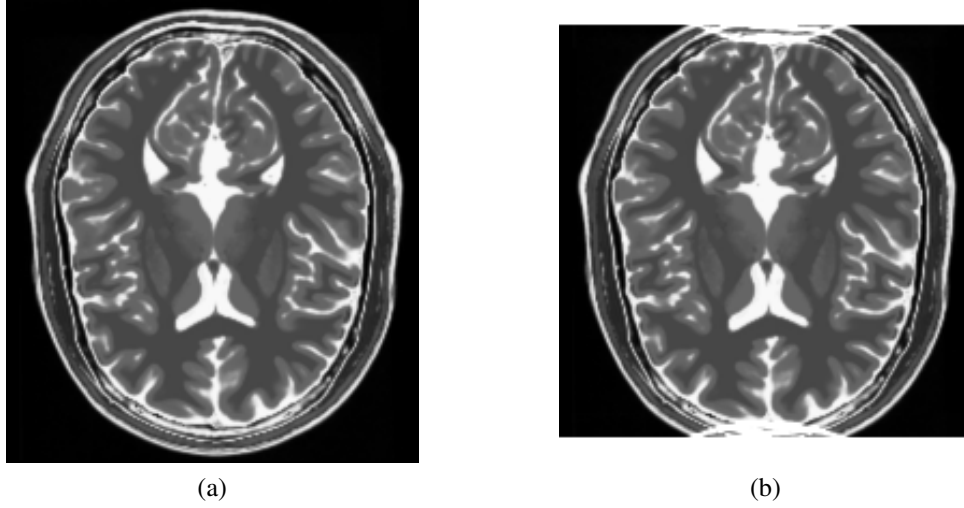


Figure 3.2: Example of tight FOV imaging. (a) Image at original FOV (192×216). (b) Image at tight FOV 192×192 with visible wraparound at the top and bottom.

large extent with minor increase in computational cost. This efficient 1D approach is also suitable for initializing ϕ for single-shot cases.

3.3.6 Tight FOV Considerations

In tight field-of-view (FOV) imaging, where the object is larger than the desired FOV, when parallel imaging (multiple receiver coils) is not available or desirable, there is unavoidable wrap-around at the edges as seen in Figure 3.2. In this section, for simplicity, we will focus on the case where wraparound occurs along only the y (phase encode) direction.

First we formulate a more accurate model for the tight FOV case that accounts for the wrap-around of the image. We assume that the image \mathbf{x} at the desired FOV is of size $N \times M$, but the actual size of the image $\tilde{\mathbf{x}}$ is $N \times M'$ with $M' > M$. Since the actual vertical size M' is not known we can assume an image size of $N \times (M + M_t + M_b)$ by adding M_t and M_b rows at the top and bottom of the image respectively to at least guarantee that $M + M_t + M_b > M'$. The resulting $NM \times N(M + M_t + M_b)$ system matrix that accounts for the wraparound and the appropriate phase map “weighting” is given by

$$\mathbf{A}(\phi) \triangleq \begin{bmatrix} \mathbf{F}_+ \mathbf{W} \\ \mathbf{F}_- \mathbf{W} \mathbf{P}(\tilde{\mathbf{T}}\phi) \end{bmatrix} \quad (3.49)$$

where $\mathbf{W} \triangleq \mathbf{I}_N \otimes \mathbf{W}_y$,

$$\mathbf{W}_y \triangleq \begin{bmatrix} \mathbf{0} & \mathbf{I}_{M_b} & \mathbf{0} & \mathbf{0} & \mathbf{I}_{M_b} \\ \mathbf{0} & \mathbf{0} & \mathbf{I}_{M-M_t-M_b} & \mathbf{0} & \mathbf{0} \\ \mathbf{I}_{M_t} & \mathbf{0} & \mathbf{0} & \mathbf{I}_{M_t} & \mathbf{0} \end{bmatrix} \quad (3.50)$$

and $[\tilde{\mathbf{T}}\phi]$ corresponds to an $N \times (M + M_t + M_b)$ phase map.

Comparing the system model of (3.49) to the one in (3.2) we see that the only difference is in the phase map “weighting” of the wraparound regions. By choosing a support constraint (mask) \mathbf{M} that excludes the pixels where all aliases contribute signal (implicitly excludes all pixels of the wraparound regions at top and bottom) similarly to Figure 3.1d the models of (3.49) and (3.2) are equivalent since the same K pixels are used in both cases. This means that for estimation purposes either model can be used, even though technically there is model mismatch when using (3.2).

However, for reconstruction purposes when the parameter vector ϕ is known (already estimated), the model mismatch from using (3.2) can lead to reconstruction artifacts in the resulting image. We will illustrate this using a Kronecker product decomposition of the system matrices and noiseless data acquired with the model in (3.49). In this case the least squares estimate of $\tilde{\mathbf{x}}$ becomes

$$\begin{aligned} \hat{\mathbf{x}} &= [\mathbf{F}'(\mathbf{T}\phi) \mathbf{F}(\mathbf{T}\phi)]^{-1} \mathbf{F}'(\mathbf{T}\phi) \mathbf{A}(\phi) \tilde{\mathbf{x}} \\ &= [\mathbf{F}'_+ \mathbf{F}_+ + \mathbf{P}'(\mathbf{T}\phi) \mathbf{F}'_- \mathbf{F}_- \mathbf{P}(\mathbf{T}\phi)]^{-1} \left[\mathbf{F}'_+ \mathbf{F}_+ \mathbf{W} + \mathbf{P}'(\mathbf{T}\phi) \mathbf{F}'_- \mathbf{F}_- \mathbf{W} \mathbf{P}(\tilde{\mathbf{T}}\phi) \right] \tilde{\mathbf{x}} \\ &= [\mathbf{I}_N \otimes \mathbf{H}_y]^{-1} \left[\mathbf{I}_N \otimes \left(\mathbf{F}'_{y,+} \mathbf{F}_{y,+} \mathbf{W}_y + \mathbf{P}'_y(\mathbf{T}\phi) \mathbf{F}'_{y,-} \mathbf{F}_{y,-} \mathbf{W}_y \mathbf{P}_y(\tilde{\mathbf{T}}\phi) \right) \right] \tilde{\mathbf{x}} \\ &= \mathbf{I}_N \otimes \left[\mathbf{H}_y^{-1} \left(\mathbf{F}'_{y,+} \mathbf{F}_{y,+} \mathbf{W}_y + \mathbf{P}'_y(\mathbf{T}\phi) \mathbf{F}'_{y,-} \mathbf{F}_{y,-} \mathbf{W}_y \mathbf{P}_y(\tilde{\mathbf{T}}\phi) \right) \right] \tilde{\mathbf{x}}, \end{aligned} \quad (3.51)$$

where $\mathbf{H}_y \triangleq \mathbf{F}'_{y,+} \mathbf{F}_{y,+} + \mathbf{P}'_y(\mathbf{T}\phi) \mathbf{F}'_{y,-} \mathbf{F}_{y,-} \mathbf{P}_y(\mathbf{T}\phi)$.

As we see from (3.51), for a 2D parametric phase map model ML estimation does not retrieve $\tilde{\mathbf{x}}$ exactly, even from noiseless data because of model mismatch. However for a 1D parametric phase map model we have $\mathbf{P}_y(\mathbf{T}\phi) = \mathbf{I}_M$ and $\mathbf{P}_y(\tilde{\mathbf{T}}\phi) = \mathbf{I}_{M+M_t+M_b}$ which reduces (3.51) to

$$\begin{aligned} \hat{\mathbf{x}} &= [\mathbf{I}_N \otimes (\mathbf{F}'_{y,+} \mathbf{F}_{y,+} + \mathbf{F}'_{y,-} \mathbf{F}_{y,-})]^{-1} [\mathbf{I}_N \otimes (\mathbf{F}'_{y,+} \mathbf{F}_{y,+} + \mathbf{F}'_{y,-} \mathbf{F}_{y,-}) \mathbf{W}_y] \tilde{\mathbf{x}} \\ &= [\mathbf{I}_N \otimes \mathbf{I}_M]^{-1} [\mathbf{I}_N \otimes \mathbf{W}_y] \tilde{\mathbf{x}} \\ &= \mathbf{W} \tilde{\mathbf{x}} = \mathbf{x}. \end{aligned} \quad (3.52)$$

From (3.52) we see that despite the model mismatch we can exactly recover the image \mathbf{x} with the unavoidable wraparound, from noiseless data. This is not surprising since the wraparound is only along y where there is no phase map “weighting” in the 1D model and thus, no residual ghosting artifacts due to model mismatch.

Reconstructing with the system model of (3.49) should enable artifact-free reconstruction of $\tilde{\mathbf{x}}$ when the 2D phase map parameters ϕ are known. However, the problem is under-determined and there is no unique solution unless we enforce a support constraint (mask) or introduce a regularization term.

For the support constraint we can choose an $N(M + M_t + M_b) \times K$ matrix \mathbf{M} that excludes pixels with zero spin-density (no signal) such that $K \leq MN$. Now we can recover a least squares estimate of $\mathbf{z} \triangleq \mathbf{M}\tilde{\mathbf{x}}$ using

$$\begin{aligned}\hat{\mathbf{z}} &= \underset{\mathbf{z}}{\operatorname{argmin}} \|\mathbf{y} - \mathbf{A}(\phi) \mathbf{M}\mathbf{z}\|_2^2 \\ &= [\mathbf{M}' \mathbf{A}'(\phi) \mathbf{A}(\phi) \mathbf{M}]^{-1} \mathbf{M}' \mathbf{A}'(\phi) \mathbf{y}, \\ \hat{\mathbf{x}} &= \mathbf{M}\hat{\mathbf{z}}.\end{aligned}\tag{3.53}$$

For the regularized least squares estimation one needs to choose an appropriate regularization term. We chose a regularizer that minimizes the energy of the ghost by forming a matrix \mathbf{R} that isolates the pixels outside the object of interest (pixels that ideally should have zero spin-density and any signal present should be attributed to ghosting artifacts). The regularization matrix \mathbf{R} can be thought of as the binary complement of the support constraint (mask) \mathbf{M} . With this formulation we reconstruct the image by minimizing the following cost function:

$$\begin{aligned}\hat{\mathbf{x}} &= \underset{\tilde{\mathbf{x}}}{\operatorname{argmin}} \|\mathbf{y} - \mathbf{A}(\phi) \tilde{\mathbf{x}}\|_2^2 + \lambda \|\mathbf{R}\tilde{\mathbf{x}}\|_2^2 \\ &= [\mathbf{A}'(\phi) \mathbf{A}(\phi) + \lambda \mathbf{R}' \mathbf{R}]^{-1} \mathbf{A}'(\phi) \mathbf{y},\end{aligned}\tag{3.54}$$

where λ is parameter that determines the “strength” of the regularizer. Because the cost function is quadratic, we use CG for minimizing it.

With either approach the reconstruction artifacts may not be completely eliminated, even with knowledge of the true 2D phase map parameters ϕ , but they are significantly reduced compared to reconstructions using the model of (3.2).

3.4 Experiments

3.4.1 Phantom Study

All the data acquisitions for our experiments were performed on a GE 3T Signa scanner and for the phantom study we used a uniform spherical phantom.

The first set of experiments used a single receiver coil and the trajectories that were used were single-shot, 2-shot, and 4-shot EPI at an axial orientation. The reconstructions from the proposed method were compared to ghost correction using the standard 1D linear phase correction and the 2D phase map correction of [14]. For both of these standard methods the 1D linear correction parameters and the 2D phase map were estimated from a central alias-free region of the half FOV images reconstructed from the positive and negative direction gradients (Figure 3.3). For multi-shot EPI, since an alias free region cannot be obtained from the positive and negative direction images, the standard methods used the values obtained from the single-shot correction. For our proposed method we initialized the parameter vector ϕ using the approximate estimation method in §3.3.5 where a 2D estimate (3.44) was used for single-shot and an 1D estimate (3.48) was used for 2-shot and 4-shot and the term ϕ_y was initialized to zero. For the proposed method in multi-shot EPI we performed the joint estimation using the multiple phase map model of (3.37).

The second set of experiments used 8 receiver coils with sensitivity maps [40] for the axial plane shown in Figure 3.4. For the multi-coil image reconstruction we used the SENSE method [5]. For these experiments we used the same trajectories and orientations as in the single coil case. The conventional 2D estimation method that we used for comparison is based on [14], where the phase map is found by unwrapping the phase difference between the full FOV images (available using SENSE reconstruction) reconstructed from the positive and negative direction echoes. The unwrapped phase difference is then used to estimate a parametric 2D phase map with weighted least squares using the image magnitude as weight. The final conventional 2D phase map is acquired by directly using the phase difference in regions within the object and the parametric 2D phase map in regions with low signal outside the object. For the 1D linear correction we again used a central region and estimated a constant and a linear (along x) phase term. For initializing our proposed method we used the same approximate method (3.44) or (3.48) as in the single-coil case.

For our iterative methods, both QS and alternating minimization, instead of performing a fixed number of iterations, we employed a stopping rule that terminates the iterative process when the normalized difference between two consecutive estimates drops below a predefined threshold. For

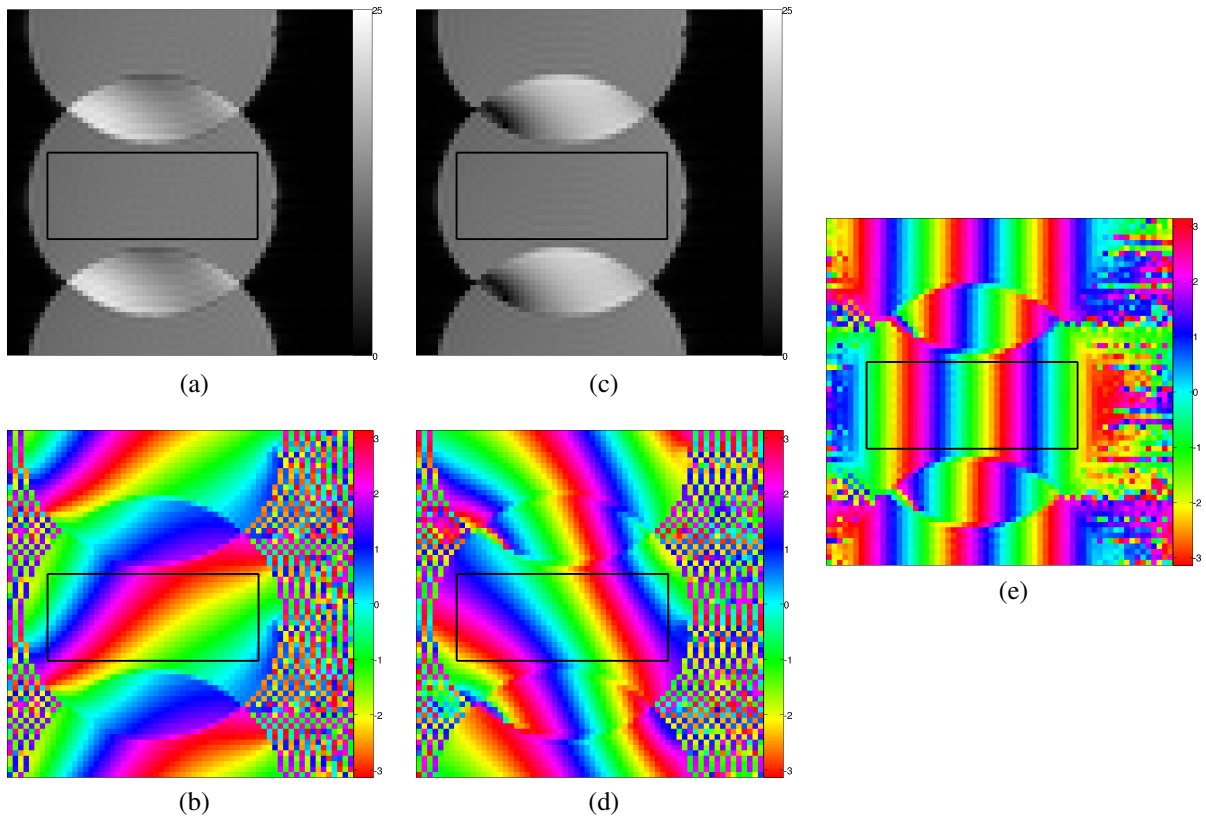


Figure 3.3: (a) Magnitude and phase image $\mathbf{x}_+ = \mathbf{F}'_+ \mathbf{y}_+$ from positive direction echoes and (b) magnitude and phase image $\mathbf{x}_- = \mathbf{F}'_- \mathbf{y}_-$ from negative direction echoes. (e) Difference of the two phase images. Rectangle denotes area used for conventional 1D linear correction and 2D phase map fitting.

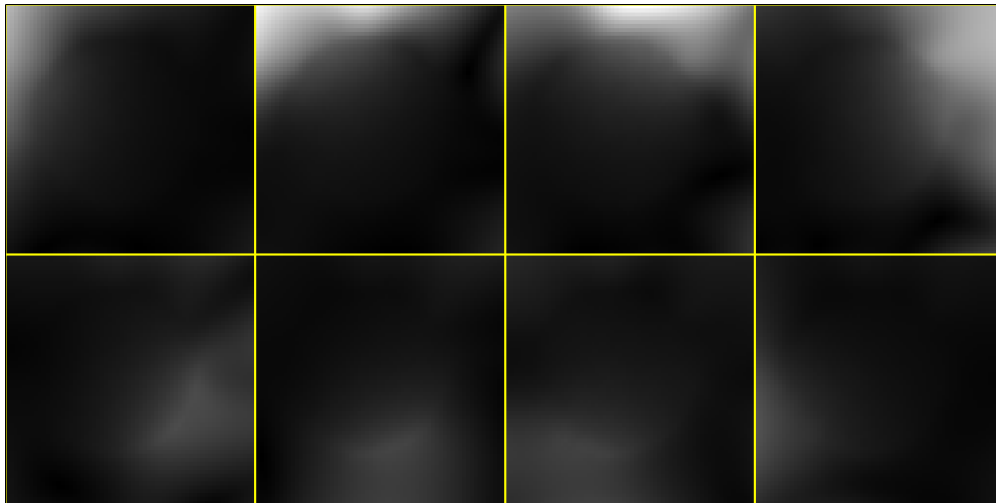


Figure 3.4: Sensitivity maps from the 8 head coils used in the multi-coil experiments.

the QS algorithm the stopping rule uses the estimated phase map parameter vector ϕ as

$$\left\| \phi^{(k)} - \phi^{(k-1)} \right\| / \left\| \phi^{(k)} \right\| < \varepsilon, \quad (3.55)$$

and for the alternating minimization method the stopping rule uses the estimated image as

$$\left\| \mathbf{x}^{(k)} - \mathbf{x}^{(k-1)} \right\| / \left\| \mathbf{x}^{(k)} \right\| < \varepsilon. \quad (3.56)$$

For both methods we chose the threshold $\varepsilon = 0.001$, *i.e.*, the algorithm stops when the difference between consecutive estimates drops below 0.1%.

3.4.2 Tight FOV

For the tight field-of-view experiment we used a digital phantom from Brainweb with full FOV of size 192×216 (Figure 3.2a) and a reconstruction FOV of 192×192 that causes wraparound along y as seen in Figure 3.2b. For this simulation we performed two separate experiments using single-coil acquisitions with single-shot trajectories and two different 2D phase map parameter vectors with the same constant term and the same linear term along x that corresponds to a shift in k_x of 1.2 samples, but different linear terms along y where the first corresponds to a shift in k_y of 0.2 samples and the second to a shift of 0.05 samples.

For 2D phase map estimation we used a support constraint as seen in Figure 3.5a and the model of (3.2). For the image reconstruction we first used the model of (3.2) to illustrate the effects of model mismatch and then reconstructed with the more accurate model of (3.49). For the reconstruction with the model of (3.49) we reconstructed the image once using (3.53) with a support constraint \mathbf{M} shown in Figure 3.5b and once using (3.54) with a regularization matrix \mathbf{R} that corresponds to the support constraint shown in Figure 3.5c. To assess the quality of the reconstructions we measured the NRMS error between the true image and the reconstructed ones. For calculating the NRMS error we used the support constraint shown in Figure 3.5d that excludes the pixels at the wraparound regions.

3.4.3 Approximate Parameter Estimation

To assess the quality of the approximate 2D estimation method of §3.3.5 we designed a simulation experiment using a single-shot trajectory and an artificial 192×256 brain image from Brainweb (Figure 3.6a). For this experiment we used both single-coil and multi-coil acquisition with 4 coils with simulated sensitivity maps (Figure 3.6c). We used a 2D parameter vector ϕ with

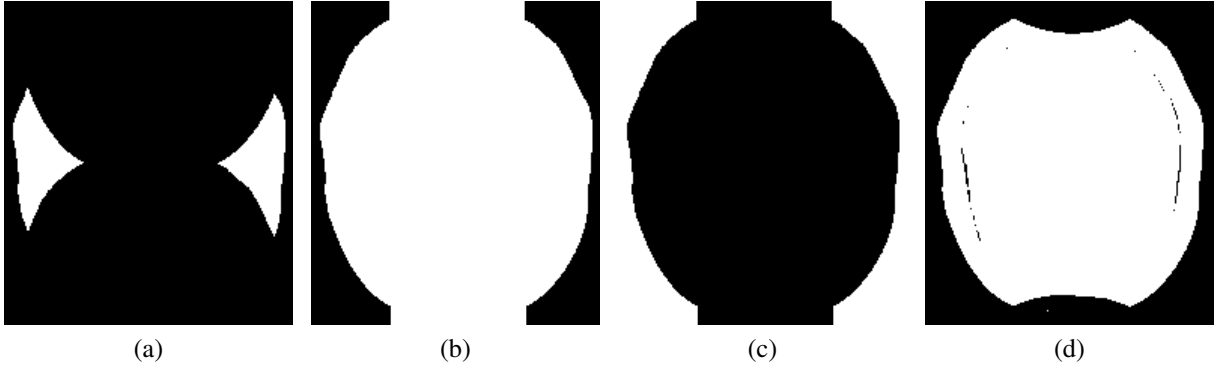


Figure 3.5: (a) Support constraint (mask) for 2D phase map estimation. (b) Support constraint for image reconstruction using (3.53). (c) Support constraint corresponding to regularization matrix \mathbf{R} for image reconstruction using (3.54). (d) Support constraint for NRMS error calculation.

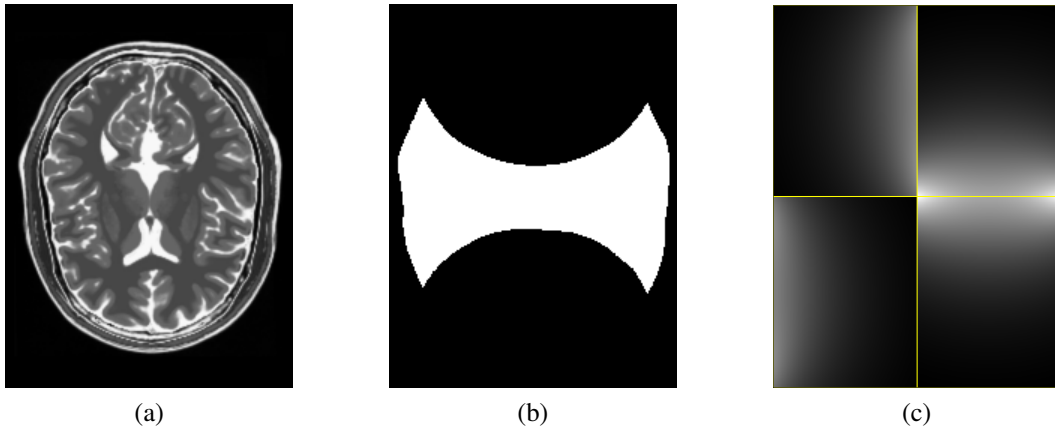


Figure 3.6: (a) Digital phantom used as true image, (b) support constraint for 2D phase map estimation, and (c) sensitivity maps used in approximate phase estimation experiments.

non-zero constant term and linear terms that correspond to k-space shifts of 1.2 samples in k_x and 0.2 samples in k_y . The approximate method was applied with varying amount of oversampling from 2 to 16 times the original size of the image using a support constraint as in Figure 3.6b. The reconstruction quality was measured quantitatively by calculating the normalized root-mean-squared (NRMS) error of the correction parameters and the reconstructed images.

3.5 Results

3.5.1 Phantom Study

In this section we present the results from the phantom study. All of the reconstructed images shown have been displayed with gamma correction to help visualize the ghosting artifacts.

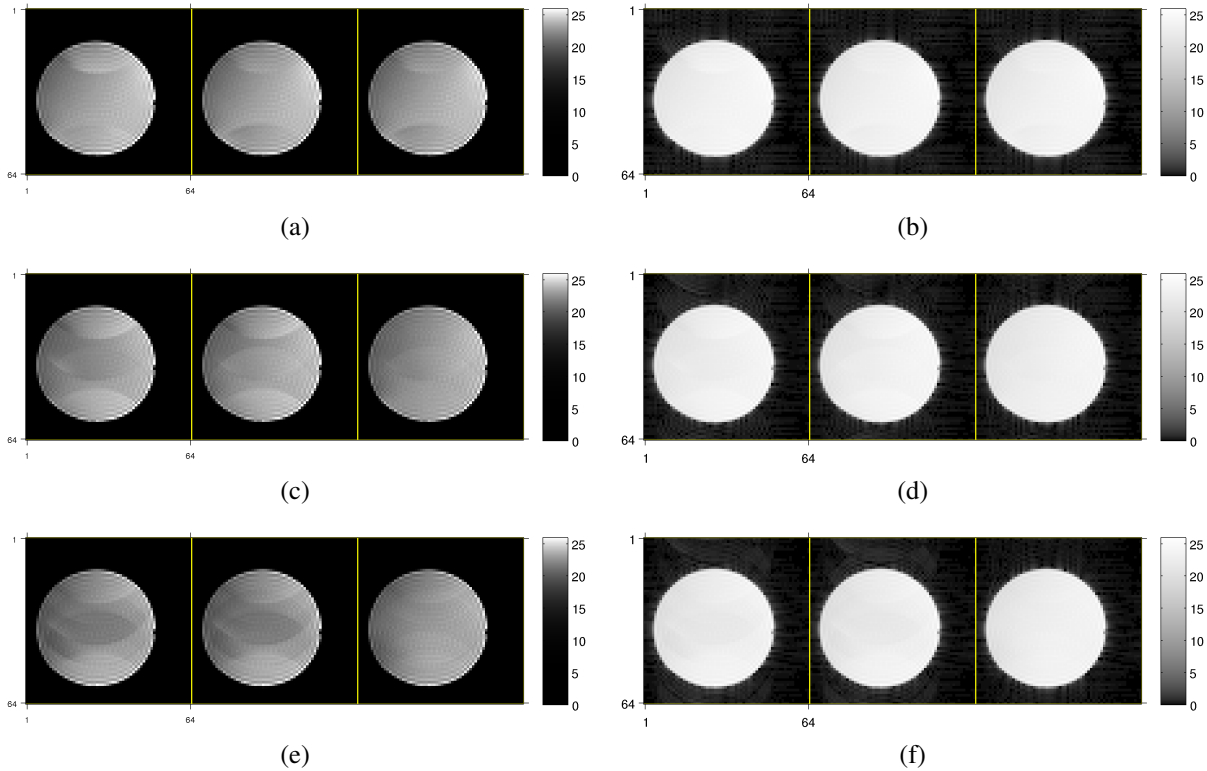


Figure 3.7: Ghost corrected images from single-coil acquisition using (a,b) single-shot, (c,d) 2-shot, and (e,f) 4-shot EPI. Images from left to right: Standard 1D linear phase correction, standard 2D phase map correction, proposed model based correction. (a,c,e) Illustration with gamma correction using $\gamma = 4$ to better visualize ghosting artifacts inside the object. (b,d,f) Illustration with gamma correction using $\gamma = 0.5$ to better visualize artifacts outside the object.

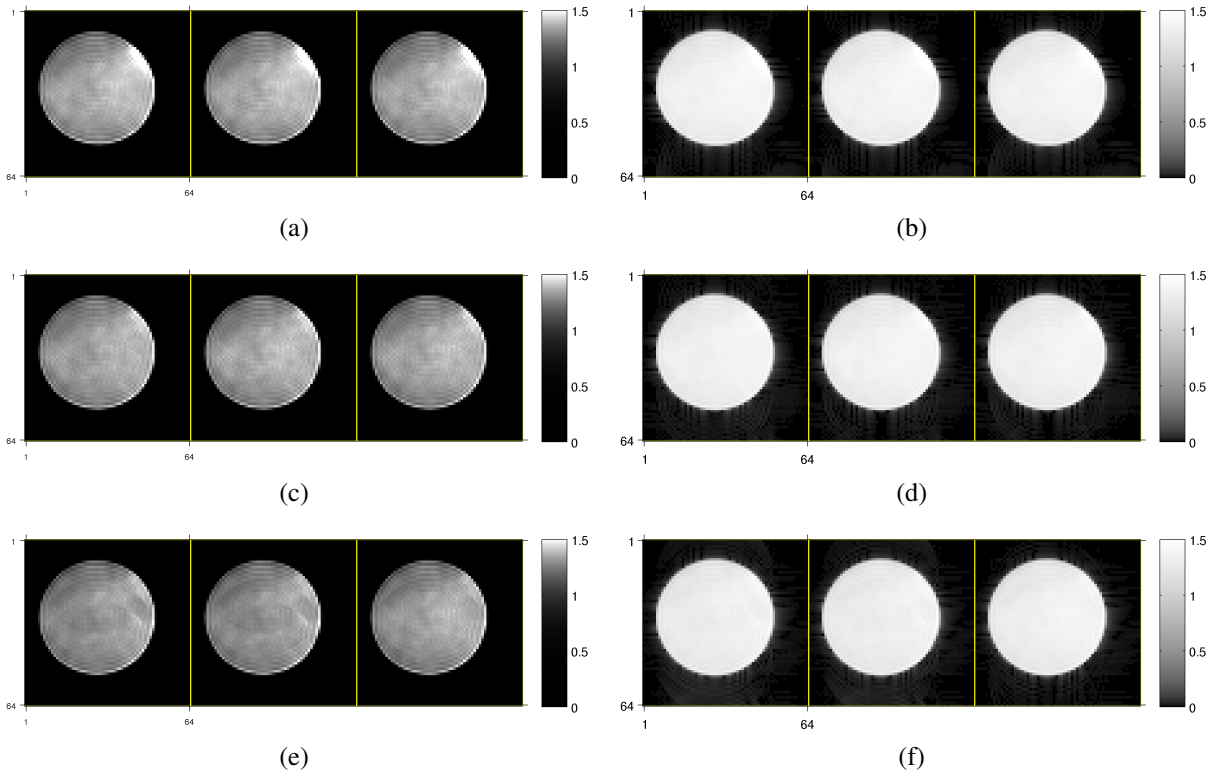


Figure 3.8: Ghost corrected images from multi-coil acquisition using (a,b) single-shot, (c,d) 2-shot, and (e,f) 4-shot EPI. Figure placement and gamma corrections same as in Figure 3.7.

Figure 3.7a shows the ghost-corrected images from a single-coil acquisition using a single-shot EPI. In this case all three methods sufficiently suppress the ghosting artifacts, although the 2D correction methods (standard and proposed) exhibit slightly improved image quality.

Figure 3.7c shows the reconstruction results from single-coil acquisition using a 2-shot EPI. In Figure 3.7c, both conventional methods perform similarly and there are visible residual ghosting artifacts. In the reconstruction from our proposed method the ghosting artifacts are significantly reduced, resulting in improved image quality. This improvement is mostly attributed to the use of the multiple phase map model of (3.37) that allows the use of individual corrections for each shot.

Figure 3.7e shows the reconstruction results from single-coil acquisition using a 4-shot EPI. In this case we also see that the conventional methods perform similarly and residual ghosting artifacts are visible. Again as in the 4-shot case we see that the proposed method using individual phase map corrections from the model in (3.37) reduces ghosting artifacts.

In Figure 3.8a we see the ghost corrected images from a multi-coil acquisition using a single-shot EPI. Here all three methods perform similarly and fully eliminate the ghosting artifacts. In this case the proposed method shows no benefit compared to the standard correction methods.

Figure 3.8c shows the reconstruction results from multi-coil acquisition using a 2-shot EPI. Here similarly to Figure 3.8a all methods perform similarly and the ghosting artifacts are almost fully suppressed. In this case the use of individual corrections for each shot of our proposed method did not visibly improve the reconstruction quality.

Figure 3.8e shows the reconstruction results from multi-coil acquisition using a 4-shot EPI. In this case both conventional methods perform similarly and there are small residual ghosting artifacts. The proposed method using individual corrections for each shot slightly improves the reconstruction quality.

The QS algorithm used for single-shot acquisitions is computationally efficient since the per iteration cost is low and the algorithm converges within a few iterations. For the chosen threshold of (3.55) the algorithm converged in only three iterations and even for a much lower threshold ($\varepsilon \approx 10^{-10}$) it converged within six or less iterations. The computation time for the QS method is comparable to the conventional 2D estimation method that uses weighted least squares fitting (25ms for single-coil and 110ms for multi-coil). Also, in the QS method most computation time is spent creating the coil combination images (3.30) (15ms for single-coil and 100ms for multi-coil), whereas the iterations are significantly faster (about 3-4ms per iteration). Thus, even using more QS iterations does not have a significant impact on the computational performance of our method.

The alternating minimization method used for multi-shot acquisitions converged in 10 to 20 iterations for our choice of threshold ε . The computational bottleneck of this method is the image reconstruction step of (3.9) that is performed using CG. Using a method similar to SENSE “unfolding” as in [19] could significantly improve the computational efficiency.

3.5.2 Tight FOV

Figure 3.9 shows the reconstructed images from the tight FOV experiment with a 2D parametric phase map with a large ϕ_y component. In this case there is a strong artifact at the middle of the image in the reconstruction using the model of (3.2) (Figure 3.9a). In the reconstructions with the more accurate model of (3.49) (Figures 3.9b and 3.9c) there are still visible artifacts the the middle but more dispersed and the NRMS error is also improved.

Figure 3.10 shows the reconstructed images from the tight FOV experiment with a 2D parametric phase map with a small ϕ_y component. In this case there is a small visible artifact at the middle of the image in the reconstruction using the model of (3.2) (Figure 3.9a). In the reconstructions with the more accurate model of (3.49) (Figures 3.9b and 3.9c) there is still some small residual artifact in the middle, but it is subtle enough that it is barely visible.

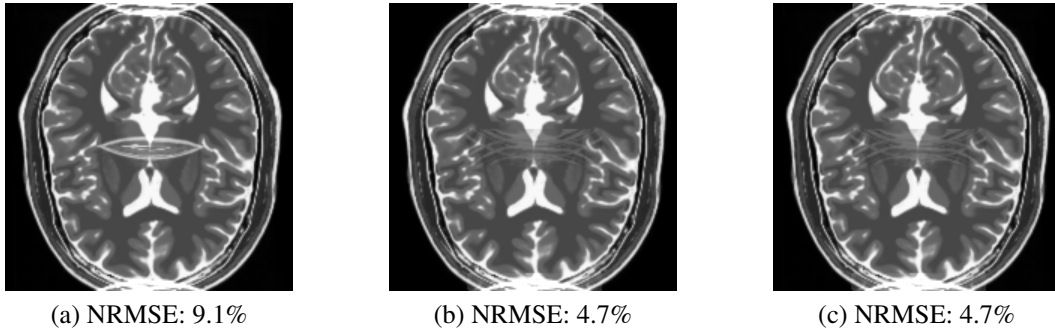


Figure 3.9: Image reconstructions for tight FOV experiment using 2D phase map with large slope in y . (a) Reconstruction with model mismatch from model of (3.2). (b) Reconstruction from accurate model (3.49) using support constraint (3.53). (c) Reconstruction from accurate model (3.49) using regularization (3.54).

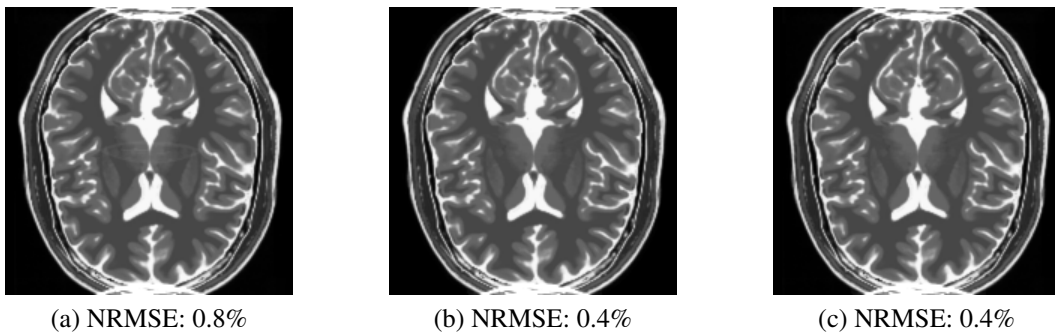


Figure 3.10: Image reconstructions for tight FOV experiment using 2D phase map with small slope in y . (a) Reconstruction with model mismatch from model of (3.2). (b) Reconstruction from accurate model (3.49) using support constraint (3.53). (c) Reconstruction from accurate model (3.49) using regularization (3.54).

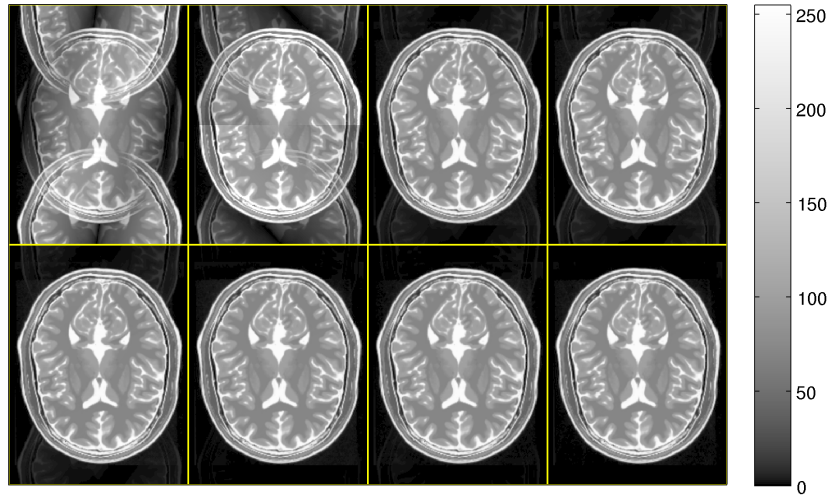
Table 3.1: Table of NRMS error (in %) of estimated phase map parameters and reconstructed images. The $N\times$ denotes the amount of oversampling of FFT and NC denotes the uncorrected for ghosting artifacts reconstruction. The results from the QS method are included as reference.

	Single-coil				Multi-coil			
	ϕ_c	ϕ_x	ϕ_y	\mathbf{x}	ϕ_c	ϕ_x	ϕ_y	\mathbf{x}
NC	100	100	100	67.3	100	100	100	48.5
$2\times$	22.6	17.8	130.1	26.3	33.4	17.8	130.1	6.2
$4\times$	1.5	2.7	15.1	2.4	2.7	2.7	15.1	1.0
$8\times$	1.5	2.7	15.1	2.4	2.7	2.7	15.1	1.0
$12\times$	1.5	2.7	15.1	2.4	2.7	2.7	15.1	1.0
$18\times$	0.5	0.4	2.3	0.3	0.9	0.4	2.3	0.2
$24\times$	0.0	0.7	4.1	0.6	0.1	0.7	4.1	0.3
QS	0.2	0.0	2.6	0.1	0.4	0.0	2.5	0.1

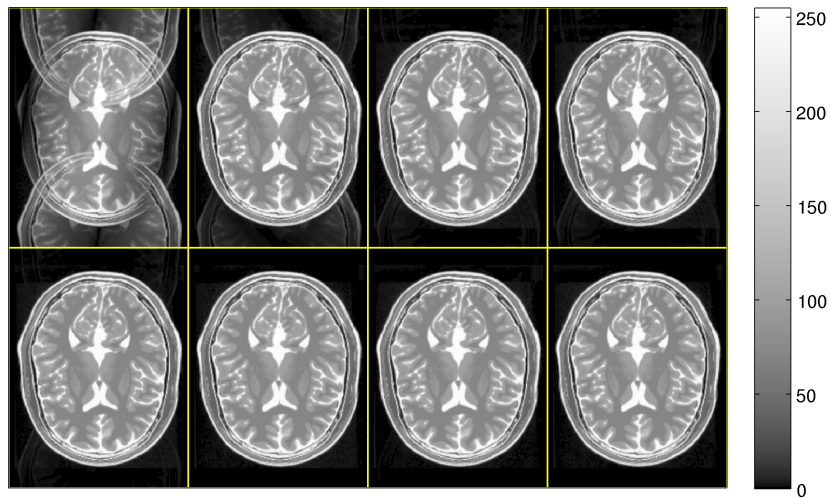
3.5.3 Approximate Parameter Estimation

Figure 3.11 shows the resulting image reconstructions that were corrected for ghosting artifacts using 2D parametric phase maps estimated with the approximate FFT-based method using (3.42) and (3.43). Figure 3.11a shows the results from the single-coil simulation and Figure 3.11b from the multi-coil simulation. The reconstructed images are displayed with gamma correction to help visualize the ghosting artifacts.

Table 3.1 shows the NRMS errors for the estimated phase map parameters and the reconstructed images. The results show that an oversampling of just four times the image size is sufficient for a decent reconstruction quality. The low NRMS error for the parameters with only modest oversampling makes this method a suitable initialization for our quadratic surrogate algorithm. On the other hand we see that the results do not really improve until we use oversampling of 18 or more times the image size. This amount of oversampling increases the computational cost significantly and performing a few iterations of our QS method is more computationally efficient compared to an 18 times oversampled FFT. Therefore, the FFT method, with a small amount of over-sampling, is probably the most useful as an approach to initializing the QS algorithm (3.35).



(a)



(b)

Figure 3.11: Reconstructed images from (a) single-coil, and (b) multi-coil acquisitions, corrected with phase maps estimated with the approximate FFT-based method. From top-left to bottom-right we have uncorrected reconstruction followed by reconstruction with parameter estimation using 2, 4, 8, 12, 18, and 24 times oversampling of FFT and the bottom-right using the QS approach (3.35) for comparison.

3.6 Discussion

Our proposed method for ghost correction does not rely on parallel imaging for the estimation of the correction parameters, but accurate sensitivity maps are important for the reconstruction of

good quality images in multi-coil acquisitions. In our work we assume that the sensitivity maps are estimated from data acquired during a calibration scan, similarly to [14, 19]. Other methods that use SENSE, like [15, 17], estimate the sensitivity maps by combining data from the current and previous temporal frames and a similar scheme is used by methods using GRAPPA [18] to update the parameters.

In some cases updating the sensitivity maps is desirable, *e.g.*, changes induced from subject motion. In our framework we can obtain these updates by using the ghost correction parameters from a previous temporal frame to reconstruct the coil images and then use them to update the sensitivity maps. Using the new sensitivity maps we estimate the ghost correction parameters for the current temporal frame and finally the ghost-corrected image. Even though the ghost correction parameters can drift during the course of a study, the changes between adjacent temporal frames are sufficiently small and should not introduce artifacts in the estimated sensitivity maps. As an alternative, since our method for estimating the ghost correction parameters does not rely on parallel imaging we could estimate the corrections from single coil data of the current temporal frame and then create ghost-corrected images for each coil. Using these images we can update the sensitivity maps and use them to reconstruct the final image using SENSE.

The proposed method improves ghost correction compared to standard correction methods for single-coil acquisitions and also for multi-shot EPI. The effectiveness of our method in multi-shot EPI, without the need for pre-scans or modifications of the acquisition pattern, is a significant advantage; most current methods rely on alternating direction schemes and data sharing across temporal frames that can reduce the temporal resolution and may not be readily applicable in a standard scanner or require computation of the correction parameters from a pre-scan with the disadvantage of being unable to adapt to dynamic changes of the misalignment of echoes due to scanner drifts [18]. Another benefit of our method that applies to multi-shot EPI is the ability to apply individual corrections for each shot and also account for misalignments between shots efficiently with no additional calibration or modification in the acquisition. As our results exhibit, these individual corrections can significantly reduce ghosting in the reconstructed images.

In addition, our model-based approach can be easily incorporated in any-model based reconstruction scheme with minimal computational overhead, instead of being an additional post processing step.

Our results show that our proposed QS method for single-shot acquisitions is computationally efficient with similar computational performance as non-iterative conventional methods. Thus, our method allows for efficient phase map estimation without increased computational overhead. However, for multi-shot acquisitions our alternating minimization method introduces significant

computations overhead since it requires solving and image estimation problem for each iteration. Our implementation of alternating minimization that uses CG to solve (3.9) is the computational bottleneck of our method and a more efficient implementation similar to SENSE “unfolding” that is used in [19] could improve the performance significantly. Despite the increased computational complexity our method could still be more efficient than phase cycling methods [19] with the additional benefit of using individual phase maps for each shot that improve the suppression of ghosting artifacts in the reconstructed images.

Throughout this work we focused on a parametric 2D phase map model that considers only translations (shifts) of k-space. If the eddy currents cause non-linear distortions of k-space one could use our method with a different parametric model or a method based on measuring the distorted k-space trajectory and use the non-uniform FFT (NUFFT) [41] for image reconstruction.

3.7 Appendix

3.7.1 Quadratic Surrogate Algorithm for 1D Correction of Multi-Shot EPI

For 1D parametric phase map estimation the Hessian of (3.8) always reduces to a diagonal form (regardless of the choice of mask), as illustrated in (3.20), and the formulation of a quadratic surrogate algorithm is similar to (3.35). The only case that is different and will be presented here is when multiple phase maps are used to account for misalignments between shots. In this case for N_s shots and using $q = 2N_s$ sets of phase map parameters, the system model is given by (3.37) with the inclusion of parallel imaging with L receiver coils, and the parameter vector is

$$\boldsymbol{\phi} \triangleq \begin{bmatrix} \phi_1 \\ \vdots \\ \phi_q \end{bmatrix}.$$

Similar to (3.20), the Hessian is a diagonal matrix containing the sum-of-squares sensitivity maps:

$$\mathbf{S} \triangleq \mathbf{F}'(\boldsymbol{\phi}) \mathbf{F}(\boldsymbol{\phi}) = \sum_{l=1}^L \mathbf{S}'_l \mathbf{S}_l.$$

By defining the coil combination images for each shot

$$\mathbf{v}_i \triangleq \sum_{l=1}^L \mathbf{S}'_l \mathbf{F}'_i \mathbf{y}_{l,i}, \text{ for } i = 1, \dots, q$$

the optimization problem of (3.10) becomes

$$\begin{aligned} \hat{\phi} &= \operatorname{argmax}_{\phi} \left(\sum_{i=1}^q \mathbf{P}'(\mathbf{T}\phi_i) \mathbf{v}_i \right)' \mathbf{S}^{-1} \left(\sum_{j=1}^q \mathbf{P}'(\mathbf{T}\phi_j) \mathbf{v}_j \right) \\ &= \operatorname{argmax}_{\phi} \sum_{i=1}^q \sum_{j=1}^q \mathbf{v}'_i \mathbf{P}(\mathbf{T}\phi_i) \mathbf{S}^{-1} \mathbf{P}'(\mathbf{T}\phi_j) \mathbf{v}_j \\ &= \operatorname{argmax}_{\phi} \sum_{i=1}^{q-1} \sum_{j=i+1}^q \Re \{ \mathbf{v}'_i \mathbf{P}(\mathbf{T}\phi_i) \mathbf{S}^{-1} \mathbf{P}'(\mathbf{T}\phi_j) \mathbf{v}_j \} \\ &= \operatorname{argmax}_{\phi} \sum_{i=1}^{q-1} \sum_{j=i+1}^q \sum_{k=1}^K u_{ij,k} \cos([\mathbf{T}_{ij}\phi]_k - \varepsilon_{ij,k}) \\ &= \operatorname{argmin}_{\phi} \sum_{i=1}^{q-1} \sum_{j=i+1}^q \sum_{k=1}^K u_{ij,k} [1 - \cos([\mathbf{T}_{ij}\phi]_k - \varepsilon_{ij,k})] \\ &= \operatorname{argmin}_{\phi} \sum_{k=1}^{Kq(q-1)/2} w_k [1 - \cos([\mathbf{T}_s\phi]_k - \eta_k)], \end{aligned}$$

where $\mathbf{u}_{ij} \triangleq (|\mathbf{v}_i| \odot |\mathbf{v}_j|) ./ \mathbf{s}$, $\varepsilon_{ij} \triangleq \angle \mathbf{v}_i - \angle \mathbf{v}_j$, $\mathbf{T}_{ij} \triangleq [0, \dots, 0, -\mathbf{T}, 0, \dots, 0, \mathbf{T}, 0, \dots, 0]$ (with non-zero blocks at locations i and j), $\mathbf{w} \triangleq [\dots, \mathbf{u}_{ij}^T, \dots]^T$ is the stack of all vectors \mathbf{u}_{ij} , $\boldsymbol{\eta} \triangleq [\dots, \varepsilon_{ij}^T, \dots]^T$ is the stack of all vectors ε_{ij} , and $\mathbf{T}_s \triangleq [\dots, \mathbf{T}_{ij}^T, \dots]^T$ is the stack of all matrices \mathbf{T}_{ij} . As a concrete example, for a 2-shot acquisition the matrix \mathbf{T}_s would be

$$\mathbf{T}_s = \begin{bmatrix} -\mathbf{T} & \mathbf{T} & 0 & 0 \\ -\mathbf{T} & 0 & \mathbf{T} & 0 \\ -\mathbf{T} & 0 & 0 & \mathbf{T} \\ 0 & -\mathbf{T} & \mathbf{T} & 0 \\ 0 & -\mathbf{T} & 0 & \mathbf{T} \\ 0 & 0 & -\mathbf{T} & \mathbf{T} \end{bmatrix}$$

By defining the cost function

$$\Psi(\boldsymbol{\phi}) \triangleq \sum_{k=1}^{Kq(q-1)/2} w_k [1 - \cos([\mathbf{T}_s \boldsymbol{\phi}]_k - \eta_k)], \quad (3.57)$$

the quadratic surrogate algorithm can be expressed as

$$\begin{aligned} \mathbf{t}^{(n)} &= \mathbf{T}_s \boldsymbol{\phi}^{(n)} - \boldsymbol{\eta} \\ \mathbf{c}^{(n)} &= \mathbf{w} \odot \text{sinc}(\mathbf{t}^{(n)}) \\ \nabla \Psi(\boldsymbol{\phi}^{(n)}) &= \mathbf{T}_s' [\mathbf{c}^{(n)} \odot \mathbf{t}^{(n)}] \\ \mathbf{H}^{(n)} &= \mathbf{T}_s' \text{diag}\{\mathbf{c}^{(n)}\} \mathbf{T}_s \\ \boldsymbol{\phi}^{(n+1)} &= \boldsymbol{\phi}^{(n)} - [\mathbf{H}^{(n)}]^{-1} \nabla \Psi(\boldsymbol{\phi}^{(n)}). \end{aligned} \quad (3.58)$$

The steps of the algorithm are computationally inexpensive since each iteration of the algorithm requires only inverting a matrix of size $2q \times 2q$, where q is twice the number of shots. Also, since the cost function is non-convex we need a good initialization $\boldsymbol{\phi}^{(0)}$ to converge to the “correct” local minimum.

CHAPTER IV

Joint Estimation of Dynamic Image and Fieldmap

We propose a method for joint reconstruction of dynamic images and fieldmaps in parallel MRI, using single-shot trajectories. We exploit the sensitivity encoding from parallel imaging to reduce the acquisition length and perform joint reconstruction using just one full k-space dataset. We also explore the use of modified trajectories (both EPI and spiral) that provide full coverage of k-space and also contain enough inherent time differences to permit accurate fieldmap estimation. Finally we improve the efficiency of the reconstruction algorithm by using a linearization technique for fieldmap estimation, which allows the use of the conjugate gradient algorithm.

4.1 Introduction

In functional MRI one reconstructs a series of dynamic images and since high temporal resolution is required it is common to use fast single-shot acquisitions such as echo-planar (EPI) or spirals. The disadvantage of these techniques is the long readout time that can cause significant artifacts in the reconstructed image due to field inhomogeneities if uncorrected. The standard approach to correct for field inhomogeneities is to acquire a static fieldmap before the dynamic series and use this to correct all the subsequent images. This method can be inaccurate, since motion and fieldmap drifts are not taken into account when reconstructing. As proposed in [3] one can reconstruct an undistorted image and undistorted dynamic fieldmap using spiral-in/spiral-out acquisition. However, acquiring two full datasets in a single acquisition can require very long readout times. In this work, motivated by [4, 42], we propose to use the sensitivity encoding [5] to

Part of the work in this chapter appears in [4].

The authors would like to acknowledge Douglas C. Noll and Jon-Fredrik Nielsen for helpful discussions and insights concerning the effects of R_2^* decay in the joint reconstruction method.

acquire just one full dataset from a single-shot acquisition (shorter readout time) and still be able to reconstruct both the image and dynamic fieldmap.

Another disadvantage of the method in [3] is that the method used for fieldmap estimation is nonlinear and computationally demanding. The linearization method described in [6] can significantly reduce the computation time of fieldmap estimation, by enabling efficient use of conjugate gradient (CG). CG converges much faster than the gradient descent (GD) method used in [3]. In this work we will use the linearization technique for fieldmap estimation [6] to improve the efficiency of the reconstruction algorithm.

Due to the long readout times of single-shot trajectories, the effects of R_2^* decay can also have a significant impact on the quality of the reconstructed images. Thus, in our method we account for the effects of R_2^* to avoid potential signal loss and other image artifacts. However, it is beyond the scope of this work to estimate accurate R_2^* maps and for our work we consider the R_2^* map as a known parameter that is estimated from reference pre-scans.

This work proposes a method for jointly estimating the image and dynamic fieldmap in parallel MRI, using a single-shot acquisition that uses just one full dataset. This method retains the advantage of high temporal resolution of single-shot trajectories along with the advantage of shorter readout time by exploiting the coil sensitivity encoding. The shorter readout time has the potential to improve the reconstruction quality since it leads to less distortion due to field inhomogeneity and through-plane gradient effects. We also propose the use of modified single-shot trajectories (both EPI and spiral) that provide full coverage of k-space and also allow for enough time differences between regions of k-space so that the fieldmap estimation is facilitated (see §4.3). Finally, we use the linearization technique for fieldmap estimation [6] to improve the efficiency of the reconstruction algorithm.

4.2 Theory

Parallel MRI uses multiple receiver coils and the coil sensitivity patterns provide extra information that can aid image reconstruction. Assuming that we have K coils, the sensitivity of each coil $c_k(\mathbf{p})$ is location dependent and the signal equation for the k th coil at time t , similarly to (2.9), is expressed as:

$$s_k(t) = \int_{\mathbf{p}} c_k(\mathbf{p}) f(\mathbf{p}) e^{-\tau(\mathbf{p})t} e^{-i\omega(\mathbf{p})t} e^{-i2\pi\mathbf{k}(t)\cdot\mathbf{p}} d\mathbf{p}, \text{ for } k = 1, \dots, K, \quad (4.1)$$

where $f(\mathbf{p})$ is the object's magnetization at location \mathbf{p} , $\omega(\mathbf{p})$ is the field inhomogeneity, $r(\mathbf{p})$ is the R_2^* decay, and $\mathbf{k}(t)$ is the k-space trajectory. By parametrizing the signal equation (4.1) using rectangular basis functions for the image, fieldmap and coil sensitivities [3], we have:

$$s_k(t) = \Phi(\mathbf{k}(t)) \sum_{n=0}^{N-1} c_{k,n} f_n e^{-r_n t} e^{-i\omega_n t} e^{-i2\pi\mathbf{k}(t)\cdot\mathbf{p}_n}, \quad (4.2)$$

where $\Phi(\mathbf{k}(t))$ is the Fourier transform of the basis function $\phi(\mathbf{p})$, and $f_n, r_n, \omega_n, c_{k,n}$ denote the pixel values of $f(\mathbf{p}), r(\mathbf{p}), \omega(\mathbf{p}),$ and $c_k(\mathbf{p})$ respectively.

The MRI measurements are noisy samples of this signal:

$$y_{k,m} = s_k(t_m) + \varepsilon_{k,m}, \text{ for } m = 1, \dots, M,$$

and we can express the noisy measurement vectors $\mathbf{y}_k \triangleq (y_{k,1}, \dots, y_{k,M})$ for each coil in matrix-vector form as follows:

$$\mathbf{y}_k = \mathbf{A}(\boldsymbol{\omega}) \text{diag}\{\mathbf{c}_k\} \mathbf{f} + \boldsymbol{\varepsilon}_k, \text{ for } k = 1, \dots, K, \quad (4.3)$$

where $\mathbf{f} \triangleq (f_1, \dots, f_N)$, $\boldsymbol{\omega} \triangleq (\omega_1, \dots, \omega_N)$ and $\mathbf{c}_k \triangleq (c_{k,1}, \dots, c_{k,N})$ are the discretized object, fieldmap and sensitivity map respectively, and the elements of the matrix $\mathbf{A}(\boldsymbol{\omega})$ are

$$a(\boldsymbol{\omega})_{m,n} = \Phi(\mathbf{k}(t_m)) e^{-r_n t_m} e^{-i\omega_n t_m} e^{-i2\pi\mathbf{k}(t_m)\cdot\mathbf{p}_n}.$$

The total measurement vector \mathbf{y} is given by stacking the measurement vectors \mathbf{y}_k for each coil: $\mathbf{y} \triangleq [\mathbf{y}_1, \dots, \mathbf{y}_K]^T$. Hence the overall $KM \times N$ system matrix $\tilde{\mathbf{A}}(\boldsymbol{\omega})$ is given by stacking the system matrices for each coil:

$$\tilde{\mathbf{A}}(\boldsymbol{\omega}) \triangleq \begin{bmatrix} \mathbf{A}(\boldsymbol{\omega}) \text{diag}\{\mathbf{c}_1\} \\ \vdots \\ \mathbf{A}(\boldsymbol{\omega}) \text{diag}\{\mathbf{c}_K\} \end{bmatrix}. \quad (4.4)$$

Using the above, the overall measurement model in matrix-vector form can be written as:

$$\mathbf{y} = \tilde{\mathbf{A}}(\boldsymbol{\omega}) \mathbf{f} + \boldsymbol{\varepsilon}. \quad (4.5)$$

The image reconstruction problem is to find the image \mathbf{f} and the fieldmap $\boldsymbol{\omega}$ given the data \mathbf{y} ,

the coil sensitivity maps \mathbf{c}_k , a baseline R_2^* map \mathbf{r} , and the k-space trajectory. To estimate \mathbf{f} and $\boldsymbol{\omega}$ we minimize a cost function similar to the one derived in [3], with the only difference that we use $\tilde{\mathbf{A}}(\boldsymbol{\omega})$ as the system matrix:

$$\Psi(\mathbf{f}, \boldsymbol{\omega}) \triangleq \frac{1}{2} \left\| \mathbf{y} - \tilde{\mathbf{A}}(\boldsymbol{\omega}) \mathbf{f} \right\|_2^2 + \beta_1 \Phi_1(\mathbf{C}_1 \mathbf{f}) + \beta_2 \Phi_2(\mathbf{C}_2 \boldsymbol{\omega}),$$

where $\Phi_1(\cdot)$ and $\Phi_2(\cdot)$ are regularization terms and \mathbf{C}_1 and \mathbf{C}_2 are sparsifying transforms. The fieldmap $\boldsymbol{\omega}$ is smooth, so we use a quadratic regularizer $\Phi_1(\cdot) \triangleq \frac{1}{2} \|\cdot\|_2^2$ and $\mathbf{C}_1 \triangleq \mathbf{\Delta}$, where $\mathbf{\Delta}$ is a matrix of second-order differences. For the image \mathbf{f} , we could use an edge-preserving regularizer, but since fMRI images are often smoothed for data analysis, we also used a quadratic regularizer $\Phi_1(\cdot) \triangleq \frac{1}{2} \|\cdot\|_2^2$ with $\mathbf{C}_2 \triangleq \mathbf{\Delta}$ here.

We want to jointly estimate \mathbf{f} and $\boldsymbol{\omega}$ by minimizing $\Psi(\cdot)$:

$$\hat{\mathbf{f}}, \hat{\boldsymbol{\omega}} = \underset{\mathbf{f}, \boldsymbol{\omega}}{\operatorname{argmin}} \Psi(\mathbf{f}, \boldsymbol{\omega}). \quad (4.6)$$

We minimize the cost function (4.6) by alternating between minimizing with respect to the image and then the fieldmap. In each step of the minimization process we find a new update for the image and then for the fieldmap and the process is repeated until convergence. For the k th step in the alternating minimization scheme, the image update is:

$$\hat{\mathbf{f}}^{(k)} = \underset{\mathbf{f}}{\operatorname{argmin}} \frac{1}{2} \left\| \mathbf{y} - \tilde{\mathbf{A}}(\hat{\boldsymbol{\omega}}^{(k-1)}) \mathbf{f} \right\|_2^2 + \beta_1 \Phi_1(\mathbf{C}_1 \mathbf{f}), \quad (4.7)$$

and the fieldmap update uses the most recent image and is given by:

$$\hat{\boldsymbol{\omega}}^{(k)} = \underset{\boldsymbol{\omega}}{\operatorname{argmin}} \frac{1}{2} \left\| \mathbf{y} - \tilde{\mathbf{A}}(\boldsymbol{\omega}) \hat{\mathbf{f}}^{(k)} \right\|_2^2 + \beta_2 \Phi_2(\mathbf{C}_2 \boldsymbol{\omega}). \quad (4.8)$$

The minimizer of (4.7) is found using the CG-NUFFT method [3], since the problem is quadratic in \mathbf{f} , which is reasonably computationally efficient. For EPI trajectories standard FFTs can be used instead of the NUFFT. However, since the problem (4.8) is non-quadratic in $\boldsymbol{\omega}$ the minimizer is found using a gradient descent (GD) method that is not as efficient as CG. To improve the computational efficiency of joint estimation we used a linearization technique that allows the use of CG for solving (4.8).

Following [6] we can solve (4.8) for $\boldsymbol{\omega}$ using a linear approximation to the dynamic changes between $\boldsymbol{\omega}$ and a carefully chosen reference $\tilde{\boldsymbol{\omega}}$. By doing that we can avoid using the computationally demanding GD method and use the CG method instead to solve for $\boldsymbol{\omega}$. The suitability of

the linearization depends on having a reasonable initial fieldmap estimate $\tilde{\omega}$; typically we obtain $\tilde{\omega}$ from a pre-scan or from the previous dynamic frame.

Given an initial fieldmap estimate $\tilde{\omega}$ we can write the signal equation for each coil (4.2) as:

$$s_k(t) = \Phi(\mathbf{k}(t)) \sum_{n=0}^{N-1} c_{k,n} f_n e^{-r_n t} e^{-i\tilde{\omega}_n t} e^{-i(\omega_n - \tilde{\omega}_n)t} e^{-i2\pi\mathbf{k}(t) \cdot \mathbf{p}_n}. \quad (4.9)$$

Now, assuming the difference of ω and $\tilde{\omega}$ is small we can use the following first-order Taylor series approximation:

$$e^{-i(\omega_n - \tilde{\omega}_n)t} \approx 1 - it(\omega_n - \tilde{\omega}_n), \quad (4.10)$$

and then by substituting (4.10) in (4.9) and rearranging the terms, the signal equation becomes:

$$\begin{aligned} s_k(t) \approx & \Phi(\mathbf{k}(t)) \sum_{n=0}^{N-1} c_{k,n} f_n e^{-r_n t} e^{-i\tilde{\omega}_n t} e^{-i2\pi\mathbf{k}(t) \cdot \mathbf{p}_n} - i(-t)\Phi(\mathbf{k}(t)) \sum_{n=0}^{N-1} c_{k,n} f_n e^{-r_n t} e^{-i\tilde{\omega}_n t} e^{-i2\pi\mathbf{k}(t) \cdot \mathbf{p}_n} \tilde{\omega}_n \\ & + i(-t)\Phi(\mathbf{k}(t)) \sum_{n=0}^{N-1} c_{k,n} f_n e^{-r_n t} e^{-i\tilde{\omega}_n t} e^{-i2\pi\mathbf{k}(t) \cdot \mathbf{p}_n} \omega_n, \text{ for } k = 1, \dots, K. \end{aligned} \quad (4.11)$$

Using the signal equation (4.11) we can rewrite the measurement model for each coil (4.3) in matrix-vector form as:

$$\mathbf{y}_k = \mathbf{A}(\tilde{\omega}) \text{diag}\{\mathbf{c}_k\} \mathbf{f} - \mathbf{B}(\tilde{\omega}, \mathbf{f}, \mathbf{c}_k) \tilde{\omega} + \mathbf{B}(\tilde{\omega}, \mathbf{f}, \mathbf{c}_k) \omega + \varepsilon_k,$$

where $\mathbf{B}(\tilde{\omega}, \mathbf{f}, \mathbf{c}_k) \triangleq -\text{diag}\{\mathbf{t}\} \mathbf{A}(\tilde{\omega}) \text{diag}\{\mathbf{c}_k\} \text{diag}\{\mathbf{f}\}$, $\mathbf{t} \triangleq (t_1, \dots, t_M)$ is a vector of discrete sampling times, and the elements of the $M \times N$ matrix $\mathbf{A}(\tilde{\omega})$ are:

$$a(\tilde{\omega})_{m,n} = \Phi(\mathbf{k}(t_m)) e^{-r_n t_m} e^{-i\tilde{\omega}_n t_m} e^{-i2\pi\mathbf{k}(t_m) \cdot \mathbf{p}_n}.$$

The overall measurement vector \mathbf{y} is given by stacking the measurement vectors \mathbf{y}_k , the matrix $\tilde{\mathbf{A}}(\tilde{\omega})$ is given by (4.4) and $\tilde{\mathbf{B}}(\tilde{\omega}, \mathbf{f})$ is given by

$$\tilde{\mathbf{B}}(\tilde{\omega}, \mathbf{f}) \triangleq \begin{bmatrix} \mathbf{B}(\tilde{\omega}, \mathbf{f}, \mathbf{c}_1) \\ \vdots \\ \mathbf{B}(\tilde{\omega}, \mathbf{f}, \mathbf{c}_K) \end{bmatrix}. \quad (4.12)$$

Hence the overall linearized measurement model is:

$$\mathbf{y} = \tilde{\mathbf{A}}(\tilde{\omega}) \mathbf{f} - \tilde{\mathbf{B}}(\tilde{\omega}, \mathbf{f}) \tilde{\omega} + \tilde{\mathbf{B}}(\tilde{\omega}, \mathbf{f}) \omega + \varepsilon.$$

Similarly to (4.6), to estimate the image \mathbf{f} and fieldmap ω we minimize the following cost function:

$$\Psi(\mathbf{f}, \omega) \triangleq \frac{1}{2} \left\| \mathbf{y} - \tilde{\mathbf{A}}(\tilde{\omega}) \mathbf{f} + \tilde{\mathbf{B}}(\tilde{\omega}, \check{\mathbf{f}}) \tilde{\omega} - \tilde{\mathbf{B}}(\tilde{\omega}, \check{\mathbf{f}}) \omega \right\|_2^2 + \beta_1 \Phi_1(\mathbf{C}_1 \mathbf{f}) + \beta_2 \Phi_2(\mathbf{C}_2 \omega). \quad (4.13)$$

Similarly to (4.6), we minimize (4.13) by employing an alternating minimization scheme. For the k th step the image update is:

$$\hat{\mathbf{f}}^{(k)} = \underset{\mathbf{f}}{\operatorname{argmin}} \frac{1}{2} \left\| \mathbf{y} - \tilde{\mathbf{A}}(\hat{\omega}^{(k-1)}) \mathbf{f} \right\|_2^2 + \beta_1 \Phi_1(\mathbf{C}_1 \mathbf{f}) \quad (4.14)$$

and the fieldmap update uses the most recent image and is given by:

$$\hat{\omega}^{(k)} = \underset{\omega}{\operatorname{argmin}} \frac{1}{2} \left\| \tilde{\mathbf{y}}^{(k)} - \tilde{\mathbf{B}}(\hat{\omega}^{(k-1)}, \hat{\mathbf{f}}^{(k)}) \omega \right\|_2^2 + \beta_2 \Phi_2(\mathbf{C}_2 \omega), \quad (4.15)$$

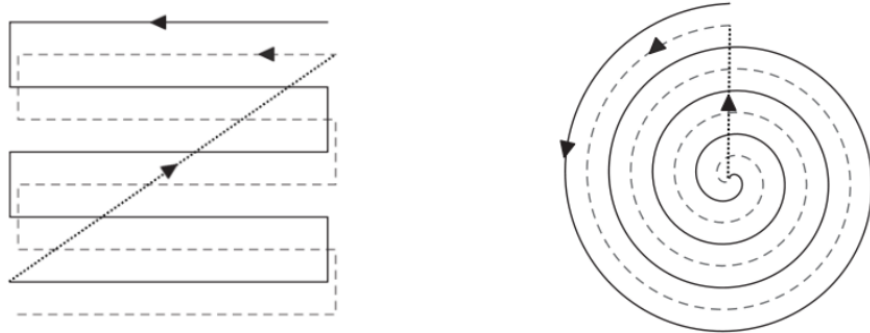
where,

$$\tilde{\mathbf{y}}^{(k)} \triangleq \mathbf{y} - \tilde{\mathbf{A}}(\hat{\omega}^{(k-1)}) \hat{\mathbf{f}}^{(k)} + \tilde{\mathbf{B}}(\hat{\omega}^{(k-1)}, \hat{\mathbf{f}}^{(k)}) \hat{\omega}^{(k-1)}.$$

Now, in both (4.14) and (4.15) the minimizers are found using the CG-NUFFT method [3] and for EPI trajectories standard FFTs can be used instead of the NUFFT.

4.3 Materials and Methods

The joint estimation method described in §4.2 can be applied with any trajectory, but the results will depend on the chosen trajectory. For parallel imaging (multiple coils) we show that we can exploit the coil sensitivities so that we can achieve joint reconstruction using only one full dataset acquired with a single-shot trajectory [4, 42]. The trajectories we investigated are a single-shot “interleaved” EPI (Figure 4.1a) and a single-shot “interleaved” spiral-in (Figure 4.1b). These trajectories provide full coverage of the k-space and also they have some time differences between neighboring parts of k-space, which intuitively should facilitate fieldmap estimation. We also investigated the performance of the joint reconstruction method using standard fully sampled EPI



(a) Interleaved EPI trajectory

(b) Interleaved spiral-in trajectory

Figure 4.1: “Interleaved” single-shot trajectories used in simulations and phantom studies.

and spiral trajectories. The parameters used for all trajectories are FOV = 24 cm, matrix size = 64×64 . For the interleaved EPI we have readout time = 46 ms and two echo times at $T_{E1} = 18$ ms and $T_{E2} = 42$ ms. In this trajectory, since we do not exactly traverse the center of k-space on the second half, we define as echo time (T_E) the time when we are closest to the center of k-space.¹ For the standard EPI we have readout time = 46 ms and one echo time at $T_E = 30$ ms. For interleaved spiral we have readout time = 20 ms and two echo times at $T_{E1} = 25$ ms and $T_{E2} = 35$ ms, and for the standard spiral we have readout time = 20 ms and one echo time at $T_E = 35$ ms.

The matrix-vector multiplications used for computing the gradients in CG are performed with time segmentation and the use of FFT for EPI trajectories (data are on a Cartesian grid) and the use of NUFFT for the spiral trajectories [9, 41]. Time segmentation was performed with $L = 9$ time segments and the NUFFT used a 6×6 interpolation neighborhood with minmax interpolation and two times oversampling for the FFT.

The regularization parameters β_1 and β_2 in (4.14) and (4.15) were chosen to achieve a specific spatial resolution [43]. The regularization parameters were chosen such that the spatial resolution, for both the image and the fieldmap, is the same for all trajectories at a specific level of data SNR. For the image reconstruction we chose the parameter β_1 so that the FWHM of the PSF was 1.2 pixels at 55dB SNR and 1.4 pixels at 30dB SNR. For the fieldmap reconstruction we chose the parameter β_2 so that the FWHM of the PSF was 1.5 pixels for both SNRs. Choosing a fixed target spatial resolution for both trajectories helps ensure a “fair” comparison between the resulting reconstructions, but these choices may not be “optimal” in terms of minimum normalized RMS

¹This echo time is reported just for intuition; it is never used explicitly by the algorithm. The method considers the time evolution during the entire readout, not just at the echo times, because of the “ t ” term in (4.2).

error. Since the noise properties of EPI and spiral trajectories are very different we could achieve lower NRMSE by using a smaller regularization parameter for the EPI and a larger for the spiral. However, then their spatial resolutions would not match. This will be evident in the Results section, where the reconstructions from the spiral trajectories are more noisy than the ones from the EPI, whereas the reconstructions from the EPI may seem a little over-smoothed.

To jointly estimate the image and fieldmap we alternated 40 times between updating the image and then updating the fieldmap. In each update we used 15 iterations of the CG method. For parallel imaging, in our simulations, we investigated the use of four coils with smooth B1 maps. We also performed simulations for single coil imaging, where we assumed a coil with uniform sensitivity.

4.3.1 Reconstruction Quality Simulation Study

For the simulations we created an elliptical digital phantom as the true image (Figure 4.2a) and a smoothed, rapid-changing susceptibility induced, fieldmap acquired from human brain data as the true fieldmap (Figure 4.2b). The range of the fieldmap is from -36 to 116 Hz. For the simulation experiments we chose to ignore R_2^* decay, for simplicity. We simulated the k-space data using the exact system model (4.5), to which we added noise to achieve a 30dB and 55dB data SNR. For image reconstruction we used an iteratively reconstructed image, uncorrected for field inhomogeneities, as an initial estimate (top-left subfigure of Figures 4.6–4.11). For the fieldmap reconstruction the initial estimate was created with the standard phase difference method from two images, acquired with 4-shot EPI trajectories, at 40dB data SNR (bottom-left subfigure of Figures 4.6–4.11). Each shot of the EPI had a 11 ms readout time and the echo-times were $T_{E1} = 6.5$ ms for the first acquisition and $T_{E2} = 8.5$ ms for the second, resulting in a $\Delta T_E = 2$ ms echo-time difference. The images used to initialize fieldmap estimation were created using iterative CG reconstruction uncorrected for field inhomogeneities and the resulting distorted fieldmaps were smoothed with a 5×5 Gaussian filter ($\sigma = 1$) to suppress noise.

To simulate the fieldmap drift during the acquisition of a dynamic series in an fMRI study, we added a constant 5 Hz drift to the true fieldmap to generate the data used for “dynamic” image reconstruction.

To further evaluate the quality of the joint reconstruction we also created “oracle” image estimates that were reconstructed with our method using the true fieldmap (subfigure (d) of Figures 4.6–4.11) and we also created “oracle” fieldmap estimates that were reconstructed with our method using the true image (subfigure (e) of Figures 4.6–4.11). These oracle estimates provide an upper bound on the accuracy of the proposed joint reconstruction method.

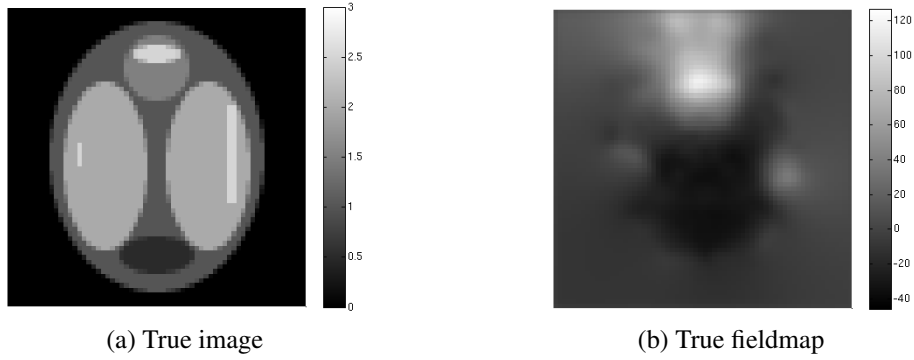


Figure 4.2: True image and fieldmap used in simulations.

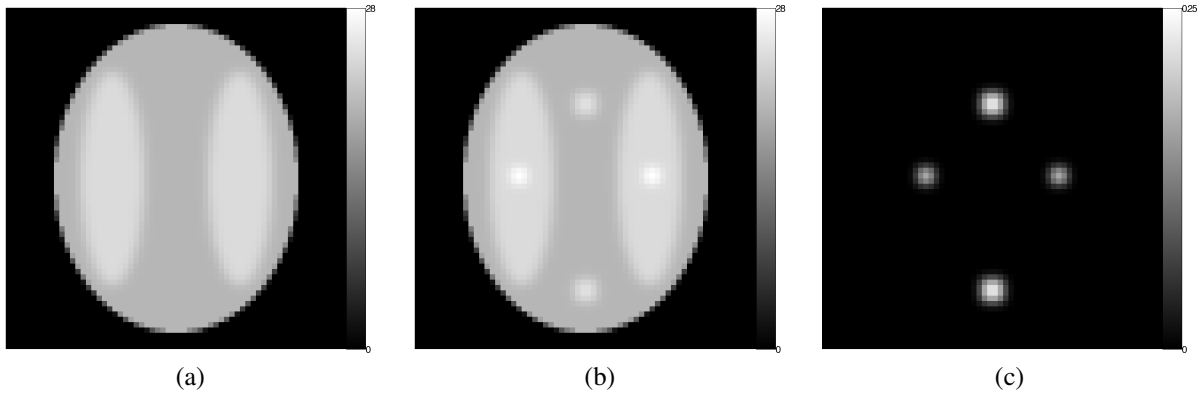


Figure 4.3: (a) Initial R_2^* map without activation regions. (b) R_2^* map during simulated fMRI study with four activation regions. (c) Normalized difference of R_2^* maps of (a) and (b) to illustrate activation.

4.3.2 Functional MRI Simulation Study

The purpose of this simulation study is to assess the ability of our proposed method to identify activation regions during an fMRI study. We used the same image and fieldmap as in §4.3.1 and a simulated R_2^* map, with a range of values between 20 and $24s^{-1}$, shown in Figure 4.3a as the initial R_2^* map without activation regions (denoted as \mathbf{r}_1). To simulate activation during an fMRI study we added four activation regions as rectangular blocks smoothed with a Gaussian blur at a maximum of 20% of the initial R_2^* map amplitude. Figure 4.3b shows the R_2^* map with activation regions (denoted as \mathbf{r}_2) and Figure 4.3c shows the normalized difference of the R_2^* maps (defined as $(\mathbf{r}_2 - \mathbf{r}_1)/\mathbf{r}_1$) that highlights the activation regions.

For this experiment we created noiseless data using both R_2^* maps to simulate the two phases

of the fMRI experiment. The initial image and fieldmap estimates were obtained with the same method as in §4.3.1. Since the “interleaved” EPI used for joint estimation exhibits large effective echo time difference, the reconstruction quality can be severely degraded if the effects of R_2^* decay are uncorrected for using a known R_2^* map. To illustrate this we perform joint estimation once ignoring R_2^* decay and then using the R_2^* map of Figure 4.3a as a known parameter. For both sets of reconstructions we identify the activation regions by taking the normalized difference of the images corresponding to the beginning (no activation as in Figure 4.3a) and during (activation regions as in Figure 4.3b) the simulated fMRI study.

4.3.3 Phantom Study

The data for the phantom study were collected on a GE 3T Signa Scanner. We used a spherical homogeneous phantom with a staple attached to induce magnetic field non-uniformity and the selected slice was 5 cm below the staple to avoid severe signal loss, but still contain significant field inhomogeneity effects. A standard SPGR sequence was used with an echo-time of $T_E = 30$ ms to acquire a reference image (Figure 4.4a). A reference fieldmap was created using data from SPGR sequences with echo-times $T_{E1} = 5$ ms and $T_{E2} = 7$ ms (Figure 4.4c). For the reference R_2^* map we used a monoexponential fitting method [44] and 2 images from standard SPGR sequences at $T_{E1} = 5$ ms and $T_{E2} = 7$ ms echo-times (Figure 4.4c). Due to the uniform nature of the phantom and the noise in the R_2^* estimates the R_2^* map was smoothed with a Gaussian filter to suppress noise. The sensitivity maps were estimated [21] using data from the 8 head coils and the body coil, acquired with a SPGR sequence with an echo-time of $T_E = 5$ ms (Figure 4.5).

For the joint estimation we acquired data using the “interleaved” and standard EPI trajectories described in §4.3. The initial fieldmap estimate was created with the same method that was used in simulations, *i.e.*, using the phase difference method on two images acquired with 4-shot EPI trajectories with $\Delta T_E = 2$ ms (Figures 4.4d). The initial image estimate was an iteratively reconstructed image, uncorrected for field inhomogeneities (subfigure (a) of Figures 4.13 and 4.14).

To further evaluate the quality of the joint reconstruction we also created “oracle” image estimates that were reconstructed with our method using the reference fieldmap (subfigure (c) of Figures 4.13 and 4.14). Unlike the simulations, creating an “oracle” fieldmap was not possible since the reference image was acquired with a standard SPGR sequence and the mismatch of trajectories did not allow for accurate fieldmap estimation. The oracle image estimates provide a standard of comparison for the qualitative assessment of the joint reconstruction method.

To reduce the N/2 ghosting artifacts in the EPI reconstructions, a simple 1D linear phase correction was applied to the data prior to the reconstruction process. To estimate the linear phase we

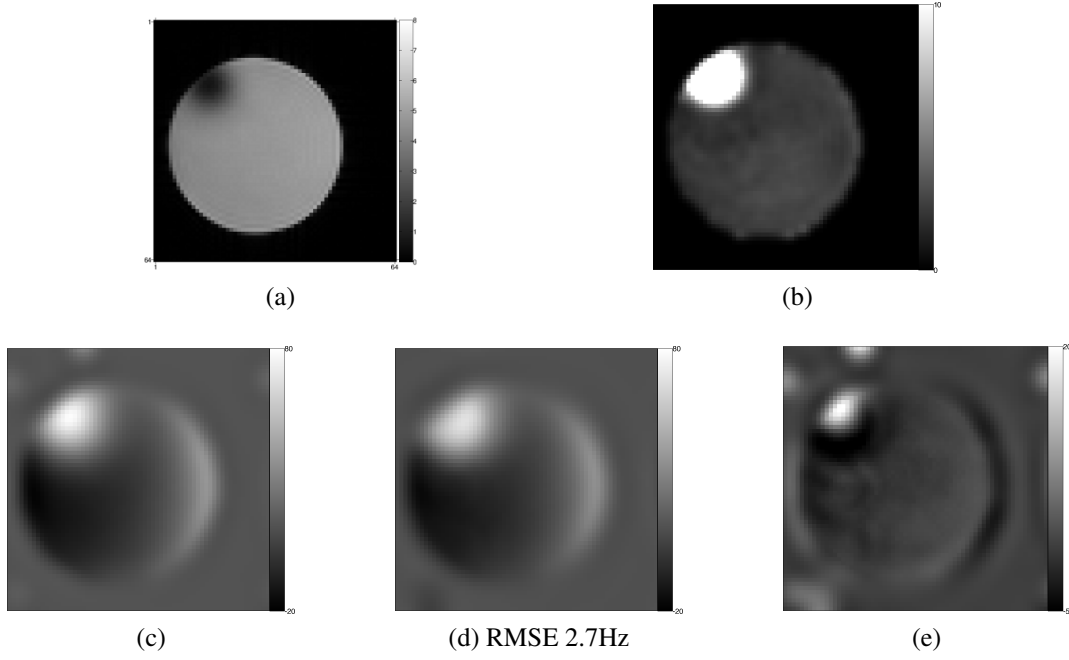


Figure 4.4: Reference (a) image, (b) R_2^* map, and (c) fieldmap along with (d) initial fieldmap estimate and (e) difference of reference and initial fieldmap, for phantom Study.

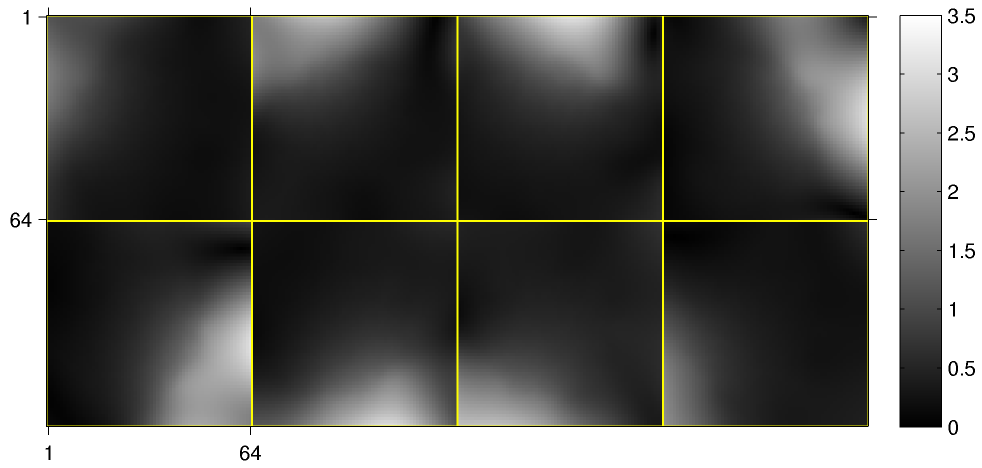


Figure 4.5: Sensitivity maps for phantom study.

used the data from a single shot standard EPI as described in §4.3. We reconstructed two images from undersampled datasets, one using only the positive direction and the other using only the negative direction, and a central line from each image was used to calculate the phase difference. Then, we estimated the linear phase with least squares fitting on the calculated phase difference. Using the values from the linear fit, we applied the phase correction to the data in the image domain (via FFT) and then created the phase corrected data via inverse FFT. Alternatively, the correction could be applied in the k-space trajectory, since the linear phase in the image domain is a shift in k-space. However, applying the correction in k-space would lead to an irregular sampling grid and require reconstruction using the slower non-uniform FFT. The calculated linear phase coefficient for both the phantom and human study was found to be 0.373 rad/sample which corresponds to a 3.8 samples shift in the readout direction of k-space. The ghost correction method presented in chapter III can be easily integrated into the joint estimation process and it could potentially improve the reconstruction results, but it was not used for now.

4.4 Results

4.4.1 Reconstruction Quality Simulation Study

Figures 4.6 and 4.7 show the resulting reconstructions from the “interleaved” EPI and “interleaved” spiral with four coils for the 55dB SNR simulations. In both figures the resulting joint reconstructions closely match the oracle reconstructions for both the image and the fieldmap. This can also be verified in terms of NRMS error as seen in Table 4.1. For the “interleaved” spiral, the reconstructed images appear to be somewhat more noisy and result in higher NRMS errors compared to the EPI reconstructions. This happens because the regularization parameter was chosen to achieve a target spatial resolution rather than minimizing the NRMS error. In all these figures the uncorrected reconstruction exhibits severe inhomogeneity artifacts. The reconstructed images using the initial distorted fieldmap exhibit obvious inhomogeneity artifacts because of the inaccuracy of the initial fieldmap estimate and the simulated fieldmap drift.

Figures 4.8 and 4.9 show the reconstructions from the *standard* EPI and spiral trajectories for four coils, at 55dB SNR. The jointly reconstructed fieldmaps do not match the oracle reconstructions and this leads to inhomogeneity artifacts in the image reconstructions. This is also verified from the NRMS errors seen in Table 4.1.

The reason why the joint fieldmap reconstruction fails to produce accurate results for standard trajectories is possibly the very small effective echo-time difference in the sampling of similar parts of k-space. For example, in the “interleaved” EPI we can think of the acquisition as two

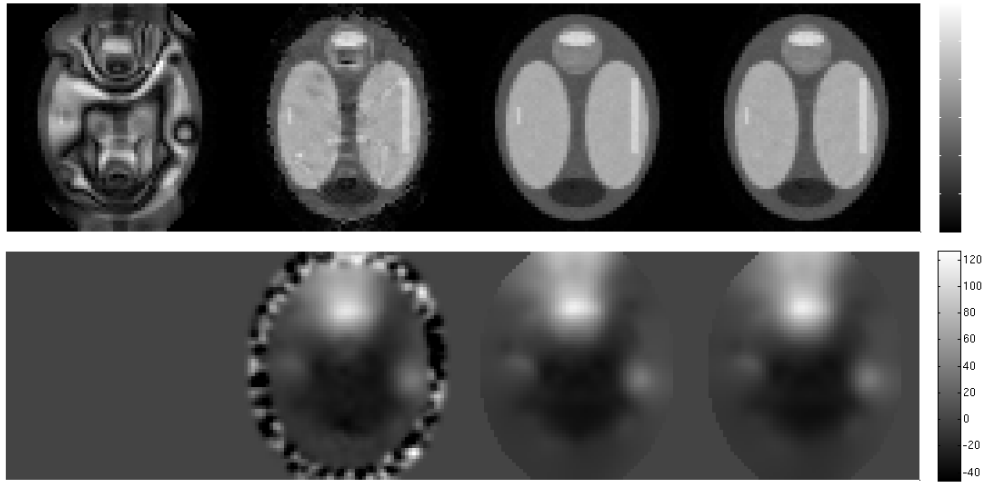


Figure 4.6: Reconstructed images and fieldmaps from “interleaved” EPI trajectory, with four coils at 55dB SNR. Top row shows the reconstructed images. From left to right: Uncorrected image; reconstructed image using standard, distorted, initial fieldmap; oracle image reconstructed using true fieldmap; jointly reconstructed image. Bottom row shows the reconstructed fieldmaps. From left to right: Standard, distorted initial fieldmap; oracle fieldmap reconstructed using true image; jointly reconstructed fieldmap.

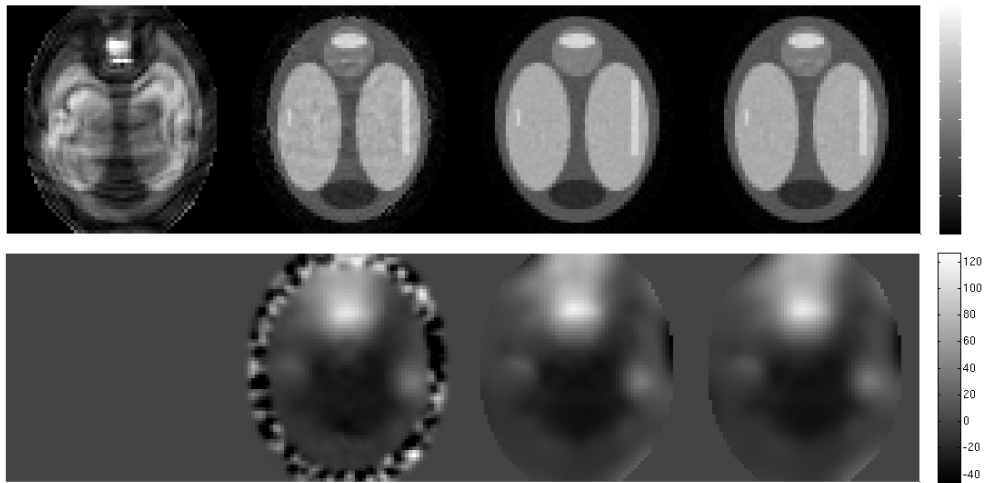


Figure 4.7: Reconstructed images and fieldmaps from “interleaved” spiral trajectory, with four coils at 55dB SNR. Subfigures same as in Figure 4.6.

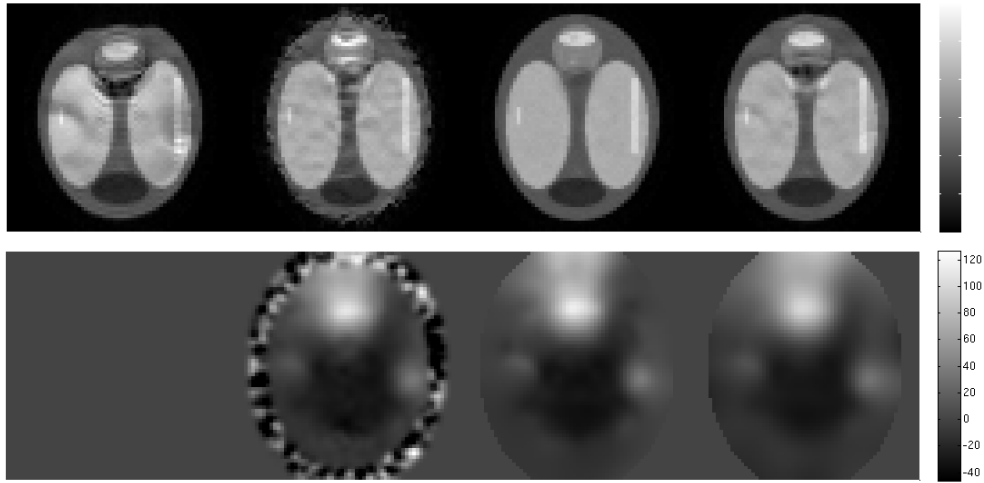


Figure 4.8: Reconstructed images and fieldmaps from standard EPI trajectory, with four coils at 55dB SNR. Subfigures same as in Figure 4.6.

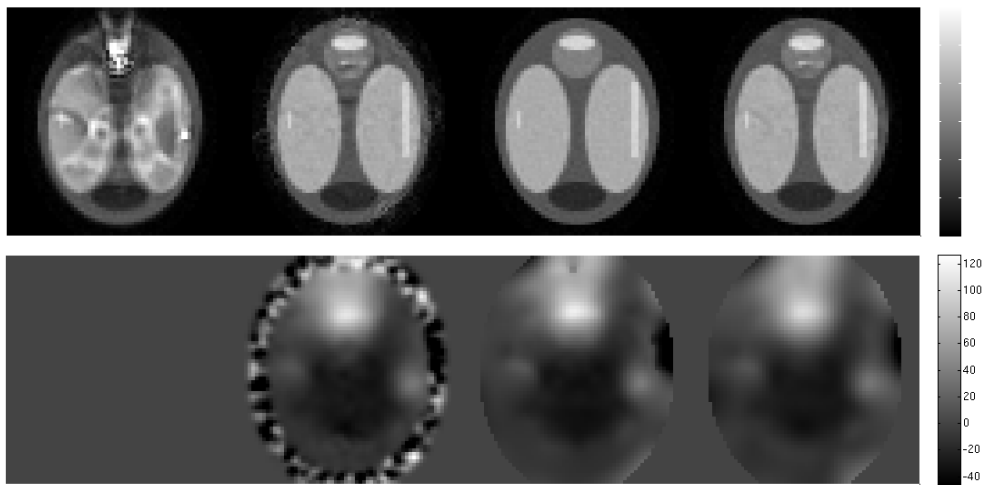


Figure 4.9: Reconstructed images and fieldmaps from standard spiral trajectory, with four coils at 55dB SNR. Subfigures same as in Figure 4.6.

undersampled acquisitions with an echo-time difference $\Delta T_E = 10.25$ ms. This ΔT_E is more than enough to allow for sufficient phase accrual due to inhomogeneity and facilitate the fieldmap estimation. On the other hand, the standard EPI can be thought of as two undersampled acquisitions with a very small echo-time difference, which is approximately $\Delta T_E = 0.32$ ms. This ΔT_E is really small and the phase accrual due to inhomogeneity is negligible, thus leading to inaccurate fieldmap estimates. One could argue that the echo-time difference of the “interleaved” EPI is too large and can lead to phase wrapping. However, this does not seem to be the case, since we start from a fairly accurate initial fieldmap estimate and the joint reconstruction method essentially estimates the difference between the true fieldmap and the initial estimate, which typically is in the order of 0–15Hz, thus avoiding the phase wrapping effects.

The reconstruction NRMS error for the spirals at 30dB SNR can be misleading, since the results are noisy especially when a single coil is used. In this case even the oracle reconstructions are of poor quality and any inhomogeneity artifacts in the joint reconstructions are buried under the high noise levels. Thus, we see NRMS errors in the joint reconstructions that are comparable to the NRMS errors in the oracle reconstructions, because the error introduced by the high noise levels overpowers the error introduced from the inhomogeneity artifacts.

Figures 4.10 and 4.11 show the reconstructions from the “interleaved” EPI and “interleaved” spiral trajectories, using just a single coil, at 55dB SNR. Here we see that the joint reconstruction for both trajectories fails to produce image and fieldmap estimates of quality comparable to the oracle reconstructions. As it is seen, the jointly reconstructed fieldmap is inaccurate and this leads to inhomogeneity artifacts in the jointly reconstructed image. This is also evident from the NRMS errors in Table 4.1.

Table 4.1 shows quantitative results, in terms of NRMS error, for all coil settings using both the “interleaved” and standard EPI and spiral trajectories. As it is evident from the NRMS errors, the problematic part of the joint estimation for standard trajectories and the single coil setting is the failure to produce accurate fieldmap estimates. This in turn impacts the image reconstruction where we have high NRMS errors because of inhomogeneity artifacts. By using multiple coils with the proposed “interleaved” trajectories, very accurate fieldmaps and images are reconstructed.

4.4.2 Functional MRI Simulation Study

Figures 4.12a and 4.12b show the reconstructed images with and without activation when the R_2^* decay is ignored during reconstruction. These reconstructions are severely distorted, possibly due to the large difference between the two effective echo times of the “interleaved” EPI trajectory that causes inconsistencies in the image contrast when R_2^* effects are ignored. However, as we

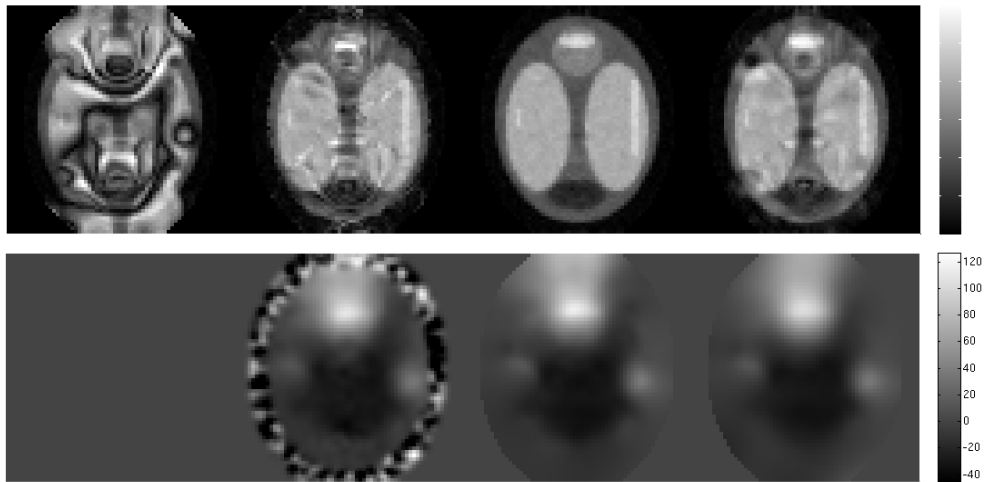


Figure 4.10: Reconstructed images and fieldmaps from “interleaved” EPI trajectory, with single coil at 55dB SNR. Subfigures same as in Figure 4.6.

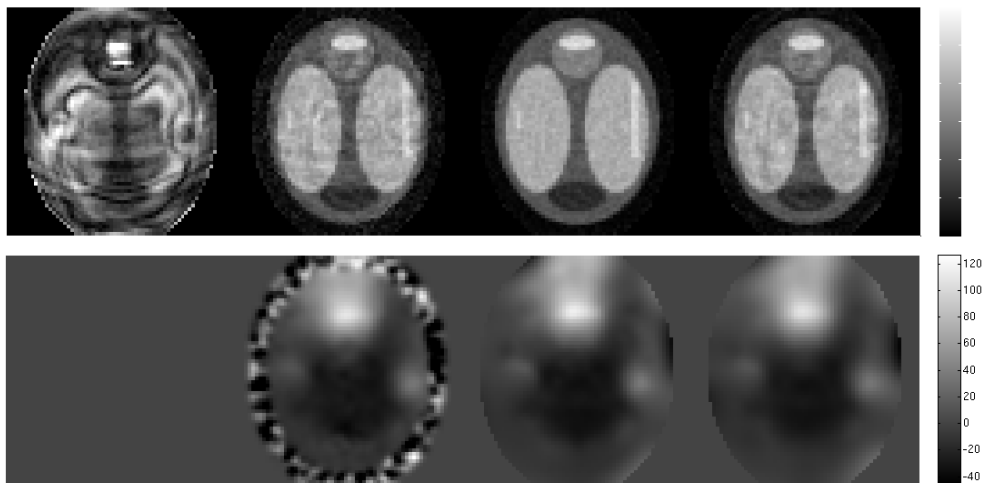


Figure 4.11: Reconstructed images and fieldmaps from “interleaved” spiral trajectory, with single coil at 55dB SNR. Subfigures same as in Figure 4.6.

Table 4.1: Comparative table of NRMS error of reconstruction with all trajectory and coil settings.
 *Note: The same standard estimate was used for all cases as initial fieldmap for joint estimation.

Traj. type	Four coils								Single coil			
	“Interleaved”				Standard				“Interleaved”			
	EPI		Spiral		EPI		Spiral		EPI		Spiral	
SNR	30dB	55dB	30dB	55dB	30dB	55dB	30dB	55dB	30dB	55dB	30dB	55dB
Reconstructed image (NRMSE in %)												
uncorrected	53.8	52.7	40.5	39.4	26.9	21.6	28.4	25.3	65.8	66.4	54.5	54.3
init. fieldmap	13.1	11.8	10.8	8.1	12.3	12.3	11.1	8.6	18.6	18.7	17.9	13.3
joint est.	6.9	3.6	8.0	3.9	10.9	9.4	8.1	5.0	18.6	14.4	16.3	10.5
oracle	6.8	3.3	7.7	3.5	6.8	3.8	7.3	3.3	11.2	6.3	13.8	6.6
Reconstructed fieldmap (RMSE in Hz)												
standard est.*	6.2	6.2	6.2	6.2	6.2	6.2	6.2	6.2	6.2	6.2	6.2	6.2
joint est.	1.0	1.2	1.3	1.4	2.9	3.4	2.9	3.4	2.4	2.4	2.8	2.6
oracle	0.3	0.2	0.8	0.3	1.2	1.2	1.9	2.3	0.7	0.5	0.8	0.4

see in Figure 4.12c the activation regions are visibly comparable to the actual activation regions of Figure 4.3c. Figures 4.12d and 4.12e show the reconstructed images with and without activation when the R_2^* decay is accounted for using the R_2^* map of Figure 4.3a as a known parameter during reconstruction. The reconstructed images are almost artifact-free and the reconstruction quality significantly improved compared to Figures 4.12a and 4.12b. In this case, as seen in Figure 4.12f, the activation regions are successfully identified and with higher relative intensity compared to Figure 4.12c. These results show that accounting for R_2^* decay in our proposed joint estimation method is beneficial not only for the obvious improvement in the reconstruction quality, but also because the activation regions are more clearly identified, thus improving robustness to noise.

4.4.3 Phantom Study

Figure 4.13 shows the resulting reconstructions from the “interleaved” EPI with eight coils for the phantom study. As we see the uncorrected image (Figure 4.13a) is severely distorted due to field inhomogeneity, and the reconstruction using the initial fieldmap estimate (Figure 4.13b) has some slight geometric distortion on the top part due to inaccuracies in the fieldmap estimate. The resulting joint reconstruction (Figure 4.13d) does not show this distortion and resembles more closely the “oracle” reconstruction (Figure 4.13c). However, due to residual ghosting artifacts these results cannot be conclusive in terms of the quality of the joint estimation method, since it’s

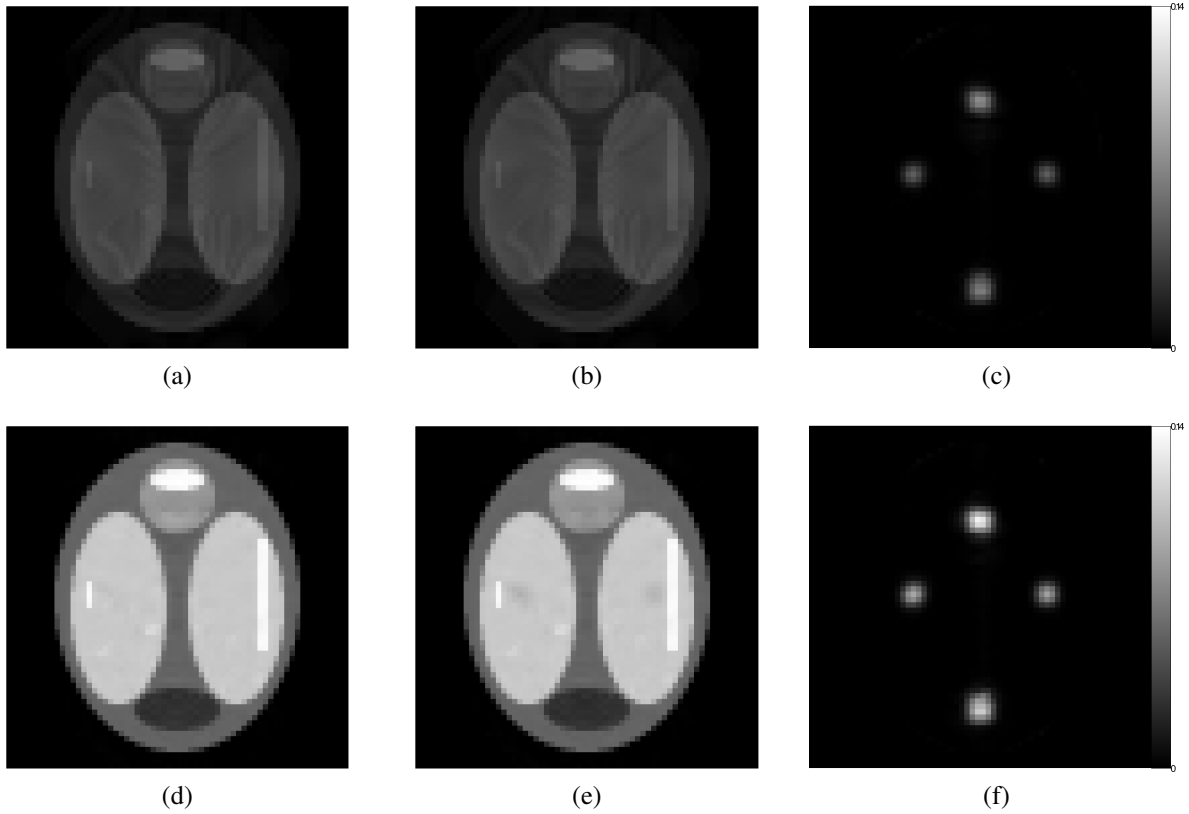


Figure 4.12: Top row (a,b,c) shows results from simulated fMRI study when R_2^* decay is ignored during reconstruction. Bottom row (d,e,f) shows results when R_2^* decay is accounted for during reconstruction using the R_2^* map of Figure 4.3a. (a,d) Reconstructed images at the beginning of study (denoted as f_1) corresponding to R_2^* map of Figure 4.3a without activation. (b,e) Reconstructed images during fMRI study (denoted as f_2) corresponding to R_2^* map of Figure 4.3b with activation regions. (c,f) Normalized difference of images (defined as $(f_1 - f_2)/f_1$) to illustrate identification of activation regions.

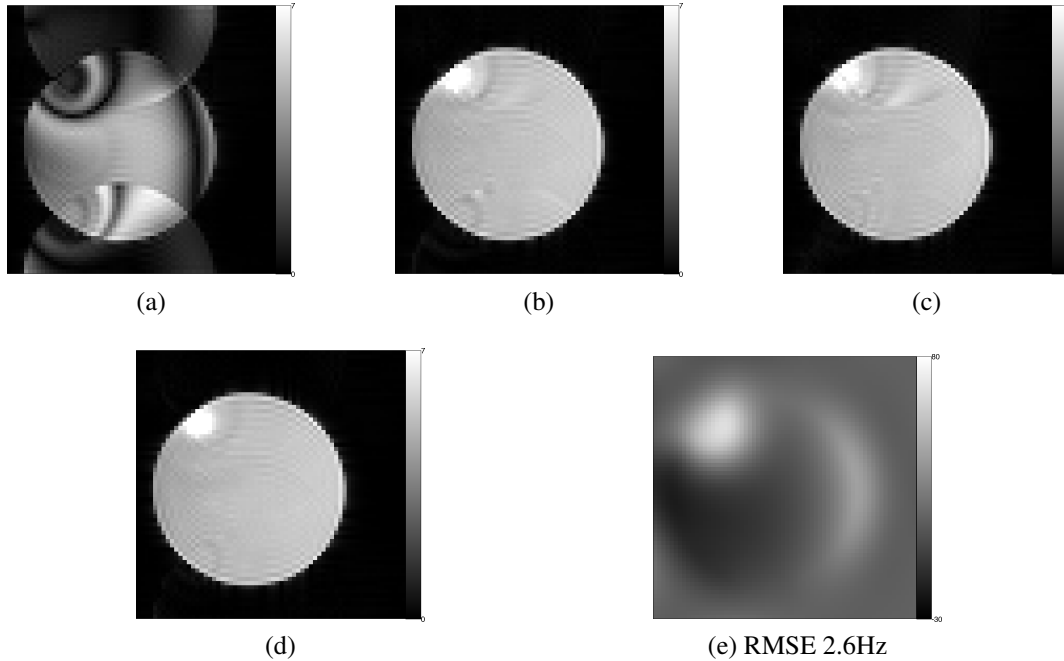


Figure 4.13: Reconstructed images and fieldmaps from phantom study using “interleaved” EPI trajectory, with eight coils. (a) Uncorrected image reconstruction. (b) Image reconstruction corrected with initial fieldmap estimate of Figure 4.4d. (c) “Oracle” image reconstruction corrected with reference fieldmap of Figure 4.4c. (d) Joint image reconstruction. (e) Joint fieldmap reconstruction.

not clear whether or not the artifacts appear due to incorrect $N/2$ ghost suppression or incorrect fieldmap estimation.

Figure 4.14 shows the resulting reconstructions from the standard EPI with eight coils for the phantom study. As we see the uncorrected image (Figure 4.14a) is severely distorted at the top part where the fieldmap is stronger, and the reconstruction using the initial fieldmap estimate (Figure 4.14b) has some slight geometric distortion on the top part due to inaccuracies in the fieldmap estimate. The resulting joint reconstruction (Figure 4.14d) shows the same type of distortion as the image that uses the initial fieldmap estimate, whereas the “oracle” reconstruction (Figure 4.13c) appears to be undistorted. Also, compared to the results from the “interleaved” EPI there are no ghosting artifacts, which means that the simple ghost suppression method that was used works well for the standard EPI unlike the “interleaved” one.

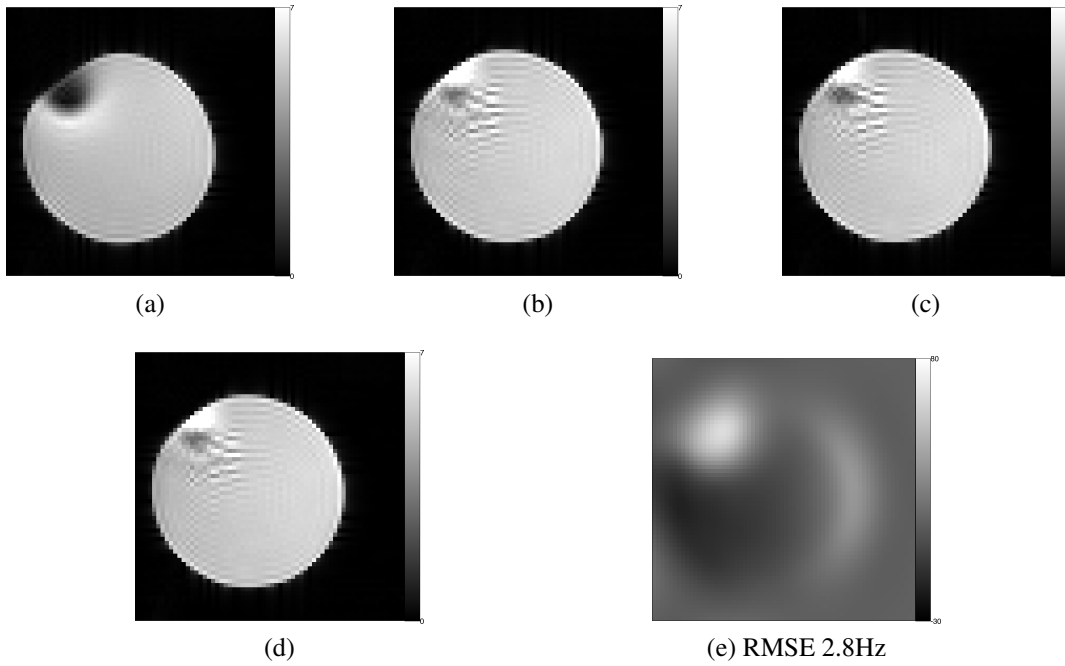


Figure 4.14: Reconstructed images and fieldmaps from phantom study using standard EPI trajectory, with eight coils. Subfigure placement same as in Figure 4.13.

4.5 Discussion

This work presented an efficient method for jointly estimating image and fieldmap in parallel MRI. The simulation results showed that we can achieve high quality reconstruction with this method by using significantly reduced datasets compared to standard methods for image and fieldmap estimation. Due to this fact, this method has the potential to be used in functional MRI where dynamic updates of the image and fieldmap are desirable. A disadvantage of this method is that non-standard single-shot trajectories seem to be required to achieve good reconstruction and also that in a real setting the “interleaved” EPI suffers from ghosting artifacts that need to be eliminated before the method can be of practical use. The ghost suppression could be significantly improved by using the proposed method in chapter III. This ghost suppression method could be very beneficial for the “interleaved” EPI for which we have seen that a simple 1D correction is not sufficient. Also, it would be interesting as a future step to find an analytic relation between trajectories and reconstruction quality as this could explain why the standard trajectories failed to perform well in our simulations. Finally our method can be easily extended for joint estimation of R_2^* decay as well combined with the estimation of image and fieldmap in a way similar to [6].

CHAPTER V

Dynamic MR Image and Fieldmap Joint Reconstruction Accounting for Through-Plane Fieldmap Gradients

In susceptibility-weighted MRI, ignoring magnetic field inhomogeneity can lead to severe reconstruction artifacts. Correcting for the effects of magnetic field inhomogeneity requires accurate fieldmaps. Especially in functional MRI, dynamic updates are desirable, since the fieldmap may change in time. Also, susceptibility effects that induce field inhomogeneity have non-zero through-plane gradients, which, if uncorrected, can cause signal loss in the reconstructed images. Most image reconstruction methods that compensate for field inhomogeneity, even using dynamic fieldmap updates, ignore through-plane fieldmap gradients. This chapter proposes a computationally efficient, model based iterative method for joint reconstruction of image and dynamic fieldmap that accounts for the through-plane gradients of the field inhomogeneity. The proposed method allows for efficient reconstruction by applying fast approximations that allow the use of the conjugate gradient algorithm along with FFTs.

5.1 Introduction

In functional MRI a series of dynamic images is reconstructed and to satisfy the need for high temporal resolution, fast single-shot acquisitions are commonly used. Also these acquisition usually have late echo-times to ensure good BOLD contrast. These characteristics of susceptibility-weighted MR imaging lead to increased sensitivity to magnetic field inhomogeneities. Correcting for these effects requires accurate inhomogeneity fieldmaps and since the fieldmap may change in time, dynamic updates are desirable. This motivated the development of methods that can jointly reconstruct undistorted images and undistorted dynamic fieldmaps [3, 4, 45].

Part of the work in this chapter appears in [8].

Most methods that correct for field inhomogeneity, even the model-based iterative ones, treat the inhomogeneity within each voxel as being a constant. However, susceptibility effects cause nonzero through-plane gradients that lead to spin dephasing across the slice within each voxel. Ignoring through-plane gradients can cause signal loss in the reconstructed images, especially in functional MR imaging where acquisitions with long readouts and late echo-times are used. To correct for the through-plane gradient effects, a fast, iterative reconstruction method is proposed in [7]. That method assumed that the through-plane gradients are known, so it cannot handle dynamic fieldmap changes.

Motivated by [4], this work proposes a computationally efficient, model based, iterative method that jointly reconstructs images and dynamic fieldmaps, accounting for through-plane gradient effects. The proposed algorithm uses the signal model presented in [7] and applies the fast approximations introduced in [9]. Finally to improve the efficiency of the reconstruction algorithm, similarly to [6], a linearization technique for fieldmap estimation is used, that allows the use of the CG algorithm.

5.2 Theory

To correct for through-plane gradient effects, we need a signal model that accounts for the slice profile and the through plane gradients of the field inhomogeneity. Assuming a total of J slices and parallel imaging with K coils, a reasonable model for the signal in slice selective MRI is:

$$s_{j,k}(t) = \iiint h(z - z_j) c_k(x, y, z) f(x, y, z) e^{-i\omega(x,y,z)t} e^{-i2\pi(k_x(t)x + k_y(t)y)} dx dy dz, \quad (5.1)$$

for $k = 1, \dots, K$ and $j = 1, \dots, J$,

where $h(z)$ is the (known) slice-selection profile, z_j is the axial center of the j th slice, $f(x, y, z)$ is the (unknown) object, $\omega(x, y, z)$ is the fieldmap, $c_k(x, y, z)$ is the coil sensitivity and $\mathbf{k}(t) \triangleq (k_x(t), k_y(t))$ is the k-space trajectory. We assume that the object f and the fieldmap ω are static during a single-shot readout. In this work we ignored the effects of R_2^* decay, but the model in (5.1) can be easily extended to accommodate a known R_2^* map similarly to (4.1).

The model in (5.1) is equivalent to that in (2.7) [7] and using the assumptions and approximations of §2.4.3, the discretized signal equation, derived from (2.8), is expressed as:

$$s_{j,k}(t) = \Phi(\mathbf{k}(t)) \sum_{n=0}^{N-1} H(g_{j,n}t) c_{j,k,n} f_{j,n} e^{-i\omega_{j,n}t} e^{-i2\pi\mathbf{k}(t) \cdot \mathbf{p}_n}, \quad (5.2)$$

where $\Phi(\mathbf{k}(t))$ is the Fourier transform of the basis function, $H(\cdot)$ is the Fourier transform of the slice profile and \mathbf{g} is the through-plane gradient map. Since the gradient map \mathbf{g} depends on the fieldmap ω (derivative along the through-plane direction z), it would be impractical to consider \mathbf{g} as an unknown parameter and jointly estimate the image, fieldmap and gradient map. Thus, we express the gradient map \mathbf{g} in terms of the fieldmap ω using central differences

$$g_{j,n} \triangleq \frac{\omega_{j+1,n} - \omega_{j-1,n}}{4\pi\Delta z}, \quad (5.3)$$

and then jointly estimate the image \mathbf{f} and fieldmap ω .

The model of (5.2) is nonlinear in ω . To avoid using a computationally demanding GD method as in [3], we follow [6] and linearize the signal equation by approximating the term $H(\mathbf{g}_j t) e^{-i\omega_j t}$ using first-order Taylor series expansion around a carefully chosen reference $\check{\omega}$. The suitability of the linearization depends on having a reasonable initial fieldmap estimate $\check{\omega}$; typically $\check{\omega}$ is obtained from a pre-scan or from the previous dynamic frame. This leads to the following approximation:

$$\begin{aligned} H(\mathbf{g}_j t) e^{-i\omega_j t} &\approx H(\check{\mathbf{g}}_j t) e^{-i\check{\omega}_j t} - itH(\check{\mathbf{g}}_j t) e^{-i\check{\omega}_j t} (\omega_j - \check{\omega}_j) \\ &\quad - \frac{t}{4\pi\Delta z} H'(\check{\mathbf{g}}_j t) e^{-i\check{\omega}_j t} (\omega_{j-1} - \check{\omega}_{j-1}) + \frac{t}{4\pi\Delta z} H'(\check{\mathbf{g}}_j t) e^{-i\check{\omega}_j t} (\omega_{j+1} - \check{\omega}_{j+1}), \end{aligned} \quad (5.4)$$

where $H'(\cdot) \triangleq \frac{dH(\cdot)}{du}$ and $\check{\mathbf{g}}_j \triangleq \frac{\check{\omega}_{j+1} - \check{\omega}_{j-1}}{4\pi\Delta z}$.

MRI measurements are noisy samples of the signal. Using the approximation (5.4) in the signal equation (5.2), the measurement vectors $\mathbf{y}_{j,k}$ for each slice and each coil can be expressed in matrix vector form as:

$$\begin{aligned} \mathbf{y}_{j,k} &= \mathbf{A}(\check{\omega}_j, \check{\mathbf{g}}_j) \mathbf{f}_j + \mathbf{B}(\check{\omega}_j, \check{\mathbf{g}}_j, \mathbf{f}_j) (\omega_j - \check{\omega}_j) + \mathbf{D}(\check{\omega}_j, \check{\mathbf{g}}_j, \mathbf{f}_j) (\omega_{j-1} - \check{\omega}_{j-1}) \\ &\quad - \mathbf{D}(\check{\omega}_j, \check{\mathbf{g}}_j, \mathbf{f}_j) (\omega_{j+1} - \check{\omega}_{j+1}) + \boldsymbol{\varepsilon}_{j,k}, \end{aligned} \quad (5.5)$$

where $\mathbf{f}_j \triangleq (f_{j,1}, \dots, f_{j,N})$, $\boldsymbol{\omega}_j \triangleq (\omega_{j,1}, \dots, \omega_{j,N})$ and $\mathbf{c}_{j,k} \triangleq (c_{j,k,1}, \dots, c_{j,k,N})$ are the discretized object, fieldmap and sensitivity map respectively, and the elements of the $M \times N$ system matrices

$\mathbf{A}(\check{\omega}_j, \check{\mathbf{g}}_j)$, $\mathbf{B}(\check{\omega}_j, \check{\mathbf{g}}_j, \mathbf{f}_j)$ and $\mathbf{D}(\check{\omega}_j, \check{\mathbf{g}}_j, \mathbf{f}_j)$ are:

$$\begin{aligned}
a(\check{\omega}_j, \check{\mathbf{g}}_j)_{m,n} &= H(\check{g}_{j,n}t_m) w(\check{\omega}_j, \check{\mathbf{g}}_j)_{m,n}, \\
b(\check{\omega}_j, \check{\mathbf{g}}_j, \mathbf{f}_j)_{m,n} &= -it_m a(\check{\omega}_j, \check{\mathbf{g}}_j)_{m,n} f_{j,n}, \\
d(\check{\omega}_j, \check{\mathbf{g}}_j, \mathbf{f}_j)_{m,n} &= -\frac{t_m}{4\pi\Delta z} H'(\check{g}_{j,n}t_m) w(\check{\omega}_j, \check{\mathbf{g}}_j)_{m,n} f_{j,n}, \\
w(\check{\omega}_j, \check{\mathbf{g}}_j)_{m,n} &\triangleq \Phi(\mathbf{k}(t_m)) e^{-i\check{\omega}_{j,n}t_m} e^{-i2\pi\mathbf{k}(t_m)\cdot\mathbf{p}_n}.
\end{aligned} \tag{5.6}$$

When one ignores through-plane gradients (assuming $\mathbf{g}_j = 0$), the measurement model in (5.5) is equivalent to the approach described in [4] and Chapter IV, and the joint reconstruction problem can be solved with the fast iterative algorithm described therein. The presence of the $H(\mathbf{g}_j, t)$ and $H'(\mathbf{g}_j, t)$ terms in (5.6) prohibits the direct application of those fast methods. To solve this problem, we used the following approximations based on the histogram PCA basis expansion approach described in [9]:

$$H(\check{g}_{j,n}t_m) e^{-i\check{\omega}_{j,n}t_m} \approx \sum_{l=1}^L p_{j,l,m} q_{j,l,n}, \tag{5.7}$$

$$H'(\check{g}_{j,n}t_m) e^{-i\check{\omega}_{j,n}t_m} \approx \sum_{l=1}^L u_{j,l,m} v_{j,l,n}. \tag{5.8}$$

Using the approximations in (5.7) and (5.8) into the expressions in (5.6), allows the evaluation of the forward model or its adjoint using L NUFFT calls. An analysis of the error introduced due to the approximations of (5.7) and (5.8) is included in this chapter's appendix.

The measurement vector for each slice \mathbf{y}_j is given by stacking the measurement vectors $\mathbf{y}_{j,k}$ for each coil and the overall $KM \times N$ system matrices are given by stacking the system matrices for each coil. Hence, the overall measurement model for each slice in matrix-vector form can be written as:

$$\begin{aligned}
\mathbf{y}_j &= \check{\mathbf{A}}(\check{\omega}_j, \check{\mathbf{g}}_j) \mathbf{f}_j + \check{\mathbf{B}}(\check{\omega}_j, \check{\mathbf{g}}_j, \mathbf{f}_j)(\omega_j - \check{\omega}_j) + \check{\mathbf{D}}(\check{\omega}_j, \check{\mathbf{g}}_j, \mathbf{f}_j)(\omega_{j-1} - \check{\omega}_{j-1}) \\
&\quad - \check{\mathbf{D}}(\check{\omega}_j, \check{\mathbf{g}}_j, \mathbf{f}_j)(\omega_{j+1} - \check{\omega}_{j+1}) + \boldsymbol{\varepsilon}_j.
\end{aligned} \tag{5.9}$$

In (5.9) there is coupling between adjacent slices of the fieldmap. It should be beneficial to account for this coupling when reconstructing, by estimating all the slices at once and treating the problem as a 3D reconstruction instead of a slice-by-slice 2D reconstruction. With this in mind, we write

the measurement model as:

$$\mathbf{y} = \tilde{\mathbf{A}}(\tilde{\boldsymbol{\omega}}) \mathbf{f} + \tilde{\mathbf{B}}(\tilde{\boldsymbol{\omega}}, \mathbf{f})(\boldsymbol{\omega} - \tilde{\boldsymbol{\omega}}) + \boldsymbol{\varepsilon}, \quad (5.10)$$

where the vectors \mathbf{y} , \mathbf{f} and $\boldsymbol{\omega}$ are created by stacking the individual slice vectors \mathbf{y}_j , \mathbf{f}_j and $\boldsymbol{\omega}_j$ respectively and the $JKM \times JN$ matrices $\tilde{\mathbf{A}}(\tilde{\boldsymbol{\omega}})$ and $\tilde{\mathbf{B}}(\tilde{\boldsymbol{\omega}}, \mathbf{f})$ are defined as follows:¹

$$\tilde{\mathbf{A}} \triangleq \begin{bmatrix} \check{\mathbf{A}}_1 & 0 & \cdots & 0 \\ 0 & \check{\mathbf{A}}_2 & \ddots & \vdots \\ \vdots & \ddots & \ddots & 0 \\ 0 & \cdots & 0 & \check{\mathbf{A}}_J \end{bmatrix} \quad (5.11)$$

$$\tilde{\mathbf{B}} \triangleq \begin{bmatrix} \check{\mathbf{B}}_1 + 2\check{\mathbf{D}}_1 & -2\check{\mathbf{D}}_1 & 0 & \cdots & 0 \\ \check{\mathbf{D}}_2 & \check{\mathbf{B}}_2 & -\check{\mathbf{D}}_2 & \ddots & \vdots \\ 0 & \ddots & \ddots & \ddots & 0 \\ \vdots & \ddots & \check{\mathbf{D}}_{J-1} & \check{\mathbf{B}}_{J-1} & -\check{\mathbf{D}}_{J-1} \\ 0 & \cdots & 0 & 2\check{\mathbf{D}}_J & \check{\mathbf{B}}_J - 2\check{\mathbf{D}}_J \end{bmatrix}$$

To estimate the image and fieldmap accounting for noise statistics, we minimize the following regularized least squares cost function:

$$\Psi(\mathbf{f}, \boldsymbol{\omega}) = \frac{1}{2} \left\| \mathbf{y} - \tilde{\mathbf{A}}(\tilde{\boldsymbol{\omega}}) \mathbf{f} - \tilde{\mathbf{B}}(\tilde{\boldsymbol{\omega}}, \mathbf{f})(\boldsymbol{\omega} - \tilde{\boldsymbol{\omega}}) \right\|_2^2 + \beta_1 \Phi_1(\mathbf{f}) + \beta_2 \Phi_2(\boldsymbol{\omega}), \quad (5.12)$$

where $\Phi_1(\mathbf{f})$ and $\Phi_2(\boldsymbol{\omega})$ are regularization terms. The fieldmap is smooth, both in the in-plane and through-plane directions, so we use a quadratic regularization penalty $\Phi_2(\boldsymbol{\omega}) \triangleq \frac{1}{2} \|\mathbf{C}_2 \boldsymbol{\omega}\|_2^2$, where \mathbf{C}_2 is a matrix of second-order differences along all three directions (x, y, z). For the image \mathbf{f} , an edge-preserving regularizer could be used, but since fMRI images are often smoothed for data analysis, we also used a quadratic regularizer $\Phi_1(\mathbf{f}) \triangleq \frac{1}{2} \|\mathbf{C}_1 \mathbf{f}\|_2^2$ here, where \mathbf{C}_1 is a matrix of second-order differences along the x and y directions.

In this chapter we applied the linearization approximation before the formulation of the cost function in (5.12) leading to a formulation using an approximate measurement model. However, the linearization approximation is a technique used to allow the application of CG in the cost

¹In (5.11), the dependency of $\check{\mathbf{A}}$, $\check{\mathbf{B}}$ and $\check{\mathbf{D}}$ on $\boldsymbol{\omega}_j$, \mathbf{g}_j and \mathbf{f}_j is only expressed through the subscript $j = 1, \dots, J$ for brevity.

function minimization. Thus, more accurately the cost function should be formulated with the exact, nonlinear model of (5.2) and then apply the linearization approximation leading to (5.12). Our approach for the cost function formulation was used here for simplicity of presentation.

We minimize the cost function (5.12) by alternating between updating the image and the fieldmap. In each step of the minimization process a new update is found for the image and then for the fieldmap and the process is repeated until convergence. For the k th step in the alternating minimization scheme, the image update is:

$$\hat{\mathbf{f}}^{(k)} = \underset{\mathbf{f}}{\operatorname{argmin}} \frac{1}{2} \left\| \mathbf{y} - \tilde{\mathbf{A}}\left(\hat{\boldsymbol{\omega}}^{(k-1)}\right) \mathbf{f} \right\|_2^2 + \beta_1 \Phi_1(\mathbf{f}) \quad (5.13)$$

and the fieldmap update uses the most recent image:

$$\hat{\boldsymbol{\omega}}^{(k)} = \underset{\boldsymbol{\omega}}{\operatorname{argmin}} \frac{1}{2} \left\| \tilde{\mathbf{y}}^{(k)} - \tilde{\mathbf{B}}\left(\hat{\boldsymbol{\omega}}^{(k-1)}, \hat{\mathbf{f}}^{(k)}\right) \boldsymbol{\omega} \right\|_2^2 + \beta_2 \Phi_2(\boldsymbol{\omega}), \quad (5.14)$$

where

$$\tilde{\mathbf{y}}^{(k)} \triangleq \mathbf{y} - \tilde{\mathbf{A}}\left(\hat{\boldsymbol{\omega}}^{(k-1)}\right) \hat{\mathbf{f}}^{(k)} + \tilde{\mathbf{B}}\left(\hat{\boldsymbol{\omega}}^{(k-1)}, \hat{\mathbf{f}}^{(k)}\right) \hat{\boldsymbol{\omega}}^{(k-1)}.$$

In both (5.13) and (5.14) we find the minimizers using the CG-Toeplitz method [9] which is reasonably computationally efficient. For EPI trajectories standard FFTs can be used instead of the NUFFT.

5.3 Materials and Methods

The proposed method is applicable with any k -space trajectory, although the results depend on the trajectory choice. As proposed in Chapter IV and [4], the choice of an ‘‘interleaved’’, single-shot EPI trajectory, along with sensitivity encoding, enables successful joint reconstruction of image and fieldmap. Thus, we used this type of trajectory to assess the proposed method. The trajectory parameters are FOV = 24 cm, matrix size = 64×64 , readout time = 46 ms and two echo-times at $T_{E1} = 18$ ms and $T_{E2} = 42$ ms. For parallel imaging in simulations, a four coil setting with smooth B1 maps was used.

For the simulation experiments human brain data (both images and fieldmaps) were used, acquired with the method described in [46]. The scans were 64×64 by 20 slices, with 24 cm transaxial FOV and 2 cm axial FOV, resulting in slice spacing of 1 mm. For the slice selection, a rectangular profile was used with 4 mm width. The choices for slice spacing and slice thickness in our sim-

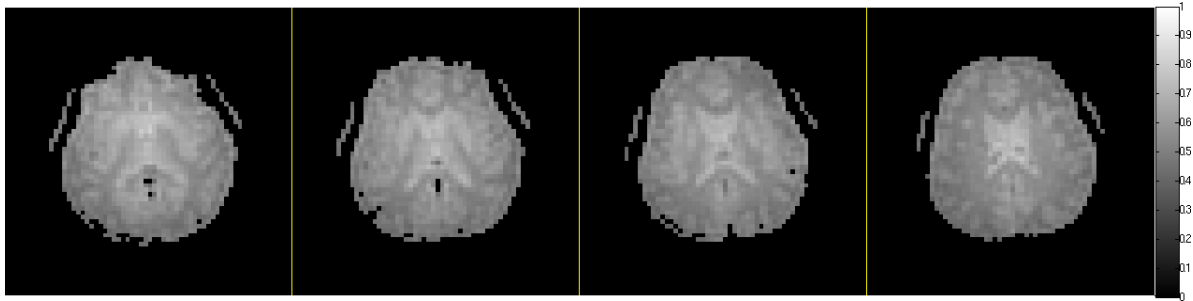
ulation experiment are unrealistic since using a wider slice compared to the spacing can lead to undesirable spin saturation effects. However, it was used in this simulation to better illustrate the effect of the through-plane gradients since a wider slice thickness results in more prominent signal loss. The magnitude images and the corresponding fieldmaps of 4 slices are shown in Figs. 5.1a and 5.1b. The fieldmap gradients, shown in Fig. 5.1c, were estimated from the fieldmaps using central differences.

The experiments were performed with simulated data, created using the exact system model (5.2), to which noise was added to make a 30dB and 50dB data SNR. We used an iteratively reconstructed image, uncorrected for field inhomogeneities, as the initial estimate $\hat{\mathbf{f}}^{(0)}$, and we created the initial estimate $\hat{\omega}^{(0)}$ with the standard phase difference method from two images using iterative CG reconstruction uncorrected for field inhomogeneities. The images were acquired with 2-shot EPI trajectories, at 40dB data SNR. Each shot of the EPI had a 22.5 ms readout time and the echo-times were $T_{E1} = 12.3$ ms for the first acquisition and $T_{E2} = 14.3$ ms for the second, resulting in a $\Delta T_E = 2$ ms echo-time difference. The resulting distorted fieldmaps were smoothed with a Gaussian filter to suppress the noise. Table 5.1 shows the RMS and maximum error of the initial fieldmap. As seen in the results section, the joint reconstruction method works well when the initial fieldmap is within 10 Hz from the true fieldmap, although a more thorough investigation of these limits is required. Nevertheless, the expected variations of the fieldmap in an fMRI study, as presented in [3], are well within this range.

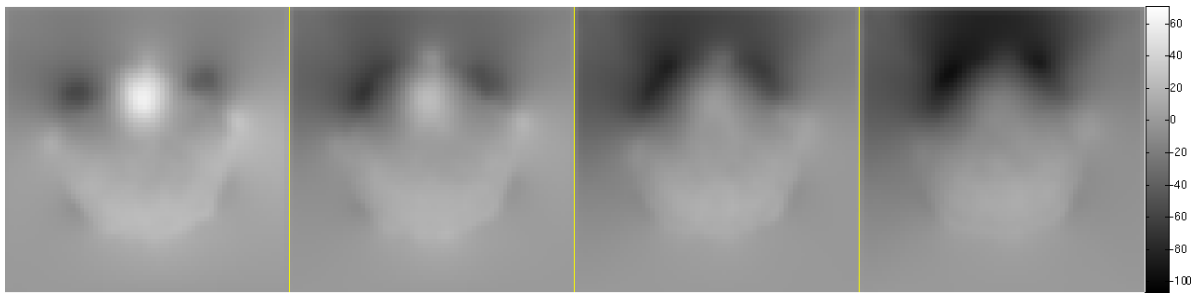
To further evaluate the quality of the joint reconstruction, an oracle image estimate was reconstructed with our method using the true fieldmap (Figure 5.2a) and an oracle fieldmap estimate was reconstructed with our method using the true image (Figure 5.2b). These oracle estimates provide an upper bound on the accuracy of the proposed joint reconstruction method.

The regularization parameters β_1 and β_2 in (5.13) and (5.14) were chosen to achieve a specific spatial resolution [43]. For the image we chose β_1 so that the FWHM of the PSF was 1.1 pixels at 50dB SNR and 1.2 pixels at 30dB SNR. For the fieldmap we chose β_2 so that the FWHM of the PSF was 1.2 voxels (since 3D regularization is applied) for both SNRs.

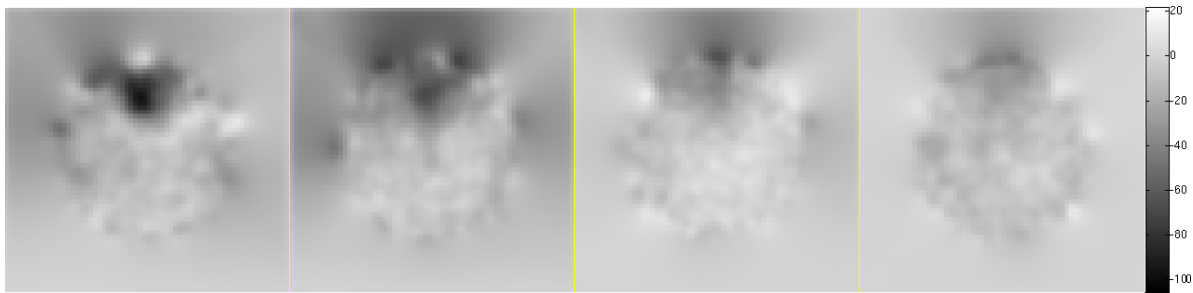
To jointly estimate the image and fieldmap we alternated 20 times between updating the image and then updating the fieldmap. In each update we used 15 iterations of the CG method. The necessary matrix-vector multiplications in each CG iteration were performed with the Toeplitz, histogram PCA method of [9], with $L = 9$ basis functions. The CG-Toeplitz method requires updates of the basis and coefficients in each alternating step, which can be a computational bottleneck, since calculating a new basis requires to perform a SVD. To alleviate this problem, the basis functions were precalculated at the beginning of the study and only the coefficients were updated



(a) True image f [arbitrary units]

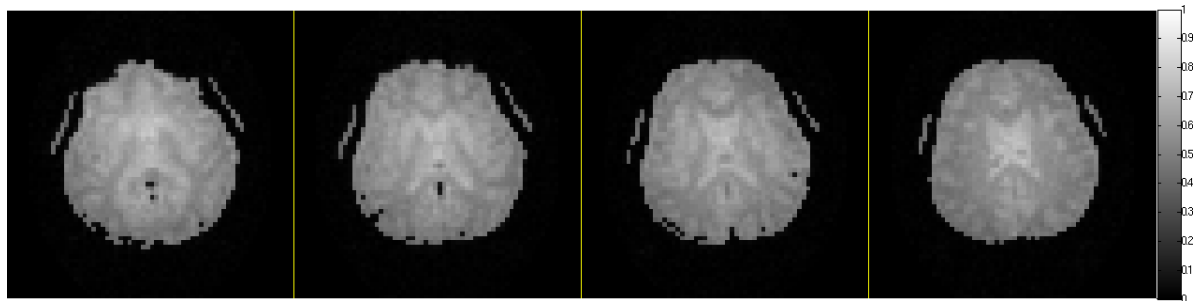


(b) True fieldmap ω [Hz]

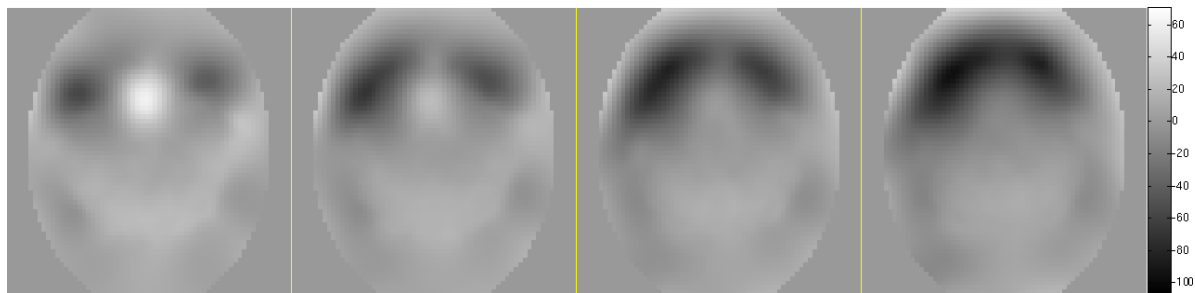


(c) True gradient map g [Hz/cm]

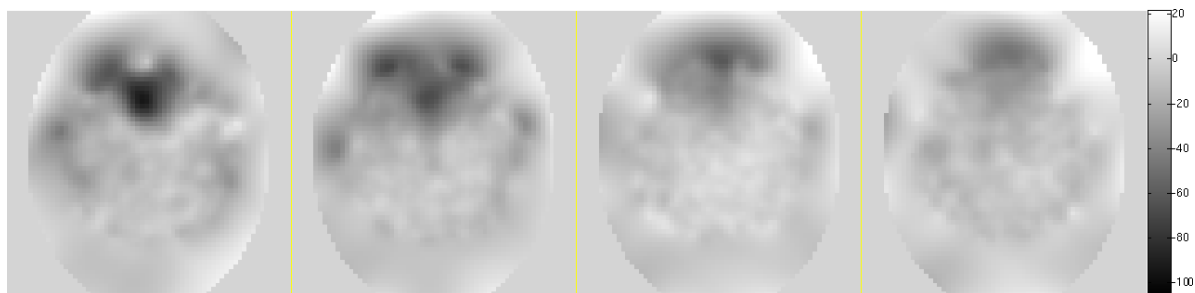
Figure 5.1: True image, fieldmap, and gradient map for 4 out of 20 slices. Slices 3, 8, 13 and 18 are shown from left to right.



(a) “Oracle” image \hat{f} [arbitrary units]



(b) “Oracle” fieldmap $\hat{\omega}$ [Hz]



(c) “Oracle” gradient map \hat{g} [Hz/cm]

Figure 5.2: “Oracle” image, fieldmap, and gradient map for 4 out of 20 slices. Slices 3, 8, 13 and 18 are shown from left to right.

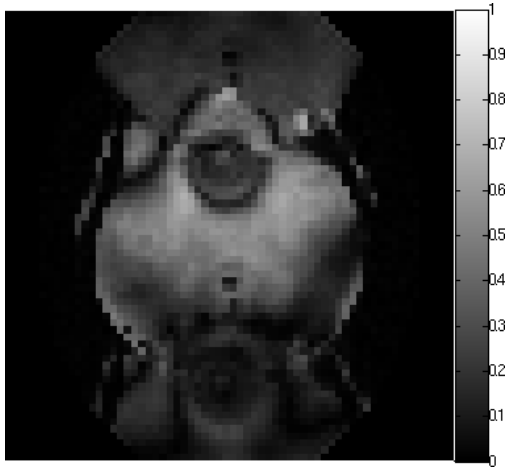
in each alteration. Given reasonable initial estimates, this is a reasonable simplification, because the nature of the image and the fieldmap does not change dramatically with each update. The computational cost per iteration is in the order of $O(N \log N)$ and it requires roughly three times more computations per iteration compared to the method in [6].

5.4 Simulation results

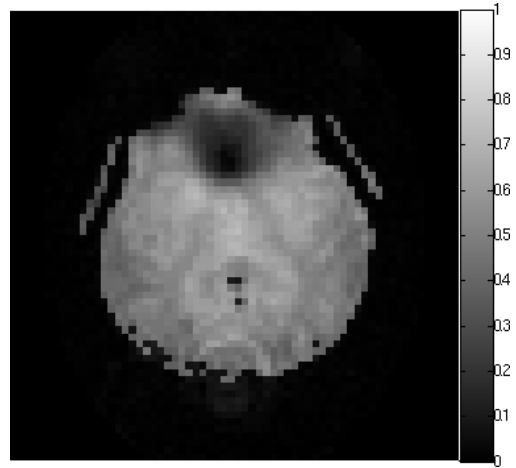
Figure 5.3a shows the reconstructed image without correction for field inhomogeneities. Because of the fieldmap and gradient strength and the long readout time, there are significant geometric artifacts along with signal loss. Figure 5.3b shows the reconstructed image when field inhomogeneities were corrected using the true fieldmap, but the through-plane gradients were ignored. In this reconstruction there are no geometric artifacts caused by field inhomogeneity, but there is significant signal loss due to the fieldmap gradients. Figure 5.3c shows the reconstructed image with correction for field inhomogeneities and through-plane gradients, using the initial, standard fieldmap estimate (Figure 5.3d) and the resulting gradients. In this case the artifacts are reduced but not completely eliminated, there is also some residual signal loss, and the reconstruction quality is not close to the one achieved in the oracle reconstruction (Figure 5.2a), where the true fieldmaps and through-plane gradients are used. This is also evident in terms of normalized RMS error, as seen in Table 5.1. Figures 5.4a, 5.4b and 5.4c show the jointly reconstructed images, fieldmaps and through-plane gradient maps that were reconstructed with our proposed method. In this case there are significantly reduced inhomogeneity artifacts and almost negligible signal loss in the reconstructed images; both the images, fieldmaps and gradients are of comparable quality to the oracle reconstructions (Figures 5.2a, 5.2b and 5.2c). This can also be seen in terms of RMS error in Table 5.1. As seen from these preliminary simulation results, the proposed method seems promising in performing efficient joint reconstruction of image and dynamic fieldmap in the presence of through-plane gradients.

5.5 Discussion

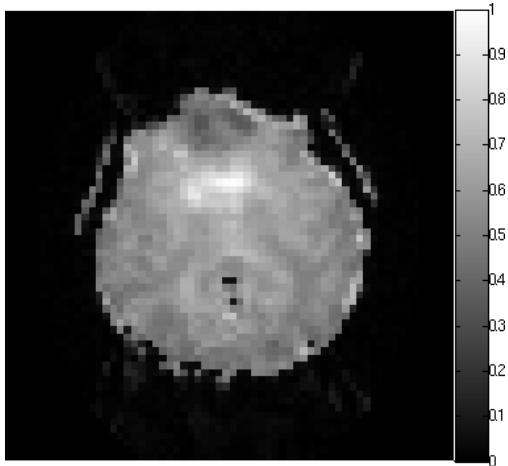
This chapter proposed an efficient method for joint estimation of dynamic images and fieldmaps compensating for through-plane gradient effects. The preliminary simulation results showed that high quality reconstruction can be achieved with this method, by using a more accurate signal model and fast approximations. Thus, this method can be potentially useful in functional MRI, where dynamic fieldmap updates are desirable and through-plane gradient effects can cause sig-



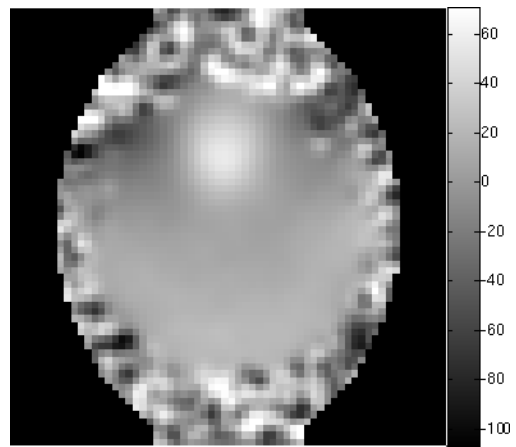
(a) Uncorrected image.



(b) Reconstructed image ignoring fieldmap gradients.

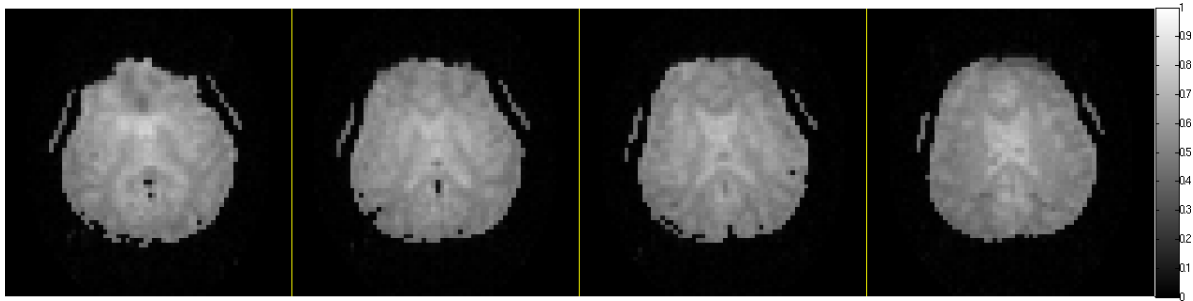


(c) Reconstructed image using initial fieldmap.

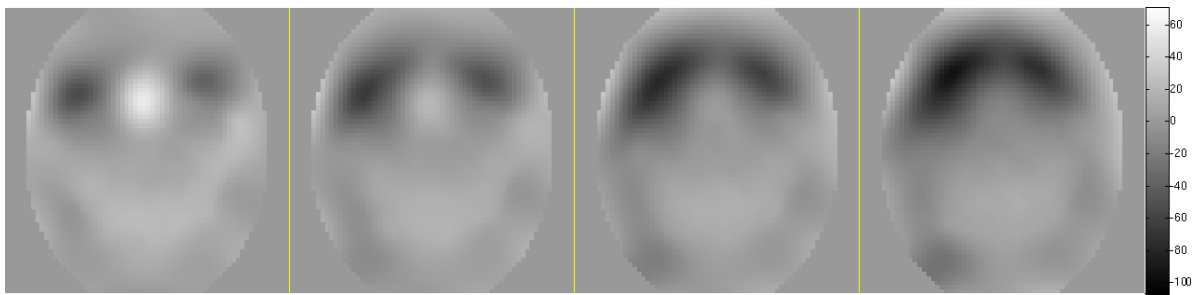


(d) Initial fieldmap estimate.

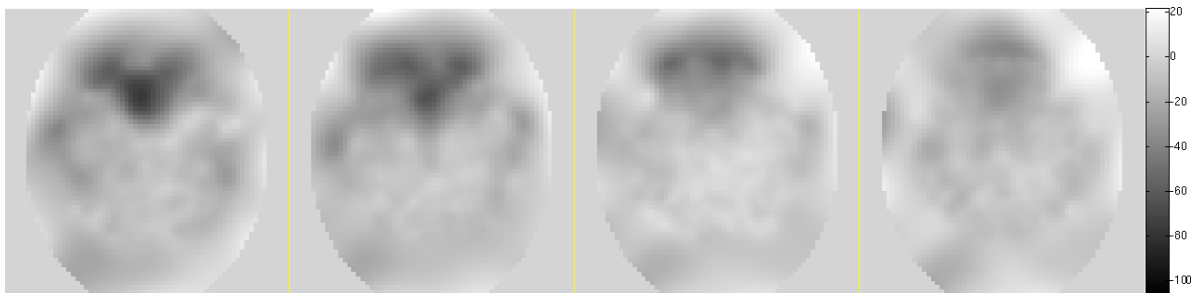
Figure 5.3: Image and fieldmap reconstructions for one slice (slice 3 of sequence).



(a) Jointly reconstructed image \hat{f} [arbitrary units]



(b) Jointly reconstructed fieldmap $\hat{\omega}$ [Hz]



(c) Jointly reconstructed gradient map \hat{g} [Hz/cm]

Figure 5.4: Jointly reconstructed image, fieldmap, and gradient map for 4 out of 20 slices. Slices 3, 8, 13 and 18 are shown from left to right.

Table 5.1: Comparative table of RMS error of reconstruction methods, for all 20 slices.

	30dB	50dB	30dB	50dB
Reconstructed images	NRMS in %		Max. Err. in %	
uncorrected	49.4	49.1	99.7	99.9
using initial fieldmap	15.4	14.5	98.3	111.0
true fieldmap, no gradients	20.2	19.0	98.9	97.1
oracle (using true fieldmap)	9.1	4.9	41.4	29.5
joint estimation	10.2	7.3	67.6	74.9
Reconstructed fieldmaps	RMS in Hz		Max. Err. in Hz	
standard estimate	3.3	3.3	15.9	15.9
oracle (using true image)	0.3	0.2	2.4	2.3
joint estimation	1.3	1.4	11.8	13.9
Reconstructed gradients	RMS in Hz/cm		Max. Err. in Hz/cm	
standard estimate	17.0	17.0	150.3	150.3
oracle (using true image)	1.4	1.1	14.3	13.4
joint estimation	3.6	3.7	49.5	59.1

nificant image quality degradation. A disadvantage of this method, as in [4], is that non-standard single-shot trajectories seem to be required to achieve good reconstruction.

As a future step it would be interesting to investigate the benefits, in terms of quality of the reconstructed images, from incorporating in-plane fieldmap gradients in the signal model. Also, in this study, a 3D regularizer was used for fieldmap reconstruction, with promising results in terms of image quality. However, a more thorough study of its effects on the reconstructed images is required. Furthermore, as illustrated in chapter IV, it is important to account for R_2^* decay in joint reconstruction and including a known R_2^* map in the system model is a straightforward extension of the proposed system model. Finally, to further evaluate the proposed method it is necessary to perform experiments using real data from phantom and human studies.

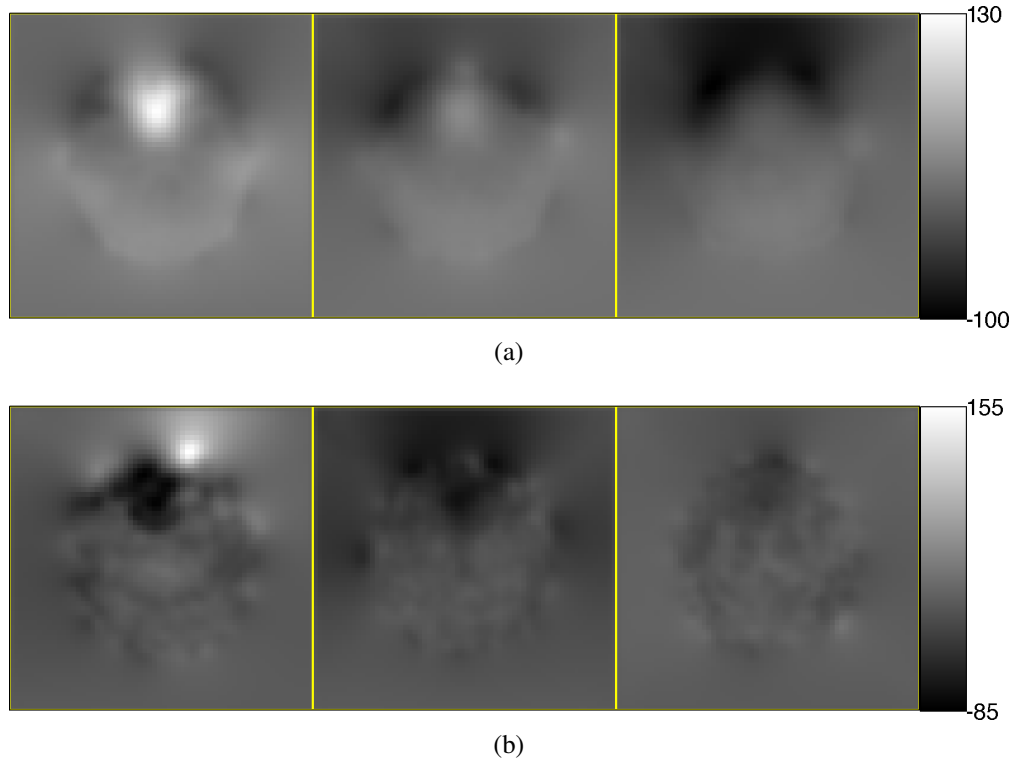


Figure 5.5: (a) Fieldmaps and (b) gradient maps used in the error analysis of the approximations in (5.7) and (5.8).

5.6 Appendix

5.6.1 Error Analysis of Approximations in (5.7) and (5.8)

In this section we present an error analysis for the basis expansion approximations of (5.7) and (5.8). The approximation error was measured for 3 slices with fieldmaps and gradient maps shown in Figure 5.5. We measured the NRMS error introduced from the approximation using from one to twenty basis functions.

Figures 5.6a and 5.6b show the approximation NRMS (in log scale) of (5.7) and (5.8) respectively, in terms of the number of basis functions used. The results show that the NRMS error depends heavily on the fieldmap and gradient map of each slice; however, choosing more than twelve basis functions seems sufficient to reduce the NRMS error to approximately 1%, even for particularly strong fieldmaps and gradient maps as in Figure 5.5. Since this analysis performed after the simulation experiments, it appears that the choice of nine basis functions used in simulations may not have been sufficient for all the slices. Thus, in subsequent experiments using the proposed

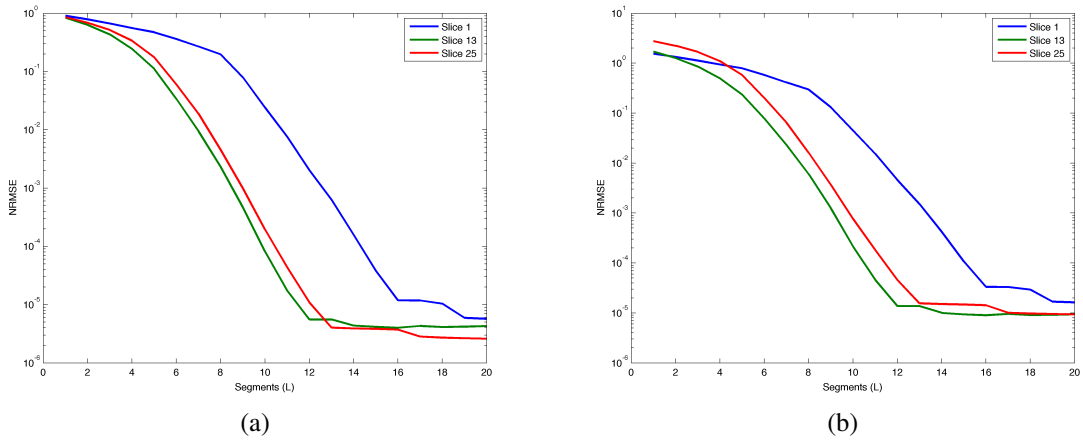


Figure 5.6: NRMS error plots in log scale in terms of number of basis functions L . (a) Approximation of (5.7). (b) Approximation of (5.8).

joint estimation method the number of basis functions used may be increased accordingly.

CHAPTER VI

Augmented Lagrangian (AL) Approach for Joint Estimation

6.1 Introduction

The iterative methods developed in Chapters IV and V for joint estimation [4, 8] use the conjugate gradient method (CG) which is computationally efficient for quadratic regularization. However, non-quadratic regularization can be beneficial to improve the reconstruction results at an increased computational cost. Recently there are several MRI reconstruction methods developed using the Augmented Lagrangian framework with variable splitting that show accelerated convergence using non-quadratic regularizers. Motivated by [10] and our work in AL methods for image restoration [11] (presented in Appendix B) we propose a joint image and fieldmap estimation method based on the AL framework. Our proposed method would benefit from the faster convergence rate of the AL methods and the improved image reconstruction quality of non-quadratic regularization. Another advantage of the AL approach is that our proposed algorithm can also be used for the nonlinear optimization problem of fieldmap estimation without the need for the linearization approximation [6].

6.2 Definitions

The $M' \times N$ Fourier encoding matrix, for image size N and M' measurements from single receiver coil, is

$$[\mathbf{G}]_{m',n} = e^{-i2\pi\mathbf{k}(t_{m'}) \cdot \mathbf{p}_n}. \quad (6.1)$$

For non-Cartesian imaging, using NUFFT, (6.1) is approximated as

$$\mathbf{G} \approx \mathbf{P}\mathbf{Q}_K\mathbf{D}_s, \quad (6.2)$$

where \mathbf{Q}_K is an oversampled DFT matrix ($K > N, M'$), such that $\mathbf{Q}'_K\mathbf{Q}_K = K\mathbf{I}_K$, \mathbf{D}_s is a diagonal ($K \times N$) matrix of scaling factors, and \mathbf{P} is a ($M' \times K$) sparse interpolation matrix. The number of non-zero elements in \mathbf{P} depends on the interpolation neighborhood ($P \times P \ll K$) for a maximum of $M' \times P^2 \ll M' \times K$ non-zero elements. For Cartesian imaging, (6.1) reduces to $\mathbf{G} = \mathbf{Q}_N$.

In the presence of fieldmap, the MRI system matrix becomes

$$[\mathbf{A}(\boldsymbol{\omega})]_{m',n} = e^{-i2\pi\mathbf{k}(t_{m'}) \cdot \mathbf{p}_n} e^{-i\omega_n t_{m'}}. \quad (6.3)$$

Using time segmentation approximation for L time segments, (6.3) becomes

$$\mathbf{A}(\boldsymbol{\omega}) \approx \sum_{l=1}^L \mathbf{B}_l \mathbf{G} \mathbf{C}_l(\boldsymbol{\omega}) = \mathbf{B} \tilde{\mathbf{G}} \mathbf{C}(\boldsymbol{\omega}), \quad (6.4)$$

where

$$\begin{aligned} \mathbf{B} &\triangleq \begin{bmatrix} \mathbf{B}_1 & \mathbf{B}_2 & \dots & \mathbf{B}_L \end{bmatrix}, \\ \mathbf{C}(\boldsymbol{\omega}) &\triangleq \begin{bmatrix} \mathbf{C}'_1(\boldsymbol{\omega}) & \mathbf{C}'_2(\boldsymbol{\omega}) & \dots & \mathbf{C}'_L(\boldsymbol{\omega}) \end{bmatrix}', \\ \tilde{\mathbf{G}} &\triangleq \mathbf{I}_L \otimes \mathbf{G} \approx (\mathbf{I}_L \otimes \mathbf{P})(\mathbf{I}_L \otimes \mathbf{Q}_K)(\mathbf{I}_L \otimes \mathbf{D}_s), \end{aligned}$$

with $\mathbf{B}_l \triangleq \text{diag}\{b_l(t_{m'})\}$ being the basis of the time segmentation approximation, and $\mathbf{C}_l(\boldsymbol{\omega}) \triangleq \text{diag}\{e^{-i\omega_n t_l}\}$ being the coefficients.

For parallel imaging with J receiver coils, and allowing for acceleration by undersampling k-space, the MRI system matrix becomes

$$\tilde{\mathbf{A}} \triangleq (\mathbf{I}_J \otimes (\mathbf{D}_u \mathbf{A})) \mathbf{S} \approx \tilde{\mathbf{B}} \tilde{\mathbf{D}}_u \tilde{\mathbf{G}} \tilde{\mathbf{C}} \mathbf{S} \quad (6.5)$$

where

$$\begin{aligned}
\mathbf{S} &\triangleq \begin{bmatrix} \mathbf{S}'_1 & \dots & \mathbf{S}'_K \end{bmatrix}', & \tilde{\mathbf{B}} &\triangleq \mathbf{I}_J \otimes \mathbf{B}, & \tilde{\mathbf{C}}(\boldsymbol{\omega}) &\triangleq \mathbf{I}_J \otimes \mathbf{C}(\boldsymbol{\omega}), \\
\check{\mathbf{G}} &\triangleq \mathbf{I}_{JL} \otimes \mathbf{G} \approx \tilde{\mathbf{P}}\tilde{\mathbf{Q}}_K\tilde{\mathbf{D}}_s, & \tilde{\mathbf{D}}_u &\triangleq \mathbf{I}_{JL} \otimes \mathbf{D}_u, & \tilde{\mathbf{P}} &\triangleq \mathbf{I}_{JL} \otimes \mathbf{P}, \\
\tilde{\mathbf{Q}}_K &\triangleq \mathbf{I}_{JL} \otimes \mathbf{Q}_K, & \tilde{\mathbf{D}}_s &\triangleq \mathbf{I}_{JL} \otimes \mathbf{D}_s.
\end{aligned}$$

The matrix \mathbf{D}_u is an $(M \times M')$, with $M \leq M'$ undersampled identity, where the missing rows correspond to the undersampled locations. Also in this case the matrix of time-segmentation coefficients \mathbf{B} is of size $(M \times LM)$ accounting for the undersampling of k-space. For non-Cartesian imaging the undersampling matrix \mathbf{D}_u can be incorporated into the interpolation matrix \mathbf{P} leading to a new interpolation matrix $\check{\mathbf{P}} \triangleq \tilde{\mathbf{D}}_u\tilde{\mathbf{P}}$ of size $(JLM \times JLK)$. From now on the undersampling matrix \mathbf{D}_u will be shown explicitly only in the case of Cartesian MRI.

6.3 System Models

The MRI measurement model for single receiver coil is

$$\mathbf{y} = \mathbf{A}\mathbf{x} + \mathbf{n}, \quad (6.6)$$

where \mathbf{y} is a $(M' \times 1)$ vector and \mathbf{n} is zero mean Gaussian noise vector of the same size. For parallel imaging (J receiver coils)

$$\tilde{\mathbf{y}} = \tilde{\mathbf{A}}\mathbf{x} + \tilde{\mathbf{n}}, \quad (6.7)$$

where $\tilde{\mathbf{y}}$ is a $(JM \times 1)$ vector and $\tilde{\mathbf{n}}$ is zero mean Gaussian noise vector of the same size. In both equations \mathbf{x} is the unknown image vectorized as a $(N \times 1)$ vector.

For image estimation, given a known fieldmap, we can find the estimate by minimizing a regularized cost function as

$$\hat{\mathbf{x}} = \underset{\mathbf{x}}{\operatorname{argmin}} \left\{ \Psi(\mathbf{x}) \triangleq \left\| \tilde{\mathbf{y}} - \tilde{\mathbf{A}}\mathbf{x} \right\|_2^2 + \lambda\Phi(\mathbf{R}\mathbf{x}) \right\}, \quad (6.8)$$

where $\Phi(\cdot)$ is a general regularizer, *e.g.*, l_2 , l_1 , or TV norm and \mathbf{R} is a sparsifying transform, *e.g.*, finite differences or wavelet transform.

For the simpler case of quadratic regularization with finite differences

$$\Phi(\mathbf{R}\mathbf{x}) \triangleq \|\mathbf{R}\mathbf{x}\|_2^2,$$

and solving the optimization problem in (6.8) for this case leads to the well-known closed-form solution

$$\hat{\mathbf{x}} = \left(\tilde{\mathbf{A}}' \tilde{\mathbf{A}} + \lambda \mathbf{R}' \mathbf{R} \right)^{-1} \tilde{\mathbf{A}}' \tilde{\mathbf{y}}. \quad (6.9)$$

The estimate in (6.9) can be easily obtained without the need for iterative algorithms only in the case of Cartesian MRI with a single receiver coil and no fieldmap, *i.e.*, $\tilde{\mathbf{A}} = \mathbf{Q}_N$. For parallel imaging, fieldmap and/or non-Cartesian trajectories a CG iterative solution is required.

If the image \mathbf{x} were known, the fieldmap $\boldsymbol{\omega}$ could be estimated by minimizing the following regularized cost function

$$\hat{\boldsymbol{\omega}} = \operatorname{argmin}_{\boldsymbol{\omega}} \left\{ \Psi(\boldsymbol{\omega}) \triangleq \left\| \mathbf{y} - \tilde{\mathbf{A}}(\boldsymbol{\omega}) \mathbf{x} \right\|_2^2 + \lambda \Phi(\mathbf{R}\boldsymbol{\omega}) \right\}. \quad (6.10)$$

The cost function in (6.10) is non-convex and non-linear in $\boldsymbol{\omega}$, thus a solution is harder to obtain compared to image estimation. One way is to apply gradient descent iterations, that converges slowly [3], or apply a linearization technique [4] and solve using CG iterations. Both methods depend on an accurate choice of the initialization due to the non-convex nature of the cost function.

We focus here on joint estimation of both an unknown image and fieldmap, by minimizing the following regularized cost function

$$[\hat{\mathbf{x}}, \hat{\boldsymbol{\omega}}] = \operatorname{argmin}_{\mathbf{x}, \boldsymbol{\omega}} \left\{ \Psi(\mathbf{x}, \boldsymbol{\omega}) \triangleq \left\| \mathbf{y} - \tilde{\mathbf{A}}(\boldsymbol{\omega}) \mathbf{x} \right\|_2^2 + \lambda_1 \Phi(\mathbf{R}_1 \mathbf{x}) + \lambda_2 \Phi(\mathbf{R}_2 \boldsymbol{\omega}) \right\}. \quad (6.11)$$

The cost function in (6.11) is convex and linear in \mathbf{x} , but non-convex and non-linear in $\boldsymbol{\omega}$. To obtain a solution of the joint estimation problem we applied an alternating minimization scheme, where the updates are given by

$$\begin{aligned} \mathbf{x}^{(k+1)} &= \operatorname{argmin}_{\mathbf{x}} \left\| \tilde{\mathbf{y}} - \tilde{\mathbf{A}}(\boldsymbol{\omega}^{(k)}) \mathbf{x} \right\|_2^2 + \lambda_1 \Phi(\mathbf{R}_1 \mathbf{x}) \\ \boldsymbol{\omega}^{(k+1)} &= \operatorname{argmin}_{\boldsymbol{\omega}} \left\| \tilde{\mathbf{y}} - \tilde{\mathbf{A}}(\boldsymbol{\omega}) \mathbf{x}^{(k+1)} \right\|_2^2 + \lambda_2 \Phi(\mathbf{R}_2 \boldsymbol{\omega}) \end{aligned}$$

The update $\mathbf{x}^{(k+1)}$ can be easily found either directly or using CG iterations. For the update $\boldsymbol{\omega}^{(k+1)}$

one can apply gradient descent [3] or linearization [4, 6], similarly to the fieldmap estimation case in (6.10).

6.4 Image Estimation with Known Fieldmap

For the general case of parallel imaging with non-Cartesian trajectories and the presence of fieldmap, when the NUFFT and time-segmentation approximations are used, the cost function (6.8) becomes

$$\hat{\mathbf{x}} = \underset{\mathbf{x}}{\operatorname{argmin}} \frac{1}{2} \left\| \tilde{\mathbf{y}} - \tilde{\mathbf{B}}\tilde{\mathbf{P}}\tilde{\mathbf{Q}}_K\tilde{\mathbf{D}}_s\tilde{\mathbf{C}}\mathbf{S}\mathbf{x} \right\|_2^2 + \lambda\Phi(\mathbf{R}\mathbf{x}). \quad (6.12)$$

The goal is to decouple the Fourier encoding matrix, the block-diagonal matrices of the time segmentation approximation and sensitivity encoding, the sparse matrix of NUFFT interpolation, and the sparsifying matrix of the regularizer. By choosing auxiliary variables $\mathbf{u}_0 = \mathbf{x}$, $\mathbf{u}_1 = \mathbf{R}\mathbf{u}_0$, $\mathbf{u}_2 = \tilde{\mathbf{Q}}_K\tilde{\mathbf{D}}_s\tilde{\mathbf{C}}\mathbf{S}\mathbf{x}$, the associated AL function of the constrained problem becomes¹

$$\begin{aligned} \mathcal{L}(\mathbf{x}, \mathbf{u}, \boldsymbol{\eta}) &= \frac{1}{2} \left\| \tilde{\mathbf{y}} - \tilde{\mathbf{B}}\tilde{\mathbf{P}}\mathbf{u}_2 \right\|_2^2 + \lambda\Phi(\mathbf{u}_1) + \frac{\mu}{2} \left\| \mathbf{u}_0 - \mathbf{x} - \boldsymbol{\eta}_0 \right\|_2^2 + \frac{\mu\nu_1}{2} \left\| \mathbf{u}_1 - \mathbf{R}\mathbf{u}_0 - \boldsymbol{\eta}_1 \right\|_2^2 \\ &\quad + \frac{\mu\nu_2}{2} \left\| \mathbf{u}_2 - \tilde{\mathbf{Q}}_K\tilde{\mathbf{D}}_s\tilde{\mathbf{C}}\mathbf{S}\mathbf{x} - \boldsymbol{\eta}_2 \right\|_2^2. \end{aligned} \quad (6.13)$$

Solving with an alternating minimization scheme the updates are obtained as

$$\mathbf{u}_0^{(k+1)} = \underset{\mathbf{u}_0}{\operatorname{argmin}} \left\| \mathbf{u}_0 - \mathbf{x}^{(k)} - \boldsymbol{\eta}_0^{(k)} \right\|_2^2 + \nu_1 \left\| \mathbf{u}_1^{(k)} - \mathbf{R}\mathbf{u}_0 - \boldsymbol{\eta}_1^{(k)} \right\|_2^2 \quad (6.14)$$

$$\mathbf{u}_1^{(k+1)} = \underset{\mathbf{u}_1}{\operatorname{argmin}} \tilde{\lambda}\Phi(\mathbf{u}_1) + \frac{1}{2} \left\| \mathbf{u}_1 - \mathbf{R}\mathbf{u}_0^{(k+1)} - \boldsymbol{\eta}_1^{(k)} \right\|_2^2 \quad (6.15)$$

$$\mathbf{u}_2^{(k+1)} = \underset{\mathbf{u}_2}{\operatorname{argmin}} \left\| \tilde{\mathbf{y}} - \tilde{\mathbf{B}}\tilde{\mathbf{P}}\mathbf{u}_2 \right\|_2^2 + \mu\nu_2 \left\| \mathbf{u}_2 - \tilde{\mathbf{Q}}_K\tilde{\mathbf{D}}_s\tilde{\mathbf{C}}\mathbf{S}\mathbf{x}^{(k)} - \boldsymbol{\eta}_2^{(k)} \right\|_2^2 \quad (6.16)$$

$$\mathbf{x}^{(k+1)} = \underset{\mathbf{x}}{\operatorname{argmin}} \left\| \mathbf{u}_0^{(k+1)} - \mathbf{x} - \boldsymbol{\eta}_0^{(k)} \right\|_2^2 + \nu_2 \left\| \mathbf{u}_2^{(k+1)} - \tilde{\mathbf{Q}}_K\tilde{\mathbf{D}}_s\tilde{\mathbf{C}}\mathbf{S}\mathbf{x} - \boldsymbol{\eta}_2^{(k)} \right\|_2^2 \quad (6.17)$$

$$\boldsymbol{\eta}_0^{(k+1)} = \boldsymbol{\eta}_0^{(k)} - \mathbf{u}_0^{(k+1)} + \mathbf{x}^{(k+1)} \quad (6.18)$$

$$\boldsymbol{\eta}_1^{(k+1)} = \boldsymbol{\eta}_1^{(k)} - \mathbf{u}_1^{(k+1)} + \mathbf{R}\mathbf{u}_0^{(k+1)} \quad (6.19)$$

$$\boldsymbol{\eta}_2^{(k+1)} = \boldsymbol{\eta}_2^{(k)} - \mathbf{u}_2^{(k+1)} + \tilde{\mathbf{Q}}_K\tilde{\mathbf{D}}_s\tilde{\mathbf{C}}\mathbf{S}\mathbf{x}^{(k+1)} \quad (6.20)$$

where $\tilde{\lambda} \triangleq \lambda/\mu\nu_1$.

¹The resulting expressions would be of equivalent complexity if we chose the alternative split $\mathbf{u}_2 = \tilde{\mathbf{D}}_s\tilde{\mathbf{C}}\mathbf{S}\mathbf{x}$

In the update for \mathbf{u}_0 both terms are quadratic and the closed form solution is

$$\mathbf{u}_0^{(k+1)} = (\nu_1 \mathbf{R}' \mathbf{R} + \mathbf{I}_N)^{-1} \left[\mathbf{x}^{(k)} + \boldsymbol{\eta}_0^{(k)} + \nu_1 \mathbf{R}' \left(\mathbf{u}_1^{(k)} - \boldsymbol{\eta}_1^{(k)} \right) \right], \quad (6.21)$$

where the inversion can be performed efficiently using FFTs, since $\mathbf{R}' \mathbf{R}$ is circulant.

In the update for \mathbf{u}_1 the form of the solution depends on the choice of regularizer. For l_1 or TV norm the solution reduces to a scalar or vector shrinkage rule as

$$\mathbf{u}_1^{(k+1)} = \text{shrink} \left\{ \mathbf{R} \mathbf{u}_0^{(k+1)} + \boldsymbol{\eta}_1^{(k)}, \tilde{\lambda} \right\}. \quad (6.22)$$

For the simpler l_2 norm regularizer, the solution is

$$\mathbf{u}_1^{(k+1)} = \frac{1}{1 + \tilde{\lambda}} \left(\mathbf{R} \mathbf{u}_0^{(k+1)} + \boldsymbol{\eta}_1^{(k)} \right). \quad (6.23)$$

For the update of \mathbf{u}_2 both terms are quadratic and the closed form solution is

$$\begin{aligned} \mathbf{u}_2^{(k+1)} &= \left(\check{\mathbf{P}}' \tilde{\mathbf{B}} \tilde{\mathbf{B}} \check{\mathbf{P}} + \mu \nu_2 \mathbf{I}_{JLK} \right)^{-1} \tilde{\mathbf{v}}_2^{(k)} \\ &= \frac{1}{\mu \nu_2} \left[\mathbf{I}_{JLK} - \check{\mathbf{P}}' \tilde{\mathbf{B}}' \left(\tilde{\mathbf{B}} \check{\mathbf{P}} \check{\mathbf{P}}' \tilde{\mathbf{B}}' + \mu \nu_2 \mathbf{I}_{JM} \right)^{-1} \tilde{\mathbf{B}} \check{\mathbf{P}} \right] \tilde{\mathbf{v}}_2^{(k)} \\ \tilde{\mathbf{v}}_2^{(k)} &\triangleq \check{\mathbf{P}}' \tilde{\mathbf{B}}' \tilde{\mathbf{y}} + \mu \nu_2 \left(\tilde{\mathbf{Q}}_K \tilde{\mathbf{D}}_s \tilde{\mathbf{C}} \mathbf{S} \mathbf{x}^{(k)} + \boldsymbol{\eta}_2^{(k)} \right). \end{aligned} \quad (6.24)$$

This update requires the inversion of the sparse matrix $\left(\tilde{\mathbf{B}} \check{\mathbf{P}} \check{\mathbf{P}}' \tilde{\mathbf{B}}' + \mu \nu_2 \mathbf{I}_{JM} \right)$. The inversion can be efficient since it only depends on the number of non-zero elements which is in the order of $O(MJ^2)$ and results in a sparse matrix making the resulting matrix-vector multiplication efficient as well.

The update for \mathbf{x} also involves quadratic terms and the solution in closed form is

$$\begin{aligned} \mathbf{x}^{(k+1)} &= \left(\nu_2 \mathbf{S}' \tilde{\mathbf{C}}' \tilde{\mathbf{D}}_s' \tilde{\mathbf{Q}}_K' \tilde{\mathbf{Q}}_K \tilde{\mathbf{D}}_s \tilde{\mathbf{C}} \mathbf{S} + \mathbf{I}_N \right)^{-1} \tilde{\mathbf{v}}_x^{(k)} \\ &= \left(\nu_2 K \mathbf{S}' \tilde{\mathbf{C}}' \tilde{\mathbf{D}}_s' \tilde{\mathbf{D}}_s \tilde{\mathbf{C}} \mathbf{S} + \mathbf{I}_N \right)^{-1} \tilde{\mathbf{v}}_x^{(k)} \\ &= \left(\nu_2 L K \mathbf{S}' \tilde{\mathbf{D}}_s' \tilde{\mathbf{D}}_s \mathbf{S} + \mathbf{I}_N \right)^{-1} \tilde{\mathbf{v}}_x^{(k)} \\ \tilde{\mathbf{v}}_x^{(k)} &\triangleq \mathbf{u}_0^{(k+1)} - \boldsymbol{\eta}_0^{(k)} + \nu_2 \mathbf{S}' \tilde{\mathbf{C}}' \tilde{\mathbf{D}}_s' \tilde{\mathbf{Q}}_K' \left(\mathbf{u}_2^{(k+1)} - \boldsymbol{\eta}_2^{(k)} \right). \end{aligned} \quad (6.25)$$

This update only involves inversion of diagonal matrices ($\mathbf{S}' \tilde{\mathbf{D}}_s' \tilde{\mathbf{D}}_s \mathbf{S}$ is diagonal) and it can be

computed efficiently. The most costly operation is the back projection with the DFT matrix $\tilde{\mathbf{Q}}_K$.

In case that the update for \mathbf{u}_2 cannot be performed efficiently an alternative set of auxiliary variables can be used by defining $\mathbf{u}_0 = \mathbf{x}$, $\mathbf{u}_1 = \mathbf{R}\mathbf{u}_0$, $\mathbf{u}_2 = \check{\mathbf{G}}\mathbf{u}_3$, and $\mathbf{u}_3 = \tilde{\mathbf{C}}\mathbf{S}\mathbf{x}$. Now, the associated AL function of the constrained problem becomes

$$\begin{aligned} \mathcal{L}(\mathbf{x}, \mathbf{u}, \boldsymbol{\eta}) &= \frac{1}{2} \left\| \tilde{\mathbf{y}} - \tilde{\mathbf{B}}\mathbf{u}_2 \right\|_2^2 + \lambda \Phi(\mathbf{u}_1) + \frac{\mu}{2} \left\| \mathbf{u}_0 - \mathbf{x} - \boldsymbol{\eta}_0 \right\|_2^2 + \frac{\mu\nu_1}{2} \left\| \mathbf{u}_1 - \mathbf{R}\mathbf{u}_0 - \boldsymbol{\eta}_1 \right\|_2^2 \\ &\quad + \frac{\mu\nu_2}{2} \left\| \mathbf{u}_2 - \check{\mathbf{G}}\mathbf{u}_3 - \boldsymbol{\eta}_2 \right\|_2^2 + \frac{\mu\nu_3}{2} \left\| \mathbf{u}_3 - \tilde{\mathbf{C}}\mathbf{S}\mathbf{x} - \boldsymbol{\eta}_3 \right\|_2^2. \end{aligned} \quad (6.26)$$

Solving with an alternating minimization scheme the updates for \mathbf{u}_0 , \mathbf{u}_1 , $\boldsymbol{\eta}_0$, and $\boldsymbol{\eta}_1$ are the same as in the previous case shown in (6.21), (6.22), (6.18), and (6.19). The remaining updates are obtained as

$$\mathbf{u}_2^{(k+1)} = \underset{\mathbf{u}_2}{\operatorname{argmin}} \left\| \tilde{\mathbf{y}} - \tilde{\mathbf{B}}\mathbf{u}_2 \right\|_2^2 + \mu\nu_2 \left\| \mathbf{u}_2 - \check{\mathbf{G}}\mathbf{u}_3^{(k)} - \boldsymbol{\eta}_2^{(k)} \right\|_2^2 \quad (6.27)$$

$$\mathbf{u}_3^{(k+1)} = \underset{\mathbf{u}_3}{\operatorname{argmin}} \nu_2 \left\| \mathbf{u}_2^{(k+1)} - \check{\mathbf{G}}\mathbf{u}_3 - \boldsymbol{\eta}_2^{(k)} \right\|_2^2 + \nu_3 \left\| \mathbf{u}_3 - \tilde{\mathbf{C}}\mathbf{S}\mathbf{x}^{(k)} - \boldsymbol{\eta}_3^{(k)} \right\|_2^2 \quad (6.28)$$

$$\mathbf{x}^{(k+1)} = \underset{\mathbf{x}}{\operatorname{argmin}} \left\| \mathbf{u}_0^{(k+1)} - \mathbf{x} - \boldsymbol{\eta}_0^{(k)} \right\|_2^2 + \nu_3 \left\| \mathbf{u}_3^{(k+1)} - \tilde{\mathbf{C}}\mathbf{S}\mathbf{x} - \boldsymbol{\eta}_3^{(k)} \right\|_2^2 \quad (6.29)$$

$$\boldsymbol{\eta}_2^{(k+1)} = \boldsymbol{\eta}_2^{(k)} - \mathbf{u}_2^{(k+1)} + \check{\mathbf{G}}\mathbf{u}_3^{(k+1)} \quad (6.30)$$

$$\boldsymbol{\eta}_3^{(k+1)} = \boldsymbol{\eta}_3^{(k+1)} - \mathbf{u}_3^{(k+1)} + \tilde{\mathbf{C}}\mathbf{S}\mathbf{x}^{(k+1)}. \quad (6.31)$$

For all three updates the minimization terms are quadratic and result to the following closed form solutions.

For the update of \mathbf{u}_2 we have

$$\begin{aligned} \mathbf{u}_2^{(k+1)} &= \left(\tilde{\mathbf{B}}' \tilde{\mathbf{B}} + \mu\nu_2 \mathbf{I}_{JLM} \right)^{-1} \tilde{\mathbf{v}}_2^{(k)} \\ &= \frac{1}{\mu\nu_2} \left[\mathbf{I}_{JLM} - \tilde{\mathbf{B}}' \left(\tilde{\mathbf{B}} \tilde{\mathbf{B}}' + \mu\nu_2 \mathbf{I}_{JM} \right)^{-1} \tilde{\mathbf{B}} \right] \tilde{\mathbf{v}}_2^{(k)} \\ \tilde{\mathbf{v}}_2^{(k)} &\triangleq \tilde{\mathbf{B}}' \tilde{\mathbf{y}} + \mu\nu_2 \left(\check{\mathbf{G}}\mathbf{u}_3^{(k)} + \boldsymbol{\eta}_2^{(k)} \right). \end{aligned} \quad (6.32)$$

This update requires the inversion of a diagonal matrix that can be performed efficiently. The most costly operation is the forward projection with the NUFFT matrix $\check{\mathbf{G}}$.

For the update of \mathbf{u}_3 we have

$$\begin{aligned}\mathbf{u}_3^{(k+1)} &= \left(\nu_2 \check{\mathbf{G}}' \check{\mathbf{G}} + \nu_3 \mathbf{I}_{JLN} \right)^{-1} \tilde{\mathbf{v}}_3^{(k)} \\ \tilde{\mathbf{v}}_3^{(k)} &\triangleq \nu_2 \check{\mathbf{G}}' \left(\mathbf{u}_2^{(k+1)} - \boldsymbol{\eta}_2^{(k)} \right) + \nu_3 \left(\check{\mathbf{C}} \mathbf{S} \mathbf{x}^{(k)} + \boldsymbol{\eta}_3^{(k)} \right).\end{aligned}\quad (6.33)$$

For this update the Hessian $\check{\mathbf{G}}' \check{\mathbf{G}}$ is block-Toeplitz but not circulant, thus exact inversion cannot be performed efficiently. However, an inexact update can be obtained efficiently using PCG with a circulant preconditioner and warm starting. An alternative way of finding such an update is presented in [10].

Finally, for the update of \mathbf{x} we have

$$\begin{aligned}\mathbf{x}^{(k+1)} &= \left(\nu_3 \mathbf{S}' \check{\mathbf{C}}' \check{\mathbf{C}} \mathbf{S} + \mathbf{I}_N \right)^{-1} \tilde{\mathbf{v}}_x^{(k)} \\ &= \left(\nu_3 L \mathbf{S}' \mathbf{S} + \mathbf{I}_N \right)^{-1} \tilde{\mathbf{v}}_x^{(k)} \\ \tilde{\mathbf{v}}_x^{(k)} &\triangleq \mathbf{u}_0^{(k+1)} - \boldsymbol{\eta}_0^{(k)} + \nu_3 \mathbf{S}' \check{\mathbf{C}}' \left(\mathbf{u}_3^{(k+1)} - \boldsymbol{\eta}_3^{(k)} \right).\end{aligned}\quad (6.34)$$

This update only involves inversion of diagonal matrices ($\mathbf{S}' \mathbf{S}$ is diagonal) and it can be computed efficiently. Also all other operations involve block-diagonal matrices and thus, they can be performed in linear time.

Another alternative is to choose the auxiliary variables $\mathbf{u}_0 = \mathbf{x}$, $\mathbf{u}_1 = \mathbf{R} \mathbf{u}_0$, $\mathbf{u}_2 = \check{\mathbf{P}} \mathbf{u}_3$, and $\mathbf{u}_3 = \check{\mathbf{Q}}_K \check{\mathbf{D}}_s \check{\mathbf{C}} \mathbf{S} \mathbf{x}$. Now, the associated AL function of the constrained problem becomes

$$\begin{aligned}\mathcal{L}(\mathbf{x}, \mathbf{u}, \boldsymbol{\eta}) &= \frac{1}{2} \left\| \tilde{\mathbf{y}} - \check{\mathbf{B}} \mathbf{u}_2 \right\|_2^2 + \lambda \Phi(\mathbf{u}_1) + \frac{\mu}{2} \left\| \mathbf{u}_0 - \mathbf{x} - \boldsymbol{\eta}_0 \right\|_2^2 + \frac{\mu \nu_1}{2} \left\| \mathbf{u}_1 - \mathbf{R} \mathbf{u}_0 - \boldsymbol{\eta}_1 \right\|_2^2 \\ &\quad + \frac{\mu \nu_2}{2} \left\| \mathbf{u}_2 - \check{\mathbf{P}} \mathbf{u}_3 - \boldsymbol{\eta}_2 \right\|_2^2 + \frac{\mu \nu_3}{2} \left\| \mathbf{u}_3 - \check{\mathbf{Q}}_K \check{\mathbf{D}}_s \check{\mathbf{C}} \mathbf{S} \mathbf{x} - \boldsymbol{\eta}_3 \right\|_2^2.\end{aligned}\quad (6.35)$$

Solving with an alternating minimization scheme the updates for \mathbf{u}_0 , \mathbf{u}_1 , $\boldsymbol{\eta}_0$, and $\boldsymbol{\eta}_1$ are the same

as in the previous case. The remaining updates are obtained as

$$\mathbf{u}_2^{(k+1)} = \underset{\mathbf{u}_2}{\operatorname{argmin}} \left\| \tilde{\mathbf{y}} - \tilde{\mathbf{B}}\mathbf{u}_2 \right\|_2^2 + \mu\nu_2 \left\| \mathbf{u}_2 - \check{\mathbf{P}}\mathbf{u}_3^{(k)} - \boldsymbol{\eta}_2^{(k)} \right\|_2^2 \quad (6.36)$$

$$\mathbf{u}_3^{(k+1)} = \underset{\mathbf{u}_3}{\operatorname{argmin}} \nu_2 \left\| \mathbf{u}_2^{(k+1)} - \check{\mathbf{P}}\mathbf{u}_3 - \boldsymbol{\eta}_2^{(k)} \right\|_2^2 + \nu_3 \left\| \mathbf{u}_3 - \tilde{\mathbf{Q}}_K \tilde{\mathbf{D}}_s \tilde{\mathbf{C}}\mathbf{S}\mathbf{x}^{(k)} - \boldsymbol{\eta}_3^{(k)} \right\|_2^2 \quad (6.37)$$

$$\mathbf{x}^{(k+1)} = \underset{\mathbf{x}}{\operatorname{argmin}} \left\| \mathbf{u}_0^{(k+1)} - \mathbf{x} - \boldsymbol{\eta}_0^{(k)} \right\|_2^2 + \nu_3 \left\| \mathbf{u}_3^{(k+1)} - \tilde{\mathbf{Q}}_K \tilde{\mathbf{D}}_s \tilde{\mathbf{C}}\mathbf{S}\mathbf{x} - \boldsymbol{\eta}_3^{(k)} \right\|_2^2 \quad (6.38)$$

$$\boldsymbol{\eta}_2^{(k+1)} = \boldsymbol{\eta}_2^{(k)} - \mathbf{u}_2^{(k+1)} + \check{\mathbf{P}}\mathbf{u}_3^{(k+1)} \quad (6.39)$$

$$\boldsymbol{\eta}_3^{(k+1)} = \boldsymbol{\eta}_3^{(k+1)} - \mathbf{u}_3^{(k+1)} + \tilde{\mathbf{Q}}_K \tilde{\mathbf{D}}_s \tilde{\mathbf{C}}\mathbf{S}\mathbf{x}^{(k+1)}. \quad (6.40)$$

For all three updates the minimization terms are quadratic and result to the following closed form solutions.

For the update of \mathbf{u}_2 we have

$$\begin{aligned} \mathbf{u}_2^{(k+1)} &= \left(\tilde{\mathbf{B}}' \tilde{\mathbf{B}} + \mu\nu_2 \mathbf{I}_{JLM} \right)^{-1} \tilde{\mathbf{v}}_2^{(k)} \\ &= \frac{1}{\mu\nu_2} \left[\mathbf{I}_{JLM} - \tilde{\mathbf{B}}' \left(\tilde{\mathbf{B}} \tilde{\mathbf{B}}' + \mu\nu_2 \mathbf{I}_{JM} \right)^{-1} \tilde{\mathbf{B}} \right] \tilde{\mathbf{v}}_2^{(k)} \\ \tilde{\mathbf{v}}_2^{(k)} &\triangleq \tilde{\mathbf{B}}' \tilde{\mathbf{y}} + \mu\nu_2 \left(\check{\mathbf{P}}\mathbf{u}_3^{(k)} + \boldsymbol{\eta}_2^{(k)} \right). \end{aligned} \quad (6.41)$$

This update requires the inversion of a diagonal matrix that can be performed efficiently. The most costly operation is the forward projection with the interpolation matrix $\check{\mathbf{P}}$.

For the update of \mathbf{u}_3 we have

$$\begin{aligned} \mathbf{u}_3^{(k+1)} &= \left(\nu_2 \check{\mathbf{P}}' \check{\mathbf{P}} + \nu_3 \mathbf{I}_{JLN} \right)^{-1} \tilde{\mathbf{v}}_3^{(k)} \\ \tilde{\mathbf{v}}_3^{(k)} &\triangleq \nu_2 \check{\mathbf{P}}' \left(\mathbf{u}_2^{(k+1)} - \boldsymbol{\eta}_2^{(k)} \right) + \nu_3 \left(\tilde{\mathbf{Q}}_K \tilde{\mathbf{D}}_s \tilde{\mathbf{C}}\mathbf{S}\mathbf{x}^{(k)} + \boldsymbol{\eta}_3^{(k)} \right). \end{aligned} \quad (6.42)$$

For this update the Hessian $\check{\mathbf{P}}' \check{\mathbf{P}}$ is sparse so the inverse could be computed efficiently. If this is not possible, an inexact update can be obtained efficiently using PCG with a circulant preconditioner and warm starting.

Finally, for the update of \mathbf{x} we have

$$\begin{aligned}
\mathbf{x}^{(k+1)} &= \left(\nu_3 \mathbf{S}' \tilde{\mathbf{C}}' \tilde{\mathbf{D}}_s' \tilde{\mathbf{Q}}_K' \tilde{\mathbf{Q}}_K \tilde{\mathbf{D}}_s \tilde{\mathbf{C}} \mathbf{S} + \mathbf{I}_N \right)^{-1} \tilde{\mathbf{v}}_x^{(k)} \\
&= \left(\nu_3 L K \mathbf{S}' \tilde{\mathbf{D}}_s' \tilde{\mathbf{D}}_s \mathbf{S} + \mathbf{I}_N \right)^{-1} \tilde{\mathbf{v}}_x^{(k)} \\
\tilde{\mathbf{v}}_x^{(k)} &\triangleq \mathbf{u}_0^{(k+1)} - \boldsymbol{\eta}_0^{(k)} + \nu_3 \mathbf{S}' \tilde{\mathbf{C}}' \tilde{\mathbf{D}}_s' \tilde{\mathbf{Q}}_K' \left(\mathbf{u}_3^{(k+1)} - \boldsymbol{\eta}_3^{(k)} \right).
\end{aligned} \tag{6.43}$$

This update only involves inversion of diagonal matrices ($\mathbf{S}' \tilde{\mathbf{D}}_s' \tilde{\mathbf{D}}_s \mathbf{S}$ is diagonal) and it can be computed efficiently. Also all other operations involve block-diagonal matrices and thus, they can be performed in linear time.

In the following subsections we will present some important special cases of the image estimation problem, namely quadratic regularization, Cartesian imaging, and single receiver coil imaging.

6.4.1 Quadratic Regularization

For quadratic regularization the cost function (6.8) becomes

$$\hat{\mathbf{x}} = \underset{\mathbf{x}}{\operatorname{argmin}} \left\| \tilde{\mathbf{y}} - \tilde{\mathbf{B}} \tilde{\mathbf{P}} \tilde{\mathbf{Q}}_K \tilde{\mathbf{D}}_s \tilde{\mathbf{C}} \mathbf{S} \mathbf{x} \right\|_2^2 + \lambda \|\mathbf{R} \mathbf{x}\|_2^2. \tag{6.44}$$

In this case the auxiliary variable $\mathbf{u}_1 = \mathbf{R} \mathbf{u}_0$ is not required and the associated AL function becomes

$$\mathcal{L}(\mathbf{x}, \mathbf{u}, \boldsymbol{\eta}) = \left\| \tilde{\mathbf{y}} - \tilde{\mathbf{B}} \tilde{\mathbf{P}} \mathbf{u}_2 \right\|_2^2 + \lambda \|\mathbf{R} \mathbf{u}_0\|_2^2 + \mu \|\mathbf{u}_0 - \mathbf{x} - \boldsymbol{\eta}_0\|_2^2 + \mu \nu_2 \left\| \mathbf{u}_2 - \tilde{\mathbf{Q}}_K \tilde{\mathbf{D}}_s \tilde{\mathbf{C}} \mathbf{S} \mathbf{x} - \boldsymbol{\eta}_2 \right\|_2^2 \tag{6.45}$$

for the first choice of auxiliary variables, or

$$\begin{aligned}
\mathcal{L}(\mathbf{x}, \mathbf{u}, \boldsymbol{\eta}) &= \left\| \tilde{\mathbf{y}} - \tilde{\mathbf{B}} \mathbf{u}_2 \right\|_2^2 + \lambda \|\mathbf{R} \mathbf{u}_0\|_2^2 + \mu \|\mathbf{u}_0 - \mathbf{x} - \boldsymbol{\eta}_0\|_2^2 + \mu \nu_2 \left\| \mathbf{u}_2 - \tilde{\mathbf{G}} \mathbf{u}_3 - \boldsymbol{\eta}_2 \right\|_2^2 \\
&\quad + \mu \nu_3 \left\| \mathbf{u}_3 - \tilde{\mathbf{C}} \mathbf{S} \mathbf{x} - \boldsymbol{\eta}_3 \right\|_2^2
\end{aligned} \tag{6.46}$$

for the alternative choice.

The only thing that changes are the updates of \mathbf{u}_0 and $\boldsymbol{\eta}_0$ which are expressed as

$$\mathbf{u}_0^{(k+1)} = \underset{\mathbf{u}_0}{\operatorname{argmin}} \lambda \|\mathbf{R}\mathbf{u}_0\|_2^2 + \mu \left\| \mathbf{u}_0 - \mathbf{x}^{(k)} - \boldsymbol{\eta}_0^{(k)} \right\|_2^2 \quad (6.47)$$

$$\boldsymbol{\eta}_0^{(k+1)} = \boldsymbol{\eta}_0^{(k)} - \mathbf{u}_0^{(k+1)} + \mathbf{x}^{(k+1)}. \quad (6.48)$$

Now, the closed form solution for the update of \mathbf{u}_0 is

$$\mathbf{u}_0^{(k+1)} = (\lambda \mathbf{R}'\mathbf{R} + \mu \mathbf{I}_N)^{-1} \left[\mu \left(\mathbf{x}^{(k)} + \boldsymbol{\eta}_0^{(k)} \right) \right], \quad (6.49)$$

and it can be computed exactly, since the Hessian is circulant ($\mathbf{R}'\mathbf{R}$ is circulant) and inversion can be performed efficiently using FFTs.

6.4.2 Cartesian MRI

For Cartesian MRI the encoding matrix reduces to $\tilde{\mathbf{G}} = \tilde{\mathbf{Q}}_{M,N} \triangleq \tilde{\mathbf{D}}_{\mathbf{u}} \tilde{\mathbf{Q}}_N$ ($\tilde{\mathbf{Q}}_{M,N}$ is an under-sampled FFT matrix of size $M \times N$) and the cost function (6.8) becomes

$$\hat{\mathbf{x}} = \underset{\mathbf{x}}{\operatorname{argmin}} \frac{1}{2} \left\| \tilde{\mathbf{y}} - \tilde{\mathbf{B}} \tilde{\mathbf{Q}}_{M,N} \tilde{\mathbf{C}} \mathbf{S} \mathbf{x} \right\|_2^2 + \lambda \Phi(\mathbf{R} \mathbf{x}). \quad (6.50)$$

By choosing auxiliary variables $\mathbf{u}_0 = \mathbf{x}$, $\mathbf{u}_1 = \mathbf{R}\mathbf{u}_0$, $\mathbf{u}_2 = \tilde{\mathbf{C}}\mathbf{S}\mathbf{x}$, the associated AL function of the constrained problem becomes²

$$\begin{aligned} \mathcal{L}(\mathbf{x}, \mathbf{u}, \boldsymbol{\eta}) &= \frac{1}{2} \left\| \tilde{\mathbf{y}} - \tilde{\mathbf{B}} \tilde{\mathbf{Q}}_{M,N} \mathbf{u}_2 \right\|_2^2 + \lambda \Phi(\mathbf{u}_1) + \frac{\mu}{2} \left\| \mathbf{u}_0 - \mathbf{x} - \boldsymbol{\eta}_0 \right\|_2^2 \\ &\quad + \frac{\mu\nu_1}{2} \left\| \mathbf{u}_1 - \mathbf{R}\mathbf{u}_0 - \boldsymbol{\eta}_1 \right\|_2^2 + \frac{\mu\nu_2}{2} \left\| \mathbf{u}_2 - \tilde{\mathbf{C}}\mathbf{S}\mathbf{x} - \boldsymbol{\eta}_2 \right\|_2^2. \end{aligned} \quad (6.51)$$

The updates for \mathbf{u}_0 , $\boldsymbol{\eta}_0$, \mathbf{u}_1 , and $\boldsymbol{\eta}_1$ are the same as in the previous section in (6.21), (6.18), (6.22), and (6.19) respectively. The remaining updates for \mathbf{u}_2 , $\boldsymbol{\eta}_2$, and \mathbf{x} are obtained as

$$\mathbf{u}_2^{(k+1)} = \underset{\mathbf{u}_2}{\operatorname{argmin}} \left\| \tilde{\mathbf{y}} - \tilde{\mathbf{B}} \tilde{\mathbf{Q}}_{M,N} \mathbf{u}_2 \right\|_2^2 + \mu\nu_2 \left\| \mathbf{u}_2 - \tilde{\mathbf{C}}\mathbf{S}\mathbf{x}^{(k)} - \boldsymbol{\eta}_2^{(k)} \right\|_2^2 \quad (6.52)$$

$$\mathbf{x}^{(k+1)} = \underset{\mathbf{x}}{\operatorname{argmin}} \left\| \mathbf{u}_0^{(k+1)} - \mathbf{x} - \boldsymbol{\eta}_0^{(k)} \right\|_2^2 + \nu_2 \left\| \mathbf{u}_2^{(k+1)} - \tilde{\mathbf{C}}\mathbf{S}\mathbf{x} - \boldsymbol{\eta}_2^{(k)} \right\|_2^2 \quad (6.53)$$

$$\boldsymbol{\eta}_2^{(k+1)} = \boldsymbol{\eta}_2^{(k)} - \mathbf{u}_2^{(k+1)} + \tilde{\mathbf{C}}\mathbf{S}\mathbf{x}^{(k+1)}. \quad (6.54)$$

²Choosing $\mathbf{u}_2 = \tilde{\mathbf{C}}\mathbf{S}\mathbf{x}$ is more beneficial compared to the choice $\mathbf{u}_2 = \tilde{\mathbf{Q}}_N \tilde{\mathbf{C}}\mathbf{S}\mathbf{x}$, since the projection with $\tilde{\mathbf{Q}}_{M,N} \triangleq \tilde{\mathbf{D}}_{\mathbf{u}} \tilde{\mathbf{Q}}_N$ can be performed as one operation of an undersampled FFT in $O(M \log N)$

For the update of \mathbf{u}_2 both terms are quadratic and the closed form solution is

$$\begin{aligned}
\mathbf{u}_2^{(k+1)} &= \left(\tilde{\mathbf{Q}}'_{M,N} \tilde{\mathbf{B}}' \tilde{\mathbf{B}} \tilde{\mathbf{Q}}_{M,N} + \mu \nu_2 \mathbf{I}_{JLN} \right)^{-1} \tilde{\mathbf{v}}_2^{(k)} \\
&= \frac{1}{\mu \nu_2} \left[\mathbf{I}_{JLN} - \tilde{\mathbf{Q}}'_{M,N} \tilde{\mathbf{B}}' \left(N \tilde{\mathbf{B}} \tilde{\mathbf{B}}' + \mu \nu_2 \mathbf{I}_{JM} \right)^{-1} \tilde{\mathbf{B}} \tilde{\mathbf{Q}}_{M,N} \right] \tilde{\mathbf{v}}_2^{(k)} \\
\tilde{\mathbf{v}}_2^{(k)} &\triangleq \tilde{\mathbf{Q}}'_{M,N} \tilde{\mathbf{B}}' \tilde{\mathbf{y}} + \mu \nu_2 \left(\tilde{\mathbf{C}} \mathbf{S} \mathbf{x}^{(k)} + \boldsymbol{\eta}_2^{(k)} \right).
\end{aligned} \tag{6.55}$$

This update can be computed exactly, since it only requires the inversion of diagonal matrices ($\tilde{\mathbf{B}} \tilde{\mathbf{B}}'$ is diagonal). The most costly operations are the multiplications with $\tilde{\mathbf{Q}}_{M,N}$ that can be performed efficiently in $O(LM \log N)$, since they correspond to undersampled FFT operations.

The update for \mathbf{x} also involves quadratic terms and the solution in closed form is

$$\begin{aligned}
\mathbf{x}^{(k+1)} &= \left(\nu_2 \mathbf{S}' \tilde{\mathbf{C}}' \tilde{\mathbf{C}} \mathbf{S} + \mathbf{I}_N \right)^{-1} \tilde{\mathbf{v}}_x^{(k)} \\
&= \left(\nu_2 L \mathbf{S}' \mathbf{S} + \mathbf{I}_N \right)^{-1} \tilde{\mathbf{v}}_x^{(k)} \\
\tilde{\mathbf{v}}_x^{(k)} &\triangleq \mathbf{u}_0^{(k+1)} - \boldsymbol{\eta}_0^{(k)} + \nu_2 \mathbf{S}' \tilde{\mathbf{C}}' \left(\mathbf{u}_2^{(k+1)} - \boldsymbol{\eta}_2^{(k)} \right).
\end{aligned} \tag{6.56}$$

This update only involves inversion of diagonal matrices ($\mathbf{S}' \tilde{\mathbf{D}}_s' \tilde{\mathbf{D}}_s \mathbf{S}$ is diagonal) and it can be computed efficiently. All remaining operations also involve block-diagonal matrices and they can be computed in linear time.

6.4.3 Single Coil Imaging

When a single receiver coil is used the sensitivity matrix reduces to $\mathbf{S} = \mathbf{I}_N$. For non-Cartesian imaging this simplification does not lead to a form with reduced number of auxiliary variables, thus the solutions of the previous sections can be applied with the simple substitution of $\mathbf{S} = \mathbf{I}_N$. However, for the case of Cartesian imaging further simplifications are possible. In this case the encoding matrix reduces to $\tilde{\mathbf{G}} = \tilde{\mathbf{Q}}_N$, with $J = 1$ and there is no undersampling ($\tilde{\mathbf{D}}_u = \mathbf{I}_{LN}$). Thus, the cost function (6.8) becomes

$$\hat{\mathbf{x}} = \underset{\mathbf{x}}{\operatorname{argmin}} \frac{1}{2} \left\| \mathbf{y} - \mathbf{B} \tilde{\mathbf{Q}}_N \mathbf{C} \mathbf{x} \right\|_2^2 + \lambda \Phi(\mathbf{R} \mathbf{x}). \tag{6.57}$$

By choosing auxiliary variables $\mathbf{u}_1 = \mathbf{R}\mathbf{x}$, and $\mathbf{u}_2 = \mathbf{C}\mathbf{x}$, the associated AL function of the constrained problem becomes³

$$\mathcal{L}(\mathbf{x}, \mathbf{u}, \boldsymbol{\eta}) = \frac{1}{2} \left\| \mathbf{y} - \mathbf{B}\tilde{\mathbf{Q}}_N \mathbf{u}_2 \right\|_2^2 + \lambda \Phi(\mathbf{u}_1) + \frac{\mu}{2} \left\| \mathbf{u}_1 - \mathbf{R}\mathbf{x} - \boldsymbol{\eta}_1 \right\|_2^2 + \frac{\mu\nu}{2} \left\| \mathbf{u}_2 - \mathbf{C}\mathbf{x} - \boldsymbol{\eta}_2 \right\|_2^2. \quad (6.58)$$

Solving with an alternating minimization scheme the updates are obtained as

$$\mathbf{u}_1^{(k+1)} = \underset{\mathbf{u}_1}{\operatorname{argmin}} \tilde{\lambda} \Phi(\mathbf{u}_1) + \frac{1}{2} \left\| \mathbf{u}_1 - \mathbf{R}\mathbf{x}^{(k)} - \boldsymbol{\eta}_1^{(k)} \right\|_2^2 \quad (6.59)$$

$$\mathbf{u}_2^{(k+1)} = \underset{\mathbf{u}_2}{\operatorname{argmin}} \left\| \mathbf{y} - \mathbf{B}\tilde{\mathbf{Q}}_N \mathbf{u}_2 \right\|_2^2 + \mu\nu \left\| \mathbf{u}_2 - \mathbf{C}\mathbf{x}^{(k)} - \boldsymbol{\eta}_2^{(k)} \right\|_2^2 \quad (6.60)$$

$$\mathbf{x}^{(k+1)} = \underset{\mathbf{x}}{\operatorname{argmin}} \left\| \mathbf{u}_1^{(k+1)} - \mathbf{R}\mathbf{x} - \boldsymbol{\eta}_1^{(k)} \right\|_2^2 + \nu \left\| \mathbf{u}_2^{(k+1)} - \mathbf{C}\mathbf{x} - \boldsymbol{\eta}_2^{(k)} \right\|_2^2 \quad (6.61)$$

$$\boldsymbol{\eta}_1^{(k+1)} = \boldsymbol{\eta}_1^{(k)} - \mathbf{u}_1^{(k+1)} + \mathbf{R}\mathbf{x}^{(k+1)} \quad (6.62)$$

$$\boldsymbol{\eta}_2^{(k+1)} = \boldsymbol{\eta}_2^{(k)} - \mathbf{u}_2^{(k+1)} + \mathbf{C}\mathbf{x}^{(k+1)} \quad (6.63)$$

where $\tilde{\lambda} \triangleq \lambda/\mu$.

In the update for \mathbf{u}_1 the form of the solution depends on the choice of regularizer. For l_1 or TV norm the solution reduces to a scalar or vector shrinkage rule as

$$\mathbf{u}_1^{(k+1)} = \operatorname{shrink} \left\{ \mathbf{R}\mathbf{x}^{(k)} + \boldsymbol{\eta}_1^{(k)}, \tilde{\lambda} \right\}. \quad (6.64)$$

For the simpler l_2 norm regularizer, the solution is

$$\mathbf{u}_1^{(k+1)} = \frac{1}{1 + \tilde{\lambda}} \left(\mathbf{R}\mathbf{x}^{(k)} + \boldsymbol{\eta}_1^{(k)} \right). \quad (6.65)$$

For the update of \mathbf{u}_2 both terms are quadratic and the closed form solution is

$$\begin{aligned} \mathbf{u}_2^{(k+1)} &= \left(\tilde{\mathbf{Q}}_N' \mathbf{B}' \mathbf{B} \tilde{\mathbf{Q}}_N + \mu\nu \mathbf{I}_{LN} \right)^{-1} \mathbf{v}_2^{(k)} \\ &= \frac{1}{\mu\nu} \left[\mathbf{I}_{LN} - \tilde{\mathbf{Q}}_N' \mathbf{B}' (N\mathbf{B}\mathbf{B}' + \mu\nu \mathbf{I}_N)^{-1} \mathbf{B} \tilde{\mathbf{Q}}_N \right] \mathbf{v}_2^{(k)} \\ \mathbf{v}_2^{(k)} &\triangleq \tilde{\mathbf{Q}}_N' \mathbf{B}' \mathbf{y} + \mu\nu \left(\mathbf{C}\mathbf{x}^{(k)} + \boldsymbol{\eta}_2^{(k)} \right). \end{aligned} \quad (6.66)$$

This update can be computed exactly, since it only requires the inversion of diagonal matrices

³The resulting expressions would be of equivalent complexity if we chose the alternative split $\mathbf{u}_2 = \tilde{\mathbf{Q}}_N \mathbf{C}\mathbf{x}$

($\mathbf{B}\mathbf{B}'$ is diagonal). The most costly operations are the forward and back projections with $\tilde{\mathbf{Q}}_N$ that can be performed efficiently in $O(LN \log N)$, since they correspond to FFT operations.

The update for \mathbf{x} also involves quadratic terms and the solution in closed form is

$$\begin{aligned}\mathbf{x}^{(k+1)} &= (\mathbf{R}'\mathbf{R} + \nu\mathbf{C}'\mathbf{C})^{-1} \mathbf{v}_x^{(k)} \\ &= (\mathbf{R}'\mathbf{R} + \nu L\mathbf{I}_N)^{-1} \mathbf{v}_x^{(k)} \\ \mathbf{v}_x^{(k)} &\triangleq \mathbf{R}' \left(\mathbf{u}_1^{(k+1)} - \boldsymbol{\eta}_1^{(k)} \right) + \nu\mathbf{C}' \left(\mathbf{u}_2^{(k+1)} - \boldsymbol{\eta}_2^{(k)} \right).\end{aligned}\tag{6.67}$$

This update is exact since the Hessian is circulant ($\mathbf{R}'\mathbf{R}$ is circulant) and can be inverted efficiently using FFTs.

6.5 Fieldmap Estimation with Known Image

For the general case of parallel imaging with non-Cartesian trajectories and the presence of fieldmap, when the NUFFT and time-segmentation approximations are used, the cost function (6.10) becomes

$$\hat{\boldsymbol{\omega}} = \underset{\boldsymbol{\omega}}{\operatorname{argmin}} \frac{1}{2} \left\| \tilde{\mathbf{y}} - \tilde{\mathbf{B}}\tilde{\mathbf{P}}\tilde{\mathbf{Q}}_K\tilde{\mathbf{D}}_s\tilde{\mathbf{C}}(\boldsymbol{\omega})\mathbf{S}\mathbf{x} \right\|_2^2 + \lambda\Phi(\mathbf{R}\boldsymbol{\omega}).\tag{6.68}$$

The goal is to decouple the time segmentation coefficient matrix $\tilde{\mathbf{C}}(\boldsymbol{\omega})$ from the encoding and sparsifying matrix. By choosing auxiliary variables $\mathbf{u}_0 = \boldsymbol{\omega}$, $\mathbf{u}_1 = \mathbf{R}\mathbf{u}_0$, $\mathbf{u}_2 = \tilde{\mathbf{G}}\mathbf{u}_3$ and $\mathbf{u}_3 = \tilde{\mathbf{C}}(\boldsymbol{\omega})\mathbf{S}\mathbf{x}$, the associated AL function of the constrained problem becomes

$$\begin{aligned}\mathcal{L}(\boldsymbol{\omega}, \mathbf{u}, \boldsymbol{\eta}) &= \frac{1}{2} \left\| \tilde{\mathbf{y}} - \tilde{\mathbf{B}}\mathbf{u}_2 \right\|_2^2 + \lambda\Phi(\mathbf{u}_1) + \frac{\mu}{2} \left\| \mathbf{u}_0 - \boldsymbol{\omega} - \boldsymbol{\eta}_0 \right\|_2^2 + \frac{\mu\nu_1}{2} \left\| \mathbf{u}_1 - \mathbf{R}\mathbf{u}_0 - \boldsymbol{\eta}_1 \right\|_2^2 \\ &\quad + \frac{\mu\nu_2}{2} \left\| \mathbf{u}_2 - \tilde{\mathbf{G}}\mathbf{u}_3 - \boldsymbol{\eta}_2 \right\|_2^2 + \frac{\mu\nu_3}{2} \left\| \mathbf{u}_3 - \tilde{\mathbf{C}}(\boldsymbol{\omega})\mathbf{S}\mathbf{x} - \boldsymbol{\eta}_3 \right\|_2^2.\end{aligned}\tag{6.69}$$

Solving with an alternating minimization scheme the updates are obtained as

$$\mathbf{u}_0^{(k+1)} = \underset{\mathbf{u}_0}{\operatorname{argmin}} \left\| \mathbf{u}_0 - \boldsymbol{\omega}^{(k)} - \boldsymbol{\eta}_0^{(k)} \right\|_2^2 + \nu_1 \left\| \mathbf{u}_1^{(k)} - \mathbf{R}\mathbf{u}_0 - \boldsymbol{\eta}_1^{(k)} \right\|_2^2 \quad (6.70)$$

$$\mathbf{u}_1^{(k+1)} = \underset{\mathbf{u}_1}{\operatorname{argmin}} \tilde{\lambda} \Phi(\mathbf{u}_1) + \frac{1}{2} \left\| \mathbf{u}_1 - \mathbf{R}\mathbf{u}_0^{(k+1)} - \boldsymbol{\eta}_1^{(k)} \right\|_2^2 \quad (6.71)$$

$$\mathbf{u}_2^{(k+1)} = \underset{\mathbf{u}_2}{\operatorname{argmin}} \left\| \tilde{\mathbf{y}} - \tilde{\mathbf{B}}\mathbf{u}_2 \right\|_2^2 + \mu\nu_2 \left\| \mathbf{u}_2 - \check{\mathbf{G}}\mathbf{u}_3^{(k)} - \boldsymbol{\eta}_2^{(k)} \right\|_2^2 \quad (6.72)$$

$$\mathbf{u}_3^{(k+1)} = \underset{\mathbf{u}_3}{\operatorname{argmin}} \nu_2 \left\| \mathbf{u}_2^{(k+1)} - \check{\mathbf{G}}\mathbf{u}_3 - \boldsymbol{\eta}_2^{(k)} \right\|_2^2 + \nu_3 \left\| \mathbf{u}_3 - \tilde{\mathbf{C}}(\boldsymbol{\omega}^{(k)}) \mathbf{S}\mathbf{x} - \boldsymbol{\eta}_3^{(k)} \right\|_2^2 \quad (6.73)$$

$$\boldsymbol{\omega}^{(k+1)} = \underset{\boldsymbol{\omega}}{\operatorname{argmin}} \left\| \mathbf{u}_0^{(k+1)} - \boldsymbol{\omega} - \boldsymbol{\eta}_0^{(k)} \right\|_2^2 + \nu_3 \left\| \mathbf{u}_3^{(k+1)} - \tilde{\mathbf{C}}(\boldsymbol{\omega}) \mathbf{S}\mathbf{x} - \boldsymbol{\eta}_3^{(k)} \right\|_2^2 \quad (6.74)$$

$$\boldsymbol{\eta}_0^{(k+1)} = \boldsymbol{\eta}_0^{(k)} - \mathbf{u}_0^{(k+1)} + \boldsymbol{\omega}^{(k+1)} \quad (6.75)$$

$$\boldsymbol{\eta}_1^{(k+1)} = \boldsymbol{\eta}_1^{(k)} - \mathbf{u}_1^{(k+1)} + \mathbf{R}\mathbf{u}_0^{(k+1)} \quad (6.76)$$

$$\boldsymbol{\eta}_2^{(k+1)} = \boldsymbol{\eta}_2^{(k)} - \mathbf{u}_2^{(k+1)} + \check{\mathbf{G}}\mathbf{u}_3^{(k+1)} \quad (6.77)$$

$$\boldsymbol{\eta}_3^{(k+1)} = \boldsymbol{\eta}_3^{(k)} - \mathbf{u}_3^{(k+1)} + \tilde{\mathbf{C}}(\boldsymbol{\omega}^{(k+1)}) \mathbf{S}\mathbf{x}. \quad (6.78)$$

where $\tilde{\lambda} \triangleq \lambda/\mu\nu_1$.

The update for \mathbf{u}_0 is given by

$$\mathbf{u}_0^{(k+1)} = (\nu_1 \mathbf{R}'\mathbf{R} + \mathbf{I}_N)^{-1} \left[\left(\boldsymbol{\omega}^{(k)} + \boldsymbol{\eta}_0^{(k)} \right) + \nu_1 \mathbf{R}' \left(\mathbf{u}_1^{(k)} - \boldsymbol{\eta}_1^{(k)} \right) \right]. \quad (6.79)$$

The update is exact since $\mathbf{R}'\mathbf{R}$ is circulant and the inverse is computed efficiently with FFTs.

In the update for \mathbf{u}_1 the form of the solution depends on the choice of regularizer. For l_1 or TV norm the solution reduces to a scalar or vector shrinkage rule as

$$\mathbf{u}_1^{(k+1)} = \operatorname{shrink} \left\{ \mathbf{R}\mathbf{u}_0^{(k+1)} + \boldsymbol{\eta}_1^{(k)}, \tilde{\lambda} \right\}. \quad (6.80)$$

For the simpler l_2 norm regularizer, the solution is

$$\mathbf{u}_1^{(k+1)} = \frac{1}{1 + \tilde{\lambda}} \left(\mathbf{R}\mathbf{u}_0^{(k+1)} + \boldsymbol{\eta}_1^{(k)} \right). \quad (6.81)$$

For the update of \mathbf{u}_2 both terms are quadratic and the closed form solution is given by

$$\begin{aligned}
\mathbf{u}_2^{(k+1)} &= \left(\tilde{\mathbf{B}}' \tilde{\mathbf{B}} + \mu \nu_2 \mathbf{I}_{JLM} \right)^{-1} \tilde{\mathbf{v}}_2^{(k)} \\
&= \frac{1}{\mu \nu_2} \left[\mathbf{I}_{JLM} - \tilde{\mathbf{B}}' \left(\tilde{\mathbf{B}} \tilde{\mathbf{B}}' + \mu \nu_2 \mathbf{I}_{JM} \right)^{-1} \tilde{\mathbf{B}} \right] \tilde{\mathbf{v}}_2^{(k)} \\
\tilde{\mathbf{v}}_2^{(k)} &\triangleq \tilde{\mathbf{B}}' \tilde{\mathbf{y}} + \mu \nu_2 \left(\check{\mathbf{G}} \mathbf{u}_3^{(k)} + \boldsymbol{\eta}_2^{(k)} \right).
\end{aligned} \tag{6.82}$$

This update requires the inversion of a diagonal matrix that can be performed efficiently. The most costly operation is the forward projection with the NUFFT matrix $\check{\mathbf{G}}$.

For the update of \mathbf{u}_3 we have

$$\begin{aligned}
\mathbf{u}_3^{(k+1)} &= \left(\nu_2 \check{\mathbf{G}}' \check{\mathbf{G}} + \nu_3 \mathbf{I}_{JLN} \right)^{-1} \tilde{\mathbf{v}}_3^{(k)} \\
\tilde{\mathbf{v}}_3^{(k)} &\triangleq \nu_2 \check{\mathbf{G}}' \left(\mathbf{u}_2^{(k+1)} - \boldsymbol{\eta}_2^{(k)} \right) + \nu_3 \left(\tilde{\mathbf{C}}(\boldsymbol{\omega}^{(k)}) \mathbf{S} \mathbf{x} + \boldsymbol{\eta}_3^{(k)} \right).
\end{aligned} \tag{6.83}$$

For this update the Hessian $\check{\mathbf{G}}' \check{\mathbf{G}}$ is block-Toeplitz but not circulant, thus exact inversion cannot be performed efficiently. However, an inexact update can be obtained efficiently using PCG with a circulant preconditioner and warm starting.

For the update of $\boldsymbol{\omega}$ the problem decouples to one-dimensional minimization problems, since the matrix $\tilde{\mathbf{C}}(\boldsymbol{\omega}) \mathbf{S}$ is block-diagonal. In this case the updates for each pixel are obtained as

$$\begin{aligned}
\omega_n^{(k+1)} &= \underset{\omega_n}{\operatorname{argmin}} \frac{1}{\nu_2} |q_n^k - \omega_n|^2 + \sum_{j=0}^{K-1} \sum_{l=0}^{L-1} \left| p_{j,l,n}^k - e^{-i\omega_n \check{t}_l} s_{j,n} x_n \right|^2 \\
&= \underset{\omega_n}{\operatorname{argmin}} \frac{1}{\nu_2} \left(\omega_n^2 - 2\omega_n \Re\{q_n^k\} \right) - 2\Re\{F(\omega_n)\} \\
F(\omega_n) &\triangleq x_n^* \sum_{j=0}^{K-1} s_{j,n} \sum_{l=0}^{L-1} p_{j,l,n}^k e^{i\omega_n \check{t}_l} \\
s_{j,n} &\triangleq [\mathbf{S}]_{jN+n,n} \\
q_n^k &\triangleq \left[\mathbf{u}_0^{(k+1)} - \boldsymbol{\eta}_0^{(k)} \right]_n \\
p_{j,l,n}^k &\triangleq \left[\mathbf{u}_3^{(k+1)} - \boldsymbol{\eta}_3^{(k)} \right]_{jLN+lN+n}.
\end{aligned} \tag{6.84}$$

For these one-dimensional problems, if an analytic solution is not feasible they can still be solved efficiently with an iterative method. Of course, since these problems are not convex the solution depends on the initialization and an accurate initializer is required to obtain a suitable local mini-

mum. From the above expressions we could conjecture that any errors in the pixel estimates of ω should be localized, but in fact any inaccuracies at a single pixel can potentially propagate to other locations because of the way the updates for \mathbf{u}_1 and \mathbf{u}_2 make use of the values of ω .

By applying the linearization technique in [4, 6], using a carefully chosen reference $\tilde{\omega}$ the minimization problem can be expressed as

$$\begin{aligned}\hat{\omega} &= \underset{\omega}{\operatorname{argmin}} \left\| \tilde{\mathbf{y}} - \mathbf{D}_t \tilde{\mathbf{B}} \tilde{\mathbf{P}} \tilde{\mathbf{Q}}_K \tilde{\mathbf{D}}_s \tilde{\mathbf{C}}(\tilde{\omega}) \mathbf{S} \mathbf{D}_x \omega \right\|_2^2 + \lambda \Phi(\mathbf{R}\omega) \quad (6.85) \\ \tilde{\mathbf{y}} &\triangleq \tilde{\mathbf{y}} - \tilde{\mathbf{B}} \tilde{\mathbf{P}} \tilde{\mathbf{Q}}_K \tilde{\mathbf{D}}_s \tilde{\mathbf{C}}(\tilde{\omega}) \mathbf{S} \mathbf{x} + \mathbf{D}_t \tilde{\mathbf{B}} \tilde{\mathbf{P}} \tilde{\mathbf{Q}}_K \tilde{\mathbf{D}}_s \tilde{\mathbf{C}}(\tilde{\omega}) \mathbf{S} \mathbf{D}_x \tilde{\omega} \\ \mathbf{D}_t &\triangleq \mathbf{I}_K \otimes \operatorname{diag}\{t_m\}, m = 0, \dots, M - 1 \\ \mathbf{D}_x &\triangleq \operatorname{diag}\{x_n\}, n = 0, \dots, N - 1.\end{aligned}$$

The problem is now linear in ω and The goal is to decouple the Fourier encoding matrix from the diagonal matrices of the time segmentation approximation. By choosing auxiliary variables $\mathbf{u}_0 = \omega$, $\mathbf{u}_1 = \mathbf{R}\mathbf{u}_0$, $\mathbf{u}_2 = \tilde{\mathbf{G}}\mathbf{u}_3$ and $\mathbf{u}_3 = \tilde{\mathbf{C}}(\tilde{\omega}) \mathbf{S} \mathbf{D}_x \omega$, the associated AL function of the constrained problem becomes

$$\begin{aligned}\mathcal{L}(\omega, \mathbf{u}, \boldsymbol{\eta}) &= \frac{1}{2} \left\| \tilde{\mathbf{y}} - \mathbf{D}_t \tilde{\mathbf{B}} \mathbf{u}_2 \right\|_2^2 + \lambda \Phi(\mathbf{u}_1) + \frac{\mu}{2} \left\| \mathbf{u}_0 - \omega - \boldsymbol{\eta}_0 \right\|_2^2 + \frac{\mu\nu_1}{2} \left\| \mathbf{u}_1 - \mathbf{R}\mathbf{u}_0 - \boldsymbol{\eta}_1 \right\|_2^2 \\ &+ \frac{\mu\nu_2}{2} \left\| \mathbf{u}_2 - \tilde{\mathbf{G}}\mathbf{u}_3 - \boldsymbol{\eta}_2 \right\|_2^2 + \frac{\mu\nu_3}{2} \left\| \mathbf{u}_3 - \tilde{\mathbf{C}}(\tilde{\omega}) \mathbf{S} \mathbf{D}_x \omega - \boldsymbol{\eta}_3 \right\|_2^2.\end{aligned} \quad (6.86)$$

Solving with an alternating minimization scheme the updates are obtained as

$$\mathbf{u}_0^{(k+1)} = \underset{\mathbf{u}_0}{\operatorname{argmin}} \left\| \mathbf{u}_0 - \boldsymbol{\omega}^{(k)} - \boldsymbol{\eta}_0^{(k)} \right\|_2^2 + \nu_1 \left\| \mathbf{u}_1^{(k)} - \mathbf{R}\mathbf{u}_0 - \boldsymbol{\eta}_1^{(k)} \right\|_2^2 \quad (6.87)$$

$$\mathbf{u}_1^{(k+1)} = \underset{\mathbf{u}_1}{\operatorname{argmin}} \tilde{\lambda} \Phi(\mathbf{u}_1) + \frac{1}{2} \left\| \mathbf{u}_1 - \mathbf{R}\mathbf{u}_0^{(k+1)} - \boldsymbol{\eta}_1^{(k)} \right\|_2^2 \quad (6.88)$$

$$\mathbf{u}_2^{(k+1)} = \underset{\mathbf{u}_2}{\operatorname{argmin}} \left\| \tilde{\mathbf{y}} - \mathbf{D}_t \tilde{\mathbf{B}} \mathbf{u}_2 \right\|_2^2 + \mu \nu_2 \left\| \mathbf{u}_2 - \check{\mathbf{G}} \mathbf{u}_3^{(k)} - \boldsymbol{\eta}_2^{(k)} \right\|_2^2 \quad (6.89)$$

$$\mathbf{u}_3^{(k+1)} = \underset{\mathbf{u}_3}{\operatorname{argmin}} \nu_2 \left\| \mathbf{u}_2^{(k+1)} - \check{\mathbf{G}} \mathbf{u}_3 - \boldsymbol{\eta}_2^{(k)} \right\|_2^2 + \nu_3 \left\| \mathbf{u}_3 - \tilde{\mathbf{C}}(\boldsymbol{\omega}^{(k)}) \mathbf{S}\mathbf{D}_x \boldsymbol{\omega}^{(k)} - \boldsymbol{\eta}_3^{(k)} \right\|_2^2 \quad (6.90)$$

$$\boldsymbol{\omega}^{(k+1)} = \underset{\boldsymbol{\omega}}{\operatorname{argmin}} \left\| \mathbf{u}_0^{(k+1)} - \boldsymbol{\omega} - \boldsymbol{\eta}_0^{(k)} \right\|_2^2 + \nu_3 \left\| \mathbf{u}_3^{(k+1)} - \tilde{\mathbf{C}}(\boldsymbol{\omega}^{(k)}) \mathbf{S}\mathbf{D}_x \boldsymbol{\omega} - \boldsymbol{\eta}_3^{(k)} \right\|_2^2 \quad (6.91)$$

$$\boldsymbol{\eta}_0^{(k+1)} = \boldsymbol{\eta}_0^{(k)} - \mathbf{u}_0^{(k+1)} + \boldsymbol{\omega}^{(k+1)} \quad (6.92)$$

$$\boldsymbol{\eta}_1^{(k+1)} = \boldsymbol{\eta}_1^{(k)} - \mathbf{u}_1^{(k+1)} + \mathbf{R}\mathbf{u}_0^{(k+1)} \quad (6.93)$$

$$\boldsymbol{\eta}_2^{(k+1)} = \boldsymbol{\eta}_2^{(k)} - \mathbf{u}_2^{(k+1)} + \check{\mathbf{G}} \mathbf{u}_3^{(k+1)} \quad (6.94)$$

$$\boldsymbol{\eta}_3^{(k+1)} = \boldsymbol{\eta}_3^{(k)} - \mathbf{u}_3^{(k+1)} + \tilde{\mathbf{C}}(\boldsymbol{\omega}^{(k+1)}) \mathbf{S}\mathbf{D}_x \boldsymbol{\omega}^{(k+1)}, \quad (6.95)$$

where $\tilde{\lambda} \triangleq \lambda / \mu \nu_1$.

The updates for \mathbf{u}_0 and \mathbf{u}_1 are the same as in the previous case and are given by (6.79), and (6.80) respectively.

In the update for \mathbf{u}_2 both terms are quadratic and the closed form solution is

$$\begin{aligned} \mathbf{u}_2^{(k+1)} &= \left(\tilde{\mathbf{B}}' \mathbf{D}_t' \mathbf{D}_t \tilde{\mathbf{B}} + \mu \nu_2 \mathbf{I}_{JLM} \right)^{-1} \tilde{\mathbf{v}}_1^{(k)} \\ &= \frac{1}{\mu \nu_2} \left[\mathbf{I}_{JLM} - \tilde{\mathbf{B}}' \mathbf{D}_t' \left(\mathbf{D}_t \tilde{\mathbf{B}} \tilde{\mathbf{B}}' \mathbf{D}_t' + \mu \nu_2 \mathbf{I}_{JM} \right)^{-1} \mathbf{D}_t \tilde{\mathbf{B}} \right] \tilde{\mathbf{v}}_1^{(k)} \\ \tilde{\mathbf{v}}_1^{(k)} &\triangleq \tilde{\mathbf{B}}' \mathbf{D}_t' \tilde{\mathbf{y}} + \mu \nu_2 \left(\check{\mathbf{G}} \mathbf{u}_3^{(k)} + \boldsymbol{\eta}_2^{(k)} \right), \end{aligned} \quad (6.96)$$

where the inversion only involves diagonal matrices ($\mathbf{D}_t \tilde{\mathbf{B}} \tilde{\mathbf{B}}' \mathbf{D}_t'$ is diagonal) and the most costly operations are the the forward projections with the Fourier encoding matrix $\check{\mathbf{G}}$.

For the update of \mathbf{u}_3 we have

$$\begin{aligned} \mathbf{u}_3^{(k+1)} &= \left(\nu_2 \check{\mathbf{G}}' \check{\mathbf{G}} + \nu_3 \mathbf{I}_{JLN} \right)^{-1} \tilde{\mathbf{v}}_3^{(k)} \\ \tilde{\mathbf{v}}_3^{(k)} &\triangleq \nu_2 \check{\mathbf{G}}' \left(\mathbf{u}_2^{(k+1)} - \boldsymbol{\eta}_2^{(k)} \right) + \nu_3 \left(\tilde{\mathbf{C}}(\boldsymbol{\omega}^{(k)}) \mathbf{S}\mathbf{D}_x \boldsymbol{\omega}^{(k)} + \boldsymbol{\eta}_3^{(k)} \right). \end{aligned} \quad (6.97)$$

As before, for this update the Hessian $\check{\mathbf{G}}' \check{\mathbf{G}}$ is block-Toeplitz but not circulant, thus exact inversion

cannot be performed efficiently. However, an inexact update can be obtained efficiently using PCG with a circulant preconditioner and warm starting.

For the update of $\boldsymbol{\omega}$, both terms are quadratic and the closed form solution is

$$\begin{aligned}\boldsymbol{\omega}^{(k+1)} &= \left(\nu_3 \mathbf{D}_x' \mathbf{S}' \tilde{\mathbf{C}}(\boldsymbol{\omega}^{(k)})' \tilde{\mathbf{C}}(\boldsymbol{\omega}^{(k)}) \mathbf{S} \mathbf{D}_x + \mathbf{I}_N \right)^{-1} \tilde{\mathbf{v}}_\omega^{(k)} \\ &= (\nu_3 L \mathbf{D}_x' \mathbf{S}' \mathbf{S} \mathbf{D}_x + \mathbf{I}_N)^{-1} \tilde{\mathbf{v}}_\omega^{(k)}\end{aligned}\quad (6.98)$$

$$\mathbf{v}_\omega^{(k)} \triangleq \mathbf{u}_0^{(k+1)} - \boldsymbol{\eta}_0^{(k)} + \nu_3 \mathbf{D}_x' \mathbf{S}' \tilde{\mathbf{C}}(\boldsymbol{\omega}^{(k)})' \left(\mathbf{u}_3^{(k+1)} - \boldsymbol{\eta}_3^{(k)} \right). \quad (6.99)$$

The update for $\boldsymbol{\omega}$ is exact, since it only requires the inversion of diagonal matrices ($\mathbf{D}_x' \mathbf{S}' \mathbf{S} \mathbf{D}_x$ is diagonal).

6.5.1 Quadratic Regularization

For quadratic regularization the cost function (6.10) becomes

$$\hat{\boldsymbol{\omega}} = \operatorname{argmin}_\omega \frac{1}{2} \left\| \tilde{\mathbf{y}} - \tilde{\mathbf{B}} \tilde{\mathbf{P}} \tilde{\mathbf{Q}}_K \tilde{\mathbf{D}}_s \tilde{\mathbf{C}}(\boldsymbol{\omega}) \mathbf{S} \mathbf{x} \right\|_2^2 + \lambda \|\mathbf{R} \boldsymbol{\omega}\|_2^2. \quad (6.100)$$

and when using linearization

$$\hat{\boldsymbol{\omega}} = \operatorname{argmin}_\omega \left\| \tilde{\mathbf{y}} - \mathbf{D}_t \tilde{\mathbf{B}} \tilde{\mathbf{P}} \tilde{\mathbf{Q}}_K \tilde{\mathbf{D}}_s \tilde{\mathbf{C}}(\tilde{\boldsymbol{\omega}}) \mathbf{S} \mathbf{D}_x \boldsymbol{\omega} \right\|_2^2 + \lambda \|\mathbf{R} \boldsymbol{\omega}\|_2^2. \quad (6.101)$$

In both cases the auxiliary variable $\mathbf{u}_1 = \mathbf{R} \mathbf{u}_0$ is not required and the associated AL functions become

$$\begin{aligned}\mathcal{L}(\boldsymbol{\omega}, \mathbf{u}, \boldsymbol{\eta}) &= \left\| \tilde{\mathbf{y}} - \tilde{\mathbf{B}} \mathbf{u}_2 \right\|_2^2 + \lambda \|\mathbf{R} \mathbf{u}_0\|_2^2 + \mu \|\mathbf{u}_0 - \boldsymbol{\omega} - \boldsymbol{\eta}_0\|_2^2 \\ &\quad + \mu \nu_2 \left\| \mathbf{u}_2 - \check{\mathbf{G}} \mathbf{u}_3 - \boldsymbol{\eta}_2 \right\|_2^2 + \mu \nu_3 \left\| \mathbf{u}_3 - \tilde{\mathbf{C}}(\boldsymbol{\omega}) \mathbf{S} \mathbf{x} - \boldsymbol{\eta}_3 \right\|_2^2,\end{aligned}\quad (6.102)$$

and for linearization

$$\begin{aligned}\mathcal{L}(\boldsymbol{\omega}, \mathbf{u}, \boldsymbol{\eta}) &= \left\| \tilde{\mathbf{y}} - \mathbf{D}_t \tilde{\mathbf{B}} \mathbf{u}_2 \right\|_2^2 + \lambda \|\mathbf{R} \mathbf{u}_0\|_2^2 + \mu \|\mathbf{u}_0 - \boldsymbol{\omega} - \boldsymbol{\eta}_0\|_2^2 \\ &\quad + \mu \nu_2 \left\| \mathbf{u}_2 - \check{\mathbf{G}} \mathbf{u}_3 - \boldsymbol{\eta}_2 \right\|_2^2 + \mu \nu_3 \left\| \mathbf{u}_3 - \tilde{\mathbf{C}}(\tilde{\boldsymbol{\omega}}) \mathbf{S} \mathbf{D}_x \boldsymbol{\omega} - \boldsymbol{\eta}_3 \right\|_2^2.\end{aligned}\quad (6.103)$$

The only thing that changes are the updates of \mathbf{u}_0 and $\boldsymbol{\eta}_0$ which are expressed as

$$\mathbf{u}_0^{(k+1)} = \underset{\mathbf{u}_0}{\operatorname{argmin}} \lambda \|\mathbf{R}\mathbf{u}_0\|_2^2 + \mu \left\| \mathbf{u}_0 - \boldsymbol{\omega}^{(k)} - \boldsymbol{\eta}_0^{(k)} \right\|_2^2 \quad (6.104)$$

$$\boldsymbol{\eta}_0^{(k+1)} = \boldsymbol{\eta}_0^{(k)} - \mathbf{u}_0^{(k+1)} + \boldsymbol{\omega}^{(k+1)}. \quad (6.105)$$

Now, the closed form solution for the update of \mathbf{u}_0 is

$$\mathbf{u}_0^{(k+1)} = (\lambda \mathbf{R}'\mathbf{R} + \mu \mathbf{I}_N)^{-1} \left[\mu \left(\boldsymbol{\omega}^{(k)} + \boldsymbol{\eta}_0^{(k)} \right) \right], \quad (6.106)$$

and it can be computed exactly, since the Hessian is circulant ($\mathbf{R}'\mathbf{R}$ is circulant) and inversion can be performed efficiently using FFTs.

6.5.2 Cartesian MRI

For parallel imaging and Cartesian MRI using the time segmentation approximation of (6.4) in the cost function (6.10) we get

$$\hat{\boldsymbol{\omega}} = \underset{\boldsymbol{\omega}}{\operatorname{argmin}} \frac{1}{2} \left\| \tilde{\mathbf{y}} - \tilde{\mathbf{B}}\tilde{\mathbf{Q}}_{M,N}\tilde{\mathbf{C}}(\boldsymbol{\omega})\mathbf{S}\mathbf{x} \right\|_2^2 + \lambda \Phi(\mathbf{R}\boldsymbol{\omega}). \quad (6.107)$$

The goal is to decouple the time segmentation coefficient matrix $\tilde{\mathbf{C}}(\boldsymbol{\omega})$ from the encoding and sparsifying matrix. By choosing auxiliary variables $\mathbf{u}_0 = \boldsymbol{\omega}$, $\mathbf{u}_1 = \mathbf{R}\mathbf{u}_0$, and $\mathbf{u}_2 = \tilde{\mathbf{C}}(\boldsymbol{\omega})\mathbf{S}\mathbf{x}$, the associated AL function of the constrained problem becomes

$$\mathcal{L}(\boldsymbol{\omega}, \mathbf{u}, \boldsymbol{\eta}) = \frac{1}{2} \left\| \tilde{\mathbf{y}} - \tilde{\mathbf{B}}\tilde{\mathbf{Q}}_{M,N}\mathbf{u}_2 \right\|_2^2 + \lambda \Phi(\mathbf{u}_1) + \frac{\mu}{2} \left\| \mathbf{u}_0 - \boldsymbol{\omega} - \boldsymbol{\eta}_0 \right\|_2^2 \quad (6.108)$$

$$+ \frac{\mu\nu_1}{2} \left\| \mathbf{u}_1 - \mathbf{R}\mathbf{u}_0 - \boldsymbol{\eta}_1 \right\|_2^2 + \frac{\mu\nu_2}{2} \left\| \mathbf{u}_2 - \tilde{\mathbf{C}}(\boldsymbol{\omega})\mathbf{S}\mathbf{x} - \boldsymbol{\eta}_2 \right\|_2^2. \quad (6.109)$$

Solving with an alternating minimization scheme the updates for \mathbf{u}_0 , \mathbf{u}_1 , $\boldsymbol{\eta}_0$, $\boldsymbol{\eta}_1$, and $\boldsymbol{\omega}$ are the same as in §6.5 and are given by (6.79), (6.80), (6.75), (6.76), (6.84) respectively, where in the case of $\boldsymbol{\omega}$ we use \mathbf{u}_2 instead of \mathbf{u}_3 in (6.84). The remaining updates are given by

$$\mathbf{u}_2^{(k+1)} = \underset{\mathbf{u}_2}{\operatorname{argmin}} \left\| \tilde{\mathbf{y}} - \tilde{\mathbf{B}}\tilde{\mathbf{Q}}_{M,N}\mathbf{u}_2 \right\|_2^2 + \mu\nu_2 \left\| \mathbf{u}_2 - \tilde{\mathbf{C}}(\boldsymbol{\omega}^{(k)})\mathbf{S}\mathbf{x} - \boldsymbol{\eta}_2^{(k)} \right\|_2^2 \quad (6.110)$$

$$\boldsymbol{\eta}_2^{(k+1)} = \boldsymbol{\eta}_2^{(k)} - \mathbf{u}_2^{(k+1)} + \tilde{\mathbf{C}}(\boldsymbol{\omega}^{(k+1)})\mathbf{S}\mathbf{x}. \quad (6.111)$$

In the update for \mathbf{u}_2 both terms are quadratic and the closed form solution is

$$\begin{aligned}
\mathbf{u}_2^{(k+1)} &= \left(\tilde{\mathbf{Q}}'_{M,N} \tilde{\mathbf{B}}' \tilde{\mathbf{B}} \tilde{\mathbf{Q}}_{M,N} + \mu\nu_2 \mathbf{I}_{JLN} \right)^{-1} \tilde{\mathbf{v}}_2^{(k)} \\
&= \frac{1}{\mu\nu_2} \left[\mathbf{I}_{JLN} - \tilde{\mathbf{Q}}'_{M,N} \tilde{\mathbf{B}}' \left(\tilde{\mathbf{B}} \tilde{\mathbf{Q}}_{M,N} \tilde{\mathbf{Q}}'_{M,N} \tilde{\mathbf{B}}' + \mu\nu_2 \mathbf{I}_{JM} \right)^{-1} \tilde{\mathbf{B}} \tilde{\mathbf{Q}}_{M,N} \right] \tilde{\mathbf{v}}_2^{(k)} \\
&= \frac{1}{\mu\nu_2} \left[\mathbf{I}_{JLN} - \tilde{\mathbf{Q}}'_{M,N} \tilde{\mathbf{B}}' \left(N \tilde{\mathbf{B}} \tilde{\mathbf{B}}' + \mu\nu_2 \mathbf{I}_{JM} \right)^{-1} \tilde{\mathbf{B}} \tilde{\mathbf{Q}}_{M,N} \right] \tilde{\mathbf{v}}_2^{(k)} \\
\tilde{\mathbf{v}}_2^{(k)} &\triangleq \tilde{\mathbf{Q}}'_{M,N} \tilde{\mathbf{B}}' \tilde{\mathbf{y}} + \mu\nu_2 \left(\tilde{\mathbf{C}}(\boldsymbol{\omega}^{(k)}) \mathbf{S} \mathbf{x} + \boldsymbol{\eta}_2^{(k)} \right),
\end{aligned} \tag{6.112}$$

where the inversion only involves diagonal matrices ($\tilde{\mathbf{B}} \tilde{\mathbf{B}}'$ is diagonal) and the most costly operations are the forward projections with the Fourier encoding matrix $\tilde{\mathbf{Q}}_{M,N}$.

By applying the linearization technique the minimization problem can be expressed as

$$\begin{aligned}
\hat{\boldsymbol{\omega}} &= \underset{\boldsymbol{\omega}}{\operatorname{argmin}} \left\| \tilde{\mathbf{y}} - \mathbf{D}_t \tilde{\mathbf{B}} \tilde{\mathbf{Q}}_{M,N} \tilde{\mathbf{C}}(\tilde{\boldsymbol{\omega}}) \mathbf{S} \mathbf{D}_x \boldsymbol{\omega} \right\|_2^2 + \lambda \Phi(\mathbf{R} \boldsymbol{\omega}) \\
\tilde{\mathbf{y}} &\triangleq \tilde{\mathbf{y}} - \tilde{\mathbf{B}} \tilde{\mathbf{Q}}_{M,N} \tilde{\mathbf{C}}(\tilde{\boldsymbol{\omega}}) \mathbf{S} \mathbf{x} + \mathbf{D}_t \tilde{\mathbf{B}} \tilde{\mathbf{Q}}_{M,N} \tilde{\mathbf{C}}(\tilde{\boldsymbol{\omega}}) \mathbf{S} \mathbf{D}_x \tilde{\boldsymbol{\omega}} \\
\mathbf{D}_t &\triangleq \mathbf{I}_K \otimes \operatorname{diag}\{t_m\}, m = 0, \dots, M-1 \\
\mathbf{D}_x &\triangleq \operatorname{diag}\{x_n\}, n = 0, \dots, N-1.
\end{aligned} \tag{6.113}$$

The problem is now linear in $\boldsymbol{\omega}$ and The goal is to decouple the Fourier encoding matrix from the diagonal matrices of the time segmentation approximation. By choosing auxiliary variables $\mathbf{u}_0 = \boldsymbol{\omega}$, $\mathbf{u}_1 = \mathbf{R} \mathbf{u}_0$, and $\mathbf{u}_2 = \tilde{\mathbf{C}}(\tilde{\boldsymbol{\omega}}) \mathbf{S} \mathbf{D}_x \boldsymbol{\omega}$, the associated AL function of the constrained problem becomes

$$\begin{aligned}
\mathcal{L}(\boldsymbol{\omega}, \mathbf{u}, \boldsymbol{\eta}) &= \frac{1}{2} \left\| \tilde{\mathbf{y}} - \mathbf{D}_t \tilde{\mathbf{B}} \tilde{\mathbf{Q}}_{M,N} \mathbf{u}_2 \right\|_2^2 + \lambda \Phi(\mathbf{u}_1) + \frac{\mu}{2} \left\| \mathbf{u}_0 - \boldsymbol{\omega} - \boldsymbol{\eta}_0 \right\|_2^2 + \frac{\mu\nu_1}{2} \left\| \mathbf{u}_1 - \mathbf{R} \mathbf{u}_0 - \boldsymbol{\eta}_1 \right\|_2^2 \\
&\quad + \frac{\mu\nu_2}{2} \left\| \mathbf{u}_2 - \tilde{\mathbf{C}}(\tilde{\boldsymbol{\omega}}) \mathbf{S} \mathbf{D}_x \boldsymbol{\omega} - \boldsymbol{\eta}_3 \right\|_2^2.
\end{aligned} \tag{6.114}$$

Solving with an alternating minimization scheme the updates for \mathbf{u}_0 , \mathbf{u}_1 , $\boldsymbol{\eta}_0$, $\boldsymbol{\eta}_1$, and $\boldsymbol{\omega}$ are the same as in §6.5 and are given by (6.79), (6.80), (6.75), (6.76), (6.98) respectively, where in the case of $\boldsymbol{\omega}$ we use \mathbf{u}_2 instead of \mathbf{u}_3 in (6.98). The remaining updates are given by

$$\begin{aligned}
\mathbf{u}_2^{(k+1)} &= \underset{\mathbf{u}_2}{\operatorname{argmin}} \left\| \tilde{\mathbf{y}} - \mathbf{D}_t \tilde{\mathbf{B}} \tilde{\mathbf{Q}}_{M,N} \mathbf{u}_2 \right\|_2^2 + \mu\nu_2 \left\| \mathbf{u}_2 - \tilde{\mathbf{C}}(\tilde{\boldsymbol{\omega}}^{(k)}) \mathbf{S} \mathbf{D}_x \boldsymbol{\omega}^{(k)} - \boldsymbol{\eta}_2^{(k)} \right\|_2^2 \\
\boldsymbol{\eta}_2^{(k+1)} &= \boldsymbol{\eta}_2^{(k)} - \mathbf{u}_2^{(k+1)} + \tilde{\mathbf{C}}(\boldsymbol{\omega}^{(k+1)}) \mathbf{S} \mathbf{D}_x \boldsymbol{\omega}^{(k+1)}.
\end{aligned} \tag{6.115}$$

In the update for \mathbf{u}_2 both terms are quadratic and the closed form solution is

$$\begin{aligned}
\mathbf{u}_2^{(k+1)} &= \left(\tilde{\mathbf{Q}}'_{M,N} \tilde{\mathbf{B}}' \mathbf{D}_t' \mathbf{D}_t \tilde{\mathbf{B}} \tilde{\mathbf{Q}}_{M,N} + \mu \nu_2 \mathbf{I}_{JLN} \right)^{-1} \tilde{\mathbf{v}}_2^{(k)} \\
&= \frac{1}{\mu \nu_2} \left[\mathbf{I}_{JLN} - \tilde{\mathbf{Q}}'_{M,N} \tilde{\mathbf{B}}' \mathbf{D}_t' \left(\mathbf{D}_t \tilde{\mathbf{B}} \tilde{\mathbf{Q}}_{M,N} \tilde{\mathbf{Q}}'_{M,N} \tilde{\mathbf{B}}' \mathbf{D}_t' + \mu \nu_2 \mathbf{I}_{JM} \right)^{-1} \mathbf{D}_t \tilde{\mathbf{B}} \tilde{\mathbf{Q}}_{M,N} \right] \tilde{\mathbf{v}}_2^{(k)} \\
&= \frac{1}{\mu \nu_2} \left[\mathbf{I}_{JLN} - \tilde{\mathbf{Q}}'_{M,N} \tilde{\mathbf{B}}' \mathbf{D}_t' \left(N \mathbf{D}_t \tilde{\mathbf{B}} \tilde{\mathbf{B}}' \mathbf{D}_t' + \mu \nu_2 \mathbf{I}_{JM} \right)^{-1} \mathbf{D}_t \tilde{\mathbf{B}} \tilde{\mathbf{Q}}_{M,N} \right] \tilde{\mathbf{v}}_2^{(k)} \quad (6.116) \\
\tilde{\mathbf{v}}_1^{(k)} &\triangleq \tilde{\mathbf{Q}}'_{M,N} \tilde{\mathbf{B}}' \mathbf{D}_t' \tilde{\mathbf{y}} + \mu \left(\tilde{\mathbf{C}}(\boldsymbol{\omega}^{(k)}) \mathbf{S} \mathbf{D}_x \boldsymbol{\omega}^{(k)} + \boldsymbol{\eta}_1^{(k)} \right),
\end{aligned}$$

where the inversion only involves diagonal matrices ($\mathbf{D}_t \tilde{\mathbf{B}} \tilde{\mathbf{B}}' \mathbf{D}_t'$ is diagonal) and the most costly operations are the the forward projections with the Fourier encoding matrix $\tilde{\mathbf{Q}}_{M,N}$.

6.5.3 Single Coil Imaging

When a single receiver coil is used the sensitivity matrix reduces to $\mathbf{S} = \mathbf{I}_N$. For non-Cartesian imaging this simplification does not lead to a form with reduced number of auxiliary variables, thus the solutions of the previous sections can be applied with the simple substitution of $\mathbf{S} = \mathbf{I}_N$. Also, even for cartesian imaging further reduction of the auxiliary variables is not possible since the splits $\mathbf{u}_0 = \boldsymbol{\omega}$ and $\mathbf{u}_1 = \mathbf{R} \mathbf{u}_0$ are necessary to decouple $\boldsymbol{\omega}$ from \mathbf{R} and allow solving for $\boldsymbol{\omega}$ using (6.84) or (6.98). Thus, the methods from §6.5.2 can be used by substituting $\tilde{\mathbf{B}}$, $\tilde{\mathbf{Q}}_{M,N}$, and $\tilde{\mathbf{C}}(\tilde{\boldsymbol{\omega}})$ with \mathbf{B} , $\tilde{\mathbf{Q}}_N$, and $\mathbf{C}(\tilde{\boldsymbol{\omega}})$ respectively.

6.6 Joint Image and Fieldmap Estimation

For the general case of parallel imaging with non-Cartesian trajectories and the presence of fieldmap, when the NUFFT and time-segmentation approximations are used, the cost function (6.11) becomes

$$\hat{\mathbf{x}}, \hat{\boldsymbol{\omega}} = \underset{\mathbf{x}, \boldsymbol{\omega}}{\operatorname{argmin}} \frac{1}{2} \left\| \tilde{\mathbf{y}} - \tilde{\mathbf{B}} \tilde{\mathbf{G}} \tilde{\mathbf{C}}(\boldsymbol{\omega}) \mathbf{S} \mathbf{x} \right\|_2^2 + \lambda_1 \Phi(\mathbf{R} \mathbf{x}) + \lambda_2 \Phi(\mathbf{R} \boldsymbol{\omega}). \quad (6.117)$$

The goal is to decouple the time segmentation coefficient matrix $\tilde{\mathbf{C}}(\boldsymbol{\omega})$ from the encoding and sparsifying matrix. By choosing auxiliary variables $\mathbf{u}_0 = \mathbf{x}$, $\mathbf{u}_1 = \mathbf{R} \mathbf{u}_0$, $\mathbf{u}_2 = \boldsymbol{\omega}$, $\mathbf{u}_3 = \mathbf{R} \mathbf{u}_2$,

$\mathbf{u}_4 = \check{\mathbf{G}}\mathbf{u}_5$ and $\mathbf{u}_5 = \tilde{\mathbf{C}}(\boldsymbol{\omega})\mathbf{S}\mathbf{x}$, the associated AL function of the constrained problem becomes

$$\begin{aligned} \mathcal{L}(\boldsymbol{\omega}, \mathbf{u}, \boldsymbol{\eta}) = & \frac{1}{2} \left\| \tilde{\mathbf{y}} - \tilde{\mathbf{B}}\mathbf{u}_4 \right\|_2^2 + \lambda_1 \Phi(\mathbf{u}_1) + \lambda_2 \Phi(\mathbf{u}_3) + \frac{\mu}{2} \left\| \mathbf{u}_0 - \mathbf{x} - \boldsymbol{\eta}_0 \right\|_2^2 \\ & + \frac{\mu\nu_1}{2} \left\| \mathbf{u}_1 - \mathbf{R}\mathbf{u}_0 - \boldsymbol{\eta}_1 \right\|_2^2 + \frac{\mu\nu_2}{2} \left\| \mathbf{u}_2 - \boldsymbol{\omega} - \boldsymbol{\eta}_2 \right\|_2^2 + \frac{\mu\nu_3}{2} \left\| \mathbf{u}_3 - \mathbf{R}\mathbf{u}_2 - \boldsymbol{\eta}_3 \right\|_2^2 \\ & + \frac{\mu\nu_4}{2} \left\| \mathbf{u}_4 - \check{\mathbf{G}}\mathbf{u}_5 - \boldsymbol{\eta}_4 \right\|_2^2 + \frac{\mu\nu_5}{2} \left\| \mathbf{u}_5 - \tilde{\mathbf{C}}(\boldsymbol{\omega})\mathbf{S}\mathbf{x} - \boldsymbol{\eta}_5 \right\|_2^2. \end{aligned} \quad (6.118)$$

Solving with an alternating minimization scheme the updates are obtained as

$$\mathbf{u}_0^{(k+1)} = \underset{\mathbf{u}_0}{\operatorname{argmin}} \left\| \mathbf{u}_0 - \mathbf{x}^{(k)} - \boldsymbol{\eta}_0^{(k)} \right\|_2^2 + \nu_1 \left\| \mathbf{u}_1^{(k)} - \mathbf{R}\mathbf{u}_0 - \boldsymbol{\eta}_1^{(k)} \right\|_2^2 \quad (6.119)$$

$$\mathbf{u}_1^{(k+1)} = \underset{\mathbf{u}_1}{\operatorname{argmin}} \tilde{\lambda}_1 \Phi(\mathbf{u}_1) + \frac{1}{2} \left\| \mathbf{u}_1 - \mathbf{R}\mathbf{u}_0^{(k+1)} - \boldsymbol{\eta}_1^{(k)} \right\|_2^2 \quad (6.120)$$

$$\mathbf{u}_2^{(k+1)} = \underset{\mathbf{u}_2}{\operatorname{argmin}} \nu_2 \left\| \mathbf{u}_2 - \boldsymbol{\omega}^{(k)} - \boldsymbol{\eta}_2^{(k)} \right\|_2^2 + \nu_3 \left\| \mathbf{u}_3^{(k)} - \mathbf{R}\mathbf{u}_2 - \boldsymbol{\eta}_3^{(k)} \right\|_2^2 \quad (6.121)$$

$$\mathbf{u}_3^{(k+1)} = \underset{\mathbf{u}_3}{\operatorname{argmin}} \tilde{\lambda}_2 \Phi(\mathbf{u}_3) + \frac{1}{2} \left\| \mathbf{u}_3 - \mathbf{R}\mathbf{u}_2^{(k+1)} - \boldsymbol{\eta}_3^{(k)} \right\|_2^2 \quad (6.122)$$

$$\mathbf{u}_4^{(k+1)} = \underset{\mathbf{u}_4}{\operatorname{argmin}} \left\| \tilde{\mathbf{y}} - \tilde{\mathbf{B}}\mathbf{u}_4 \right\|_2^2 + \mu\nu_4 \left\| \mathbf{u}_4 - \check{\mathbf{G}}\mathbf{u}_5^{(k)} - \boldsymbol{\eta}_4^{(k)} \right\|_2^2 \quad (6.123)$$

$$\mathbf{u}_5^{(k+1)} = \underset{\mathbf{u}_5}{\operatorname{argmin}} \nu_4 \left\| \mathbf{u}_4^{(k+1)} - \check{\mathbf{G}}\mathbf{u}_5 - \boldsymbol{\eta}_4^{(k)} \right\|_2^2 + \nu_5 \left\| \mathbf{u}_5 - \tilde{\mathbf{C}}(\boldsymbol{\omega}^{(k)})\mathbf{S}\mathbf{x} - \boldsymbol{\eta}_5^{(k)} \right\|_2^2 \quad (6.124)$$

$$\mathbf{x}^{(k+1)} = \underset{\mathbf{x}}{\operatorname{argmin}} \left\| \mathbf{u}_0^{(k+1)} - \mathbf{x} - \boldsymbol{\eta}_0^{(k)} \right\|_2^2 + \nu_5 \left\| \mathbf{u}_5^{(k+1)} - \tilde{\mathbf{C}}(\boldsymbol{\omega}^{(k)})\mathbf{S}\mathbf{x} - \boldsymbol{\eta}_5^{(k)} \right\|_2^2 \quad (6.125)$$

$$\boldsymbol{\omega}^{(k+1)} = \underset{\boldsymbol{\omega}}{\operatorname{argmin}} \nu_2 \left\| \mathbf{u}_2^{(k+1)} - \boldsymbol{\omega} - \boldsymbol{\eta}_2^{(k)} \right\|_2^2 + \nu_5 \left\| \mathbf{u}_5^{(k+1)} - \tilde{\mathbf{C}}(\boldsymbol{\omega})\mathbf{S}\mathbf{x}^{(k+1)} - \boldsymbol{\eta}_5^{(k)} \right\|_2^2 \quad (6.126)$$

$$\boldsymbol{\eta}_0^{(k+1)} = \boldsymbol{\eta}_0^{(k)} - \mathbf{u}_0^{(k+1)} + \mathbf{x}^{(k+1)} \quad (6.127)$$

$$\boldsymbol{\eta}_1^{(k+1)} = \boldsymbol{\eta}_1^{(k)} - \mathbf{u}_1^{(k+1)} + \mathbf{R}\mathbf{u}_0^{(k+1)} \quad (6.128)$$

$$\boldsymbol{\eta}_2^{(k+1)} = \boldsymbol{\eta}_2^{(k)} - \mathbf{u}_2^{(k+1)} + \boldsymbol{\omega}^{(k+1)} \quad (6.129)$$

$$\boldsymbol{\eta}_3^{(k+1)} = \boldsymbol{\eta}_3^{(k)} - \mathbf{u}_3^{(k+1)} + \mathbf{R}\mathbf{u}_2^{(k+1)} \quad (6.130)$$

$$\boldsymbol{\eta}_4^{(k+1)} = \boldsymbol{\eta}_4^{(k)} - \mathbf{u}_4^{(k+1)} + \check{\mathbf{G}}\mathbf{u}_5^{(k+1)} \quad (6.131)$$

$$\boldsymbol{\eta}_5^{(k+1)} = \boldsymbol{\eta}_5^{(k)} - \mathbf{u}_5^{(k+1)} + \tilde{\mathbf{C}}(\boldsymbol{\omega}^{(k+1)})\mathbf{S}\mathbf{x}^{(k+1)}. \quad (6.132)$$

where $\tilde{\lambda}_1 \triangleq \lambda/\mu\nu_1$, and $\tilde{\lambda}_2 \triangleq \lambda/\mu\nu_3$.

The updates for \mathbf{u}_0 and \mathbf{u}_2 are given by

$$\mathbf{u}_0^{(k+1)} = (\nu_1 \mathbf{R}' \mathbf{R} + \mathbf{I}_N)^{-1} \left[\left(\mathbf{x}^{(k)} + \boldsymbol{\eta}_0^{(k)} \right) + \nu_1 \mathbf{R}' \left(\mathbf{u}_1^{(k)} - \boldsymbol{\eta}_1^{(k)} \right) \right] \quad (6.133)$$

$$\mathbf{u}_2^{(k+1)} = (\nu_3 \mathbf{R}' \mathbf{R} + \nu_2 \mathbf{I}_N)^{-1} \left[\nu_2 \left(\boldsymbol{\omega}^{(k)} + \boldsymbol{\eta}_2^{(k)} \right) + \nu_3 \mathbf{R}' \left(\mathbf{u}_3^{(k)} - \boldsymbol{\eta}_3^{(k)} \right) \right]. \quad (6.134)$$

The update is exact since $\mathbf{R}' \mathbf{R}$ is circulant and the inverse is computed efficiently with FFTs.

In the updates for \mathbf{u}_1 and \mathbf{u}_3 the form of the solution depends on the choice of regularizer. For l_1 or TV norm the solution reduces to a scalar or vector shrinkage rule as

$$\mathbf{u}_1^{(k+1)} = \text{shrink} \left\{ \mathbf{R} \mathbf{u}_0^{(k+1)} + \boldsymbol{\eta}_1^{(k)}, \tilde{\lambda}_1 \right\} \quad (6.135)$$

$$\mathbf{u}_3^{(k+1)} = \text{shrink} \left\{ \mathbf{R} \mathbf{u}_2^{(k+1)} + \boldsymbol{\eta}_3^{(k)}, \tilde{\lambda}_2 \right\}. \quad (6.136)$$

For the simpler l_2 norm regularizer, the solution is

$$\mathbf{u}_1^{(k+1)} = \frac{1}{1 + \tilde{\lambda}_1} \left(\mathbf{R} \mathbf{u}_0^{(k+1)} + \boldsymbol{\eta}_1^{(k)} \right). \quad (6.137)$$

$$\mathbf{u}_3^{(k+1)} = \frac{1}{1 + \tilde{\lambda}_2} \left(\mathbf{R} \mathbf{u}_2^{(k+1)} + \boldsymbol{\eta}_3^{(k)} \right). \quad (6.138)$$

For the update of \mathbf{u}_4 both terms are quadratic and the closed form solution is given by

$$\begin{aligned} \mathbf{u}_4^{(k+1)} &= \left(\tilde{\mathbf{B}}' \tilde{\mathbf{B}} + \mu \nu_4 \mathbf{I}_{JLM} \right)^{-1} \tilde{\mathbf{v}}_4^{(k)} \\ &= \frac{1}{\mu \nu_4} \left[\mathbf{I}_{JLM} - \tilde{\mathbf{B}}' \left(\tilde{\mathbf{B}} \tilde{\mathbf{B}}' + \mu \nu_4 \mathbf{I}_{JM} \right)^{-1} \tilde{\mathbf{B}} \right] \tilde{\mathbf{v}}_4^{(k)} \\ \tilde{\mathbf{v}}_2^{(k)} &\triangleq \tilde{\mathbf{B}}' \tilde{\mathbf{y}} + \mu \nu_4 \left(\check{\mathbf{G}} \mathbf{u}_5^{(k)} + \boldsymbol{\eta}_4^{(k)} \right). \end{aligned} \quad (6.139)$$

This update requires the inversion of a diagonal matrix that can be performed efficiently. The most costly operation is the forward projection with the NUFFT matrix $\check{\mathbf{G}}$.

For the update of \mathbf{u}_5 we have

$$\begin{aligned} \mathbf{u}_5^{(k+1)} &= \left(\nu_4 \check{\mathbf{G}}' \check{\mathbf{G}} + \nu_5 \mathbf{I}_{JLN} \right)^{-1} \tilde{\mathbf{v}}_5^{(k)} \\ \tilde{\mathbf{v}}_5^{(k)} &\triangleq \nu_4 \check{\mathbf{G}}' \left(\mathbf{u}_4^{(k+1)} - \boldsymbol{\eta}_4^{(k)} \right) + \nu_5 \left(\tilde{\mathbf{C}} \left(\boldsymbol{\omega}^{(k)} \right) \mathbf{S} \mathbf{x}^{(k)} + \boldsymbol{\eta}_5^{(k)} \right). \end{aligned} \quad (6.140)$$

For this update the Hessian $\check{\mathbf{G}}' \check{\mathbf{G}}$ is block-Toeplitz but not circulant, thus exact inversion cannot be performed efficiently. However, an inexact update can be obtained efficiently using PCG with a

circulant preconditioner and warm starting.

For the update of \mathbf{x} we have

$$\begin{aligned}
\mathbf{x}^{(k+1)} &= \left(\nu_5 \mathbf{S}' \tilde{\mathbf{C}}(\boldsymbol{\omega}^{(k)})' \tilde{\mathbf{C}}(\boldsymbol{\omega}^{(k)}) \mathbf{S} + \mathbf{I}_N \right)^{-1} \tilde{\mathbf{v}}_x^{(k)} \\
&= (\nu_5 L \mathbf{S}' \mathbf{S} + \mathbf{I}_N)^{-1} \tilde{\mathbf{v}}_x^{(k)} \\
\tilde{\mathbf{v}}_x^{(k)} &\triangleq \mathbf{u}_0^{(k+1)} - \boldsymbol{\eta}_0^{(k)} + \nu_5 \mathbf{S}' \tilde{\mathbf{C}}(\boldsymbol{\omega}^{(k)})' \left(\mathbf{u}_5^{(k+1)} - \boldsymbol{\eta}_5^{(k)} \right).
\end{aligned} \tag{6.141}$$

This update only involves inversion of diagonal matrices ($\mathbf{S}'\mathbf{S}$ is diagonal) and it can be computed efficiently. Also all other operations involve block-diagonal matrices and thus, they can be performed in linear time.

For the update of $\boldsymbol{\omega}$ the problem decouples to one-dimensional minimization problems, since the matrix $\tilde{\mathbf{C}}(\boldsymbol{\omega}) \mathbf{S}$ is block-diagonal. In this case the updates for each pixel are obtained as

$$\begin{aligned}
\omega_n^{(k+1)} &= \underset{\omega_n}{\operatorname{argmin}} \frac{1}{\nu_2} |q_n^k - \omega_n|^2 + \sum_{j=0}^{K-1} \sum_{l=0}^{L-1} \left| p_{j,l,n}^k - e^{-i\omega_n \tilde{t}_l} s_{j,n} x_n \right|^2 \\
&= \underset{\omega_n}{\operatorname{argmin}} \frac{1}{\nu_2} (\omega_n^2 - 2\omega_n \Re\{q_n^k\}) - 2\Re\{F(\omega_n)\} \\
F(\omega_n) &\triangleq x_n^* \sum_{j=0}^{K-1} s_{j,n} \sum_{l=0}^{L-1} p_{j,l,n}^k e^{i\omega_n \tilde{t}_l} \\
s_{j,n} &\triangleq [\mathbf{S}]_{jN+n,n} \\
x_n &\triangleq [\mathbf{x}^{(k+1)}]_n \\
q_n^k &\triangleq \left[\mathbf{u}_2^{(k+1)} - \boldsymbol{\eta}_2^{(k)} \right]_n \\
p_{j,l,n}^k &\triangleq \left[\mathbf{u}_5^{(k+1)} - \boldsymbol{\eta}_5^{(k)} \right]_{jLN+lN+n}.
\end{aligned} \tag{6.142}$$

This update is equivalent to (6.84) and the same methods can be used to find a solution.

When linearization is used along with an alternating minimization scheme the joint estimation

problem becomes

$$\mathbf{x}^{(k+1)} = \underset{\mathbf{x}}{\operatorname{argmin}} \left\| \tilde{\mathbf{y}} - \tilde{\mathbf{B}}\check{\mathbf{G}}\tilde{\mathbf{C}}(\boldsymbol{\omega}^{(k)}) \mathbf{S}\mathbf{x} \right\|_2^2 + \lambda_1 \Phi(\mathbf{R}\mathbf{x}) \quad (6.143)$$

$$\boldsymbol{\omega}^{(k+1)} = \underset{\boldsymbol{\omega}}{\operatorname{argmin}} \left\| \tilde{\mathbf{y}} - \mathbf{D}_t \check{\mathbf{G}}\tilde{\mathbf{C}}(\boldsymbol{\omega}^{(k)}) \mathbf{S}\mathbf{D}_x \boldsymbol{\omega} \right\|_2^2 + \lambda_2 \Phi(\mathbf{R}\boldsymbol{\omega}) \quad (6.144)$$

$$\tilde{\mathbf{y}} \triangleq \tilde{\mathbf{y}} - \tilde{\mathbf{B}}\check{\mathbf{G}}\tilde{\mathbf{C}}(\boldsymbol{\omega}^{(k)}) \mathbf{S}\mathbf{x}^{(k+1)} + \mathbf{D}_t \check{\mathbf{G}}\tilde{\mathbf{C}}(\boldsymbol{\omega}^{(k)}) \mathbf{S}\mathbf{D}_x \boldsymbol{\omega}^{(k)}$$

$$\mathbf{D}_t \triangleq \mathbf{I}_K \otimes \operatorname{diag}\{t_m\}, m = 0, \dots, M - 1$$

$$\mathbf{D}_x \triangleq \operatorname{diag}\{x_n^{k+1}\}, n = 0, \dots, N - 1.$$

for the k th update.

Using this formulation we can apply the AL methodology of §6.4 to find the one step updates for (6.143) and then use the $\mathbf{x}^{(k+1)}$ update and the AL methodology of §6.5 to find the one step updates for (6.144). This process is then repeated until convergence.

All special cases of interest like quadratic regularization, cartesian imaging and single receiver coil can be easily derived from the methods presented for image and fieldmap estimation in §6.4 and §6.5 respectively. Using the presented methodology the results for joint estimation will be equivalent to those in the above section for each special case.

CHAPTER VII

Discussion and Future Work

In this work we presented an efficient method for jointly estimating image and fieldmap in parallel MRI. The simulation results showed that we can achieve high quality reconstruction with this method by using significantly reduced datasets compared to standard methods for image and fieldmap estimation. Due to this fact, this method has the potential to be used in functional MRI where dynamic updates of the image and fieldmap are desirable. A disadvantage of this method is that non-standard single-shot trajectories seem to be required to achieve good reconstruction and also that in a real setting the “interleaved” EPI suffers from ghosting artifacts that need to be eliminated before the method can be of practical use. Our model-based ghost correction method has the potential to reduce the ghosting artifacts and can be easily incorporated into the joint reconstruction of image and fieldmap. As a future step we plan to use this ghost correction when performing joint reconstruction for phantom and in-vivo studies. Also, it would be interesting as a future step to find an analytic relation between trajectories and reconstruction quality as this could explain why the standard trajectories failed to perform well in our simulations.

Furthermore we proposed an efficient method for joint estimation of dynamic images and fieldmaps compensating for through-plane gradient effects. The preliminary simulation results showed that high quality reconstruction can be achieved with this method, by using a more accurate signal model and fast approximations. Thus, this method can be potentially useful in functional MRI, where dynamic fieldmap updates are desirable and through-plane gradient effects can cause significant image quality degradation. As a future step it would be interesting to investigate the benefits, in terms of quality of the reconstructed images, from incorporating in-plane fieldmap gradients in the signal model. Also, in this study, a 3D regularizer was used for fieldmap reconstruction, with promising results in terms of image quality. However, a more thorough study of its effects on the reconstructed images is required. Finally, to further evaluate the proposed method it is necessary to perform experiments using real data from phantom and human studies.

Finally we proposed a method for joint image and fieldmap estimation based on the Augmented Lagrangian (AL) framework with variable splitting. This methodology has the potential to significantly improve the performance of joint estimation especially in cases of non-quadratic regularization where standard CG methods cannot be used directly. Another benefit of the proposed method is that the non-convex and non-linear fieldmap estimation problem can be handled efficiently as a set of one-dimensional optimization problems without the need for the linearization approximation. As part of our future work we intend to validate our proposed method through simulation and phantom studies. Also we intend to investigate the possibility of applying the proposed AL methodology to the joint estimation problem in the presence of through-plane fieldmap gradients.

APPENDICES

APPENDIX A

CRB Analysis for Trajectory Optimization

Echo-Time Optimization

Motivation

As stated in the introduction, in image reconstruction for MRI the selection of trajectory is a major consideration, since the quality of the obtained results can greatly depend on the chosen trajectory. Therefore, optimizing the trajectory used for the problem at hand may greatly improve the reconstruction quality. Motivated by this fact, we develop a simple theoretical method that optimizes the choice of echo-time given the model parameters that we wish to estimate. Even though echo-time is just one trajectory parameter, it is possibly the most important one since image contrast and reconstruction quality can be greatly affected by the choice of echo time. In our method we derive the Cramer-Rao bound for the estimated parameters and we minimize this lower bound on variance with respect to the echo-time.

Model formulation and CRB derivation

For this problem we will consider a complex circularly gaussian noise model consisting of n measurements at echo times t_i for $i = 1, \dots, n$. The parameters that we use for the signal model are the complex image $f \triangleq f_R + if_I$, field inhomogeneity ω through the term $e^{-i\omega t_i}$, R_2^* decay through the term e^{-rt_i} and through-plane gradients through the term $H(t_i g)$.

For simplicity we perform our analysis on a single voxel and the measurement at time t_i will be a noisy version of the signal, that can be expressed as:

$$y_i = fH(t_i g)e^{-i\omega t_i}e^{-rt_i} + \varepsilon_i$$

where ε_i is the complex gaussian noise. To avoid using complex analysis for the CRB we split each measurement in real and imaginary part and the resulting measurement model can be expressed as:

$$\mathbf{Y} = N \left(\begin{pmatrix} \begin{bmatrix} g_{R,1} \\ g_{I,1} \end{bmatrix} H(t_1 g)e^{-rt_1} \\ \vdots \\ \begin{bmatrix} g_{R,n} \\ g_{I,n} \end{bmatrix} H(t_n g)e^{-rt_n} \end{pmatrix}, \sigma^2 \mathbf{I}_{2n \times 2n} \right), \quad (\text{A.1})$$

where $g_{R,i} \triangleq f_R \cos(\omega t_i) + f_I \sin(\omega t_i)$ and $g_{I,i} \triangleq -f_R \sin(\omega t_i) + f_I \cos(\omega t_i)$.

From (A.1) we can see that the log-likelihood function is:

$$\begin{aligned} L(f_R, f_I, r, \omega) &= -\frac{1}{2\sigma^2} \sum_{i=1}^N \left((x_{R,i} - g_{R,i}H(t_i g)e^{-rt_i})^2 + (x_{I,i} - g_{I,i}H(t_i g)e^{-rt_i})^2 \right) \\ &= \frac{1}{2\sigma^2} \sum_{i=1}^N \left(|x_i|^2 - 2x_{R,i}g_{R,i}H(t_i g)e^{-rt_i} - 2x_{I,i}g_{I,i}H(t_i g)e^{-rt_i} + |f|^2 H^2(t_i g)e^{-2rt_i} \right) \end{aligned}$$

For the general case the vector of parameters θ that we wish to estimate is: $\theta = [f_R, f_I, r, \omega]^T$. Since we have a vector of parameters we will derive the vector CRB which is based on calculating the Fisher information matrix.

To find the Fisher information matrix \mathbf{F} we first need to find the partial derivatives of L w.r.t.

the estimation parameters. Hence, we have:

$$\frac{\partial L}{\partial f_R} = \frac{1}{\sigma^2} \sum_{i=1}^N H(t_i g) e^{-rt_i} ((x_{R,i} - \mu_{R,i}) \cos(\omega t_i) - (x_{I,i} - \mu_{I,i}) \sin(\omega t_i)) \quad (\text{A.2})$$

$$= \frac{1}{\sigma^2} \sum_{i=1}^N H(t_i g) e^{-rt_i} (x_{R,i} \cos(\omega t_i) - x_{I,i} \sin(\omega t_i) - f_R H(t_i g) e^{-rt_i})$$

$$\frac{\partial L}{\partial f_I} = \frac{1}{\sigma^2} \sum_{i=1}^N H(t_i g) e^{-rt_i} ((x_{R,i} - \mu_{R,i}) \sin(\omega t_i) + (x_{I,i} - \mu_{I,i}) \cos(\omega t_i)) \quad (\text{A.3})$$

$$= \frac{1}{\sigma^2} \sum_{i=1}^N H(t_i g) e^{-rt_i} (x_{R,i} \sin(\omega t_i) + x_{I,i} \cos(\omega t_i) - f_I H(t_i g) e^{-rt_i})$$

$$\frac{\partial L}{\partial r} = -\frac{1}{\sigma^2} \sum_{i=1}^N t_i H(t_i g) e^{-rt_i} ((x_{R,i} - \mu_{R,i}) g_{R,i} + (x_{I,i} - \mu_{I,i}) g_{I,i}) \quad (\text{A.4})$$

$$= -\frac{1}{\sigma^2} \sum_{i=1}^N t_i H(t_i g) e^{-rt_i} (x_{R,i} g_{R,i} + x_{I,i} g_{I,i} - |f|^2 H(t_i g) e^{-rt_i})$$

$$\frac{\partial L}{\partial \omega} = -\frac{1}{\sigma^2} \sum_{i=1}^N t_i H(t_i g) e^{-rt_i} ((x_{R,i} - \mu_{R,i}) g_{I,i} - (x_{I,i} - \mu_{I,i}) g_{R,i}) \quad (\text{A.5})$$

$$= -\frac{1}{\sigma^2} \sum_{i=1}^N t_i H(t_i g) e^{-rt_i} (x_{R,i} g_{I,i} - x_{I,i} g_{R,i}),$$

where $\mu_{R,i} \triangleq g_{R,i} H(t_i g) e^{-rt_i}$ and $\mu_{I,i} \triangleq g_{I,i} H(t_i g) e^{-rt_i}$.

We now find the matrix \mathbf{F} by taking the expectation of products of the partial derivatives in the form $E \left[\frac{\partial L}{\partial p} \frac{\partial L}{\partial q} \right]$, where p and q are some estimated parameters. Since the random variables $x_{R,i}$, $x_{I,i}$ are independent the cross terms will be zero and thus the matrix \mathbf{F} is

$$\mathbf{F} = \begin{bmatrix} \sum_{i=1}^N b_i/t_i & 0 & -f_R \sum_{i=1}^N b_i & f_I \sum_{i=1}^N b_i \\ 0 & \sum_{i=1}^N b_i/t_i & -f_I \sum_{i=1}^N b_i & -f_R \sum_{i=1}^N b_i \\ -f_R \sum_{i=1}^N b_i & -f_I \sum_{i=1}^N b_i & |f|^2 \sum_{i=1}^N b_i t_i & 0 \\ f_I \sum_{i=1}^N b_i & -f_R \sum_{i=1}^N b_i & 0 & |f|^2 \sum_{i=1}^N b_i t_i \end{bmatrix}$$

where $b_i \triangleq \frac{1}{\sigma^2} t_i H^2(t_i g) e^{-2rt_i}$.

To find the Cramer-Rao lower bound on estimator variance we need to find the diagonal elements of the inverse matrix \mathbf{F}^{-1} . For this purpose we need the determinant $|\mathbf{F}|$ and the minor

determinants $|M_{jj}|$. After some algebra we get:

$$\begin{aligned}
|\mathbf{F}| &= |f|^4 \left(\left(\sum_{i=1}^N b_i/t_i \right) \left(\sum_{i=1}^N b_i t_i \right) - \left(\sum_{i=1}^N b_i \right)^2 \right)^2 \\
M_{11} &= |f|^4 \left(\sum_{i=1}^N b_i t_i \right) \left(\left(\sum_{i=1}^N b_i/t_i \right) \left(\sum_{i=1}^N b_i t_i \right) - \left(\sum_{i=1}^N b_i \right)^2 \right) \\
M_{22} &= |f|^4 \left(\sum_{i=1}^N b_i t_i \right) \left(\left(\sum_{i=1}^N b_i/t_i \right) \left(\sum_{i=1}^N b_i t_i \right) - \left(\sum_{i=1}^N b_i \right)^2 \right) \\
M_{33} &= |f|^2 \left(\sum_{i=1}^N b_i/t_i \right) \left(\left(\sum_{i=1}^N b_i/t_i \right) \left(\sum_{i=1}^N b_i t_i \right) - \left(\sum_{i=1}^N b_i \right)^2 \right) \\
M_{44} &= |f|^2 \left(\sum_{i=1}^N b_i/t_i \right) \left(\left(\sum_{i=1}^N b_i/t_i \right) \left(\sum_{i=1}^N b_i t_i \right) - \left(\sum_{i=1}^N b_i \right)^2 \right)
\end{aligned}$$

For the variance of the image parameters (f_R, f_I) we have:

$$\text{var } \hat{f}_R \geq [\mathbf{F}^{-1}]_{11} = \frac{|M_{11}|}{|\mathbf{F}|} = \frac{\sum_{i=1}^N b_i t_i}{\left(\sum_{i=1}^N b_i/t_i \right) \left(\sum_{i=1}^N b_i t_i \right) - \left(\sum_{i=1}^N b_i \right)^2} \quad (\text{A.6})$$

$$\text{var } \hat{f}_I \geq [\mathbf{F}^{-1}]_{22} = \frac{|M_{22}|}{|\mathbf{F}|} = \frac{\sum_{i=1}^N b_i t_i}{\left(\sum_{i=1}^N b_i/t_i \right) \left(\sum_{i=1}^N b_i t_i \right) - \left(\sum_{i=1}^N b_i \right)^2} \quad (\text{A.7})$$

For the variance of the R_2^* relaxation (r) we have:

$$\text{var } \hat{r} \geq [\mathbf{F}^{-1}]_{33} = \frac{|M_{33}|}{|\mathbf{F}|} = \frac{1}{|f|^2} \frac{\sum_{i=1}^N b_i/t_i}{\left(\sum_{i=1}^N b_i/t_i \right) \left(\sum_{i=1}^N b_i t_i \right) - \left(\sum_{i=1}^N b_i \right)^2} \quad (\text{A.8})$$

Finally, for the variance of the fieldmap (ω) we have:

$$\text{var } \hat{\omega} \geq [\mathbf{F}^{-1}]_{44} = \frac{|M_{44}|}{|\mathbf{F}|} = \frac{1}{|f|^2} \frac{\sum_{i=1}^N b_i/t_i}{\left(\sum_{i=1}^N b_i/t_i \right) \left(\sum_{i=1}^N b_i t_i \right) - \left(\sum_{i=1}^N b_i \right)^2} \quad (\text{A.9})$$

In the subsequent sections we will use the equations derived above to solve the optimization problem of choosing the echo times t_i that minimize these lower bounds.

Optimization problem

Simplified form

To find the optimal echo times we have to solve the following optimization problems:

$$\min_{t_1, \dots, t_n} [\mathbf{F}^{-1}]_{jj} \text{ for } j = 1, 2, 3, 4.$$

As we see from equations (A.6), (A.7), (A.8) and (A.9) an analytic solution may be intractable or computationally intensive. To simplify the optimization problem we will focus on the case of a two measurement model with $t_1 = 0$ and $t_2 = t$. Also for this part we will ignore the effect of through-plane gradients ($H(t_i g) \triangleq 1$). By applying these simplifications and after some algebra we get:

$$[\mathbf{F}^{-1}]_{11} = [\mathbf{F}^{-1}]_{22} = \frac{\frac{1}{\sigma^2} t^2 e^{-2rt}}{\frac{1}{\sigma^4} t^2 e^{-2rt}} = \sigma^2 \quad (\text{A.10})$$

$$[\mathbf{F}^{-1}]_{33} = [\mathbf{F}^{-1}]_{44} = \frac{\frac{1}{\sigma^2} (1 + e^{-2rt})}{\frac{|f|^2}{\sigma^4} t^2 e^{-2rt}} = \frac{\sigma^2}{|f|^2 t^2} (1 + e^{-2rt}) \quad (\text{A.11})$$

From equation (A.10) we see that the lower bounds for image parameter (f_R, f_I) estimation are constant. Thus any choice of echo time t can be considered optimal since it has no effect on the lower bound. From equation (A.11) we can see that the optimal echo time that minimizes the lower bound on variance for r and ω can be found from solving the following optimization problem:

$$\begin{aligned} t_{opt} &= \arg \min_t \frac{\sigma^2}{|f|^2 t^2} (1 + e^{-2rt}) \\ &= \arg \min_t \frac{1}{t^2} (1 + e^{-2rt}) \end{aligned}$$

We can solve this by taking the derivative w.r.t. t and equating to zero which leads to:

$$1 + e^{-2rt} - r t e^{-2rt} = 0.$$

The solution of this problem is:

$$t_{opt} = \frac{1.1089}{r}$$

Effect of through-plane gradients

In this section we will again solve the simplified optimization problem for the case of a two measurement model with $t_1 = 0$ and $t_2 = t$. This time we will account for the effect of through-plane gradients and we will investigate how they affect the solution of the echo time optimization. Taking the equations (A.6), (A.7), (A.8) and (A.9) and applying for the case of two echo times we get:

$$[\mathbf{F}^{-1}]_{11} = [\mathbf{F}^{-1}]_{22} = \frac{\frac{1}{\sigma^2} t^2 H^2(tg) e^{-2rt}}{\frac{1}{\sigma^4} h_0^2 t^2 H^2(tg) e^{-2rt}} = \frac{\sigma^2}{h_0^2} \quad (\text{A.12})$$

$$[\mathbf{F}^{-1}]_{33} = [\mathbf{F}^{-1}]_{44} = \frac{\frac{1}{\sigma^2} (h_0^2 + H^2(tg) e^{-2rt})}{\frac{|f|^2}{\sigma^4} h_0^2 t^2 H^2(tg) e^{-2rt}} = \frac{\sigma^2}{|f|^2 h_0^2 t^2 H^2(tg)} (H^2(tg) + e^{2rt}) \quad (\text{A.13})$$

where $H(u)$ is the Fourier transform of the slice profile and $h_0 \triangleq H(0)$. For simplicity since h_0 is just a scaling factor we can consider $h_0 = 1$.

From equation (A.12) we see again that the lower bounds for image parameter (f_R, f_I) estimation are constant. Thus any choice of echo time t can be considered optimal since it has no effect on the lower bound. From equation (A.13) we can see that the optimal echo time that minimizes the lower bound on variance for r and ω can be found from solving the following optimization problem:

$$\begin{aligned} t_{opt} &= \arg \min_t \frac{\sigma^2}{|f|^2 h_0^2 t^2 H^2(tg)} (H^2(tg) + e^{2rt}) \\ &= \arg \min_t \frac{1}{t^2 H^2(tg)} (H^2(tg) + e^{2rt}) \\ &= \arg \min_t \frac{1}{t^2} + \frac{e^{2rt}}{t^2 H^2(tg)}. \end{aligned} \quad (\text{A.14})$$

This minimization problem depends on the slice profile $H(u)$ and in this case we will try to solve using the simple case of rect slice profile which leads to $H(u) = \text{sinc}(wu)$. Now the problem becomes:

$$\begin{aligned} t_{opt} &= \arg \min_t \frac{1}{t^2 \text{sinc}^2(wtg)} ((\text{sinc}(wtg))^2 + e^{2rt}) \\ &= \arg \min_t \frac{1}{t^2} + \frac{e^{2rt}}{t^2 \text{sinc}^2(wtg)}. \end{aligned} \quad (\text{A.15})$$

An analytic solution for this problem is elusive so we draw some conclusions through simulations.

By setting $y \triangleq rt$ and $p \triangleq wg/r$ we get a parametrized problem:

$$\begin{aligned}
y_{opt} &= \arg \min_y \frac{r^2}{y^2 \operatorname{sinc}^2(y p)} ((\operatorname{sinc}(y p))^2 + e^{2y}) \\
&= \arg \min_y \frac{r^2}{y^2} + \frac{r^2 e^{2y}}{y^2 \operatorname{sinc}^2(y p)}.
\end{aligned} \tag{A.16}$$

From simulations for various values of the parameter p we have seen that by increasing p the values of the solution y decrease (see Figure A.1). This roughly means that for stronger through-plane gradients we require smaller values for the echo times, but still those values will depend on the relaxation parameter r .

Special cases for image and fieldmap estimation

The derivations of the previous sections apply to cases when we want to estimate all parameters. In some interesting cases some of the parameters can be considered known or their effect can be ignored. In this section we will see those cases and we will make analogous derivations comparing the results to the ones presented in the sections A and A.

Estimating image and fieldmap

In this case we estimate the image parameters (f_R, f_I) and the fieldmap ω . First we will see the optimization problem in the full form and then see how it changes by ignoring R_2^* decay and through-plane gradients.

Starting from the partial derivatives of the log likelihood (equations (A.2), (A.3) and (A.5)) we get the Fisher information matrix:

$$\mathbf{F} = \begin{bmatrix} \sum_{i=1}^N b_i/t_i & 0 & f_I \sum_{i=1}^N b_i \\ 0 & \sum_{i=1}^N b_i/t_i & -f_R \sum_{i=1}^N b_i \\ f_I \sum_{i=1}^N b_i & -f_R \sum_{i=1}^N b_i & |f|^2 \sum_{i=1}^N b_i t_i \end{bmatrix}$$

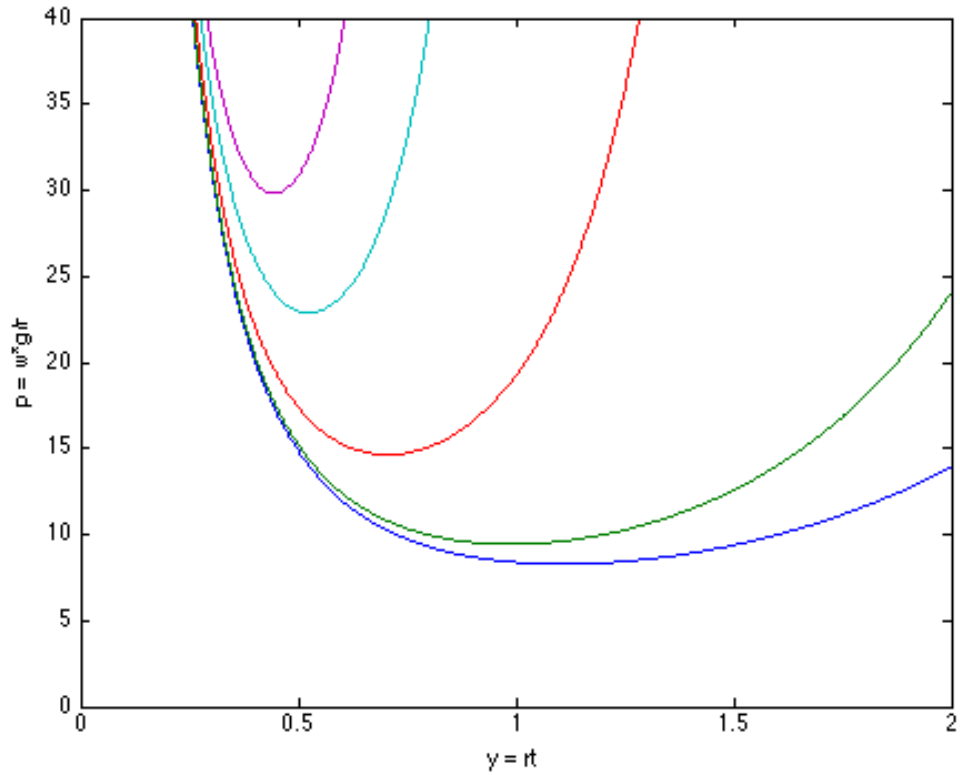


Figure A.1: Plot showing how echo-time is affected by the through-plane gradients. Horizontal axis represents the parameter y depending on the echo-time t , as $y = r t$. Each curve represents a different value of the parameter p (increasing value from bottom to top curve) that depends on the through-plane gradient g , as $p = w g / r$. The curves show that the optimal echo-time (value of y where curve attains minimum value) shifts to the left (smaller echo-time) as the through-plane gradient strength increases (increased values of p). The bottom line corresponds to the case where there are no through plane gradients.

Now we need the determinant $|\mathbf{F}|$ and the minor determinants $|M_{jj}|$. After some algebra we get:

$$\begin{aligned} |\mathbf{F}| &= |f|^2 \left(\sum_{i=1}^N b_i/t_i \right) \left(\left(\sum_{i=1}^N b_i/t_i \right) \left(\sum_{i=1}^N b_i t_i \right) - \left(\sum_{i=1}^N b_i \right)^2 \right) \\ M_{11} &= |f|^2 \left(\sum_{i=1}^N b_i/t_i \right) \left(\sum_{i=1}^N b_i t_i \right) - f_R^2 \left(\sum_{i=1}^N b_i \right)^2 \\ M_{22} &= |f|^2 \left(\sum_{i=1}^N b_i/t_i \right) \left(\sum_{i=1}^N b_i t_i \right) - f_I^2 \left(\sum_{i=1}^N b_i \right)^2 \\ M_{33} &= \left(\sum_{i=1}^N b_i/t_i \right)^2 \end{aligned}$$

For the variance of the image parameters (f_R, f_I) we have:

$$\begin{aligned} \text{var } f_R \geq [\mathbf{F}^{-1}]_{11} &= \frac{|M_{11}|}{|\mathbf{F}|} = \frac{|f|^2 \left(\sum_{i=1}^N b_i/t_i \right) \left(\sum_{i=1}^N b_i t_i \right) - f_R^2 \left(\sum_{i=1}^N b_i \right)^2}{|f|^2 \left(\sum_{i=1}^N b_i/t_i \right) \left(\left(\sum_{i=1}^N b_i/t_i \right) \left(\sum_{i=1}^N b_i t_i \right) - \left(\sum_{i=1}^N b_i \right)^2 \right)} \\ &= \frac{1}{\left(\sum_{i=1}^N b_i/t_i \right)} \left(1 + \frac{f_I^2 \left(\sum_{i=1}^N b_i \right)^2}{|f|^2 \left(\left(\sum_{i=1}^N b_i/t_i \right) \left(\sum_{i=1}^N b_i t_i \right) - \left(\sum_{i=1}^N b_i \right)^2 \right)} \right) \\ \text{var } f_I \geq [\mathbf{F}^{-1}]_{22} &= \frac{|M_{22}|}{|\mathbf{F}|} = \frac{|f|^2 \left(\sum_{i=1}^N b_i/t_i \right) \left(\sum_{i=1}^N b_i t_i \right) - f_I^2 \left(\sum_{i=1}^N b_i \right)^2}{|f|^2 \left(\sum_{i=1}^N b_i/t_i \right) \left(\left(\sum_{i=1}^N b_i/t_i \right) \left(\sum_{i=1}^N b_i t_i \right) - \left(\sum_{i=1}^N b_i \right)^2 \right)} \\ &= \frac{1}{\left(\sum_{i=1}^N b_i/t_i \right)} \left(1 + \frac{f_R^2 \left(\sum_{i=1}^N b_i \right)^2}{|f|^2 \left(\left(\sum_{i=1}^N b_i/t_i \right) \left(\sum_{i=1}^N b_i t_i \right) - \left(\sum_{i=1}^N b_i \right)^2 \right)} \right) \end{aligned}$$

and for the variance of the fieldmap (ω) we have:

$$\text{var } \omega \geq [\mathbf{F}^{-1}]_{33} = \frac{|M_{33}|}{|\mathbf{F}|} = \frac{1}{|f|^2} \frac{\sum_{i=1}^N b_i/t_i}{\left(\sum_{i=1}^N b_i/t_i \right) \left(\sum_{i=1}^N b_i t_i \right) - \left(\sum_{i=1}^N b_i \right)^2}$$

As we see from the lower bound for the variance of the image parameters, direct minimization may be intractable. Hence, we will try to minimize using the simplified two measurement model,

which after some algebra leads to:

$$\begin{aligned}
[\mathbf{F}^{-1}]_{11} &= \frac{1}{\frac{1}{\sigma^2}(h_0^2 + H^2(tg)e^{-2rt})} \left(1 + \frac{f_I^2}{|f|^2 h_0^2} H^2(tg)e^{-2rt} \right) \\
&= \frac{|f|^2 h_0^2 + f_I^2 H^2(tg)e^{-2rt}}{\frac{1}{\sigma^2} |f|^2 h_0^2 (h_0^2 + H^2(tg)e^{-2rt})} \\
&= \frac{\sigma^2}{h_0^2} \left(1 - \frac{f_R^2}{|f|^2 \left(1 + \frac{h_0^2}{H^2(tg)} e^{2rt} \right)} \right) \\
[\mathbf{F}^{-1}]_{22} &= \frac{1}{\frac{1}{\sigma^2}(h_0^2 + H^2(tg)e^{-2rt})} \left(1 + \frac{f_R^2}{|f|^2 h_0^2} H^2(tg)e^{-2rt} \right) \\
&= \frac{|f|^2 h_0^2 + f_R^2 H^2(tg)e^{-2rt}}{\frac{1}{\sigma^2} |f|^2 h_0^2 (h_0^2 + H^2(tg)e^{-2rt})} \\
&= \frac{\sigma^2}{h_0^2} \left(1 - \frac{f_I^2}{|f|^2 \left(1 + \frac{h_0^2}{H^2(tg)} e^{2rt} \right)} \right)
\end{aligned}$$

From the above equations the minimization problem for the real part can be formed as:

$$\begin{aligned}
t_{opt} &= \arg \min_t \frac{\sigma^2}{h_0^2} \left(1 - \frac{f_I^2}{|f|^2 \left(1 + \frac{h_0^2}{H^2(tg)} e^{2rt} \right)} \right) \\
&= \arg \max_t \frac{1}{1 + \frac{h_0^2}{H^2(tg)} e^{2rt}} \\
&= \arg \min_t \frac{1}{H^2(tg)} e^{2rt}
\end{aligned}$$

By following the same derivation we end up in the same problem for the imaginary part of the image. Now from the above equation we can see the minimizer is $t = 0$ if we assume that the slice profile function is maximum at zero (this holds true for the rect profile). If we ignore through-plane gradients the results is the same and if we ignore R_2^* decay then the result depends only on the maximum of the slice profile, which is again zero for the rect profile. Ignoring both terms makes the function to be minimized a constant and any choice of t can be considered as a solution to the problem.

Now, as we see from the lower bound on the variance of the fieldmap it is the same as the one derived in the previous sections. This means that the optimization problem in this case is the same as before and the solutions we found apply to this case. The only case that we need to consider is when we ignore the R_2^* relaxation ($r = 0$). In this case and for the two measurement model equation (A.13) becomes:

$$[\mathbf{F}^{-1}]_{33} = \frac{\frac{1}{\sigma^2}(h_0^2 + H^2(tg))}{\frac{|f|^2}{\sigma^4}h_0^2t^2H^2(tg)} = \frac{\sigma^2}{|f|^2h_0^2t^2H^2(tg)}(1 + H^2(tg))$$

Now the minimization problem becomes:

$$\begin{aligned} t_{opt} &= \arg \min_t \frac{\sigma^2}{|f|^2h_0^2t^2H^2(tg)}(1 + H^2(tg)) \\ &= \arg \min_t \frac{1}{t^2H^2(tg)}(1 + H^2(tg)) \end{aligned}$$

Using the rect slice profile we have:

$$\begin{aligned} t_{opt} &= \arg \min_t \frac{1}{t^2 \text{sinc}^2(wgt)}(1 + \text{sinc}^2(wgt)) \\ &= \arg \min_t \frac{1}{t^2} + \frac{\pi^2 w^2 g^2}{\sin^2(\pi wgt)} \end{aligned}$$

We can easily see that the first term is minimized when t goes to infinity and the second term when the sine is maximized which means $t = \frac{1}{wg}(k + \frac{1}{2})$. Combining both we see that the optimal echo time is when t goes to infinity and is of the previous form which means choose $t = \frac{1}{wg}(k + \frac{1}{2})$ for large k .

If we also ignore the through-plane gradients then we have:

$$[\mathbf{F}^{-1}]_{33} = \frac{2\frac{1}{\sigma^2}}{\frac{|f|^2}{\sigma^4}t^2} = \frac{2\sigma^2}{|f|^2t^2}$$

From that we see that the optimal echo time would be for time going to infinity which may make sense since larger echo time leads to better estimation of the fieldmap, but such a choice is not feasible. We could say that it would be reasonable to choose the largest possible time such that the effect of R_2^* and others can still be ignored without significant error in the computation.

Estimating fieldmap and R_2^* decay

In this case we estimate the fieldmap (ω) and the R_2^* decay r , while we consider the image parameters to be known. First we will see the optimization problem in the full form and then see how it changes by ignoring through-plane gradients.

Starting from the partial derivatives of the log likelihood (equations (A.5) and (A.4)) we get the Fisher information matrix:

$$\mathbf{F} = \begin{bmatrix} |f|^2 \sum_{i=1}^N b_i t_i & 0 \\ 0 & |f|^2 \sum_{i=1}^N b_i t_i \end{bmatrix}$$

It is easy to see that the determinant is:

$$|\mathbf{F}| = |f|^4 \left(\sum_{i=1}^N b_i t_i \right)^2$$

and the lower bounds on variance are:

$$[\mathbf{F}^{-1}]_{11} = [\mathbf{F}^{-1}]_{22} = \frac{1}{|f|^2 \left(\sum_{i=1}^N b_i t_i \right)}$$

Instead of trying to minimize the lower bound we will try to maximize the inverse. Thus we will solve the problem:

$$\begin{aligned} \max_{t_i} \frac{1}{[\mathbf{F}^{-1}]_{11}} &= \max_{t_i} |f|^2 \left(\sum_{i=1}^N b_i t_i \right) \\ &= \max_{t_i} \frac{1}{\sigma^2} |f|^2 \sum_{i=1}^N t_i^2 H^2(t_i g) e^{-2rt_i} \\ &= \max_{t_i} \sum_{i=1}^N t_i^2 H^2(t_i g) e^{-2rt_i} \end{aligned}$$

As we see this problem can be solved independently for each t_i since by taking the derivatives only

the corresponding term is non-zero. Hence, for every t_i we solve the problem:

$$\begin{aligned} t_{opt} &= \arg \max_{t_i} t_i^2 H^2(t_i g) e^{-2rt_i} \\ &= \arg \min_{t_i} \frac{e^{2rt_i}}{t_i^2 H^2(t_i g)}. \end{aligned} \quad (\text{A.17})$$

Comparing (A.17) with (A.14) we see that they only differ in the additive term $\frac{1}{t_i^2}$. This term can be viewed as the effect of the unknown image (which is a nuisance parameter when estimating the fieldmap) in the optimization problem.

Without ignoring the through-plane gradients and considering a rect slice profile we have:

$$\begin{aligned} t_{opt} &= \arg \min_{t_i} \frac{e^{2rt_i}}{t_i^2 \text{sinc}^2(\omega t_i g)} \\ &= \arg \min_{t_i} \frac{\pi^2 \omega^2 g^2 e^{2rt_i}}{\sin^2(\pi \omega t_i g)}. \end{aligned} \quad (\text{A.18})$$

If we apply a parametrization similar to the one in equation (A.16) we get the following expression:

$$y_{opt} = \arg \min_y \frac{r^2 e^{2y}}{y^2 \text{sinc}^2(y p)}. \quad (\text{A.19})$$

From equation (A.18) we see that the solution oscillates and the minimum can roughly be found for the smallest possible value of t_i such that the sine is maximized. We can see this intuitive result in Figure A.2 where we plot equation (A.19) for several values of the parameter p . Again we see that the presence of through-plane gradients will lead to smaller values for the optimal echo times.

This intuition can be verified by the analytic solution of this problem. Therefore, by taking the derivative and equating to zero we have:

$$\begin{aligned} \frac{\pi^2 \omega^2 g^2 (2r e^{2rt_i} \sin^2(\pi \omega t_i g) - 2\pi \omega g \sin(\pi \omega t_i g) \cos(\pi \omega t_i g) e^{2rt_i})}{\sin^4(\pi \omega t_i g)} &= 0 \\ 2\pi^2 \omega^2 g^2 e^{2rt_i} (r \sin(\pi \omega t_i g) - \pi \omega g \cos(\pi \omega t_i g)) &= 0 \\ r \sin(\pi \omega t_i g) - \pi \omega g \cos(\pi \omega t_i g) &= 0 \\ \tan(\pi \omega g t_i) &= \frac{\pi \omega g}{r} \\ t_i &= \frac{\arctan\left(\frac{\pi \omega g}{r}\right)}{\pi \omega g} \end{aligned}$$

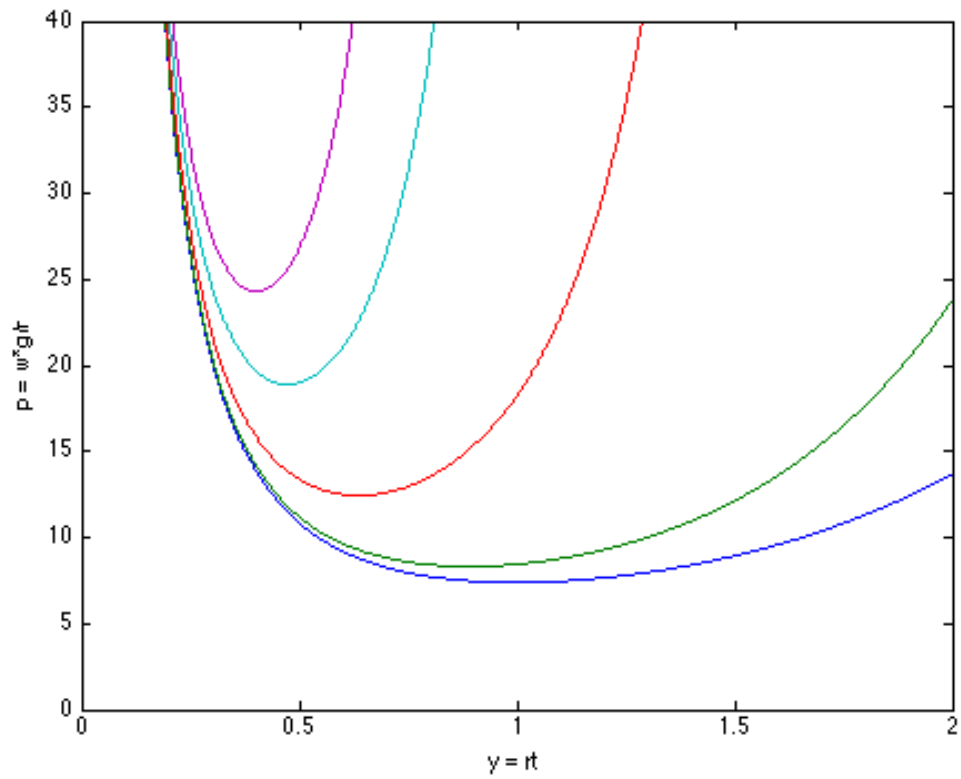


Figure A.2: Plot showing how echo-time is affected by the through-plane gradients similarly to Figure A.1. The bottom line corresponds to the case where there are no through plane gradients. Comparing to Figure A.1 we see that the optimal echo-times have slightly smaller values for the same value of the parameter p .

The last equation is the solution to the minimization problem and applies for each t_i .

Now we will solve the problem by ignoring the effect of through-plane gradients and the minimization problem becomes:

$$t_{opt} = \arg \min_{t_i} \frac{1}{t_i^2} e^{2rt_i}.$$

For this case we have the well known solution:

$$t_{opt} = \frac{1}{r}.$$

The solutions we found apply to both parameters r and ω . Also since the formulation is independent for each parameter we would get the same results if we tried to estimate only one parameter (either r or ω).

In the case that we only estimate r we can ignore the field inhomogeneity in some cases. However, since ω is not involved in the optimization process the results will be the same with the ones presented previously.

Another interesting case is to see how the optimization problem changes when we only estimate ω and we ignore R_2^* decay. In this case the problem is formulated as:

$$t_{opt} = \arg \min_{t_i} \frac{1}{t_i^2 H^2(t_i g)}.$$

Considering the rect slice profile we can see that the solution can be found as:

$$\begin{aligned} t_{opt} &= \arg \min_{t_i} \frac{1}{t_i^2 \text{sinc}^2(\pi w g t_i)} \\ &= \arg \min_{t_i} \frac{\pi^2 w^2 g^2}{\sin^2(\pi w g t_i)} \\ &= \arg \max_{t_i} \sin^2(\pi w g t_i) \\ &= \frac{1}{w g} \left(k + \frac{1}{2} \right) \text{ for } k = 0, 1, 2, \dots \end{aligned}$$

From the last equation we see that we have infinite choices for the optimal echo times. The smallest echo time that satisfies the optimization problem is $t_i = \frac{1}{2wg}$.

Now if we ignore the effect of through-plane dephasing we have the following problem:

$$t_{opt} = \arg \min_{t_i} \frac{1}{t_i^2}.$$

Obviously the solution of this problem is for t_i going to infinity and we have seen a similar result in a previous case (see section A).

Estimating image

The last special case of interest is when we only estimate the image parameters (f_R and f_I) and we consider the fieldmap and R_2^* decay as known. Later we will also derive results for cases when we can ignore these two effects.

Starting from the partial derivatives of the log likelihood (equations (A.2) and (A.3)) we get the Fisher information matrix:

$$\mathbf{F} = \begin{bmatrix} \sum_{i=1}^N b_i/t_i & 0 \\ 0 & \sum_{i=1}^N b_i/t_i \end{bmatrix}$$

It is easy to see that the determinant is:

$$|\mathbf{F}| = \left(\sum_{i=1}^N b_i/t_i \right)^2$$

and the lower bounds on variance are:

$$[\mathbf{F}^{-1}]_{11} = [\mathbf{F}^{-1}]_{22} = \frac{1}{\sum_{i=1}^N b_i/t_i}$$

Instead of trying to minimize the lower bound we will try to maximize the inverse. Thus we will

solve the problem:

$$\begin{aligned}
\max_{t_i} \frac{1}{[\mathbf{F}^{-1}]_{11}} &= \max_{t_i} \sum_{i=1}^N b_i/t_i \\
&= \max_{t_i} \frac{1}{\sigma^2} \sum_{i=1}^N H^2(t_i g) e^{-2rt_i} \\
&= \max_{t_i} \sum_{i=1}^N H^2(t_i g) e^{-2rt_i}
\end{aligned}$$

As we see this problem can be solved independently for each t_i since by taking the derivatives only the corresponding term is non-zero. Hence, for every t_i we solve the problem:

$$t_{opt} = \arg \max_{t_i} H^2(t_i g) e^{-2rt_i}.$$

Assuming that the function of the slice profile has its maximum at zero (which is true for the rect profile) we can easily see that the above problem is maximized for $t_i = 0$. This solution does not change if we ignore field inhomogeneity since the parameter ω does not appear in the problem and if we also ignore the through-plane gradients since we only maximize the factor e^{-2rt_i} . If we ignore the R_2^* decay the maximum depends only on the function of the slice profile and we have to find t_i that maximizes $H^2(t_i g)$. For the rect profile this happens again at $t_i = 0$. Finally if we ignore all other effects then the function we wish to maximize is just a constant and then any choice of t_i can be a solution to the problem.

Trajectory Performance

Motivation

CRB Derivation

The Cramér-Rao analysis is based on the Complex CRB methods presented in [12]. Assuming a complex circularly Gaussian noise model and the measurement model of (4.5), the measurement vector \mathbf{y} is a Gaussian random vector with mean

$$\mathbf{m} = \tilde{\mathbf{A}}(\omega) \mathbf{f}$$

and covariance matrix

$$\mathbf{R} = \sigma^2 \mathbf{I}_N,$$

and for simplicity we will also assume that the image \mathbf{f} is real. Following the method in [12] we have:

$$\tilde{\mathbf{m}} \triangleq \begin{bmatrix} \mathbf{m} \\ \mathbf{m}^* \end{bmatrix} = \begin{bmatrix} \tilde{\mathbf{A}}(\boldsymbol{\omega}) \mathbf{f} \\ \tilde{\mathbf{A}}^*(\boldsymbol{\omega}) \mathbf{f} \end{bmatrix}$$

and

$$\tilde{\mathbf{R}} \triangleq \begin{bmatrix} \mathbf{R} & \mathbf{0} \\ \mathbf{0} & \mathbf{R}^* \end{bmatrix} = \sigma^2 \mathbf{I}_{2N},$$

where $*$ denotes complex conjugation. Now using the Slepian-Bangs formula the elements of the Fisher information matrix are given by

$$[\mathbf{F}]_{mn} = \left(\frac{\partial \tilde{\mathbf{m}}}{\partial \theta_m} \right)' \tilde{\mathbf{R}}^{-1} \left(\frac{\partial \tilde{\mathbf{m}}}{\partial \theta_n} \right), \quad (\text{A.20})$$

where $'$ denotes conjugate transpose and the parameter vector is $\boldsymbol{\theta} \triangleq \begin{bmatrix} \mathbf{f} \\ \boldsymbol{\omega} \end{bmatrix}$. For this parameter vector we have

$$\frac{\partial \tilde{\mathbf{m}}}{\partial f_n} = \begin{bmatrix} \tilde{\mathbf{A}} \mathbf{e}_n \\ \tilde{\mathbf{A}}^* \mathbf{e}_n \end{bmatrix} \quad (\text{A.21})$$

and

$$\frac{\partial \tilde{\mathbf{m}}}{\partial \omega_n} = \begin{bmatrix} -i \tilde{\mathbf{D}}_t \tilde{\mathbf{A}} \mathbf{e}_n f_n \\ i \tilde{\mathbf{D}}_t \tilde{\mathbf{A}}^* \mathbf{e}_n f_n \end{bmatrix}, \quad (\text{A.22})$$

where \mathbf{e}_n is an indicator vector with only one “1” at the n th position and $\tilde{\mathbf{D}}_t$ is a diagonal matrix of sampling times

$$\tilde{\mathbf{D}}_t \triangleq \mathbf{I}_K \otimes \text{diag}\{t_m\} \text{ for } m = 1, \dots, M.$$

Using (A.20), (A.21), (A.22) and the fact that $\tilde{\mathbf{R}}^{-1} = \frac{1}{\sigma^2} \mathbf{I}_{2N}$, the Fisher information matrix is given by:

$$\mathbf{F} = \frac{2}{\sigma^2} \begin{bmatrix} \Re\{\tilde{\mathbf{A}}' \tilde{\mathbf{A}}\} & \Im\{\tilde{\mathbf{A}}' \tilde{\mathbf{D}}_t \tilde{\mathbf{A}}\} \mathbf{D}_f \\ -\mathbf{D}_f \Im\{\tilde{\mathbf{A}} \tilde{\mathbf{D}}_t \tilde{\mathbf{A}}\} & \mathbf{D}_f \Re\{\tilde{\mathbf{A}} \tilde{\mathbf{D}}_t^2 \tilde{\mathbf{A}}\} \mathbf{D}_f \end{bmatrix}, \quad (\text{A.23})$$

where $\mathbf{D}_f \triangleq \text{diag}\{f_n\}$ for $n = 1, \dots, N$.

The general expression for the Fisher information matrix in (A.23) applies to any trajectory, but it does not provide any insight on the variance bounds and it is also impractical for computational purposes since it requires the inversion of a large $2N \times 2N$ matrix. To simplify the analysis and acquire a tractable form of the Fisher information matrix we will assume the use of Cartesian (or EPI) trajectories, with Dirac basis functions, of size $N = N_x N_y$ for an image with $N_x N_y$ pixels and we will also assume that the sampling of each readout line happens simultaneously, thus reducing the number of distinct sampling points from N to only $N_y = \sqrt{N}$ for a square image.

Under the above simplifications the elements of the system matrix $\tilde{\mathbf{A}}$ can be written as:

$$\begin{aligned} a_{(k,m),n} &= e^{-i\omega_{(n_x, n_y)} t_{(m_x, m_y)}} e^{-i2\pi \mathbf{k}(t_{(m_x, m_y)}) \cdot \mathbf{r}_{(n_x, n_y)}} c_{k, (n_x, n_y)} \\ &= e^{-i\omega_{(n_x, n_y)} t_{m_y}} e^{-i2\pi n_x m_x / N_x} e^{-i2\pi n_y m_y / N_y} c_{k, (n_x, n_y)}, \end{aligned}$$

where the paired indexes $((m_x, m_y), (n_x, n_y))$ are equivalent to the vectorized indexes (m, n) . Now we can rewrite the blocks of the Fisher information matrix (A.23) using the following simplifications:

$$\begin{aligned} \left[\tilde{\mathbf{A}}' \tilde{\mathbf{A}} \right]_{n, n'} &= \sum_{k=1}^K c_{k, n'}^* c_{k, n} \sum_{m_x=1}^{N_x} e^{-i2\pi(n_x - n'_x) m_x / N_x} \sum_{m_y=1}^{N_y} e^{-i(\omega_n - \omega_{n'}) t_{m_y}} e^{-i2\pi(n_y - n'_y) m_y / N_y} \\ &= N_x \delta[n_x - n'_x] \sum_{k=1}^K c_{k, n'}^* c_{k, n} \sum_{m_y=1}^{N_y} e^{-i(\omega_n - \omega_{n'}) t_{m_y}} e^{-i2\pi(n_y - n'_y) m_y / N_y} \end{aligned} \quad (\text{A.24})$$

$$\left[\tilde{\mathbf{A}}' \tilde{\mathbf{D}}_t \tilde{\mathbf{A}} \right]_{n, n'} = N_x \delta[n_x - n'_x] \sum_{k=1}^K c_{k, n'}^* c_{k, n} \sum_{m_y=1}^{N_y} e^{-i(\omega_n - \omega_{n'}) t_{m_y}} e^{-i2\pi(n_y - n'_y) m_y / N_y} t_{m_y} \quad (\text{A.25})$$

$$\left[\tilde{\mathbf{A}}' \tilde{\mathbf{D}}_{\mathbf{t}}^2 \tilde{\mathbf{A}} \right]_{n,n'} = N_x \delta[n_x - n'_x] \sum_{k=1}^K c_{k,n'}^* c_{k,n} \sum_{m_y=1}^{N_y} e^{-i(\omega_n - \omega_{n'}) t_{m_y}} e^{-i2\pi(n_y - n'_y) m_y / N_y} t_{m_y}^2 \quad (\text{A.26})$$

From the expressions in (A.24), (A.25) and (A.26) we see that the blocks of the Fisher information matrix reduce to diagonal block matrices and by rearranging the matrix in (A.23) we can write it as a diagonal block matrix

$$\mathbf{F} = \text{diag}\{\mathbf{F}_i\} \text{ for } i = 1, \dots, N_x. \quad (\text{A.27})$$

Each block \mathbf{F}_i is given by:

$$\mathbf{F}_i = \frac{2N_x}{\sigma^2} \begin{bmatrix} \Re\{\tilde{\mathbf{A}}_i' \tilde{\mathbf{A}}_i\} & \Im\{\tilde{\mathbf{A}}_i' \mathbf{D}_{\mathbf{t}} \tilde{\mathbf{A}}_i\} \mathbf{D}_{\mathbf{f},i} \\ \mathbf{D}_{\mathbf{f},i} \Im\{\tilde{\mathbf{A}}_i' \mathbf{D}_{\mathbf{t}} \tilde{\mathbf{A}}_i\}' & \mathbf{D}_{\mathbf{f},i} \Re\{\tilde{\mathbf{A}}_i' \mathbf{D}_{\mathbf{t}}^2 \tilde{\mathbf{A}}_i\} \mathbf{D}_{\mathbf{f},i} \end{bmatrix}, \quad (\text{A.28})$$

where $\mathbf{D}_{\mathbf{f},i}$ is a diagonal matrix from the i th row of \mathbf{f} , $\mathbf{D}_{\mathbf{f},i} \triangleq \text{diag}\{f_{i,j}\}$, $j = 1, \dots, N_y$, $\mathbf{D}_{\mathbf{t}}$ is a diagonal matrix from the sample times of each phase encode, $\mathbf{D}_{\mathbf{t}} \triangleq \mathbf{I}_K \otimes \text{diag}\{t_{m_y}\}$, $m_y = 1, \dots, N_y$, and $\tilde{\mathbf{A}}_i$ is a $KN_y \times N_y$ matrix given by

$$\tilde{\mathbf{A}}_i \triangleq \begin{bmatrix} \mathbf{A}_i \mathbf{S}_{i,1} \\ \vdots \\ \mathbf{A}_i \mathbf{S}_{i,K} \end{bmatrix},$$

where $\mathbf{S}_{i,k}$ is a diagonal matrix from the i th row of the sensitivity map of the k th coil, $\mathbf{S}_{i,k} \triangleq \text{diag}\{c_{k,(i,j)}\}$, $j = 1, \dots, N_y$, $k = 1, \dots, K$, and \mathbf{A}_i is a 1D MRI encoding matrix, of size $N_y \times N_y$, that depends on the i th row of the fieldmap $\boldsymbol{\omega}_i$, with elements given by

$$a_{m_y,j}(\boldsymbol{\omega}_i) = e^{-i\omega_{i,j} t_{m_y}} e^{-i2\pi m_y j / N_y}.$$

As we see from (A.27), the diagonal block structure of the Fisher information matrix reduces the CRB analysis of the joint reconstruction to the analysis of N_x smaller 1D reconstructions. Thus, the numerical computation of the CRB can be performed efficiently, since it requires only the inversion of the smaller blocks \mathbf{F}_i (A.28). However, the expression in (A.28) still does not provide any insight on how the CRB is affected by the choice of trajectory (standard or ‘‘interleaved’’ EPI) and other imaging parameters. To achieve that, further assumptions on the structure of the Fisher information matrix are required.

Using the block inversion formulas on (A.28) and by defining $\mathbf{H}_{f,i} \triangleq \Re\{\tilde{\mathbf{A}}_i' \tilde{\mathbf{A}}_i\}$, $\mathbf{H}_{f\omega,i} \triangleq \Im\{\tilde{\mathbf{A}}_i' \mathbf{D}_t \tilde{\mathbf{A}}_i\}$, and $\mathbf{H}_{\omega,i} \triangleq \Re\{\tilde{\mathbf{A}}_i' \mathbf{D}_t^2 \tilde{\mathbf{A}}_i\}$ we have

$$\begin{aligned} \mathbf{F}_{f,i}^{-1} &\triangleq \frac{\sigma^2}{2N_x} (\mathbf{H}_{f,i} - \mathbf{H}'_{f\omega,i} \mathbf{D}_{f,i} \mathbf{D}_{f,i}^{-1} \mathbf{H}_{\omega,i}^{-1} \mathbf{D}_{f,i}^{-1} \mathbf{D}_{f,i} \mathbf{H}_{f\omega,i})^{-1} \\ &= \frac{\sigma^2}{2N_x} (\mathbf{H}_{f,i} - \mathbf{H}'_{f\omega,i} \mathbf{H}_{\omega,i}^{-1} \mathbf{H}_{f\omega,i})^{-1} \end{aligned} \quad (\text{A.29})$$

$$\begin{aligned} \mathbf{F}_{\omega,i}^{-1} &\triangleq \frac{\sigma^2}{2N_x} (\mathbf{D}_{f,i} \mathbf{H}_{\omega,i} \mathbf{D}_{f,i} - \mathbf{D}_{f,i} \mathbf{H}'_{f\omega,i} \mathbf{H}_{f,i}^{-1} \mathbf{H}_{f\omega,i} \mathbf{D}_{f,i})^{-1} \\ &= \frac{\sigma^2}{2N_x} \mathbf{D}_{f,i}^{-1} (\mathbf{H}_{\omega,i} - \mathbf{H}'_{f\omega,i} \mathbf{H}_{f,i}^{-1} \mathbf{H}_{f\omega,i})^{-1} \mathbf{D}_{f,i}^{-1} \end{aligned} \quad (\text{A.30})$$

Now, we can use the expressions in (A.29) and (A.30) to calculate the CRB for any given pixel (i, j) of the image and fieldmap as follows:

$$\begin{aligned} \text{var}\{f_{i,j}\} &\geq [\mathbf{F}_{f,i}^{-1}]_{j,j} \\ &= \frac{\sigma^2}{2N_x} \left[(\mathbf{H}_{f,i} - \mathbf{H}'_{f\omega,i} \mathbf{H}_{\omega,i}^{-1} \mathbf{H}_{f\omega,i})^{-1} \right]_{j,j} \end{aligned} \quad (\text{A.31})$$

$$\begin{aligned} \text{var}\{\omega_{i,j}\} &\geq [\mathbf{F}_{\omega,i}^{-1}]_{l,l} \\ &= \frac{\sigma^2}{2N_x f_{i,j}^2} \left[(\mathbf{H}_{\omega,i} - \mathbf{H}'_{f\omega,i} \mathbf{H}_{f,i}^{-1} \mathbf{H}_{f\omega,i})^{-1} \right]_{j,j} \end{aligned} \quad (\text{A.32})$$

From (A.32) we see an explicit dependence of the fieldmap variance on the image magnitude at the given pixel. This dependence essentially means that higher magnitude values lead to higher SNR and in turn to lower variance. Since, this dependence is well understood and simple to quantify we will consider from now on a uniform image, so that we can focus on the dependence of the CRB on implicit parameters like the trajectory choice and the fieldmap.

For a given trajectory choice the expressions in (A.31) and (A.32) can be used to calculate the CRB provided that the fieldmap is known. However, the fieldmap is an unknown parameter to be estimated, but these expressions can still be used by using the initial fieldmap estimate instead of the actual fieldmap. Unfortunately, we cannot use these expressions to find an optimal trajectory for joint reconstruction or optimize the parameters (like echo-time or readout duration) of a chosen trajectory. Thus, in this work, we will evaluate the CRB for the standard and “interleaved” EPI trajectories presented in §4.3, using the true fieldmap for the simulation data and the initial fieldmap estimate for the phantom and brain data. We will also compare the CRB for joint estimation to the CRB for “oracle” image estimation (known fieldmap) and fieldmap estimation (known image).

The expression for these “oracle” bounds are given by

$$\begin{aligned}
\text{var}\{f_{i,j}\} &\geq \frac{\sigma^2}{2N_x} [\mathbf{H}_{f,i}^{-1}]_{j,j} \\
&\approx \frac{\sigma^2}{2N_x N_y s_{i,j}} \\
&\approx \frac{\sigma^2}{2N_x N_y} \text{ for single coil} \\
\text{var}\{\omega_{i,j}\} &\geq \frac{\sigma^2}{2N_x f_{i,j}^2} [\mathbf{H}_{\omega,i}^{-1}]_{j,j} \\
&\approx \frac{\sigma^2}{2N_x N_y T_E^2 s_{i,j}} \\
&\approx \frac{\sigma^2}{2N_x N_y T_E^2} \text{ for single coil,}
\end{aligned}$$

assuming the image is uniform, where $s_{i,j} \triangleq \sum_{k=1}^K |c_{k,(i,j)}|^2$ and T_E is the echo-time defined in this case as the time at the midpoint of the readout. The approximate expressions were derived under the assumption that the implicit effect of the fieldmap on the encoding matrix can be ignored and provide the lowest possible bound. As we will see from the results, the actual oracle bounds are affected by the effects of the fieldmap.

APPENDIX B

Accelerated Edge-Preserving Image Restoration Without Boundary Artifacts

To reduce blur in noisy images, regularized image restoration methods have been proposed that use non-quadratic regularizers (like l_1 regularization or total-variation) that suppress noise while preserving edges in the image. Most of these methods assume a circulant blur (periodic convolution with a blurring kernel) that can lead to wraparound artifacts along the boundaries of the image due to the implied periodicity of the circulant model. Using a non-circulant model could prevent these artifacts at the cost of increased computational complexity.

In this work we propose to use a circulant blur model combined with a masking operator that prevents wraparound artifacts. The resulting model is non-circulant, so we propose an efficient algorithm using variable splitting and augmented Lagrangian (AL) strategies. Our variable splitting scheme when combined with the AL framework and alternating minimization leads to simple linear systems that can be solved non-iteratively using FFTs, eliminating the need for more expensive CG-type solvers. The proposed method can also efficiently tackle a variety of convex regularizers including edge-preserving (*e.g.*, total-variation) and sparsity promoting (*e.g.*, l_1 norm) regularizers. Simulation results show fast convergence of the proposed method, along with improved image quality at the boundaries where the circulant model is inaccurate.

Introduction

Image restoration is a well studied problem and there are several proposed methods for deblurring and denoising. Usually image restoration is treated as an optimization problem where

The work in this chapter appears in [11].

the restored image is obtained by minimizing a cost function consisting of a data fidelity term and a regularization term. The data fidelity term ensures good fit of the blur model to the measurements, and the regularizer ensures stability of the solution and incorporates smoothness to suppress noise. A quadratic data fidelity term is often used, based on the additive zero-mean Gaussian noise model. For the regularizer, using a quadratic term can lead to over-smoothing. Recently there is increasing interest in non-quadratic regularizers, especially edge-preserving ones like total variation (TV) [47–49] and sparsity promoting ones like l_1 regularization [50, 51].

Most existing restoration methods make simplifying assumptions concerning the system model and the most common one is the use of a circulant blurring model [49–56] because it facilitates FFT-based optimization (*e.g.*, non-iterative matrix inversions [52, 56]). Despite its popularity, the purely circulant model is inaccurate, since it implies an unrealistic periodic extension at the image boundaries that can lead to severe reconstruction artifacts [2].

In this work we focus on a more realistic non-circulant blurring model that is shift-invariant within the region of interest and propose an efficient algorithm for image restoration with non-quadratic regularization. Our model is equivalent to that proposed in [2], and similarly to [57] we focus on edge-preserving regularizers instead of the quadratic regularizer used in [2]. However, unlike [2, 57] which treat boundaries explicitly via a low-dimensional auxiliary variable, our approach is based on an elegant formulation that requires no pre-processing of the data or explicit treatment of the unknown, extrapolated boundaries. In addition, the methods in [2, 57] require CG-type solvers to optimize the associated auxiliary variable that is avoided in our proposed algorithm based on the AL framework with variable splitting.

Our formulation combines a circulant blur model with a masking operator to prevent wrap-around artifacts. Then we use a specific variable splitting strategy that decouples the circulant blur and the mask. When combined with the AL framework and alternating minimization, our splitting leads to an iterative algorithm with simple update steps that can be implemented non-iteratively in closed-form. We present numerical results that illustrate the improved quality of reconstructed images using a non-circulant model and also the improved convergence speed of our proposed algorithm compared to other state-of-the-art methods that can be used to tackle the non-circulant reconstruction problem.

Problem Formulation

Regularized image restoration can be approached in two main ways. One is the analysis formulation [58], where the objective is to obtain an estimate of the true image $\hat{\mathbf{x}}$, and the other is the

synthesis formulation [50], where the objective is to estimate a set of transform coefficients $\hat{\mathbf{w}}$ and obtain the reconstructed image through a transform as $\hat{\mathbf{x}} = \mathbf{W}\hat{\mathbf{w}}$. In this work, we focus on the analysis formulation. Our approach can be extended to the synthesis one using techniques similar to that proposed in [52].

For image restoration, we consider the following analysis formulation, where the image estimate $\hat{\mathbf{x}}$ is obtained by minimizing a cost function

$$\hat{\mathbf{x}} = \underset{\mathbf{x}}{\operatorname{argmin}} \left\{ \Psi(\mathbf{x}) \triangleq J(\mathbf{x}) + \lambda\Phi(\mathbf{R}\mathbf{x}) \right\}, \quad (\text{B.1})$$

$J(\cdot)$ is the data fidelity term, $\Phi(\cdot)$ is a regularizer function, \mathbf{R} is a sparsifying transform (*e.g.*, wavelet frames or finite differences) and λ is the regularization parameter.

Data Fidelity

To design a restoration algorithm one must make some modeling assumptions. Often deblurring algorithms are developed assuming a circulant blur model represented by $\check{\mathbf{A}}$ and the data fidelity term is modeled as [49–56]:

$$J(\check{\mathbf{x}}) \triangleq \|\mathbf{y} - \check{\mathbf{A}}\check{\mathbf{x}}\|_2^2 \quad (\text{B.2})$$

where \mathbf{y} is the observed ($M \times 1$) vectorized blurred and noisy image, $\check{\mathbf{x}}$ is the vectorized ($M \times 1$) image to be reconstructed, and $\check{\mathbf{A}}$ is a ($M \times M$) circulant blurring matrix. Even though this model is very popular in the image restoration literature [49–56], it is inaccurate since the assumption of circulant blur rarely, if ever, applies in practice.

Reconstructing images under the assumption of a purely circulant model can lead to severe artifacts due to discontinuities at the boundaries caused by the periodic extension of the image [2]. Simple approaches like zero-padding or replicated boundary extension do not resolve this issue since they do not eliminate the discontinuity at the boundaries. As suggested in [2] data preprocessing techniques like replicated boundary extension combined with edge-tapering can reduce, but not completely eliminate the artifacts. This will be illustrated in the experiments section (§B). A typical data preprocessing approach yields an augmented ($N \times 1$, with $N > M$)¹ data vector

$$\tilde{\mathbf{y}} \triangleq \operatorname{edgetaper}\{\operatorname{replicate}(\mathbf{y})\}, \quad (\text{B.3})$$

¹For an observed image \mathbf{y} of size $M = N_y \times N_y$ and a PSF of size $N_h \times N_h$ the size of the processed data is $N = (N_y + N_h - 1) \times (N_y + N_h - 1)$.

where `replicate` corresponds to boundary extension using Matlab's `padarray` function with the `'replicate'` option and `edgetaper` corresponds to Matlab's `edgetaper` function. A corresponding data fidelity term is given by:

$$J(\mathbf{x}) \triangleq \|\tilde{\mathbf{y}} - \mathbf{A}\mathbf{x}\|_2^2, \quad (\text{B.4})$$

where \mathbf{x} is the $(N \times 1)$ image to be reconstructed, and \mathbf{A} is a $(N \times N)$ circulant blurring matrix.

An alternative to the circulant model (that corresponds to periodic boundary extension) is to use reflexive boundary conditions along with DCT, as suggested in [1]. In this case the blurring matrix has the Toeplitz-plus-Hankel form and can be diagonalized using the DCT. A corresponding data fidelity term is given by:

$$J(\tilde{\mathbf{x}}) \triangleq \|\mathbf{y} - \mathbf{A}_R \tilde{\mathbf{x}}\|_2^2, \quad (\text{B.5})$$

where $\tilde{\mathbf{x}}$ is the $(M \times 1)$ image to be reconstructed, and \mathbf{A}_R is a $(M \times M)$ Toeplitz-plus-Hankel blurring matrix. This DCT method requires the PSF to be symmetric [1, 2], which may not hold for some applications *e.g.*, motion blur. In cases of non-symmetric PSFs this method can only be used to find preconditioners that facilitate iterative solvers like CG [1].

To eliminate boundary artifacts, the methods in [2, 57] use a data fidelity term

$$J(\mathbf{x}) \triangleq \left\| \mathbf{y} - \tilde{\mathbf{A}}\mathbf{x} \right\|_2^2, \quad (\text{B.6})$$

with a $(M \times N)$ non-circulant blurring matrix $\tilde{\mathbf{A}}$. Then, the non-circulant matrix $\tilde{\mathbf{A}}$ is augmented with additional rows (using a low dimensional auxiliary matrix \mathbf{a}) to create a circulant $(N \times N)$ system matrix \mathbf{A} . Instead of tackling the non-circulant Hessian $\tilde{\mathbf{A}}'\tilde{\mathbf{A}}$ directly, it is rewritten as:

$$\tilde{\mathbf{A}}'\tilde{\mathbf{A}} = \mathbf{A}'\mathbf{A} - \mathbf{a}'\mathbf{a}, \quad (\text{B.7})$$

consisting of a block-circulant (with circulant blocks) Hessian $\mathbf{A}'\mathbf{A}$ and a low rank component $\mathbf{a}'\mathbf{a}$. Inverting the non-circulant Hessian $\tilde{\mathbf{A}}'\tilde{\mathbf{A}}$ (along with a suitable block-circulant regularization matrix) is then carried out using the Sherman–Morrison Matrix Inversion Lemma (MIL) [2, Eq. (5)–(7)]. The MIL separates the two terms in the RHS of (B.7) and involves inverting the circulant part (*i.e.*, $\mathbf{A}'\mathbf{A}$ with the regularization term) and a low-dimensional matrix involving the auxiliary matrix \mathbf{a} . The circulant component is inverted using FFTs and inversion of the low dimensional component can be performed with an iterative algorithm (*e.g.*, CG).

In this work, similarly to [2, 57], we consider a more realistic non-circulant model, that is shift-invariant within the region of interest, but avoids the assumption of periodic end conditions. However, instead of using the manipulation in (B.7), we introduce a masking operator that eliminates the wraparound artifacts at the boundaries caused by periodic convolution. With our proposed model the data fidelity term becomes

$$J(\mathbf{x}) \triangleq \|\mathbf{y} - \mathbf{T}\mathbf{A}\mathbf{x}\|_2^2, \quad (\text{B.8})$$

where \mathbf{T} is a $(M \times N)$ masking matrix that truncates the circular wraparound at the boundaries, \mathbf{A} is a $(N \times N)$ circulant matrix, and \mathbf{x} is a $(N \times 1)$ vector as in (B.4) and (B.6)². The matrix \mathbf{T} is a truncated identity matrix resulting from the removal of rows corresponding to boundary pixels, and thus, $\mathbf{T}'\mathbf{T}$ is a $(N \times N)$ diagonal matrix with 0s and 1s. Even though the model in (B.8) is shift-invariant within the image, the masking operator makes the overall system model $\mathbf{T}\mathbf{A}$ shift-variant. To efficiently handle this shift-variant model, we propose to use a variable splitting scheme that decouples \mathbf{T} and \mathbf{A} and in turn allows the use of FFT-based computations as described in §B.

Regularizer

The algorithms discussed in this paper can tackle a general class of convex regularizers $\Phi(\cdot)$ in (B.1), but we will focus on edge-preserving and sparsity promoting regularizers like Total Variation (TV) and analysis l_1 regularization, respectively, for brevity.

1. l_1 regularization or discrete anisotropic total-variation:

$$\Phi(\mathbf{R}\mathbf{x}) = \|\mathbf{R}\mathbf{x}\|_1, \quad (\text{B.9})$$

where $\mathbf{R} = \mathbf{W}$ is a wavelet frame, typically excluding the approximation level, or $\mathbf{R} = \mathbf{C} \triangleq [\mathbf{C}'_1 \ \mathbf{C}'_2]'$ is a matrix of horizontal and vertical finite differences.

2. Discrete isotropic total-variation

$$\Phi(\mathbf{C}\mathbf{x}) = \sum_{n=1}^N \sqrt{|[\mathbf{C}_1\mathbf{x}]_n|^2 + |[\mathbf{C}_2\mathbf{x}]_n|^2}. \quad (\text{B.10})$$

²For the overall system model we have $\mathbf{T}\mathbf{A} = \tilde{\mathbf{A}}$ and it corresponds to a non-circular convolution operator with extended end conditions. For a blurring kernel \mathbf{h} of size $N_h \times N_h$ we have $\mathbf{y} = \mathbf{h} * * \mathbf{x}$ and the size of \mathbf{x} is $N = (N_y + N_h - 1) \times (N_y + N_h - 1)$, which corresponds to the size of the unknown image that contributes to the observed $N_y \times N_y$ image.

To reduce computational complexity and allow FFT-based non-iterative solving of linear systems, the sparsifying matrix \mathbf{R} (wavelet frame or finite differences) is assumed to have periodic end conditions such that $\mathbf{R}'\mathbf{R}$ is circulant.

Proposed Model-Based Restoration

In this work, our goal is to estimate the image \mathbf{x} by minimizing the following cost function that we call problem **P1**:

$$\hat{\mathbf{x}} = \underset{\mathbf{x}}{\operatorname{argmin}} \left\{ \Psi(\mathbf{x}) \triangleq \frac{1}{2} \|\mathbf{y} - \mathbf{T}\mathbf{A}\mathbf{x}\|_2^2 + \lambda\Phi(\mathbf{R}\mathbf{x}) \right\}. \quad (\text{B.11})$$

Minimizing (B.11) is a non-trivial optimization problem. Existing methods include non-linear conjugate gradient (**NCG**) [59], iterative shrinkage/thresholding (**ISTA**) [50, 60], (**M**)**FISTA** [54, 61], and variable splitting/ADMM (Alternating Direction Method of Multipliers) algorithms [52, 56, 62–64]. Some of these methods, *e.g.*, (**M**)**FISTA**, **SALSA** [52], **Split-Bregman (SB)** [64], and **FTVd** [62] are computationally efficient when used with the data model in (B.2) since they exploit the circulant nature of \mathbf{A} in (B.2). However, a straightforward application of these methods to the non-circulant model in (B.8) may increase their computation time since the inner sub-problems of these algorithms may no longer admit explicit closed-form updates. We discuss this in detail in §B and also provide experimental evidence in §B. To handle the non-circulant model in (B.8) we propose a specific variable splitting strategy [10, 52] presented in §B. We then use the AL framework and alternating minimization to obtain an iterative algorithm that exploits the structures of \mathbf{T} and \mathbf{A} and thereby, converges faster.

Existing Restoration Algorithms

Non-linear Conjugate Gradient (NCG)

Using **NCG** to solve **P1** requires computing the gradient of $\Psi(\mathbf{x})$. This is problematic for TV or l_1 norm regularizers that use the non-smooth absolute value function. To alleviate this problem the common approach is to use a rounding parameter to approximate the absolute value function as

$$|x| \approx \sqrt{|x|^2 + \varepsilon}, \quad (\text{B.12})$$

where ε is the rounding parameter. **NCG** also needs a line search method for which we can use the technique proposed in [59, Sec. IV].

The disadvantages of **NCG** are slow convergence, and perhaps, the fact that it does not converge to a solution of **P1**, due to the approximation in (B.12).

(MF)ISTA

ISTA was first introduced for restoration problems with synthesis-type priors [50, 60] and it was later generalized to analysis-type priors [54, 61]. **(M)FISTA** is an improvement on **ISTA** that converges faster to a solution of **P1**. The general methodology of both **ISTA** and **(M)FISTA** is to convert the original problem **P1** into a denoising problem that can be solved non-iteratively for l_1 -synthesis priors or iteratively for analysis priors. The difference between **ISTA** and **(M)FISTA** is the use of a specific two-step update in **(M)FISTA** [54, Eq. (4.1)–(4.3)] that accelerates convergence [54, Thm. 4.4]. For analysis regularizers, the denoising step cannot be performed in a single-step, in which case one can use a Chambolle-type algorithm as in [53, Eq. (5)–(7)].

Even though **MFISTA** converges faster than the simpler **ISTA**, variable-splitting/ADMM algorithms [10, 52, 56] have been developed that exhibit faster convergence.

Variable-Splitting/ADMM Algorithms [52, 62, 64]

The main idea of these algorithms is to break down the original problem **P1** into smaller tasks by introducing appropriate auxiliary constraint variables. The resulting minimization subproblems are decoupled and easier to solve compared to the original minimization problem **P1**. There are several different ways to choose the splitting variables that lead to a variety of such variable-splitting based algorithms [10, 52, 56]. These algorithms have been shown to converge faster than **MFISTA** [52]. The algorithm we developed for the non-circulant image restoration problem is based on the variable-splitting ADMM framework presented in [10, 56, 65].

SALSA [52] One approach for solving **P1** is to split the regularization term by introducing an auxiliary variable $\mathbf{u} = \mathbf{x}$. The constrained problem is formulated as:

$$\min_{\mathbf{x}, \mathbf{u}} \left\{ \Psi(\mathbf{x}, \mathbf{u}) \triangleq \frac{1}{2} \|\mathbf{y} - \mathbf{T}\mathbf{A}\mathbf{x}\|_2^2 + \lambda\Phi(\mathbf{R}\mathbf{u}) \right\} \text{ s.t. } \mathbf{u} = \mathbf{x}, \quad (\text{B.13})$$

and the associated AL function is

$$\mathcal{L}(\mathbf{x}, \mathbf{u}, \mu, \boldsymbol{\eta}) = \Psi(\mathbf{x}, \mathbf{u}) + \frac{\mu}{2} \|\mathbf{u} - \mathbf{x} - \boldsymbol{\eta}\|_2^2, \quad (\text{B.14})$$

where $\boldsymbol{\eta}$ is linearly related to the Lagrange multiplier for the constraint in (B.13) and $\mu > 0$ is an AL penalty parameter [10, 52, 56, 65].

This formulation leads to **SALSA** [52], where (B.13) is solved with the following alternating minimization scheme:

$$\mathbf{x}^{(k+1)} = \underset{\mathbf{x}}{\operatorname{argmin}} \left\{ \begin{array}{l} \frac{1}{2} \|\mathbf{y} - \mathbf{T}\mathbf{A}\mathbf{x}\|_2^2 \\ + \frac{\mu}{2} \|\mathbf{u}^{(k)} - \mathbf{x} - \boldsymbol{\eta}^{(k)}\|_2^2 \end{array} \right\} \quad (\text{B.15})$$

$$\mathbf{u}^{(k+1)} = \underset{\mathbf{u}}{\operatorname{argmin}} \left\{ \lambda\Phi(\mathbf{R}\mathbf{u}) + \frac{\mu}{2} \|\mathbf{u} - \mathbf{x}^{(k+1)} - \boldsymbol{\eta}^{(k)}\|_2^2 \right\} \quad (\text{B.16})$$

$$\boldsymbol{\eta}^{(k+1)} = \boldsymbol{\eta}^{(k)} - \mathbf{u}^{(k+1)} + \mathbf{x}^{(k+1)}. \quad (\text{B.17})$$

Since the cost function (B.15) is quadratic, the minimization with respect to \mathbf{x} can be expressed in closed form as:

$$\mathbf{x}^{(k+1)} = \mathbf{H}_{\mu,1}^{-1} \left[\mathbf{A}'\mathbf{T}'\mathbf{y} + \mu \left(\mathbf{u}^{(k+1)} - \boldsymbol{\eta}_1^{(k)} \right) \right], \quad (\text{B.18})$$

where

$$\mathbf{H}_{\mu,1} \triangleq \mathbf{A}'\mathbf{T}'\mathbf{T}\mathbf{A} + \mu\mathbf{I}. \quad (\text{B.19})$$

For the purely circulant model in (B.2), $\mathbf{T} = \mathbf{I}$ and one can invert $\mathbf{H}_{\mu,1}$ using FFTs. However, for the more realistic model in (B.8), the Hessian $\mathbf{H}_{\mu,1}$ has no exploitable structure and finding a minimizer non-iteratively can be computationally intensive for large N . Instead, one can apply a few PCG iterations using the circulant preconditioner $\mathbf{M}_1 \triangleq (\mathbf{A}'\mathbf{A} + \mu\mathbf{I})^{-1}$ along with warm starting to find an approximate solution.

The minimization with respect to \mathbf{u} in (B.16) can be implemented non-iteratively for certain synthesis-type regularizers. However, for analysis-type regularizers (*e.g.*, involving finite differences or wavelet frames), it has to be performed iteratively. Following the implementation of **SALSA** [52], we used the Chambolle-type algorithm [53, Eq. (6)–(7)] for the update of \mathbf{u} . Despite the approximate update steps, **SALSA** can be shown to converge to a solution of **P1** [52, 66].

Split-Bregman Algorithm [64] An alternative approach is to split the regularization term by introducing the auxiliary variable $\mathbf{v} = \mathbf{R}\mathbf{x}$. In this case the constrained problem is formulated as

$$\min_{\mathbf{x}, \mathbf{v}} \left\{ \Psi(\mathbf{x}, \mathbf{v}) \triangleq \frac{1}{2} \|\mathbf{y} - \mathbf{T}\mathbf{A}\mathbf{x}\|_2^2 + \lambda\Phi(\mathbf{v}) \right\} \text{ s.t. } \mathbf{v} = \mathbf{R}\mathbf{x}, \quad (\text{B.20})$$

and the associated AL function is

$$\mathcal{L}(\mathbf{x}, \mathbf{v}, \mu, \boldsymbol{\eta}) = \Psi(\mathbf{x}, \mathbf{v}) + \frac{\mu}{2} \|\mathbf{v} - \mathbf{R}\mathbf{x} - \boldsymbol{\eta}\|_2^2, \quad (\text{B.21})$$

where $\boldsymbol{\eta}$ is related to the Lagrange multiplier for the constraint in (B.20).

The splitting in (B.20) is similar to that in the **SB** [64] and **FTVd** [62] algorithms, and the problem is again solved using the AL framework and by performing the following minimizations alternatively:

$$\mathbf{x}^{(k+1)} = \underset{\mathbf{x}}{\operatorname{argmin}} \left\{ \begin{array}{l} \frac{1}{2} \|\mathbf{y} - \mathbf{T}\mathbf{A}\mathbf{x}\|_2^2 \\ + \frac{\mu}{2} \|\mathbf{v}^{(k)} - \mathbf{R}\mathbf{x} - \boldsymbol{\eta}^{(k)}\|_2^2 \end{array} \right\} \quad (\text{B.22})$$

$$\mathbf{v}^{(k+1)} = \underset{\mathbf{v}}{\operatorname{argmin}} \left\{ \lambda\Phi(\mathbf{v}) + \frac{\mu}{2} \|\mathbf{v} - \mathbf{R}\mathbf{x}^{(k+1)} - \boldsymbol{\eta}^{(k)}\|_2^2 \right\} \quad (\text{B.23})$$

$$\boldsymbol{\eta}^{(k+1)} = \boldsymbol{\eta}^{(k)} - \mathbf{v}^{(k+1)} + \mathbf{R}\mathbf{x}^{(k+1)}. \quad (\text{B.24})$$

As in **SALSA**, the minimization with respect to \mathbf{x} in (B.22) has a closed-form solution since the associated cost function is quadratic:

$$\mathbf{x}^{(k+1)} = \mathbf{H}_{\mu,2}^{-1} [\mathbf{A}'\mathbf{T}'\mathbf{y} + \mu\mathbf{R}'(\mathbf{v}^{(k+1)} - \boldsymbol{\eta}^{(k)})], \quad (\text{B.25})$$

where

$$\mathbf{H}_{\mu,2} \triangleq \mathbf{A}'\mathbf{T}'\mathbf{T}\mathbf{A} + \mu\mathbf{R}'\mathbf{R}. \quad (\text{B.26})$$

Again in this case, for the model in (B.8), the Hessian matrix $\mathbf{H}_{\mu,2}$ has no exploitable structure and solving (B.25) can be computationally intensive for large N . As in **SALSA**, one can apply a few PCG iterations with warm starting and a circulant preconditioner $\mathbf{M}_2 \triangleq (\mathbf{A}'\mathbf{A} + \mu\mathbf{R}'\mathbf{R})^{-1}$.

The minimization with respect to \mathbf{v} in (B.23) can be performed non-iteratively for several synthesis- and analysis-type regularizers, including TV and l_1 norm of wavelet coefficients, using

a soft thresholding/shrinkage rule:

$$\mathbf{v}^{(k+1)} = \text{shrink} \left\{ \mathbf{R}\mathbf{x}^{(k)} + \boldsymbol{\eta}^{(k)}, \frac{\lambda}{\mu} \right\}. \quad (\text{B.27})$$

For the bilateral TV and l_1 regularization the shrinkage operator is element-wise, whereas for isotropic TV a vector shrinkage rule can be used, as in [62, §2.1].

A reviewer suggested a variation of the **SB** algorithm, formulated by using the method in [2] for the updates of \mathbf{x} in (B.22). Although it is more complicated than applying CG to (B.25), this formulation has the benefit of solving a much smaller problem using CG iterations only for the boundaries and updates the rest of the image with the use of FFTs. The method is explained in detail in [2] and also in the alternating minimization scheme of [57]. For the purpose of convergence speed comparisons we will refer to this variation as the **Split-Bregman-MIL (SB-MIL)** algorithm. This name was used since the method is based on the Matrix Inversion Lemma (MIL) to decouple the circulant part from the boundaries and efficiently perform the update for \mathbf{x} .

Compared to **SALSA**, the benefit of **SB** and **SB-MIL** is the single-step update for \mathbf{v} that avoids the inner iterations of the Chambolle-type [53, Eq. (6)–(7)] algorithm required in **SALSA**.

Proposed Algorithm: ADMM-P2

Even though both **SALSA** and **SB**-based algorithms (*e.g.*, **SB** [64] and **SB-MIL** studied here) decouple the regularization term, their main caveat is the need for (P)CG iterations to obtain the update of \mathbf{x} ((B.18) and (B.25)) or a low-dimension vector corresponding to the boundaries in **SB-MIL**. These inner iterations can increase convergence time. Our method alleviates this problem by introducing a second auxiliary variable $\mathbf{u}_0 = \mathbf{A}\mathbf{x}$. This additional splitting is similar to those used in [10, Sec. IV-B] for MRI, [65, Sec. III] for CT, and [56] for image restoration, although in [56] the goal is to separate the entire data-fidelity term from the data model, whereas in our case the additional splitting \mathbf{u}_0 separates the blur and the masking operator inside the data-fidelity term in (B.11). The resulting constrained problem **P2** is given by:

$$\begin{aligned} \min_{\mathbf{x}, \mathbf{u}_0, \mathbf{u}_1} & \left\{ \Psi(\mathbf{u}_0, \mathbf{u}_1) \triangleq \frac{1}{2} \|\mathbf{y} - \mathbf{T}\mathbf{u}_0\|_2^2 + \lambda\Phi(\mathbf{u}_1) \right\} \\ \text{s.t. } & \mathbf{u}_0 = \mathbf{A}\mathbf{x} \text{ and } \mathbf{u}_1 = \mathbf{R}\mathbf{x}. \end{aligned} \quad (\text{B.28})$$

where \mathbf{A} is the $N \times N$ circulant blurring matrix and \mathbf{R} is an $R \times N$ sparsifying transform matrix. We can now rewrite **P2** in a more concise form as follows:

$$\min_{\mathbf{x}, \mathbf{w}} \Psi(\mathbf{w}) \quad \text{s.t.} \quad \mathbf{w} = \mathbf{D}\mathbf{x} \quad (\text{B.29})$$

where

$$\mathbf{w} \triangleq \begin{bmatrix} \mathbf{u}_0 \\ \mathbf{u}_1 \end{bmatrix}, \quad \mathbf{D} \triangleq \begin{bmatrix} \mathbf{A} \\ \mathbf{R} \end{bmatrix}. \quad (\text{B.30})$$

From this formulation it is evident that the constraint matrix \mathbf{D} is full column rank provided that the null spaces of $\mathbf{A}'\mathbf{A}$ and $\mathbf{R}'\mathbf{R}$ intersect only trivially, which is usually true in image restoration problems (low-pass nature of \mathbf{A} and high-pass nature of \mathbf{R}). This requirement does not impose serious restrictions on \mathbf{R} for deblurring problems, *i.e.*, it is not necessary for \mathbf{R} to be full column rank, which can be the case with commonly used sparsifying transforms, *e.g.*, finite differences, wavelets (excluding the approximation level). The importance of \mathbf{D} being full column rank relates to the hypothesis of a theorem due to Eckstein and Bertsekas [66, Thm. 8], summarized below, that guarantees convergence of ADMM type algorithms.

To solve the problem **P2** with the method of multipliers we construct the Augmented Lagrangian (AL) function, which can be expressed as:

$$\mathcal{L}(\mathbf{x}, \mathbf{w}, \boldsymbol{\gamma}) = \Psi(\mathbf{w}) + \frac{\mu}{2} \|\mathbf{w} - \mathbf{D}\mathbf{x} - \boldsymbol{\eta}\|_{\Lambda}^2, \quad (\text{B.31})$$

where μ is the AL penalty parameter, the parameter $\boldsymbol{\eta}$ relates to the Lagrange multiplier, and Λ is a symmetric positive definite weighting matrix defined as

$$\Lambda \triangleq \begin{bmatrix} \mathbf{I}_N & \mathbf{0} \\ \mathbf{0} & \nu \mathbf{I}_R \end{bmatrix}, \quad (\text{B.32})$$

where $\nu > 0$.

To solve **P2** in (B.28) we apply an alternating minimization scheme, which at the k th iteration,

leads to the following updates

$$\mathbf{x}^{(k+1)} = \underset{\mathbf{x}}{\operatorname{argmin}} \left\| \mathbf{w}^{(k)} - \mathbf{D}\mathbf{x} - \boldsymbol{\eta}^{(k)} \right\|_{\Lambda}^2 \quad (\text{B.33})$$

$$\mathbf{w}^{(k+1)} = \underset{\mathbf{w}}{\operatorname{argmin}} \Psi(\mathbf{w}) + \frac{\mu}{2} \left\| \mathbf{w} - \mathbf{D}\mathbf{x}^{(k+1)} - \boldsymbol{\eta}^{(k)} \right\|_{\Lambda}^2 \quad (\text{B.34})$$

$$\boldsymbol{\eta}^{(k+1)} = \boldsymbol{\eta}^{(k)} - \mathbf{w}^{(k+1)} + \mathbf{D}\mathbf{x}^{(k+1)}. \quad (\text{B.35})$$

Although the theorem [66, Thm. 8] allows for inexact updates, *i.e.*, $\varepsilon_{\mathbf{x}}^k \triangleq \left\| \mathbf{x}^{(k)} - \mathbf{x}_*^{(k)} \right\|_2 > 0$ and $\varepsilon_{\mathbf{w}}^k \triangleq \left\| \mathbf{w}^{(k)} - \mathbf{w}_*^{(k)} \right\|_2 > 0$ where $(\mathbf{x}_*^{(k)}, \mathbf{w}_*^{(k)})$ are solutions of (B.33) and (B.34) respectively, our formulation leads to closed-form updates for (B.33)–(B.34), that can be implemented non-iteratively, *i.e.*, $\varepsilon_{\mathbf{x}}^k = \varepsilon_{\mathbf{w}}^k = 0$ (up to numerical round-off errors). We review below the theorem of Eckstein and Bertsekas [66, Thm. 8] that is useful for analyzing the convergence of (B.33)–(B.35).

Theorem 1. *Consider (B.28) where $\Psi(\cdot)$ is closed, proper and convex and \mathbf{D} has full column rank. Let $\boldsymbol{\eta}^{(0)} \in \mathcal{R}^{N+R}$, $\mu > 0$, $\sum_k \varepsilon_{\mathbf{x}}^k < \infty$, and $\sum_k \varepsilon_{\mathbf{w}}^k < \infty$. If (B.28) has a solution $(\mathbf{x}^*, \mathbf{w}^*)$ then the sequence of updates $\{(\mathbf{x}^{(k)}, \mathbf{w}^{(k)})\}_k$ generated by (B.33)–(B.35) converges to $(\mathbf{x}^*, \mathbf{w}^*)$. If (B.28) has no solution then at least one of the sequences $\{(\mathbf{x}^{(k)}, \mathbf{w}^{(k)})\}_k$ or $\{\boldsymbol{\eta}^{(k)}\}_k$ diverges.*

Even though the theorem of Eckstein and Bertsekas [66, Thm. 8] uses an AL function with $\Lambda = \mathbf{I}$, we can still apply the theorem to (B.31) through a simple variable transformation [65, Footnote 3].

Using the structure of $\Psi(\mathbf{w})$ and \mathbf{D} , we can reformulate the AL function from (B.31) as

$$\begin{aligned} \mathcal{L}(\mathbf{x}, \mathbf{u}, \mu, \nu, \boldsymbol{\eta}) &= \Psi(\mathbf{u}_0, \mathbf{u}_1) + \frac{\mu}{2} \left\| \mathbf{u}_0 - \mathbf{A}\mathbf{x} - \boldsymbol{\eta}_0 \right\|_2^2 \\ &\quad + \frac{\mu\nu}{2} \left\| \mathbf{u}_1 - \mathbf{R}\mathbf{x} - \boldsymbol{\eta}_1 \right\|_2^2, \end{aligned} \quad (\text{B.36})$$

where $\boldsymbol{\eta}_0$ and $\boldsymbol{\eta}_1$ are related to the Lagrange multipliers for the constraints in (B.28). Using this

form of the AL function, the alternating minimization scheme at the k th step can be expressed as:

$$\mathbf{u}_0^{(k+1)} = \underset{\mathbf{u}_0}{\operatorname{argmin}} \left\{ \begin{array}{l} \frac{1}{2} \|\mathbf{y} - \mathbf{T}\mathbf{u}_0\|_2^2 \\ + \frac{\mu}{2} \|\mathbf{u}_0 - \mathbf{A}\mathbf{x}^{(k)} - \boldsymbol{\eta}_0^{(k)}\|_2^2 \end{array} \right\} \quad (\text{B.37})$$

$$\mathbf{u}_1^{(k+1)} = \underset{\mathbf{u}_1}{\operatorname{argmin}} \left\{ \lambda\Phi(\mathbf{u}_1) + \frac{\mu\nu}{2} \|\mathbf{u}_1 - \mathbf{R}\mathbf{x}^{(k)} - \boldsymbol{\eta}_1^{(k)}\|_2^2 \right\} \quad (\text{B.38})$$

$$\mathbf{x}^{(k+1)} = \underset{\mathbf{x}}{\operatorname{argmin}} \left\{ \begin{array}{l} \frac{\mu}{2} \|\mathbf{u}_0^{(k+1)} - \mathbf{A}\mathbf{x} - \boldsymbol{\eta}_0^{(k)}\|_2^2 \\ + \frac{\mu\nu}{2} \|\mathbf{u}_1^{(k+1)} - \mathbf{R}\mathbf{x} - \boldsymbol{\eta}_1^{(k)}\|_2^2 \end{array} \right\} \quad (\text{B.39})$$

$$\boldsymbol{\eta}_0^{(k+1)} = \boldsymbol{\eta}_0^{(k)} - \mathbf{u}_0^{(k+1)} + \mathbf{A}\mathbf{x}^{(k+1)} \quad (\text{B.40})$$

$$\boldsymbol{\eta}_1^{(k+1)} = \boldsymbol{\eta}_1^{(k)} - \mathbf{u}_1^{(k+1)} + \mathbf{R}\mathbf{x}^{(k+1)}. \quad (\text{B.41})$$

The minimization with respect to \mathbf{u}_0 in (B.37) is straightforward since the corresponding cost function is quadratic. The closed-form solution is expressed as

$$\mathbf{u}_0^{(k+1)} = (\mathbf{T}'\mathbf{T} + \mu\mathbf{I}_N)^{-1} \left[\mathbf{T}'\mathbf{y} + \mu \left(\mathbf{A}\mathbf{x}^{(k)} + \boldsymbol{\eta}_0^{(k)} \right) \right], \quad (\text{B.42})$$

and can be easily computed in a single-step update since it only requires inversion of the diagonal matrix $(\mathbf{T}'\mathbf{T} + \mu\mathbf{I}_N)$.

The minimization with respect to \mathbf{u}_1 in (B.38) can be performed non-iteratively using a (vector) soft thresholding/shrinkage rule similar to (B.27), using a threshold value $\frac{\lambda}{\mu\nu}$ instead of $\frac{\lambda}{\mu}$ used in (B.27).

Finally the minimization with respect to \mathbf{x} in (B.39) is also straightforward due to the corresponding quadratic cost function. The closed form of the update is

$$\mathbf{x}^{(k+1)} = \mathbf{H}_\nu^{-1} \left[\mathbf{A}' \left(\mathbf{u}_0^{(k+1)} - \boldsymbol{\eta}_0^{(k)} \right) + \nu\mathbf{R}' \left(\mathbf{u}_1^{(k+1)} - \boldsymbol{\eta}_1^{(k)} \right) \right], \quad (\text{B.43})$$

where

$$\mathbf{H}_\nu \triangleq \mathbf{A}'\mathbf{A} + \nu\mathbf{R}'\mathbf{R}. \quad (\text{B.44})$$

We perform multiplication by \mathbf{H}_ν^{-1} in (B.43) efficiently using FFTs since the blurring matrix \mathbf{A} is circulant and the sparsifying operator \mathbf{R} (frame or differencing matrix) consists of circulant blocks (periodic end conditions) such that $\mathbf{R}'\mathbf{R}$ is circulant. Thus, the update of \mathbf{x} can be computed non-iteratively.

Combining the above expressions for the updates, we now summarize the proposed AL algorithm for solving **P2**.

ADMM-P2: AL algorithm for P2.

- 1: Select $\mathbf{x}^{(0)}$, $\nu > 0$, and $\mu > 0$
- 2: Precompute $\mathbf{T}'\mathbf{y}$
- 3: Set $\boldsymbol{\eta}_0^{(0)} = 0$, $\boldsymbol{\eta}_1^{(0)} = 0$ and $k = 0$
- 4: **repeat**
- 5: Obtain $\mathbf{u}_0^{(k+1)}$ using (B.42)
- 6: Obtain $\mathbf{u}_1^{(k+1)}$ using (B.27)
- 7: Obtain $\mathbf{x}^{(k+1)}$ using (B.43)
- 8: $\boldsymbol{\eta}_0^{(k+1)} = \boldsymbol{\eta}_0^{(k)} - \left(\mathbf{u}_0^{(k+1)} - \mathbf{A}\mathbf{x}^{(k+1)} \right)$
- 9: $\boldsymbol{\eta}_1^{(k+1)} = \boldsymbol{\eta}_1^{(k)} - \left(\mathbf{u}_1^{(k+1)} - \mathbf{R}\mathbf{x}^{(k+1)} \right)$
- 10: $k = k + 1$
- 11: **until** stop criterion is met

Unlike **SB**-based algorithms (including **SB-MIL**) and **SALSA** for solving (B.11), all the steps of **ADMM-P2** are single-step updates due to the extra splitting that decouples the circulant blur operator \mathbf{A} from the masking operator \mathbf{T} . The experiments in §B show that the non-iterative updates of **ADMM-P2** help achieve convergence in less time than other methods.

AL Parameter Selection

SALSA and **ADMM-P2** belong to the general class of ADMM algorithms. Thus, the ADMM convergence theorem of Eckstein and Bertsekas [66, Thm. 8] applies in these cases and the algorithms are guaranteed to converge to a solution of the original problem **P1**, even when the inner minimization steps are not performed exactly. The **SB**-based algorithms are also convergent, although the convergence theory is different from that of ADMM [63, 64].

SALSA, **ADMM-P2**, **SB**, and **SB-MIL** are guaranteed to converge regardless of the choice of AL parameters μ and ν [66]. However, the choice of AL parameters affects the convergence speed of these algorithms. We found experimentally that the best AL parameters for fast convergence depend on the regularization parameter λ and the maximum intensity (x_{\max}) of the blurred image, similarly to the choice proposed in [55]. The best parameters can also depend on the spread of eigenvalues of $\mathbf{A}'\mathbf{A}$ and $\mathbf{R}'\mathbf{R}$.

For **SALSA** we found that a choice of $\mu = 2^7\lambda/x_{\max}$ works well for several different choices of regularization parameter λ .

For **SB** and **SB-MIL**, we found experimentally that the choice of the AL parameter μ also depends on $\mu_{\min} \triangleq \operatorname{argmin}_{\mu} \kappa(\mathbf{A}'\mathbf{A} + \mu\mathbf{R}'\mathbf{R})$, where $\kappa(\cdot)$ is the condition number. As a rule of thumb we choose the AL parameter as $\mu = 2^8 \lambda \mu_{\min} / x_{\max}$.

For **ADMM-P2**, we found experimentally that the best product $\mu\nu$ depends on λ , x_{\max} and $\nu_{\min} \triangleq \operatorname{argmin}_{\nu} \kappa(\mathbf{A}'\mathbf{A} + \nu\mathbf{R}'\mathbf{R})$. Thus, for fast convergence we choose the AL parameters to achieve $\mu\nu = 2^8 \lambda \nu_{\min} / x_{\max}$. Also, we found that we can fix the parameter μ to a value $\mu_0 = 2^{-4}$ and then choose the parameter ν as: $\nu = 2^8 \lambda \nu_{\min} / \mu_0 x_{\max}$.

The above rules for the parameter selection work well when the blurring system matrix \mathbf{A} is scaled such that the maximum eigenvalue of $\mathbf{A}'\mathbf{A}$ is equal to 1.

Experiments

The first part of the experiments compares the quality of the reconstructed images obtained using the proposed non-circulant (B.8) and the purely circulant (B.2) reconstruction models. The second part compares the convergence speed of the proposed **ADMM-P2** algorithm to that of **NCG**, **ISTA**, **MFISTA**, **SALSA**, **SB**, and **SB-MIL** for restoration using the proposed non-circulant model.

Non-Circulant Versus Circulant Restoration

For all our experiments we used the 256×256 cameraman image as the true, noise-free image, and following the experimental setting in [54] we scaled it to the range $[0, 1]$ (Figure B.1a). For the blurring kernel we used a uniform 9×9 blur, a uniform 15×15 blur and a 15 pixel straight motion blur at a 30° angle. For this image and blur sizes the valid part of the convolution is the 248×248 (for 9×9 blur) or 242×242 (for 15×15 blur) central region and the data simulated with Matlab's `conv2` function using the `'valid'` option are of this size.

To assess the quality of our proposed non-circulant reconstruction method we compared it to reconstructions from

- a purely circulant model (B.2) without data pre-processing,
- a purely circulant model (B.2) where we used data pre-processing with boundary replication combined with edge tapering,
- and reflexive end conditions and DCT (B.5).

When using the non-circulant model in (B.8) or the purely circulant model with data pre-processing in (B.4), the reconstructed images have original 256×256 size and then they are truncated to match the data size. When reconstructing with the purely circulant model without pre-processing in (B.2) or with the DCT method in (B.5), the reconstructed image has the same size as the data, so no truncation is necessary.

For our experiments, we used three types of regularizers, namely isotropic and anisotropic Total Variation, and l_1 norm of the coefficients of the undecimated 2-level Haar wavelet transform, excluding the approximation level.

We performed three sets of experiments with different levels of Blurred Signal-to-Noise Ratio (BSNR $\triangleq 10 \log_{10}(\text{var}(\mathbf{Ax}) / \sigma^2)$) [49] and we chose the regularization parameter λ to achieve low Normalized Root Mean Square (NRMS) error for a given BSNR level. The experimental setup is as follows

1. 20 dB BSNR ($\sigma^2 = 5.03 \times 10^{-4}$) with $\lambda = 2^{-10}$,
2. 30 dB BSNR ($\sigma^2 = 5.03 \times 10^{-5}$) with $\lambda = 2^{-12}$,
3. 40 dB BSNR ($\sigma^2 = 5.03 \times 10^{-6}$) with $\lambda = 2^{-15}$,
4. 50 dB BSNR ($\sigma^2 = 5.03 \times 10^{-7}$) with $\lambda = 2^{-17}$,

where σ^2 is the Gaussian noise variance. We quantified the reconstruction quality by computing the Improvement in Signal-to-Noise Ratio (ISNR) between the restored image $\hat{\mathbf{x}}$ and the true image \mathbf{x}_{true} . The ISNR was measured in the 248×248 or 242×242 (depending on the blur size) central region that corresponds to the valid part of the convolution, since this was the actual size of the input data vector \mathbf{y} . Any extrapolated values (when reconstructing with the non-circulant model) are not used in the ISNR calculations and not shown in any of the figures.

Figure B.1 shows the restored images from experiment 4 (50dB BSNR) with uniform 15×15 blur using isotropic TV regularization. Figure B.1c shows that the restored image using the purely circulant model in (B.2) exhibits severe ringing artifacts, similar to those in the results of [2], that are not confined to the boundaries of the image. When data pre-processing is used, the ringing artifacts are significantly reduced, but not completely removed (Figure B.1d). These artifacts can be more severe and lead to more degradation when the strength of the regularizer decreases as seen in the quantitative results in Table B.1. When reflexive boundary conditions and the DCT are used, the artifacts are again significantly reduced but clearly visible in high BSNR cases. Finally, we see that the reconstructed images from the proposed non-circulant model in (B.8) are free

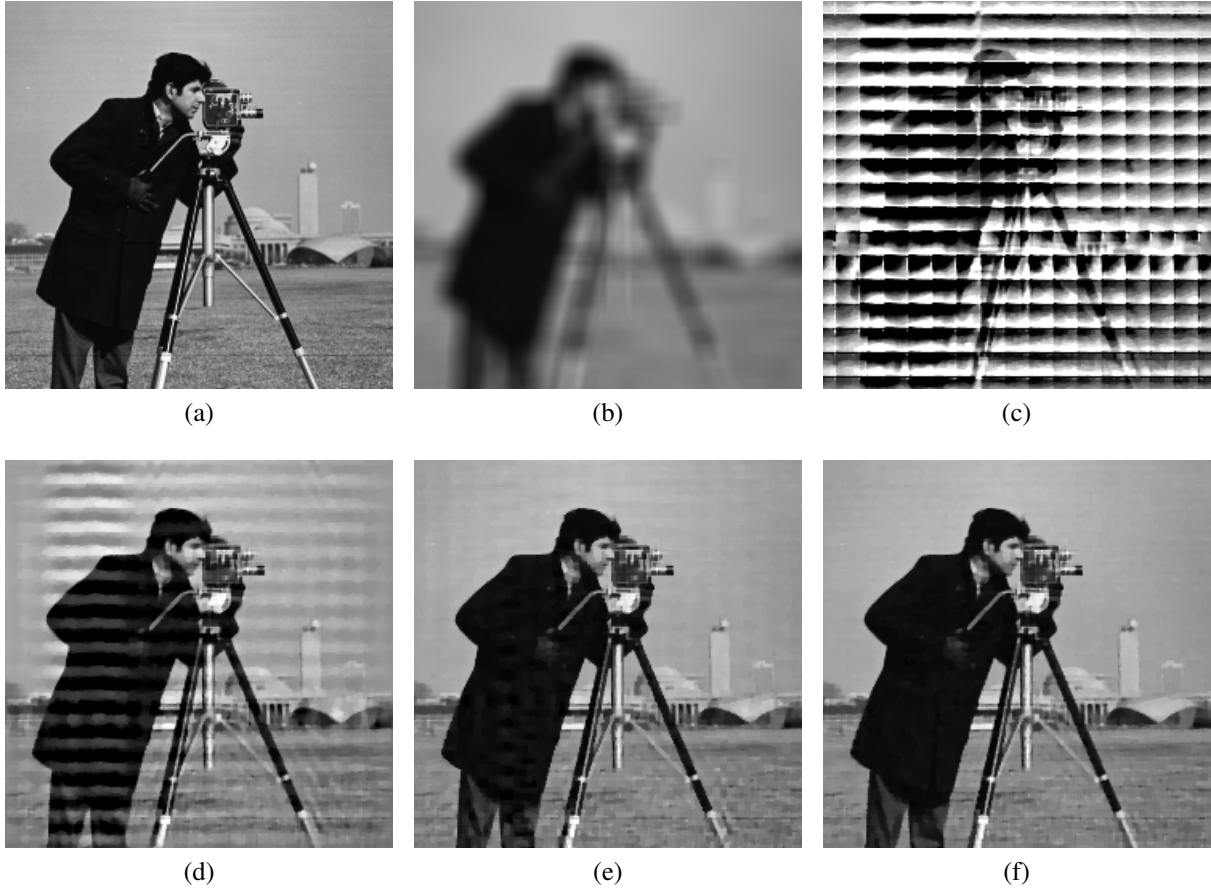


Figure B.1: Experiment 4 using 15×15 uniform blur: Restoration results using isotropic TV regularization. (a) Cameraman true image (242×242), scaled to the range $[0, 1]$. (b) Blurred and noisy image from Matlab's 'valid' `conv2` operation. (c) Restored image from purely circulant model (B.2). (d) Restored image from purely circulant model with data pre-processing (B.4). (e) Restored image using reflexive boundary conditions and DCT (B.5). (f) Restored image from proposed non-circulant model (B.8).

of any ringing artifacts and the reconstructed image closely resembles the true noise-free image (Figure B.1f).

Figure B.2 shows the restored images from experiment 2 (30dB BSNR) with 15 pixel straight motion blur using isotropic TV regularization. Figure B.2c shows that the restored image using the purely circulant model in (B.2) exhibits severe ringing artifacts, similar to those in Figure B.1c. When data pre-processing is used (Figure B.2d) the ringing artifacts are reduced and are less obvious compared to Figure B.1d because of the high regularization parameter for low BSNR. When reflexive boundary conditions and the DCT are used (Figure B.1e) the method fails to produce ac-



Figure B.2: Experiment 3 using 15 pixel motion blur: Restoration results using isotropic TV regularization. (a) Cameraman true image (248×248), scaled to the range $[0, 1]$. (b) Blurred and noisy image from Matlab's 'valid' `conv2` operation. (c) Restored image from purely circulant model (B.2). (d) Restored image from purely circulant model with data pre-processing (B.4). (e) Restored image using reflexive boundary conditions and DCT (B.5). For this case, the results are inaccurate since this method is not applicable for non-symmetric PSF [1,2]. Also the image had to be scaled to fit the dynamic range of the rest of the reconstructed images. (f) Restored image from proposed non-circulant model (B.8).

curate results since the PSF is non-symmetric [1,2]. Finally, we see that the reconstructed images from the proposed non-circulant model in (B.8) are free of any ringing artifacts and the reconstructed image closely resembles the true noise-free image (Figure B.2f).

Figure B.3 shows the restored images from experiment 1 (20dB BSNR) with with uniform 9×9 blur using isotropic TV regularization. The restored image using the purely circulant model (Figure B.3c) exhibits severe ringing artifacts as in the previous cases. However, the reconstructed images using data pre-processing (Figure B.3d) and using reflexive boundary conditions and DCT

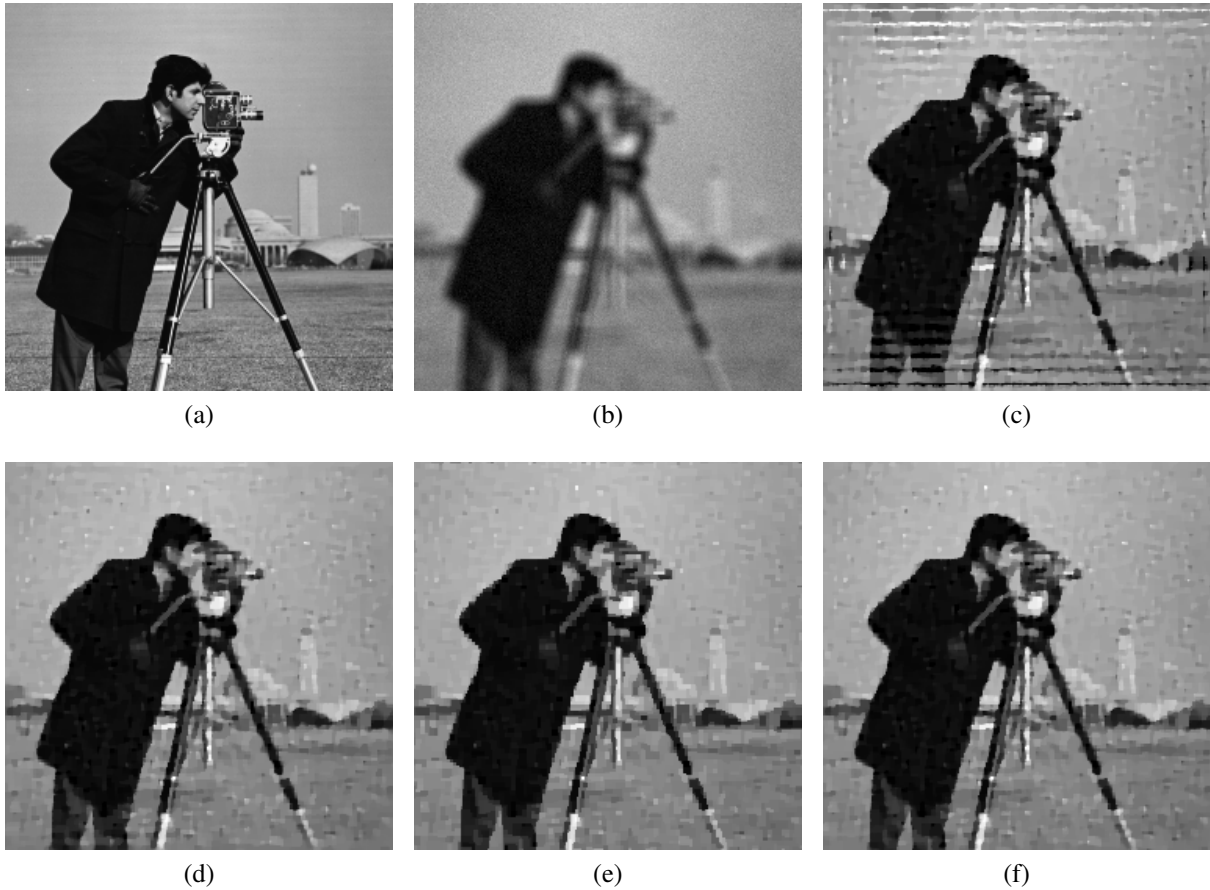


Figure B.3: Experiment 1 using 15×15 uniform blur: Restoration results using isotropic TV regularization. (a) Cameraman true image (248×248), scaled to the range $[0, 1]$. (b) Blurred and noisy image from Matlab's 'valid' `conv2` operation. (c) Restored image from purely circulant model (B.2). (d) Restored image from purely circulant model with data pre-processing (B.4). (e) Restored image using reflexive boundary conditions and DCT (B.5). (f) Restored image from proposed non-circulant model (B.8).

(Figure B.3e) look very similar to the reconstructed images from the non-circulant model (Figure B.3f). This happens because the strong regularizer used to suppress noise over-smooths the image and thus the reconstruction artifacts are smoothed out as well making the images look almost identical.

Table B.1 gives the quantitative results in terms ISNR for all experiments. In all cases, the ISNR of reconstructions based on the non-circulant model are higher than that of the reconstructions based on the purely circulant model without data pre-processing. In the case of reconstruction with the circulant model and data preprocessing or with reflexive boundary conditions and DCT,

we can see that for lower SNR, where stronger regularization is required, the smoothing of the regularizer can suppress the ringing artifacts leading to reconstruction ISNR comparable to that of the proposed non-circulant model reconstruction. However, in higher SNR regimes, where less smoothing is required, the artifacts from the circulant model reconstruction become more prominent and the non-circulant reconstruction shows significantly reconstruction quality.

Table B.1: ISNR in dB for all experiments. The * denotes reconstruction using the purely circulant model with data pre-processing (B.4). For the case of motion blur the results for reflexive end conditions are not presented since the method is not appropriate for non symmetric PSF.

Blur Type	9 × 9 Unif.				15 × 15 Unif.				15 Pix. Mot.			
Reg. Type	Non-Circ.	Circ.	Circ.*	Refl.	Non-Circ.	Circ.	Circ.*	Refl.	Non-Circ.	Circ.	Circ.*	Refl.
Experiment 1: BSNR = 20 dB												
Wavelet l_1	3.7	-0.9	3.6	3.6	3.4	-2.7	3.3	3.4	4.1	-1.3	4.1	N/A
TV _{ANISO}	3.5	-1.2	3.4	3.4	3.7	-2.9	3.6	3.7	4.3	-1.5	4.3	N/A
TV _{ISO}	3.6	-1.4	3.6	3.4	4.0	-3.1	3.9	3.7	4.5	-1.7	4.4	N/A
Experiment 2: BSNR = 30 dB												
Wavelet l_1	5.7	-3.3	5.6	5.7	4.9	-5.3	4.7	4.8	7.1	-4.4	6.7	N/A
TV _{ANISO}	5.4	-3.5	5.4	5.4	5.1	-5.6	4.8	5.1	7.1	-4.6	6.7	N/A
TV _{ISO}	5.8	-3.7	5.7	5.4	5.4	-5.8	5.1	5.1	7.4	-4.8	6.8	N/A
Experiment 3: BSNR = 40 dB												
Wavelet l_1	8.6	-8.1	7.9	8.2	7.2	-12.8	6.4	7.1	11.6	-9.2	8.8	N/A
TV _{ANISO}	8.4	-8.4	7.5	7.9	7.2	-13.5	6.2	6.9	11.4	-10.2	8.1	N/A
TV _{ISO}	8.3	-8.6	7.3	7.9	7.4	-13.8	6.3	6.9	11.4	-10.6	7.7	N/A
Experiment 4: BSNR = 50 dB												
Wavelet l_1	11.8	-10.5	9.0	10.6	9.8	-15.0	6.4	9.3	15.7	-13.2	8.1	N/A
TV _{ANISO}	11.5	-10.4	8.3	10.1	9.7	-15.2	3.1	9.3	15.0	-13.5	6.6	N/A
TV _{ISO}	11.6	-10.6	8.2	10.1	9.9	-15.3	2.4	9.3	14.7	-13.8	5.8	N/A

Convergence Speed Comparison

For the convergence speed experiments we used the setting from Experiment 3 (*i.e.*, 40 dB BSNR, $\sigma^2 = 5.03 \times 10^{-6}$ with $\lambda = 2^{-15}$) with 9×9 uniform blur. We compared the convergence speed of the following algorithms that were all implemented in Matlab.

- NCG- L with L line-search sub-iterations [59];
- ISTA [53];

- **MFISTA- M** with M sub-iterations of the Chambolle-type algorithm [53, Eq. (6)–(7)];
- **SALSA- N - M** with N CG sub-iterations and M sub-iterations of [53, Eq. (6)–(7)];
- **SB- N** with N CG sub-iterations;
- **SB-MIL- N** with N CG sub-iterations;
- **ADMM-P2** (proposed).

For these experiments we focused on algorithms that solve **P1** in (B.11). Thus, methods that use approximations in the data-fit term, *i.e.*, circulant reconstruction (with or without data pre-processing (B.2) and (B.4)) and reflexive end conditions with DCT (B.5), were not included, since they would obviously not converge to a solution of (B.11). **NCG** is an exception since the approximation affects the regularization and not the data-fit term.

For **NCG** we chose the rounding parameter to be $\varepsilon = 10^{-6}$, which yielded good convergence speed without compromising too much the resulting solution. We also used $L = 2$, and 5 line-search iterations. For **MFISTA**, we used $M = 1, 4, 10$, and 20 iterations of [53, Eq. (6)–(7)]. For **SALSA** we used $N = 1, 4$, and 10 CG iterations and $M = 1, 4, 10$, and 15 iterations of [53, Eq. (6)–(7)]. Finally, for **SB** and **SB-MIL** we used $N = 1, 4$, and 10 CG iterations. The CG-solvers inside **SALSA** and **SB** were terminated when $\|\mathbf{x}^{(k+1)}\|_2^2 / \alpha^{(k)} \|\mathbf{d}^{(k)}\|_2^2 < \delta$, where $\mathbf{x}^{(k+1)}$ is the new update, $\mathbf{d}^{(k)}$ is the search direction vector, $\alpha^{(k)}$ is the step size after the k th iteration, and δ is a threshold chosen as $\delta = 10^{-6}$. For all AL-based algorithms we chose the parameters μ and ν using the rules described in §B, with $\lambda = 2^{-15}$, $x_{\max} = 1$, and $\mu_0 = 2^{-4}$.

All the experiments were conducted on a PC with a dual quad-core 2.6GHz Intel Xeon processor. Table B.2 shows the per-iteration time of each algorithm measured in milliseconds.

Since the goal of the restoration problem is to find a solution to the original problem **P1**, we quantified the speed of convergence as the normalized l_2 distance between the estimate at iteration k ($\mathbf{x}^{(k)}$), and the limit $\mathbf{x}^{(\infty)}$ (that represents a solution of **P1**) given by

$$\xi^{(k)} = 10 \log_{10} \left(\frac{\|\mathbf{x}^{(k)} - \mathbf{x}^{(\infty)}\|_2^2}{\|\mathbf{x}^{(\infty)}\|_2^2} \right).$$

The limit $\mathbf{x}^{(\infty)}$ was obtained by running 10^5 iterations of **MFISTA-20**, since **MFISTA** converges to a solution of **P1** and also it would not give an unfair advantage to the proposed ADMM algorithm. Since the computational load per-iteration of each algorithm varies, we evaluated $\xi^{(k)}$ as a function of both iteration number and algorithm run-time. For all algorithms we used $\mathbf{x}^{(0)} = \mathbf{A}'\mathbf{T}'\mathbf{y}$ as the

Table B.2: Outer iteration time of competing algorithms measured in milliseconds. L is the number of line-search iterations, M is the number of Chambolle-type iterations and N is the number of CG iterations.

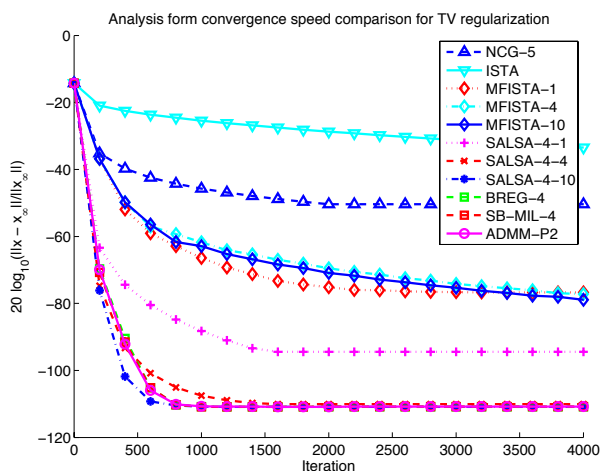
	TV	Wavelet l_1 norm
NCG	$36 + 7L$	$95 + 15L$
ISTA	34	159
MFISTA	$17 + 19M$	$57 + 135M$
SALSA	$20 + 19M + 23N$	$22 + 135M + 24N$
SB	$39 + 31N$	$100 + 30N$
SB-MIL	$40 + 13N$	$102 + 14N$
ADMM-P2	38	90

initial guess. Table B.3 shows the time and iteration number required from each algorithm to reach a -50dB error $\xi^{(k)}$. The threshold of -50dB was chosen as a benchmark since below this point there are practically no visual differences between the reconstructed image $\mathbf{x}^{(k)}$ and the converged image $\mathbf{x}^{(\infty)}$.

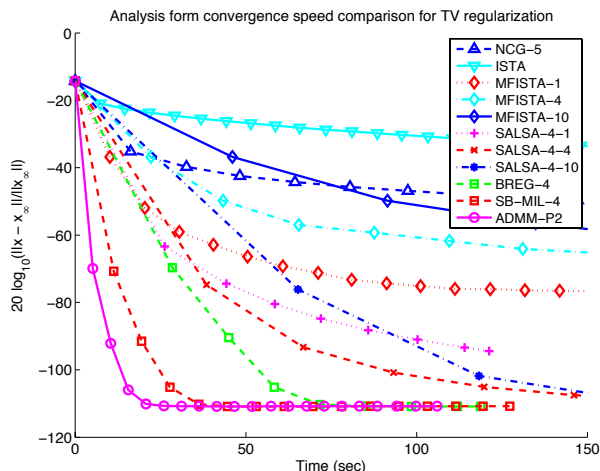
Table B.3: Time and iteration number required for every algorithm to reach -50dB error compared to the converged image $\mathbf{x}^{(\infty)}$.

	TV		Wavelet l_1	
	Time	Iter. #	Time	Iter. #
NCG-5	56.1	298	155.6	1897
ISTA	559.1	15000	885.0	8000
MFISTA-1	18.1	355	46.8	323
MFISTA-4	44.1	407	161.8	367
SALSA-4-1	11.7	88	15.4	71
SALSA-4-4	13.6	71	29.6	60
SALSA-4-10	24.3	74	66.2	61
SB-4	12.5	82	21.9	103
SB-MIL-4	4.9	80	10.7	100
ADMM-P2	2.8	107	5.8	109

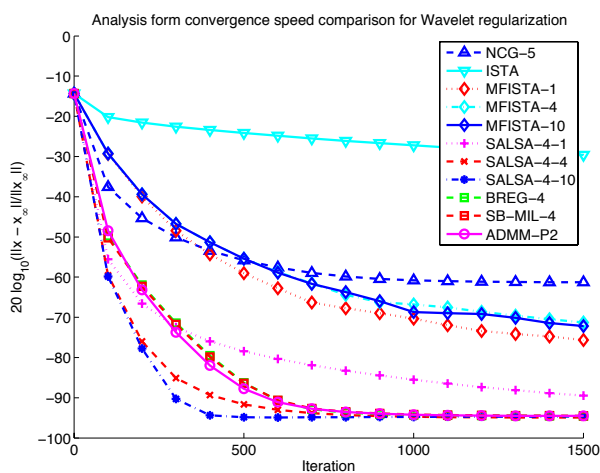
Figure B.4 shows the convergence rate $\xi^{(k)}$ in terms of iteration and run-time for experiments involving TV and wavelet l_1 norm regularizers. The AL based algorithms (**SALSA**, **SB**, **SB-MIL**



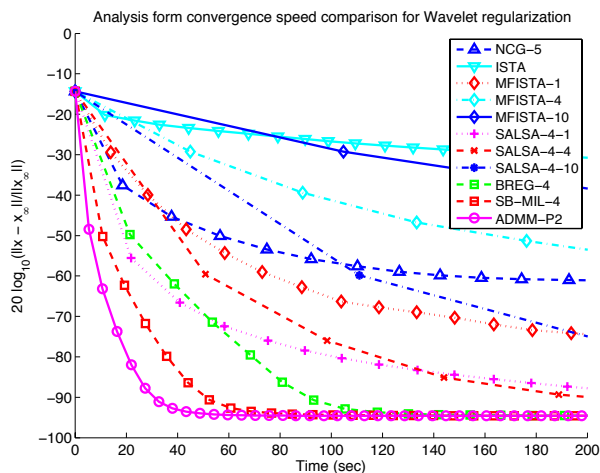
(a) Convergence speed comparison for TV regularization measured in terms of iteration number



(b) Convergence speed comparison for TV regularization measured in terms of run-time



(c) Convergence speed comparison for wavelet l_1 norm regularization measured in terms of iteration number



(d) Convergence speed comparison for wavelet l_1 norm regularization measured in terms of run-time

Figure B.4: Experiment 3: Algorithm convergence speed results with convergence measured in terms of drop in NRMSE in dB, $\xi^{(k)}$, between the estimated image \hat{x} and the converged image $x^{(\infty)}$. Left column (a,c) is convergence per iteration, and right column (b,d) is convergence in run-time. First row (a,b) is from TV regularizer, and second row (c,d) is from wavelet l_1 norm regularizer.

and **ADMM-P2**) converge significantly faster than the rest for all cases.

In terms of convergence rate per iteration, **SALSA** has a slight advantage over **SB**, **SB-MIL** and **ADMM-P2** when we use enough inner Chambolle-type iterations. However, since the inner iterations can be computationally expensive, especially for the analysis l_1 regularization with a wavelet frame, its run-time is significantly higher. In terms of run-time, **ADMM-P2** is the fastest

algorithm with a speed-up of about 2 times compared to the **Split-Bregman-MIL** algorithm, which is the closest competitor.

Discussion

As seen in Figure B.1, image restoration with a circulant model can lead to severe image distortion, when applied to data with realistic boundaries. The ringing artifacts due to the discontinuity at the boundaries are not localized and even existing methods for data-preprocessing [2] either cannot fully suppress these artifacts and/or may be applicable only in specific cases like symmetric PSFs.

Our proposed method showed significant improvement of the restored images compared to the standard method (that uses an unrealistic, purely circulant blur model), when applied to data with more realistic boundaries. Our results reinforce the importance of using reconstruction models that do not make any specific assumptions about boundary extension in the data, and also show that the effects of model mismatch at the boundaries (although often ignored) can be severe in terms of image quality degradation. In the case of reflexive boundary conditions the artifacts can be significantly reduced, but the applicability of this method is only limited to symmetric PSFs [1, 2], whereas our more general model based approach can handle efficiently any type of PSF. In addition, the formulation of our model, even though similar to the one used in [2, 57], leads to a more elegant approach of the non-circulant reconstruction problem that does not require any data pre-processing and estimation of the extrapolated image boundaries.

Our proposed **ADMM-P2** algorithm, using an additional splitting variable, can efficiently handle the additional complexity introduced by the masking operator without the need for costly CG iterations for the inner sub-problems. The fact that our algorithm uses only non-iterative updates enhances its efficiency even when compared to more sophisticated approaches like **SB-MIL**. In addition the formulation is more straightforward compared to **SB-MIL** and allows for easier implementation. The caveat of tuning one additional AL parameter can be easily alleviated by using an empirical method like the one presented in §B. In conclusion, our **ADMM-P2** algorithm, being specifically designed for non-circulant deblurring problems, exhibits improved performance compared to existing state-of-the-art methods [52, 61, 64].

BIBLIOGRAPHY

BIBLIOGRAPHY

- [1] M. Ng, R. Chan, and W. Tang, “A fast algorithm for deblurring models with Neumann boundary conditions,” *siam-js*, vol. 21, no. 3, pp. 851–66, 1999.
- [2] S. J. Reeves, “Fast image restoration without boundary artifacts,” *IEEE Trans. Im. Proc.*, vol. 14, no. 10, pp. 1448–53, Oct. 2005.
- [3] B. P. Sutton, D. C. Noll, and J. A. Fessler, “Dynamic field map estimation using a spiral-in / spiral-out acquisition,” *Mag. Res. Med.*, vol. 51, no. 6, pp. 1194–204, June 2004.
- [4] A. Matakos and J. A. Fessler, “Joint estimation of image and fieldmap in parallel MRI using single-shot acquisitions,” in *Proc. IEEE Intl. Symp. Biomed. Imag.*, 2010, pp. 984–7.
- [5] K. P. Pruessmann, M. Weiger, M. B. Scheidegger, and P. Boesiger, “SENSE: sensitivity encoding for fast MRI,” *Mag. Res. Med.*, vol. 42, no. 5, pp. 952–62, Nov. 1999.
- [6] V. T. Olafsson, D. C. Noll, and J. A. Fessler, “Fast joint reconstruction of dynamic R_2^* and field maps in functional MRI,” *IEEE Trans. Med. Imag.*, vol. 27, no. 9, pp. 1177–88, Sept. 2008.
- [7] J. A. Fessler and D. C. Noll, “Model-based MR image reconstruction with compensation for through-plane field inhomogeneity,” in *Proc. IEEE Intl. Symp. Biomed. Imag.*, 2007, pp. 920–3, Invited paper.
- [8] A. Matakos and J. A. Fessler, “Dynamic MR image and fieldmap joint reconstruction accounting for through-plane fieldmap gradients,” in *Proc. IEEE Intl. Symp. Biomed. Imag.*, 2011, pp. 393–6.
- [9] J. A. Fessler, S. Lee, V. T. Olafsson, H. R. Shi, and D. C. Noll, “Toeplitz-based iterative image reconstruction for MRI with correction for magnetic field inhomogeneity,” *IEEE Trans. Sig. Proc.*, vol. 53, no. 9, pp. 3393–402, Sept. 2005.
- [10] S. Ramani and J. A. Fessler, “Parallel MR image reconstruction using augmented Lagrangian methods,” *IEEE Trans. Med. Imag.*, vol. 30, no. 3, pp. 694–706, Mar. 2011.
- [11] A. Matakos, S. Ramani, and J. A. Fessler, “Accelerated edge-preserving image restoration without boundary artifacts,” *IEEE Trans. Im. Proc.*, vol. 22, no. 5, pp. 2019–29, May 2013.

- [12] J. P. Delmas and H. Abeida, “Stochastic cramer-rao bound for noncircular signals with application to DOA estimation,” *IEEE Trans. Sig. Proc.*, vol. 52, no. 11, pp. 3192–99, Nov. 2004.
- [13] H. Bruder, H. Fischer, H-E. Reinfelder, and F. Schmitt, “Image reconstruction for echo planar imaging with nonequidistant k-space sampling,” *Mag. Res. Med.*, vol. 23, no. 2, pp. 311–23, Feb. 1992.
- [14] N. Chen and A. M. Wyrwicz, “Removal of EPI Nyquist ghost artifacts with two-dimensional phase correction,” *Mag. Res. Med.*, vol. 51, no. 6, pp. 1247–53, June 2004.
- [15] P. Kellman and E. R. McVeigh, “Phased array ghost elimination,” *NMR Biomed.*, vol. 19, pp. 352–61, 2006.
- [16] Q-S. Xiang and F. Q. Ye, “Correction for geometric distortion and N/2 ghosting in EPI by phase labeling for additional coordinate encoding (PLACE),” *Mag. Res. Med.*, vol. 57, no. 4, pp. 731–41, Apr. 2007.
- [17] Y-C. Kim, J-F. Nielsen, and K. S. Nayak, “Automatic correction of echo-planar imaging (EPI) ghosting artifacts in real-time interactive cardiac MRI using sensitivity encoding,” *J. Mag. Res. Im.*, vol. 27, no. 1, pp. 239–45, Jan. 2008.
- [18] W. S. Hoge, H. Tan, and R. A. Kraft, “Robust EPI Nyquist ghost elimination via spatial and temporal encoding,” *Mag. Res. Med.*, vol. 64, no. 6, pp. 1781–91, 2010.
- [19] N-K. Chen, A. V. Avram, and A. W. Song, “Two-dimensional phase cycled reconstruction for inherent correction of EPI Nyquist artifacts,” *Mag. Res. Med.*, vol. 66, no. 4, pp. 1057–66, Oct. 2011.
- [20] D. C. Noll, C. H. Meyer, J. M. Pauly, D. G. Nishimura, and A. Macovski, “A homogeneity correction method for magnetic resonance imaging with time-varying gradients,” *IEEE Trans. Med. Imag.*, vol. 10, no. 4, pp. 629–37, Dec. 1991.
- [21] A. K. Funai, J. A. Fessler, D. T. B. Yeo, V. T. Olafsson, and D. C. Noll, “Regularized field map estimation in MRI,” *IEEE Trans. Med. Imag.*, vol. 27, no. 10, pp. 1484–94, Oct. 2008.
- [22] A. Matakos, J-F. Nielsen, and J. A. Fessler, “Model based Nyquist ghost correction for EPI,” *IEEE Trans. Med. Imag.*, 2013, Submitted.
- [23] C. B. Ahn and Z. H. Cho, “A new phase correction method in NMR imaging based on autocorrelation and histogram analysis,” *IEEE Trans. Med. Imag.*, vol. 6, no. 1, pp. 32–6, Mar. 1987.
- [24] X. Hu and T. H. Le, “Artifact reduction in EPI with phase-encoded reference scan,” *Mag. Res. Med.*, vol. 36, no. 1, pp. 166–71, July 1996.

- [25] M. H. Buonocore and L. Gao, “Ghost artifact reduction for echo planar imaging using image phase correction,” *Mag. Res. Med.*, vol. 38, no. 1, pp. 89–100, July 1997.
- [26] M. H. Buonocore and D. C. Zhu, “Image-based ghost correction for interleaved EPI,” *Mag. Res. Med.*, vol. 45, no. 1, pp. 96–108, Jan. 2001.
- [27] F. Hennel, “Image-based reduction of artifacts in multishot echo-planar imaging,” *J. Mag. Res.*, vol. 134, no. 2, pp. 206–13, Oct. 1998.
- [28] M. H. Buonocore and D. C. Zhu, “High spatial resolution epi using an odd number of interleaves,” *Mag. Res. Med.*, vol. 41, no. 6, pp. 1199–205, June 1999.
- [29] D. L. Foxall, P. R. Harvey, and J. Huang, “Rapid iterative reconstruction for echo planar imaging,” *Mag. Res. Med.*, vol. 42, no. 3, pp. 541–7, Sept. 1999.
- [30] S. Clare, “Iterative Nyquist ghost correction for single and multi-shot EPI using an entropy measure,” in *Proc. Intl. Soc. Mag. Res. Med.*, 2003, p. 1041.
- [31] S. B. Reeder, E. Atalar, A. Z. Faranesh, and E. R. McVeigh, “Referenceless interleaved echo-planar imaging,” *Mag. Res. Med.*, vol. 41, no. 1, pp. 87–94, Jan. 1999.
- [32] S. M. Grieve, A. M. Blamire, and P. Styles, “Elimination of Nyquist ghosting caused by read-out to phase-encode gradient cross-terms in EPI,” *Mag. Res. Med.*, vol. 47, no. 2, pp. 337–43, Feb. 2002.
- [33] Q. X. Yang, S. Posse, D. Le Bihan, and M. B. Smith, “Double-sampled echo-planar imaging at 3 Tesla,” *J. Mag. Res. B*, vol. 113, no. 2, pp. 145–50, Nov. 1996.
- [34] B. A. Poser, M. Barth, P-E. Goa, W. Deng, and V. A. Stenger, “Single-shot echo-planar imaging with Nyquist ghost compensation: Interleaved dual echo with acceleration (IDEA) echo-planar imaging (EPI),” *Mag. Res. Med.*, vol. 69, no. 1, pp. 37–47, Jan. 2013.
- [35] A. Macovski, “Noise in MRI,” *Mag. Res. Med.*, vol. 36, no. 3, pp. 494–7, Sept. 1996.
- [36] J. A. Fessler, “Model-based image reconstruction for MRI,” *IEEE Sig. Proc. Mag.*, vol. 27, no. 4, pp. 81–9, July 2010, Invited submission to special issue on medical imaging.
- [37] G. Golub and V. Pereyra, “Separable nonlinear least squares: the variable projection method and its applications,” *Inverse Prob.*, vol. 19, no. 2, pp. R1–26, Apr. 2003.
- [38] D. R. Hunter and K. Lange, “A tutorial on MM algorithms,” *American Statistician*, vol. 58, no. 1, pp. 30–7, Feb. 2004.
- [39] P. B. Roemer, W. A. Edelstein, C. E. Hayes, S. P. Souza, and O. M. Mueller, “The NMR phased array,” *Mag. Res. Med.*, vol. 16, no. 2, pp. 192–225, Nov. 1990.

- [40] M. J. Allison, S. Ramani, and J. A. Fessler, “Accelerated regularized estimation of MR coil sensitivities using augmented Lagrangian methods,” *IEEE Trans. Med. Imag.*, vol. 32, no. 3, pp. 556–64, Mar. 2013.
- [41] J. A. Fessler and B. P. Sutton, “Nonuniform fast Fourier transforms using min-max interpolation,” *IEEE Trans. Sig. Proc.*, vol. 51, no. 2, pp. 560–74, Feb. 2003.
- [42] U. Techavipoo, J. Lackey, J. Shi, T. Leist, and S. Lai, “Geometric distortion correction in EPI by phase labeling using sensitivity encoding (PLUS),” in *Proc. IEEE Intl. Symp. Biomed. Imag.*, 2008, pp. 556–9.
- [43] J. A. Fessler and W. L. Rogers, “Spatial resolution properties of penalized-likelihood image reconstruction methods: Space-invariant tomographs,” *IEEE Trans. Im. Proc.*, vol. 5, no. 9, pp. 1346–58, Sept. 1996.
- [44] O. Speck and J. Hennig, “Functional imaging by I_0 and T_2^* -parameter mapping using multi-image EPI,” *Mag. Res. Med.*, vol. 40, no. 2, pp. 243–8, Aug. 1998.
- [45] D. B. Twieg and S. J. Reeves, “Basic properties of SS-PARSE parameter estimates,” *IEEE Trans. Med. Imag.*, vol. 29, no. 5, pp. 1156–72, May 2010.
- [46] C. Yip, J. A. Fessler, and D. C. Noll, “Advanced three-dimensional tailored RF pulse for signal recovery in T_2^* -weighted functional magnetic resonance imaging,” *Mag. Res. Med.*, vol. 56, no. 5, pp. 1050–9, Nov. 2006.
- [47] L. I. Rudin, S. Osher, and E. Fatemi, “Nonlinear total variation based noise removal algorithm,” *Physica D*, vol. 60, no. 1-4, pp. 259–68, Nov. 1992.
- [48] T. F. Chan, S. Osher, and J. Shen, “The digital TV filter and nonlinear denoising,” *IEEE Trans. Im. Proc.*, vol. 10, no. 2, pp. 231–41, Feb. 2001.
- [49] J. P. Oliveira, J. M. Bioucas-Dias, and M. A. T. Figueiredo, “Adaptive total variation image deblurring: A majorization-minimization approach,” *Signal Processing*, vol. 89, no. 9, pp. 1683–93, Sept. 2009.
- [50] M. A. T. Figueiredo and R. D. Nowak, “An EM algorithm for wavelet-based image restoration,” *IEEE Trans. Im. Proc.*, vol. 12, no. 8, pp. 906–16, Aug. 2003.
- [51] C. Vonesch and M. Unser, “A fast multilevel algorithm for wavelet-regularized image restoration,” *IEEE Trans. Im. Proc.*, vol. 18, no. 3, pp. 509–23, Mar. 2009.
- [52] M. V. Afonso, J. M. Bioucas-Dias, and M. A. T. Figueiredo, “Fast image recovery using variable splitting and constrained optimization,” *IEEE Trans. Im. Proc.*, vol. 19, no. 9, pp. 2345–56, Sept. 2010.

- [53] I. W. Selesnick and M. A. T. Figueiredo, “Signal restoration with overcomplete wavelet transforms: comparison of analysis and synthesis priors,” in *Proc. SPIE 7446 Wavelets XIII*, 2009, p. 74460D, Wavelets XIII.
- [54] A. Beck and M. Teboulle, “A fast iterative shrinkage-thresholding algorithm for linear inverse problems,” *SIAM J. Imaging Sci.*, vol. 2, no. 1, pp. 183–202, 2009.
- [55] M. A. T. Figueiredo and J. M. Bioucas-Dias, “Restoration of Poissonian images using alternating direction optimization,” *IEEE Trans. Im. Proc.*, vol. 19, no. 12, pp. 3133–45, Dec. 2010.
- [56] M. V. Afonso, J. M. Bioucas-Dias, and M. A. T. Figueiredo, “An augmented Lagrangian approach to the constrained optimization formulation of imaging inverse problems,” *IEEE Trans. Im. Proc.*, vol. 20, no. 3, pp. 681–695, Mar. 2011.
- [57] M. Sorel, “Removing boundary artifacts for real-time iterated shrinkage deconvolution,” *IEEE Trans. Im. Proc.*, vol. 21, no. 4, pp. 2329–34, Apr. 2012.
- [58] M. Elad, P. Milanfar, and R. Rubinstein, “Analysis versus synthesis in signal priors,” *Inverse Prob.*, vol. 23, no. 3, pp. 947–68, June 2007.
- [59] J. A. Fessler and S. D. Booth, “Conjugate-gradient preconditioning methods for shift-variant PET image reconstruction,” *IEEE Trans. Im. Proc.*, vol. 8, no. 5, pp. 688–99, May 1999.
- [60] I. Daubechies, M. Defrise, and C. D. Mol, “An iterative thresholding algorithm for linear inverse problems with a sparsity constraint,” *Comm. Pure Appl. Math.*, vol. 57, no. 11, pp. 1413–57, Nov. 2004.
- [61] A. Beck and M. Teboulle, “Fast gradient-based algorithms for constrained total variation image denoising and deblurring problems,” *IEEE Trans. Im. Proc.*, vol. 18, no. 11, pp. 2419–34, Nov. 2009.
- [62] Y. Wang, J. Yang, W. Yin, and Y. Zhang, “A new alternating minimization algorithm for total variation image reconstruction,” *SIAM J. Imaging Sci.*, vol. 1, no. 3, pp. 248–72, 2008.
- [63] W. Yin, S. Osher, D. Goldfarb, and J. Darbon, “Bregman iterative algorithms for l_1 -minimization with applications to compressed sensing,” *SIAM J. Imaging Sci.*, vol. 1, no. 1, pp. 143–68, 2008.
- [64] T. Goldstein and S. Osher, “The split Bregman method for L1-regularized problems,” *SIAM J. Imaging Sci.*, vol. 2, no. 2, pp. 323–43, 2009.
- [65] S. Ramani and J. A. Fessler, “A splitting-based iterative algorithm for accelerated statistical X-ray CT reconstruction,” *IEEE Trans. Med. Imag.*, vol. 31, no. 3, pp. 677–88, Mar. 2012.

- [66] J. Eckstein and D. P. Bertsekas, “On the Douglas-Rachford splitting method and the proximal point algorithm for maximal monotone operators,” *Mathematical Programming*, vol. 55, no. 1-3, pp. 293–318, Apr. 1992.